Enabling More Accurate Calculation Of Thermoelectric Properties From Density Functional Perturbation Theory.

Ben Durham

Doctor of Philosophy

Physics
University of York

July 2025

Abstract

Significant progress has been made over recent years in improving the accuracy of density functional approximations for electronic structure simulations. The advent of the so called "meta generalised gradient approximations" (meta-GGAs) has significantly improved the chemical accuracy possible using density functional theory methods, with minor additional computational cost. However, the introduction of meta-GGAs poses additional challenges that need to be overcome. Much work has been done to develop the formalism of density functional perturbation theory as an accurate and efficient method to calculate material properties; however, the formalism must be extended to enable such calculations using meta-GGA functionals. In addition to this, following the development of the first successful meta-GGAs, it was quickly observed that many meta-GGA functionals suffer from severe numerical instability, which can have significant effects on the physical properties predicted by electronic structure simulations. This thesis gives details of the necessary steps to extend the framework of density functional perturbation theory calculations of material properties with meta-GGA functionals, as well as approaches to quantify and address the numerical instability present in calculations using meta-GGAs. This is then applied to the calculation of commonly calculated material response functions, phonon modes and elastic constants tensors. The developed methods are verified against finite difference calculations.

Contents

List of Figures

List of Tables

Declarations

I declare that the work presented in this thesis, except where otherwise stated, is based on my own research and has not been submitted previously for a degree in this or any other university. All sources have been acknowledged as references.

Parts of the work reported in this thesis have been published, or are being prepared for publication in the following papers.

B. Durham, M. I. J. Probert and P. J. Hasnip, "Beating the Egg-box Effect in Plane-Wave DFT Simulations", *Electronic Structure* **7(2)**, May 2025 DOI: 10.1088/2516-1075/adc056

B. Durham, M. I. J. Probert and P. J. Hasnip, "Density Functional Perturbation Theory applied to meta-GGA functionals"

Signed

Ben Durham

Acknowledgements

I would firstly like to thank my supervisors Dr. Phil Hasnip and Prof. Matt Probert for providing constant support, guidance, and useful advice, as well as their patience with my propensity to take up "side projects" which quickly snowballed into the bulk of this thesis. Without their encouragement, none of the work described could have been completed, and certainly would not have been written up.

No less important to the completion of this thesis, I would also like to thank my partner Anna Weatherburn. At many times during my PhD she has provided me with invaluable assistance, and crucially perspective. For all the times she was my "rubber duck", for the countless grammatical corrections she pointed out, and for all the ways she reminded me that life extends beyond the PhD, I am extremely grateful to have Anna in my life.

I would also like to express my gratitude to my family. Thanks to my mother, for her unwavering support of many forms throughout all the years, ranging from emotional, to financial to medical. Thanks also to my brother Andrew, for providing me with inspiration throughout my life, particularly for inspiring holidays which formed several non-negotiable deadlines which were crucial in the completion of this thesis.

Finally, thanks to all of my friends, particularly Ed, Connor, Rachel, and Eleanor, for their support, patience, and love.

For Dad.

Glossary of terms and common symbols

- Notation

  $\boldsymbol{V}$ A vector is designated by being in bold font.

  V_α, V^α The particular component of a vector is designated by a subscript or superscript, Greek letters are used to denote the Cartesian direction, x, y and z.

  $M_{\alpha\beta}$, $M^{\alpha\beta}$ The particular component of a matrix or rank-2 tensor is designated by a double subscript or superscript, Greek letters are used to denote a Cartesian direction, x, y and z.

  $|\boldsymbol{V}|$ The euclidean norm of a vector.

  ∇ The gradient operator. Takes the derivative of a function with respect to position, $\boldsymbol{r}$.

  ∇^2 The Laplacian operator.

  The Einstein summation convention will be used for the tensor notation throughout.

- Constants

  $k_{\mathbf{B}}$ The Boltzmann constant.

  $m_{\mathbf{e}}$ The mass of an electron.

  $\hbar$ Reduced Plank's constant, Plank's constant divided by 2π.

- Variables

  Ω The volume of the unit cell.

  M_I Mass of an atom with the label I.

  $\boldsymbol{R}_I$ Position in the unit cell of an atom with the label I.

- Abbreviations

  FFT Fast Fourier Transform

  DFT Density Functional Theory

  KED Kinetic Energy Density

  LDA Local Density Approximation

  GGA Generalised Gradient Approximation

  mGGA meta Generalised Gradient Approximation

Chapter 1

Introduction

1.1 Material Simulation

World energy consumption is increasing each year, resulting in the burning of more fossil fuels, releasing more CO_2 into the atmosphere and causing steadily larger contributions to climate change [8]. It is of vital importance that we reduce this contribution in several ways; reducing our power consumption and improving the efficiency of power generation and usage [9]. By finding new materials, and improving the properties of the materials we currently use, these goals can be accomplished. One class of materials that may play an important role in achieving the goal of improving energy efficiency are thermoelectric materials [10].

As our requirements and material designs become increasingly complex, testing these materials also becomes more challenging, requiring more time and greater financial investment. In contrast to this, as time goes on, computers become more powerful and cheaper to produce and run. Eventually, it becomes a far more viable option to run simulations of materials and use computational experiments rather than physical experiments. Computer simulations can be used to perform a detailed study of extreme conditions where experiments are very difficult or impossible to replicate [11]. Simulations can also be used to make cheap predictions about the properties of materials without having to physically make them. The downside is that the simulations require accurate physical theories that must then be translated correctly into software.

Density Functional Theory (DFT) is a quantum-mechanical modelling method used to study the electronic structure of materials. It is widely used in predicting material properties such as electronic band structure, density of states, magnetism, and mechanical properties [12]. DFT simplifies the many-body Schrödinger equation by expressing the system's energy as a functional of the electron density, making it computationally feasible for large systems [13].

DFT strikes a balance between accuracy and computational efficiency. It can provide reliable predictions for a wide range of materials at a fraction of the computational cost of more accurate wavefunction-based methods (e.g. Quantum Monte Carlo [14] or Coupled Cluster [15] simulations). However, the accuracy of DFT depends on the choice of approximation for the exchange-correlation functional. The commonly used Generalised Gradient Approximation (GGA) [2] and Local Density Approximation (LDA) [16] offer reasonable results for many materials but struggle with strongly correlated systems and van der Waals interactions. Hybrid functionals which mix DFT with wavefunction methods like Hartree-Fock theory and more advanced methods such as many-body perturbation theory can improve accuracy but at a far higher computational cost. Despite these limitations, DFT remains a powerful and widely used tool in materials science because of its ability to predict material properties with reasonable accuracy at a manageable computational cost.

1.1.1 Thermoelectric Materials

Thermoelectric materials are materials that can convert a temperature gradient across the material into a potential difference, which can be used to drive a current. Simply put, anywhere heat is generated, a thermoelectric device can convert that thermal energy into useful energy. Since all waste energy is eventually lost as heat, thermoelectric materials offer the capability to reclaim some of this lost energy and greatly improve the efficiency of these devices [17]. The ability of a thermoelectric material to convert heat to electrical energy is judged by the dimensionless figure of merit, ZT [18]. The thermoelectric efficiency, η, is a function of ZT and the temperatures at each side of the thermal gradient,

$$\eta = \frac{T_{\mathrm{H}} - T_{\mathrm{C}}}{T_{\mathrm{H}}} \cdot \frac{\sqrt{1+Z\bar{T}}-1}{\sqrt{1+Z\bar{T}}+\frac{T_{\mathrm{C}}}{T_{\mathrm{H}}}}, \tag{1.1}$$

where T_{H} & T_{C} are the hot and cold sides of the temperature gradient and $\bar{T}$ is the average of these temperatures. The Carnot efficiency is the first term on the right-hand side of the above expression and is the maximum possible efficiency that can be achieved by an ideal heat engine. In the limit of ZT tending to infinity, an ideal heat engine is achieved.

The ZT of a material is calculated from several material properties,

$$ZT = \frac{S^2\sigma}{\kappa_{\mathrm{elec}} + \kappa_{\mathrm{lat}}}\bar{T} \tag{1.2}$$

where σ is the electrical conductivity of the material; κ_{elec} and κ_{lat} are the ther-

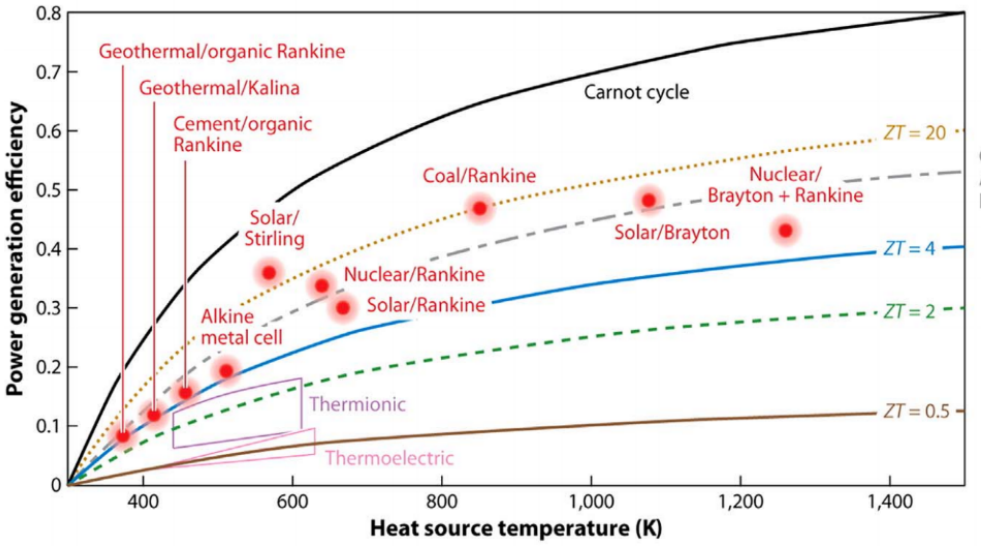

Figure 1.1: Comparison of thermoelectric materials with particular ZT values against other forms of energy generation [1].

mal conductivity of the material due to the electrons and the lattice vibrations (phonons) respectively, and S is the Seebeck coefficient of the material. The Seebeck coefficient is defined as $S = -\frac{\Delta V}{\Delta T}$, where ΔV is the voltage between the two ends of the material due to a temperature difference of ΔT. The Seebeck coefficient can be considered as a measure of the asymmetry of the density of states around the Fermi level, high asymmetry giving a high Seebeck coefficient. For a material to have high thermoelectric efficiency, it must have a large ZT value and therefore requires low thermal conductivity, a high Seebeck coefficient and high electrical conductivity.

Figure 1.1 shows a comparison of the efficiency of various power generation methods with an ideal Carnot engine and the thermoelectric efficiency of various values for ZT. A stable, reliable and inexpensive thermoelectric material with $ZT \geq 2$ would be efficient and cost effective enough to be considered a viable method of recovering waste heat. With a $ZT \geq 4$, a thermoelectric device would be efficient enough to compete with other methods of energy generation, for example, it could be used to make geothermal power generation more viable.

Current thermoelectric materials that are easily manufacturable have ZT values of around $0.5 - 1.0$. and are made of materials such as bismuth telluride (Bi_2Te_3) [19, 20]. One major problem with these materials is that they further increase our dependence on rare materials which are becoming increasingly scarce. From an economic perspective, the cost reduction resulting from the efficiency gained from introducing thermoelectric materials into devices is not yet enough to offset the expense of sourcing the raw materials required. In order for thermoelectric materials to become practically useful for reclaiming wasted heat, they first need

to become more efficient at doing so, this requires the condensed matter physics community to research ways to improve our existing materials or discover other materials with improved thermoelectric properties [1].

One set of materials that has shown promise in the development of thermoelectric materials is half-Heusler alloys [21, 22, 23, 24, 25, 26]. In particular, simulations employing DFT and perturbation theory have predicted TaFeSb to have a very high value for ZT at high temperatures, $ZT = 1.5$ at $T = 1000$ K [23, 24], which makes this material of particular interest for future research. The experimental synthesis of high-quality, single-crystal TaFeSb has proved to be difficult so far [27]; therefore, the predictions from DFT and perturbation theory remain unconfirmed for now. However, robust predictions of ZT are particularly difficult to make.

As shown in equation 1.2, a calculation of ZT is dependent on several physical properties of the material, none of them being trivial to determine. Each of these properties requires careful calculation and a sufficient theoretical treatment so that all the dominant effects are accurately captured. However, for many materials, the computational cost of these calculations can be immense and prohibitive, requiring a huge amount of time and energy to be performed accurately using our existing methods.

Even when performed at a high level of precision, existing methods are often not accurate due to assumptions made when constructing the supporting theory. Therefore, the calculation of each property allows inaccuracies to be introduced in the final predicted value of ZT and reduces the confidence of any predictions made. The reduced confidence in the theoretical predictions means that it is obviously less likely that the material exhibits the predicted ZT, but also a decreased likelihood that experimental efforts will be directed towards synthesising, characterising and testing the material. This compounds the likelihood that predictions of this nature will continue to go unconfirmed. Improving the robustness of theoretical predictions, whilst still maintaining relatively low computational costs, will enable theoretical methods to lead the way in material discovery.

In order to make robust predictions, work must be done to address areas where the computational cost is prohibitive or where our theory is not sufficiently accurate. Recent progress has been made in the development of more accurate density functional approximations for electronic structure simulations. The Strongly Constrained and Appropriately Normed (SCAN) functional was the first meta-Generalised-Gradient Approximation (mGGA) to adhere to all known constraints for a mGGA functional [28]. This was a major achievement for chemical accuracy; however, it was quickly observed that SCAN, as with many other meta-GGA functionals, suffered from severe numerical instability [29, 30, 31, 32, 33, 34, 35].

This led to the creation of several related functionals [29, 36, 37, 38], which attempted to regularise the numerical behaviour of SCAN, while maintaining SCAN's physical accuracy. These attempts have been mostly successful, leading to many recent publications displaying the accuracy of these functionals [31, 39, 40, 41, 42, 43, 44, 45, 46].

When considering half-Heusler materials, almost all research in the literature has used GGA functionals rather than the more chemically accurate mGGA functionals. In fact, there have been cases where the GGA level of theory has completely failed to accurately describe the electronic structure of materials, and researchers have had to resort to empirically fitting corrections to their theory [25]. This displays a clear need for more accurate theoretical frameworks when modelling the thermoelectric properties of half-Heuslers. The sparse usage of mGGAs for the investigation of half-Heuslers is hardly surprising, since the development of accurate mGGAs only occurred relatively recently; however, when mGGAs have been employed, they have been used successfully [22, 26]. One of the reasons that limits the usage of the more accurate mGGA functionals is that they have not been integrated into the perturbation theory formalism of DFT. This makes the prediction of several material properties significantly more expensive and highly subject to the aforementioned numerical issues, which can make the calculations even more expensive.

Considering one of the most promising half-Heusler materials, TaFeSb, it can be seen that a change in the XC functional can make some differences in the physical and electronic structure properties. When the crystal structure of TaFeSb is found using a GGA functional and a mGGA functional, PBE [2] and r2SCAN [36] respectively, the lattice constants are found to be $a_{\mathrm{PBE}} = 4.22$ and $a_{\mathrm{r2SCAN}} = 4.19$, which only differ by $\sim 0.6\%$. It can be seen from Figures 1.2 and 1.3 that there is also no dramatic change in the predicted electronic structure of TaFeSb when switching to a higher level of theory. The main features of both the band structure and the DOS remain largely similar when compared between the two functionals; however, when r2SCAN is used, the band gap opens up a bit wider, from a gap of 0.813 eV when using PBE, to a gap of 1.05 eV, a change of around 20%, which is more significant.

The BoltzTraP2 software package [47] can be used to predict several of the transport coefficients relevant to calculating the thermoelectric figure of merit, ZT. The transport coefficients are calculated from the band energies produced by an electronic structure package and are calculated as functions of temperature and chemical potential, which is related to the doping of the material. This is done by solving the Boltzmann transport equation for electrons in the Constant Relaxation Time Approximation (CRTA) [48]. In the CRTA, the Seebeck coefficient

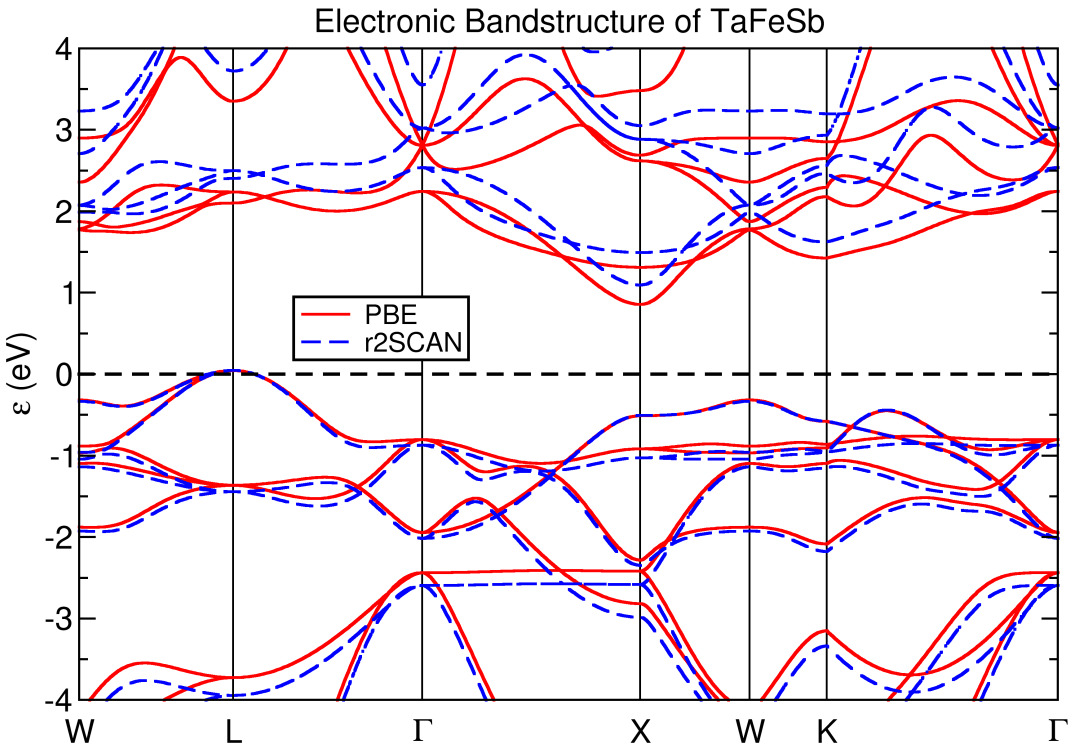

Figure 1.2: Electronic band-structure of TaFeSb computed using DFT with a GGA functional (PBE) and a mGGA functional (r2SCAN), where the energies of both calculations have been shifted so that the valence band maximum is at 0 eV.

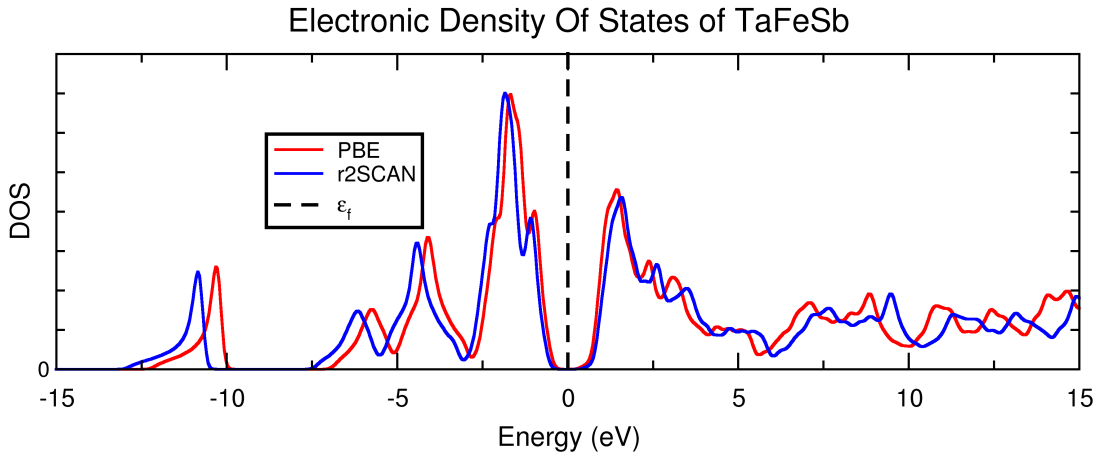

Figure 1.3: Electronic density of states (DOS) of TaFeSb computed using DFT with a GGA functional (PBE) and a mGGA functional (r2SCAN), where the energies of both calculations have been shifted so that the Fermi level is at 0 eV.

can be calculated explicitly; however, the values for the electrical conductivity, σ, and the thermal conductivity due to the electrons, κ_{elec}, are calculated per charge carrier relaxation time, τ, which is not determined by BoltzTraP2.

Figures 1.4 and 1.5 show comparisons of the BoltzTraP2 predicted values for the "Power Factor" and thermal conductivity due to electrons per charge carrier relaxation time, $\frac{S^2\sigma}{\tau}$ and $\frac{\kappa_{\text{elec}}}{\tau}$, as a function of the doped Fermi energy. From these plots it can be seen that besides the obvious change in the band gap, the predictions of the GGA functional and meta-GGA functional are very similar in features under doping. Therefore, any change in the predicted values of ZT between the two functionals will likely come from changes in the properties involved in the calculation of ZT, τ and κ_{lat}.

Calculations of τ and κ_{lat} can be achieved by various methods, all of which depend in some way on calculating the response of the electrons to some perturbation. Methods of calculating this response are discussed at greater length in Chapter 3, currently however, calculations of materials responses using mGGAs are limited due to the numerical stability of the mGGA functionals and the absence of the proper incorporation of the mGGAs into the more efficient Density Functional Perturbation Theory (DFPT) methods. The work in this thesis addresses each of these limitations.

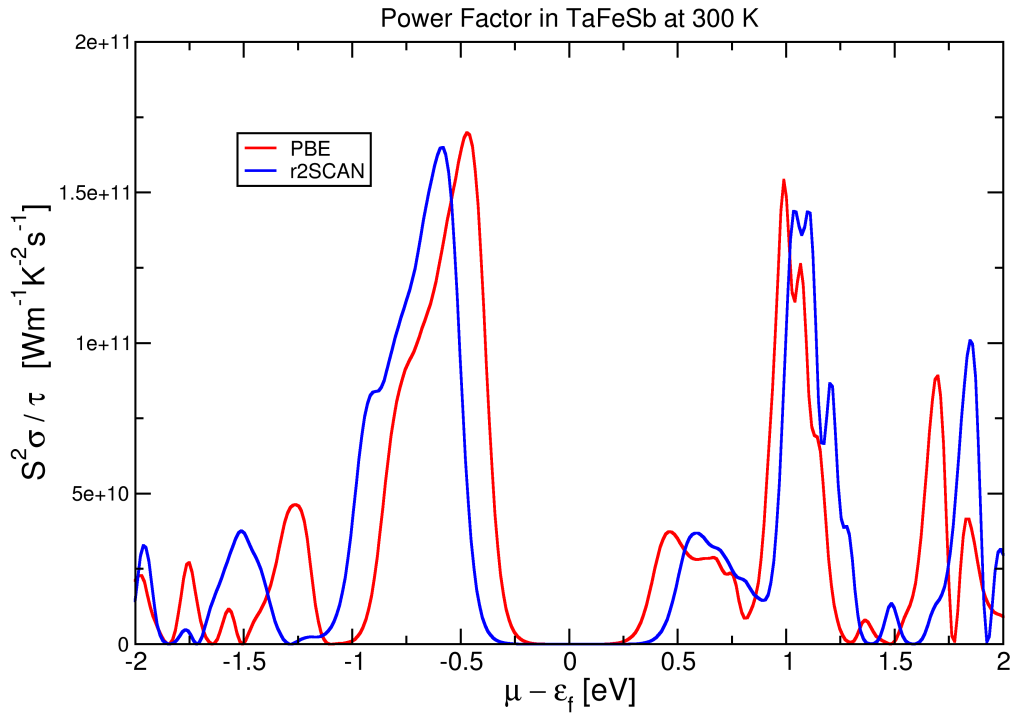

Figure 1.4: Power Factor ($S^2\sigma$) per charge carrier relaxation time (τ) of TaFeSb computed using DFT with a GGA functional (PBE) and a mGGA functional (r2SCAN), at 300 K as a function of the doped chemical potential μ.

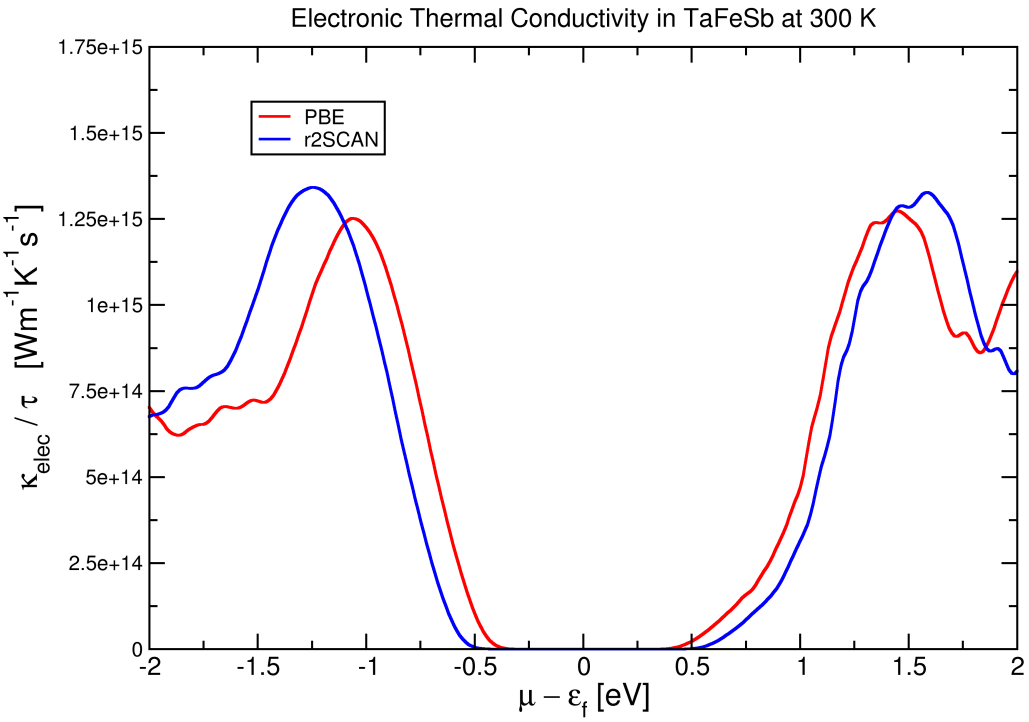

Figure 1.5: Thermal Conductivity due to electrons (κ_{elec}) per charge carrier relaxation time (τ) of TaFeSb computed using DFT with a GGA functional (PBE) and a mGGA functional (r2SCAN), at 300 K as a function of the doped chemical potential μ.

1.2 Layout of Thesis

The over-arching aim of this thesis is to extend the framework of density functional perturbation theory to enable linear response calculations of material properties with mGGA functionals. This will mean that calculations of thermoelectric materials can be performed more efficiently and with a more accurate description of the electronic states, which will strongly influence the prediction of material properties.

The thesis is set out as follows:

- Chapter 2 sets out the fundamentals of DFT and details the formalism of the local and semi-local density functional approximations, in particular noting additional terms that must be included when using mGGA functionals.
- Chapter 3 describes how particular material properties can be understood as derivatives of a system's total energy, and how the approach of density functional perturbation theory can be used to access these energy derivatives. Expressions are derived for the energy derivatives with respect to general perturbations for the mGGA formalism.
- Chapter 4 focuses on the specifics of calculating the phonon modes of a material in the harmonic approximation using perturbation theory, expressions for the energy derivatives required for this are given within the mGGA formalism. The derivations are implemented in a DFT simulation software and verified using silicon as a test case.
- Chapter 5 concentrates on the numerical issues that arise when using mGGA functionals. An uncertainty quantification technique for these numerical errors is proposed as well as a more efficient technique to address them.
- Chapter 6 focusses on the method of determining the elastic constants of a material using perturbation theory, providing the energy derivative expressions necessary within the mGGA framework. These derivations are incorporated into a DFT simulation program and validated again using silicon as a test case. Then a comparison is made between the prediction of the elastic constants for several materials obtained using different theoretical approaches, each of which is compared to experimental results.
- Chapter 7 summarises the work carried out in this thesis and combines the results on the future work to be carried out. To illustrate the methods developed in this thesis, they are applied to the case of TaFeSb. A comparison is then made between the prediction of the phonon band structure

and density of states for TaFeSb obtained using a GGA functional and a more accurate mGGA functional. Finally, elastic response calculations are used to compute values for τ and κ_{lat}, which are then used to calculate predictions of ZT for TaFeSb in using both the PBE functional and the r2SCAN functional.

The aim of this thesis is not to make any grand predictions of previously unknown thermoelectric materials, nor is it to take a study from recent years and duplicate their work with the latest exchange-correlation approximation. Rather, the aim is to make a significant extension to our current capabilities within density functional perturbation theory, enabling more efficient and more accurate calculation of material properties using higher levels of theory, as well as addressing the challenges of using said theories in practical simulations.

1.3 Software

In this work, we will be using a number of software packages to simulate these materials and subsequently analyse the results using methods described below. These packages include:

- CASTEP [49] - CASTEP is a leading software package for calculating the properties of materials from first principles using density functional theory. It enables the simulation of a wide range of material properties, including energetics, atomic-level structures, vibrational characteristics, and electronic responses. Notably, CASTEP offers extensive spectroscopic features that directly correlate with experimental techniques, such as infrared and Raman spectroscopy. A Sternheimer solver underpins the calculation of a variety of such response functions and its performance characteristics are the limiting factor in studying various spectroscopic phenomena such as phonons. All DFT calculations will be performed using CASTEP and all derived extensions to theory will be implemented as functionality within CASTEP.

- LibXC [50] - A library of exchange, correlation and kinetic energy functionals for DFT. LibXC includes various types of functionals (LDA, GGA, and meta-GGA (mGGA) functionals) and for each can evaluate the energy density and its derivatives in a correct fashion. LibXC is based on the use of computer algebra and automatic code generation to enable the generation of bug-free code. LibXC can calculate both the functional itself and its first- through fourth derivatives. The second order derivatives in particular

are utilised in this work for calculating the response of the exchange and correlation potential.

- BoltzTraP2 [47] - A software package for predicting several material transport coefficients for extended systems using the linearized Boltzmann transport equation. It uses only the band energies calculated across the 1st Brillouin zone. Its use in this thesis has already been demonstrated in the figures above, calculating the power factor and thermal conductivity per relaxation time of the charge carriers for TaFeSb.

Chapter 2

Density Functional Theory

This chapter outlines the fundamental principles of density functional theory (DFT), which is the theory that underpins all subsequent work in this thesis. Particular attention is given to distinguishing among various types of density functional approximations, especially the "meta generalised gradient approximation" (mGGA) functionals. Following a discussion of the essential theoretical framework, details are given for the practical application of DFT, describing the specifics of the "plane-wave pseudopotential DFT" approach and the implementation of mGGA functionals therein. These sections will serve as an essential reference in the following chapters, as this work aims to extend the framework of perturbation theory to include these more advanced approximations.

2.1 Introduction

The properties of materials are governed by interactions of electrons with nuclei and electrons with electrons, occurring at the atomic scale (length scale $O\left(10^{-10}\right)$m). If we wish to use theory and simulation to understand and predict material properties, we must use quantum mechanics. Our starting place is many-body Schrödinger equation (MBSE); in this work, we focus on the time-independent form, which assumes that any external fields are static. By applying the Hamiltonian operator, $\hat{H}$, to wavefunction, Φ, of a material or system of electrons and nuclei the energy of the system, E, can be calculated,

$$\hat{H}\left|\Phi_s\left(\{\boldsymbol{r}_i\},\{\boldsymbol{R}_I\}\right)\right\rangle = E_s\left|\Phi_s\left(\{\boldsymbol{r}_i\},\{\boldsymbol{R}_I\}\right)\right\rangle, \tag{2.1}$$

where the position of the i^{th} electron is $\boldsymbol{r}_i$, the position of the I^{th} nuclei is denoted by $\boldsymbol{R}_I$ and s labels the states of the system. In this form, it is not feasible to attempt to solve the MBSE, since the size of the problem scales exponentially with

number of electrons and nuclei, such that beyond 3 or 4 particles, a satisfactory solution becomes unfeasible. Density functional theory is an approach that can circumvent this scaling problem which has become more popular over the last $30-40$ years due to its accurate reproduction of experimental results, e.g. material lattice constants to within an error of a few percent [51].

2.2 Solving the Many Body Schrödinger Equation

In the many-body Schrödinger equation we calculate the energy of a many-body system of nuclei and electrons by applying the Hamiltonian of the system. The Hamiltonian can be split up into the different energy contributions,

$$\hat{H} = \hat{T}^{\text{nuc}} + \hat{T}^{\text{elec}} + \hat{V}^{\text{nuc-nuc}} + \hat{V}^{\text{nuc-elec}} + \hat{V}^{\text{elec-elec}}, \tag{2.2}$$

where $\hat{T}^{\text{nuc}}$ and $\hat{T}^{\text{elec}}$ are the kinetic energy operators for the nuclei and electrons respectively, $\hat{V}^{\text{nuc-nuc}}$, $\hat{V}^{\text{nuc-elec}}$ and $\hat{V}^{\text{elec-elec}}$ denote the operators for the nuclear-nuclear, nuclear-electron and electron-electron interactions respectively. We are neglecting spin effects and magnetism.

By "solving" the MBSE, we mean finding the eigenstates of the coupled system, $|\Phi_s\rangle$, that satisfy 2.1. Except in certain very specific scenarios, the MBSE cannot be solved analytically, and therefore we turn to numerical methods. Again, solving the MBSE numerically poses it's own challenges. Consider a coupled state of the system: $|\Phi_s\rangle$ is a $3N_{\text{elec}} + 3N_{\text{nuc}}$ dimensional object, as it depends on the electron and nuclei states at *all* positions throughout the system. For a 3 dimensional system broken up onto a very coarse $10 \times 10 \times 10$ grid, the number of values, N_{val}, that are require to store a state $|\Phi_s\rangle$ scales exponentially with the number of particles,

$$O\left(N_{\text{val}}\right) = (10)^{3N_{\text{elec}}+3N_{\text{nuc}}}. \tag{2.3}$$

For a system of 8 electrons and 1 nucleus, the number of values required to store a single state is of the order 10^{27}, even on a very coarse grid. This is vastly greater than any storage available to us. For systems of more than few particles, the storage of such a single state is the immediate problem, as opposed to any attempts to actually solve the MBSE.

Clearly, it is impractical to consider directly solving the MBSE for real materials. We must therefore look to make approximations.

2.2.1 The Born-Oppenheimer Approximation

The first thing that we can consider is that there is a large mass difference between the nuclei and electrons, even for a hydrogen nucleus the ratio is around $2000:1$. If we consider the expression for the kinetic energy operator for the nuclei,

$$\hat{T}^{\text{nuc}} = -\sum_I \frac{\hbar^2}{2M_I}\nabla_I^2 \tag{2.4}$$

we can see that the kinetic energy of the nuclei will be much smaller in comparison to other terms in the Hamiltonian due to its dependence on the inverse nuclear mass.

We can therefore very reasonably approximate the nuclei as "slow-moving particles" when compared to the electrons. Mathematically, we are approximating the nuclei as having infinite mass and, therefore, zero kinetic energy, removing that term from the Hamiltonian. This allows us to approximate the system wavefunction, Φ, by separating it into the product of an electron wavefunction, Ψ_{elec}, and a nuclear wavefunction, Ψ_{nuc},

$$\Phi \approx \Psi_{\text{elec}} \cdot \Psi_{\text{nuc}}. \tag{2.5}$$

Compared to the electrons, the nuclei are massive enough that their wave functions are very localised, such that the electron wavefunction depends on the nuclear positions parametrically, but not on full nuclear wavefunctions. In other words, when the nuclei move, the electrons respond to the change instantaneously and remain in their ground state. This is the Born-Oppenheimer approximation first put forward in 1927 [52]. In this approximation there is no coupling of the electron states and nuclear motion, i.e. nuclear motion cannot lead to the excitation of electrons. The coupling can be reintroduced by a perturbative approach, provided that the nuclear motion is slow, i.e. the kinetic energy term is still small enough to be neglected.

The nuclei can be treated classically and have no effect in the quantum regime on the electron properties. By treating the nuclei classically as point charges, the calculation of the nucleus-nucleus interactions is also simplified and can be handled very efficiently and accurately through numerical methods.

This assumption only breaks down when simulating systems with very light nuclei and when simulating systems at very low temperatures; even at these extremes there are specialised techniques to incorporate the quantum effects of the nuclei with significantly less cost than full quantum-nuclei + electron treatment.

Having successfully simplified the handling of the nuclei, we can now turn our

attention to addressing the pure electron problem.

2.2.2 The MBSE for electrons

Applying the Born-Oppenheimer approximation leads to a somewhat simplified Hamiltonian for the system. The nuclear kinetic energy term can be neglected and the nuclear-nuclear interaction is handled by treating the nuclei as classical point charges. This leads to a Hamiltonian for the system that only acts on the electron wavefunction,

$$\begin{aligned}\hat{H} &= \hat{T}^{\text{elec}} + \hat{V}^{\text{nuc-elec}} + \hat{V}^{\text{elec-elec}} + E^{\text{nuc-nuc}} \\ &= -\frac{\hbar^2}{2m_e}\sum_i \nabla_i^2 - \sum_{i,I}\frac{Z_I e^2}{4\pi\epsilon_0|\boldsymbol{r}_i - \boldsymbol{R}_I|} + \frac{1}{2}\sum_{i\neq j}\frac{e^2}{4\pi\epsilon_0|\boldsymbol{r}_i - \boldsymbol{r}_j|} + E^{\text{nuc-nuc}} \\ &= -\frac{\hbar^2}{2m_e}\sum_i \nabla_i^2 + \sum_i V^{\text{ext}}(\boldsymbol{r}_i) + \frac{1}{2}\sum_{i\neq j}\frac{e^2}{4\pi\epsilon_0|\boldsymbol{r}_i - \boldsymbol{r}_j|} + E^{\text{nuc-nuc}}, \end{aligned} \tag{2.6}$$

where $E^{\text{nuc-nuc}}$ is the energy of the nuclear-nuclear interaction, going from the second line to the third line we have also abstracted the interaction between the electrons and all nuclei into a single external potential, V^{ext}. However, solving the MBSE just for the electrons is no more a tangible task than solving for the full coupled system of electrons and nuclei. The exponential scaling with the number of particles still applies, limiting any calculations to no more than 3 or 4 electrons.

The Hamiltonian above is given with no assumed units. From here on in, unless otherwise explicitly stated all expressions will be now be given in atomic units, where $m_e = \hbar = 4\pi\epsilon_0 = e = 1$. In atomic units the Hamiltonian of the many-electron systems becomes somewhat clearer to read,

$$\hat{H} = -\frac{1}{2}\sum_i \nabla_i^2 + \sum_i V^{\text{ext}}(\boldsymbol{r}_i) + \frac{1}{2}\sum_{i\neq j}\frac{1}{|\boldsymbol{r}_i - \boldsymbol{r}_j|} + E^{\text{nuc-nuc}}. \tag{2.7}$$

2.3 Density Functional Theory

There have been several approaches to tackling the MBSE for electrons through various reformulations of the problem. This work focusses on the methods of Density Functional Theory, first introduced in 1964 by Hohenberg and Kohn [13].

2.3.1 Hohenberg-Kohn Theorems

In their 1964 paper Hohenberg and Kohn (HK) put forward two theorems,

1. For a system of interacting particles under an external potential $V^{\text{ext}}(\boldsymbol{r})$, there is a unique mapping (except for a constant shift) between the ground state particle density, $\rho_0(\boldsymbol{r})$ and $V^{\text{ext}}(\boldsymbol{r})$.

2. There exists a universal functional for the system's total energy $E[\rho]$ in terms of the density $\rho(\boldsymbol{r})$. The density function $\rho(\boldsymbol{r})$ that minimises this functional is the exact ground state, $\rho_0(\boldsymbol{r})$.

The significance of the first theorem is that if $\rho_0(\boldsymbol{r})$ uniquely defines a particular V^{ext}, when we consider 2.6 we can see that the Hamiltonian is also uniquely defined. From this it follows that the many-body wavefunction Ψ_{elec} is also uniquely defined, and therefore in principle, every observable is completely determined from only the ground state density, $\rho_0(\boldsymbol{r})$.

The universal functional of the energy posited in the second theorem follows from the first theorem, energy being an observable of the system. HK then show that by varying density function to minimise the energy functional one can find the exact ground state energy. By definition, the density function that produces the minimum energy is the ground state density, $\rho_0(\boldsymbol{r})$.

The first proof tells us that if we know ground state density of a system of interacting particles, in principle we have all the information that we need to calculate any observable of the system. The second proof tells us that if we know the universal energy functional of the density, we can find the ground state density of the system and hence from the first proof, all observables for the system. Together, these theorems and their proofs are sufficient to allow us to completely avoid the need to determine the many-body electron wavefunction. This avoids the requirement for a mathematical object that scales exponentially with the number of particles. Provided we know the exact universal energy functional of course ... which we do not.

It is, however, instructive to have a go at writing down the different contributions to the exact functional and take our approach from there. To begin, we can separate out the interaction of the density and the external potential,

$$E[\rho(\boldsymbol{r})] = \int V^{\text{ext}}(\boldsymbol{r})\,\rho(\boldsymbol{r})\ \mathrm{d}^3\boldsymbol{r} + F[\rho(\boldsymbol{r})], \tag{2.8}$$

where $F[\rho(\boldsymbol{r})]$ denotes the unknown universal functional of HK. From here we can split the unknown functional into the different contributions to the total energy, the kinetic energy of the particle and the interactions of the particles with each

other,

$$F[\rho(\boldsymbol{r})] = T[\rho(\boldsymbol{r})] + U[\rho(\boldsymbol{r})] \tag{2.9}$$

where $T[\rho(\boldsymbol{r})]$ is the functional of the kinetic energy and $U[\rho(\boldsymbol{r})]$ is the functional of the energy of the interaction between the particles. Both of these functionals are unknown, however in the case of the interaction between particles we can again separate out terms that we do know,

$$U[\rho(\boldsymbol{r})] = \frac{1}{2}\iint \frac{\rho(\boldsymbol{r})\,\rho(\boldsymbol{r'})}{|\boldsymbol{r}-\boldsymbol{r'}|}\ \mathrm{d}^3\boldsymbol{r}\mathrm{d}^3\boldsymbol{r'} + E_{\mathrm{HK}}^{\mathrm{XC}}[\rho(\boldsymbol{r})]\,. \tag{2.10}$$

The first term here is the classical electrostatic energy for a charge distribution, often known as the Hartree energy E^{H}, and the second term $E_{\mathrm{HK}}^{\mathrm{XC}}[\rho(\boldsymbol{r})]$ must account for the so-called exchange and correlation interactions, which shall be discussed in due course.

Thomas-Fermi theory [53, 54] predates the introduction of DFT, but it is an attempt is made to formulate a functional for the kinetic energy under certain approximations. Generally, Thomas-Fermi is not accurate enough to make robust theoretical predictions, and the lack of an accurate kinetic energy functional restricts approaches that rely solely on the density as the basic variable.

2.3.2 Kohn-Sham Theory

The next advance for DFT approaches came a year later from Kohn and Sham [55]. They proposed to replace the MBSE for N strongly interacting particles with an auxiliary system of N non-interacting, independent particles. The ground-state density of the fictitious auxiliary system is assumed to be the same as that of the original many-body problem. They take the universal functional of equation 2.8 and separate out the kinetic energy of fictitious Kohn-Sham system, T^{KS}, which is the functional of the ground state density,

$$F[\rho(\boldsymbol{r})] \equiv T^{\mathrm{KS}}[\rho(\boldsymbol{r})] + G[\rho(\boldsymbol{r})]\,. \tag{2.11}$$

The Kohn-Sham formulation for the energy can therefore be written as,

$$E^{\mathrm{KS}} = T^{\mathrm{KS}}[\rho(\boldsymbol{r})] + G[\rho(\boldsymbol{r})] \tag{2.12}$$

$$= T^{\mathrm{KS}}[\rho(\boldsymbol{r})] + \int V^{\mathrm{ext}}(\boldsymbol{r})\,\rho(\boldsymbol{r})\ \mathrm{d}^3\boldsymbol{r} + E^{\mathrm{H}}[\rho(\boldsymbol{r})] + E^{\mathrm{XC}}[\rho(\boldsymbol{r})]\,. \tag{2.13}$$

In this case the exact exchange and correlation energy functional, E^{XC} is

$$E^{\mathrm{XC}}[\rho(\boldsymbol{r})] = T_{\mathrm{MB}}[\rho(\boldsymbol{r})] - T^{\mathrm{KS}} + E_{MB}^{\text{elec-elec}} - E^{\mathrm{H}}[\rho(\boldsymbol{r})]\,, \tag{2.14}$$

where T_{MB} is the exact kinetic energy of the many body system and $E_{\mathrm{MB}}^{\text{elec-elec}}$ is the exact electron-electron interaction energy of the many body system. Note that E^{XC} of equation 2.14 and $E_{\mathrm{HK}}^{\mathrm{XC}}$ of equation 2.10 subtly differ in definition. In the Hohenberg-Kohn definition, it is assumed that the exact density functional of the many-body kinetic energy, $T_{\mathrm{MB}}[\rho(\boldsymbol{r})]$, is known and determined separately. For the Hohenberg-Kohn definition of $E_{\mathrm{HK}}^{\mathrm{XC}}$, only the last two terms of equation 2.14 are required.

If the exact E^{XC} functional is known, then the ground state density and energy can be found using the Kohn-Sham density. The density of the Kohn-Sham system can be calculated from the Kohn-Sham states

$$\rho(\boldsymbol{r}) = 2\Omega^{-1}\sum_{i}^{\mathrm{occ}}|\psi_i(\boldsymbol{r})|^2, \tag{2.15}$$

where Ω is the volume of the system, i is the label for each of the Kohn-Sham states and the sum only over occupied states which for N electrons, will be the $\frac{N}{2}$ lowest energy states since we are assuming spin degeneracy for now.

So, how exactly does this help? With a sleight of hand, we have replaced two unknowns, $T_{\mathrm{MB}}[\rho(\boldsymbol{r})]$ and $E_{\mathrm{MB}}^{\text{elec-elec}}[\rho(\boldsymbol{r})]$, with a single unknown, E^{XC}. The key to the success of Kohn-Sham theory comes from introducing the fictitious non-interacting electrons, $\psi_s(\boldsymbol{r})$, for which the kinetic energy, T^{KS}, is known and can be calculated very straight forwardly using the usual kinetic energy operator,

$$T^{\mathrm{KS}} = -\frac{1}{2}\sum_{i}^{\mathrm{occ}}\langle\psi_i|\nabla^2|\psi_i\rangle. \tag{2.16}$$

Any discrepancy between the many-body kinetic energy and kinetic energy of the Kohn-Sham states is accounted for by the unknown exchange and correlation functional, so in principle the theory is exact. Therefore, without having to make any of the coarse approximations, we have reduced the unknown components from the full kinetic energy to a correction to the Kohn-Sham kinetic energy. This turns out to be a far better approximation of the kinetic energy of the many-body system than the approach of Thomas-Fermi theory.

The set of states that minimise the total energy functional are the self-consistent solutions to the Kohn-Sham equations,

$$\hat{H}^{\mathrm{KS}}|\psi_i\rangle = \left[\hat{T} + V^{\mathrm{KS}}(\boldsymbol{r})\right]|\psi_i\rangle = \epsilon_i|\psi_i\rangle, \tag{2.17}$$

where ϵ_i are the Kohn-Sham eigenvalues and $\hat{H}^{\mathrm{KS}}$ is the effective Hamiltonian operator, comprised of the kinetic energy operator and the Kohn-Sham potential $V^{\mathrm{KS}}(\boldsymbol{r})$. The Kohn-Sham potential is chosen to ensure that the Kohn-Sham

density is identical to the density of the exact many-body system and is explicitly defined as *local* and *multiplicative*. The potential consists of the external potential and the functional derivatives of the Hartree energy and the XC energy,

$$V^{\mathrm{KS}}(\boldsymbol{r}) = V^{\mathrm{ext}}(\boldsymbol{r}) + V^{\mathrm{H}}(\boldsymbol{r}) + V^{\mathrm{XC}}(\boldsymbol{r}), \tag{2.18}$$

where $V^{\mathrm{H}} = \frac{\delta E^{\mathrm{H}}}{\delta \rho(\boldsymbol{r})}$ is the Hartree potential and $V^{\mathrm{XC}} = \frac{\delta E^{\mathrm{XC}}}{\delta \rho(\boldsymbol{r})}$ is the XC potential. The fictitious Kohn-Sham electrons, $\psi_s(\boldsymbol{r})$ are the eigenvectors of the effective Hamiltonian, subject to an orthonormality constraint of

$$\langle \psi_i | \psi_j \rangle = \delta_{i,j}. \tag{2.19}$$

2.3.3 Exchange and Correlation Functionals

The final component of the Kohn-Sham formalism is the exchange and correlation functional. "Exchange" here refers to the energy contributions arising from the requirement of the many-body electron wavefunction to be antisymmetric, since electrons are fermions. In the many-body interacting system, if two electrons exchange position, the sign of the overall wavefunction would change, e.g. in a two-electron system $\Psi(\boldsymbol{r}_1, \boldsymbol{r}_2) = -\Psi(\boldsymbol{r}_2, \boldsymbol{r}_1)$. The antisymmetry of the wavefunction enforces the Pauli exclusion principle and causes a repulsion between the electrons. Slater determinants are objects that obey this antisymmetry rule, by using them to represent the electron wavefunction the antisymmetry can be directly incorporated into the model. This is the basis of the Hartree-Fock method; however, the added computational expense of calculating the Fock operator limits the applicability of this method.

"Correlation" has a rather vague definition. Broadly, correlation refers to any interaction between electrons, but of course the Hartree and exchange energies are both interaction energies. So what is meant by a "correlation functional" in DFT formalism, is all the parts of the exact energy that are not accounted for by the Hartree and exchange energy. A system can lower its total energy dynamically through Coulomb repulsions, which cannot be captured in the Hartree-Fock method and would require a sum over all possible Slater determinants. The degrees of freedom that the additional Slater determinants permit enables the energy to be lowered. The amount of energy that the total energy is lowered by is the correlation energy. In essence, if the Hartree and exchange energies are accounted for, e.g. by the Hartree-Fock method with a single Slater determinant, "correlation" refers to the other energy contributions.

The exact Exchange and Correlation functional is unknown, we must therefore

approximate. There are various approaches to approximate the XC energy functional that are often classified as different rungs on a Jacob's ladder [56] of accuracy, based on the information required for each functional. In general, it is observed that each step up the Jacob's ladder results in an step towards increased physical accuracy at the cost of increased calculation time.

2.3.3.1 Local Density Approximation

The simplest approximations are Local Density Approximations (LDA) [16, 3] which describe the contribution to the XC energy at a specific point $\boldsymbol{r}$ using only the density at that specific point, $\rho(\boldsymbol{r})$. The LDA suggested by Perdew and Zunger in 1981 [16] is based on the exchange and correlation energies of the homogeneous electron gas, a system in which the electron density is uniform throughout. The PZ LDA functional is written in the form,

$$E_{\mathrm{LDA}}^{\mathrm{XC}} = F[\rho] = \int_{\Omega} \rho(\boldsymbol{r})\, \epsilon_{\mathrm{LDA}}^{\mathrm{XC}}(\rho(\boldsymbol{r}))\ \mathrm{d}^3\boldsymbol{r} = \int_{\Omega} f_{\mathrm{LDA}}^{\mathrm{XC}}(\rho(\boldsymbol{r}))\ \mathrm{d}^3\boldsymbol{r}, \tag{2.20}$$

where ρ is the electron density and $\epsilon_{\mathrm{LDA}}^{\mathrm{XC}}$ is the exchange and correlation energy density per particle at point $\boldsymbol{r}$. The functional form of LDAs shown above means that LDAs are therefore purely local functionals. The functional derivative and therefore the XC potential is straight forward to derive and compute,

$$\frac{\delta E^{\mathrm{XC}}}{\delta \rho(\boldsymbol{r})} = \frac{\partial f_{\mathrm{LDA}}^{\mathrm{XC}}}{\partial \rho(\boldsymbol{r})}. \tag{2.21}$$

The LDA of PZ approximates $\epsilon_{\mathrm{LDA}}^{\mathrm{XC}}$ as the exchange and correlation energy per particle of a uniform electron density that has a density the same as the real density at that point in the system. The value of the exact exchange energy for the homogenous electron gas can be calculated analytically, and values can be calculated for the correlation energy using more advanced theoretical methods such as Quantum Monte Carlo [14] and the Random Phase Approximation [57] and a functional fit to this data. The Perdew-Zunger LDA functional is a simple and surprisingly effective functional, enabling "accurate enough [1]" simulations for the first time, marking a turning point in DFT development.

Vosko, Wilk, and Nusair (VWN) developed several functionals that varied in the theoretical data sets used to parameterise the functionals and the function that was used to interpolate the correlation energy between the fully spin-polarised electron gas and the non-spin-polarised electron gas. Perdew and Wang pub-

[1] The definition of accurate enough obviously varies between use cases, but the PZ LDA functional was a simple and general implementation that was deemed "accurate enough" for many use cases.

lished an LDA functional in 1992 [3] that used the most successful of the VWN interpolation functions and used more theoretical data to make the fit of the final functional. The PW LDA improved upon the numerical stability of the PZ LDA by choosing a functional form that was not a piecewise function but avoided some of the overly complicated forms of the VWN functionals. The PW LDA has since been used as the starting point for more advanced approximations of the XC functional.

2.3.3.2 Generalised Gradient Approximation

The next class of approximation are the Generalised Gradient Approximations (GGAs) [2] which include additional information about the surrounding electron density via the gradient of the density $|\nabla\rho|$ at each point. GGAs are often referred to as semi-local functionals, in general they are of the following form,

$$\begin{aligned} E^{\mathrm{XC}}_{\mathrm{GGA}} = F\left[\rho, |\nabla\rho|\right] &= \int_{\Omega} \rho\left(\boldsymbol{r}\right) \epsilon^{\mathrm{XC}}_{\mathrm{GGA}}\left(\rho\left(\boldsymbol{r}\right), |\nabla\rho\left(\boldsymbol{r}\right)|\right) \mathrm{d}^3\ \boldsymbol{r} \\ &= \int_{\Omega} f^{\mathrm{XC}}_{\mathrm{GGA}}\left(\rho\left(\boldsymbol{r}\right), |\nabla\rho\left(\boldsymbol{r}\right)|\right) \mathrm{d}^3\ \boldsymbol{r}. \end{aligned} \tag{2.22}$$

$f^{\mathrm{XC}}_{\mathrm{GGA}}$ now also depends on the local gradient, so there are additional terms to the functional derivative. We shall use the form for the functional derivative put forward by White and Bird [58] which they showed to be more numerically stable,

$$\frac{\delta E^{\mathrm{XC}}}{\delta\rho\left(\boldsymbol{r}\right)} = \frac{\partial f^{\mathrm{XC}}_{\mathrm{GGA}}}{\partial\rho\left(\boldsymbol{r}\right)} - \nabla\left(\frac{\partial f^{\mathrm{XC}}_{\mathrm{GGA}}}{\partial|\nabla\rho\left(\boldsymbol{r}\right)|} \frac{\nabla\rho\left(\boldsymbol{r}\right)}{|\nabla\rho\left(\boldsymbol{r}\right)|}\right). \tag{2.23}$$

Several attempts were made to construct gradient expansion approximations for the XC functional, but they failed to improve upon the general behaviour of the LDA functionals. This was until the functional of Perdew and Wang in 1991 (PW91) which satisfied certain constraints of the exact functional in particular limits. The numerical behaviour of the PW91 functional meant that it was superseded by a functional published by Perdew Burke and Enzerhof in 1996 [2] (PBE) which has by far been the most widely used approximation to date.

2.3.3.3 Meta Generalised Gradient Approximation

Next are so called "meta-GGAs" (mGGAs), which will also depend on the Laplacian of the density, $\nabla^2\rho$, and/or the orbital kinetic energy density, τ computed from the Kohn-Sham states,

$$\tau\left(\boldsymbol{r}\right) = \frac{1}{2}\Omega^{-1}\sum_{i}^{\mathrm{occ}} |\nabla\psi_i\left(\boldsymbol{r}\right)|^2. \tag{2.24}$$

The general expression for the mGGA functionals is

$$E_{\mathrm{mGGA}}^{\mathrm{XC}} = F\left[\rho, |\nabla\rho|, \nabla^2\rho, \tau\right] = \int_\Omega \rho(\boldsymbol{r})\, \epsilon_{\mathrm{mGGA}}^{\mathrm{XC}}\left(\rho(\boldsymbol{r}), |\nabla\rho(\boldsymbol{r})|, \nabla^2\rho(\boldsymbol{r}), \tau(\boldsymbol{r})\right) \mathrm{d}^3\boldsymbol{r}. \tag{2.25}$$

They are still semi-local functionals, but the inclusion of the Kinetic Energy Density (KED) allows further information to be included, particularly giving an indication of the electron localisation. The functionals that adopt the use of τ have so far been far more successful than the approaches involving the Laplacian of the density, since τ can be found in Taylor expansions of exact exchange [59] and correlation expressions [60]. In this thesis, the focus is on perturbation theory as applied to functionals that do not depend on the Laplacian of the density but those that depend on the KED. Those functionals are of the form,

$$\begin{aligned} E_{\mathrm{mGGA}}^{\mathrm{XC}} = F\left[\rho, |\nabla\rho|, \tau\right] &= \int_\Omega \rho(\boldsymbol{r})\, \epsilon_{\mathrm{mGGA}}^{\mathrm{XC}}\left(\rho(\boldsymbol{r}), |\nabla\rho(\boldsymbol{r})|, \tau(\boldsymbol{r})\right)\, \mathrm{d}^3\boldsymbol{r} \\ &= \int_\Omega f_{\mathrm{mGGA}}^{\mathrm{XC}}\left(\rho(\boldsymbol{r}), |\nabla\rho(\boldsymbol{r})|, \tau(\boldsymbol{r})\right)\, \mathrm{d}^3\boldsymbol{r}. \end{aligned} \tag{2.26}$$

Inclusion of τ means that the XC potential can no longer be expressed in a truly multiplicative form, as was done for the LDA and GGA functionals. In fact, it is no longer well defined as the functional derivative of the XC energy with respect to the density, since it is not known how to directly calculate τ from the density. There are two options for how to proceed from here [61], the first is to use the Optimised Effective Potential (OEP) method [62, 63] which produces an XC potential that is a local and multiplicative operator, which is the same for all orbitals; however, this is computationally expensive and difficult to use beyond total energy calculations. The second option is to instead take the approach that we are minimising the total energy with respect to variations in the orbitals, not the density. We therefore take the functional derivative with respect to the Kohn-Sham orbitals [64], such that the potential now includes gradient operator terms that are applied to the Kohn-Sham states,

$$\frac{\delta E^{\mathrm{XC}}}{\delta\langle\psi|} = \left[\frac{\partial f_{\mathrm{mGGA}}^{\mathrm{XC}}}{\partial\rho(\boldsymbol{r})} - \nabla\left(\frac{\partial f_{\mathrm{mGGA}}^{\mathrm{XC}}}{\partial|\nabla\rho(\boldsymbol{r})|}\frac{\nabla\rho(\boldsymbol{r})}{|\nabla\rho(\boldsymbol{r})|}\right) - \frac{1}{2}\nabla\cdot\left(\frac{\partial f_{\mathrm{mGGA}}^{\mathrm{XC}}}{\partial\tau(\boldsymbol{r})}\nabla\right)\right]|\psi\rangle, \tag{2.27}$$

where the terms in the square brackets are considered to be the XC potential. Since the potential is no longer multiplicative and each orbital experiences a different effective potential, this approach is generally considered to be a form of generalised Kohn-Sham theory [65]. These additional terms in the potential require careful handling when considering perturbation theory.

Similar to the gradient expansion functionals, several attempts were made to construct mGGA functionals; however, they failed to provide consistent and general

improvements on the GGA functionals. Again, the key seems to lie in approximate functionals that correctly adhere to the exact constraints of the true functional. The Strongly Constrained and Appropriately Normed (SCAN) functional was the first mGGA to adhere to all known constraints for a mGGA functional [28]. This was a major achievement for chemical accuracy; however, it was quickly observed that SCAN, as with many other meta-GGA functionals, suffered from severe numerical instability [29, 30, 31, 32, 33, 34, 35]. This led to the creation of several related functionals [29, 36, 37, 38], which attempted to regularise the numerical behaviour of SCAN, while maintaining SCAN's physical accuracy. Considerable improvements have been achieved with respect to SCAN, but, as recent work has shown, many modern XC functionals including the SCAN family are numerically ill behaved [35].

The numerical behaviour of these recent functionals can cause severe problems when performing practical calculations for material properties, as we shall see in chapter 4. Understanding the cause of these numerical issues is tackled in chapter 5 where I put forward a method that can be used within plane-wave DFT to estimate the numerical errors and address the errors in a minimal additional computation (§5.3). The methods set out in chapter 5 allow us to better understand the numerical instabilities for a chosen XC functional "in situ", for the particular system being considered, and adapt our approach to minimise errors occurring for numerical integration.

2.3.3.4 A library of Exchange and Correlation

Since the publication of PBE there has been an explosion of XC functionals, mostly of the GGA variety. LibXC, a library of exchange and correlation functionals [50], contains more than 400. The variety comes from the choice of which exact constraints are obeyed and the systems used to parametrise the functionals. LibXC is of particular importance to the work described in this thesis as it not only provides a general interface allowing use of all included functionals, it also uses algorithmic differentiation to enable computation of up to the 4^{th} derivatives for all the functionals. This additional point is key for the work presented in this thesis as the 2^{nd} derivatives are required for constructing the first-order response potential when performing perturbation theory calculations. The functional forms of XC functionals are inherently complicated, making analytical derivation and computational implementation of their derivatives a time-consuming and error-prone process. The automatic calculation of these derivatives greatly reduces the overhead involved in attempting to implement perturbation theory calculations and helps avoid sources of noise that would be introduced from numerical differentiation approaches.

2.4 DFT For Materials

We now have all the ingredients to make an 'accurate enough' attempt atmaterial simulations however, we still face practical challenges. For an N electron system, the time to compute the solution to the Kohn-Sham equations scales to $O\left(N^3\right)$ which means simulations are quickly limited by the number of electrons that are included. How then can we attempt to perform simulations of systems larger than the smallest of molecules, considering that the number of electrons in a few grammes of a material is of the order 10^{23}?

2.4.1 Bloch's Theorem

The alternative approach is to recognise that in most materials the atoms are positioned at regular distances apart and form a highly periodic crystal. When we are interested in a large-scale material, we can approximate the material as a perfect crystal using a small unit cell that is repeated periodically across space. The unit cell is defined by a set of primitive vectors, $\boldsymbol{a}$, and the types and relative positions of the atoms in the unit cell. Integer multiples of the vectors are used to define a set of translations of the unit cell, which generates the rest of the crystal, the translations also form a set of points known as the Bravais lattice.

The unit cell and the position of the atoms therein is perfectly periodic; therefore, the external potential from the nuclei is also periodic. The effective Hamiltonian and electron density are therefore also guaranteed to be periodic; however, the electron wavefunctions themselves are not. An electron wavefunction can vary from one unit cell to another by a complex phase factor and still have the same electron density in each cell. Using Bloch's theorem, we therefore write a particular Kohn-Sham state ψ_b as the product of a cell-periodic function, $u_{\boldsymbol{k}}(\boldsymbol{r})$ and a wavelike function,

$$\psi_{b\boldsymbol{k}}(\boldsymbol{r}) = e^{i\boldsymbol{k}\cdot\boldsymbol{r}} u_{b\boldsymbol{k}}(\boldsymbol{r}), \tag{2.28}$$

where we have introduced an additional free parameter $\boldsymbol{k}$, into the problem, which defines the complex phase of the electron state. In order to accurately capture the contributions to the total energy of a system, changes in the complex phase need to be accounted for. This is done by sampling the Kohn-Sham states at all possible values for the complex phase as defined by $\boldsymbol{k}$, i.e. across a $\boldsymbol{k}$-space.

Bloch's theorem allows us to change the problem from having to calculate the Kohn-Sham states for the whole material to having to calculate the Kohn-Sham states in a small section of real space, but over infinite $\boldsymbol{k}$-space. In fact, the problem is not quite that bad; beyond the 1$^{\text{st}}$ Brillouin zone the states are repeated; therefore, to get a complete sampling only this region of $\boldsymbol{k}$-space needs to be

sampled. Points next to each other in $\boldsymbol{k}$-space will have very similar Kohn-Sham states, and we can therefore represent the states over a region of k-space using the states at a single point. This means that we can sample the 1st Brillouin zone with a relatively coarse numerical integration grid and still make good predictions of the total energy. For the integration grid sampling, we use an unbiased grid of evenly spaced points in a 3 dimensional grid, called a Monkhorst-Pack grid [66], which can be defined in terms of the spacing between the points and an offset from the origin.

2.4.1.1 Symmetry

The number of k-points required to sample the 1st Brillouin zone can be significantly reduced by using the crystallographic symmetry of the material under study. The choice of a Monkhorst-Pack grid allows us to fold the grid into a symmetric, irreducible set under the symmetry operations, since the solutions of the Kohn-Sham equations at symmetry-related k-points will also be related by symmetry. The symmetry operations can also be used to restrict further degrees of freedom in the calculation, such as by symmetrising atomic forces and the cell stress. Not having the solutions of the Kohn-Sham equations at every k-point means that the calculated density must also be symmetrised using the crystal symmetry operations.

2.4.2 The Plane-Wave Basis Set

The cell-periodic part of the Kohn-Sham states, $u_{b\boldsymbol{k}}(\boldsymbol{r})$, must also be considered. Since this function must have the periodicity of the unit cell, a natural choice is to expand this function as a Fourier series of plane-waves that have the periodicity of the unit cell

$$u_{b\boldsymbol{k}}(\boldsymbol{r}) = \sum_{\boldsymbol{G}} c_{b\boldsymbol{G}} e^{i\boldsymbol{G}\cdot\boldsymbol{r}}. \tag{2.29}$$

The wave vectors, $\boldsymbol{G}$, are reciprocal lattice vectors of the Bravais lattice, defined as $\boldsymbol{G}\cdot\boldsymbol{L} = 2\pi m$ for all $\boldsymbol{L}$ where $\boldsymbol{L}$ is a primitive vector of the unit cell and m is an integer. $c_{b\boldsymbol{G}}$ in equation 2.29 is the Fourier expansion coefficient, for the plane-wave with wave-vector $\boldsymbol{G}$.

The Kohn-Sham wavefunctions can therefore be written as an infinite sum of plane waves; however, this must necessarily be truncated to allow practical calculations. The infinite expansion is restricted such that only plane-waves that have a kinetic

energy less than some cut-off energy, E_{cut}, are considered,

$$\psi_{b\boldsymbol{k}}(\boldsymbol{r}) = \sum_{\boldsymbol{G}}^{|\boldsymbol{k}+\boldsymbol{G}|\leq G_{\text{cut}}} c_{b\boldsymbol{k}G} e^{i(\boldsymbol{k}+\boldsymbol{G})\cdot\boldsymbol{r}}, \tag{2.30}$$

where $\psi_{b\boldsymbol{k}}$ is the wavefunction for a particular k-point $\boldsymbol{k}$ and state labelled b, $G_{\text{cut}} = \sqrt{\frac{2m_e E_{\text{cut}}}{\hbar^2}}$, and $c_{b\boldsymbol{k}G}$ is the Fourier expansion coefficient for that particular plane-wave labelled G. The truncation of the basis set can be done without loss of accuracy, as the neglected plane waves vary very quickly in real space, and therefore their contribution to the wave function and the total energy can safely be assumed to be small, provided a large enough cut-off is chosen. The use of the plane-wave basis set means that Fast Fourier Transforms (FFTs) can be used to quickly move between reciprocal space and real space representations of the Kohn-Sham wavefunctions.

When calculating the total energy of a system, it is found that the total energy converges as the number of plane waves used and as the number of sampling points in $\boldsymbol{k}$-space is increased. These are important convergence parameters of our simulation. With well converged calculations the plane-wave representation allows us to accurately solve the Kohn-Sham equations for a material.

2.4.2.1 Representation of the Density

The Kohn-Sham wavefunctions are used to calculate the electron density, the analytic expression involves an integrating with respect to $\boldsymbol{k}$ over the 1$^{\text{st}}$ Brillouin zone,

$$\rho(\boldsymbol{r}) = \Omega^{-1} \sum_b \int_{\text{BZ}} f_{b\boldsymbol{k}} \left|\psi_{b\boldsymbol{k}}(\boldsymbol{r})\right|^2 \, \mathrm{d}^3\boldsymbol{k}, \tag{2.31}$$

however, the numerical expression is a sum over discrete sampling points in $\boldsymbol{k}$-space, the k-points,

$$\rho(\boldsymbol{r}) = \Omega^{-1} \sum_{b,k} w_k f_{bk} \left|\psi_{bk}(\boldsymbol{r})\right|^2, \tag{2.32}$$

where f_{bk} is the occupancy of the state labelled b, at the k-point $\boldsymbol{k}$ labelled k and w_k is the weighting of that k-point in the calculation which is determined by the number of symmetry equivalent points to the k^{th} k-point.

The calculation of the density must be carried out using a real space representation of the Kohn-Sham wavefunctions, i.e. the plane-wave expansion of the states must be Fourier-transformed from their natural reciprocal space representation into a real space representation. This is most efficiently carried out using FFTs, which must be carried out using a regular mesh of points, an FFT grid. If the representation of the wavefunctions is restricted to wave-vectors with magnitude

$|\boldsymbol{G}| \leq G_{\text{cut}}$ then the Fourier components of the charge density are restricted to $|\boldsymbol{G}| \leq 2G_{\text{cut}}$ such that:

$$\rho(\boldsymbol{r}) = \sum_{\boldsymbol{G}}^{|\boldsymbol{G}|\leq 2G_{\text{cut}}} a_{\boldsymbol{G}} e^{i\boldsymbol{G}\cdot\boldsymbol{r}} \tag{2.33}$$

where $a_{\boldsymbol{G}}$ is the coefficient in the Fourier expansion of the charge density. This means that for a particular cut-off for the wavefunction states, G_{cut}, there is a minimum FFT grid size required to compute the exact Fourier expansion representation of the resultant density (and the orbital kinetic energy density, τ). The minimum FFT grid required to represent all Fourier components of the density is a grid that is twice as dense as that of the plane-wave basis used for the wavefunctions.

Since there is a potential efficiency gain from neglecting the contributions from the largest frequency components of the density, many simulation codes allow the scale of the grid used for the density to be slightly reduced. CASTEP uses the `GRID_SCALE` parameter to control the scale of the density grid compared to the wavefunction basis. For the entirety of this thesis, unless otherwise stated, it can be assumed that any CASTEP calculations were performed with the `GRID_SCALE` parameter set to 2, that is, the density and orbital kinetic energy density are exactly represented.

There can be other terms that contribute to the total density that arise from the use of pseudopotentials (§2.4.4). These contributions may have non-negligible terms in their Fourier expansion, which require finer grids to represent, meaning that another FFT grid has to be used with more points than the density grid. In CASTEP, this is called the "fine grid", and it's scale relative to the plane-wave grid used for the Kohn-Sham states is controlled by the `FINE_GRID_SCALE` parameter. The fine grid is the grid used for calculating the contributions to the energy and potential that are derived from the density.

2.4.3 A note on Localised Basis Sets

When simulating single atoms or molecules, it is more natural to expand the Kohn-Sham states in terms of a localised basis set, such as a Gaussian set [67, 68] or combinations of atomic orbitals. These basis sets are generally centred around a particular point, usually the position of an atom, and decay quickly over space to zero. The advantages of these methods are that the basis sets are generally much smaller than a plane-wave basis set and that the Hamiltonian matrix can more easily be constructed for the system. The downsides are that they do not tend to describe delocalised (spread out over space) electrons very well, making simulation of metallic systems difficult. The basis functions also depend on the

atomic positions, which can make it difficult to compare systems in which the atoms have been moved relative to each other, and introduces so called "Pulay" forces and stresses [69].

2.4.4 Pseudopotentials

The external potential from the nuclei that acts on the electrons is due to the electrostatic attraction of their opposite charges. We are treating the nuclei as point particles, so the external potential takes the form,

$$V^{\text{ext}}(\boldsymbol{r}) = \sum_{I}^{N_{\text{nuc}}} \frac{-Z_I}{|\boldsymbol{r} - \boldsymbol{R}_I|}, \tag{2.34}$$

where N_{nuc} is the number of nuclei in the system, Z_I is the charge of the nucleus labelled I and $\boldsymbol{R}_I$ is it's position. The dependence on $|r|^{-1}$ causes the potential to go to infinity asymptotically as $\boldsymbol{r} \to \boldsymbol{R}_I$. This poses a major challenge in plane-wave calculations as the kinetic energy of states localised around the nucleus has to be very high, which means that a large number of plane-waves are required to represent those states. This is particularly galling, since the states localised around the nucleus are usually inconsequential to most properties in the material, whereas the valence states are of much greater importance. These localised states, or core states, generally remain unchanged when the nuclei are moved between different environments.

To exploit this fact and gain faster computation, pseudopotentials are often used. In place of the bare nuclear potential, a different, weaker potential is used that combines the effects of the nucleus and the core electrons into a potential for the ion. The pseudopotential only differs from the nuclear potential in the region close to the nucleus, the "core region". The pseudopotential and the bare nuclear potential for an iron atom is shown in figure 2.1.

By construction, the pseudopotential will provide pseudo wavefunctions for the valence electrons which are identical outside the core region. The pseudopotential is much weaker; therefore, the pseudo wavefunction vary more smoothly within the core region. The difference between the wavefunctions calculated using the pseudopotential and the "all electron" wavefunctions (calculated using the bare nuclear potential) are shown in figure 2.2. The advantage of the pseudopotential approach is that it reduces the number of Kohn-Sham equations that have to be solved by pre-computing the behaviour of the core electrons. Therefore, we only explicitly compute the valence states in the main calculation. Due to the pseudopotential being weaker than the nuclear potential, the pseudo wavefunction of the valence states are smoother and can therefore be represented with fewer

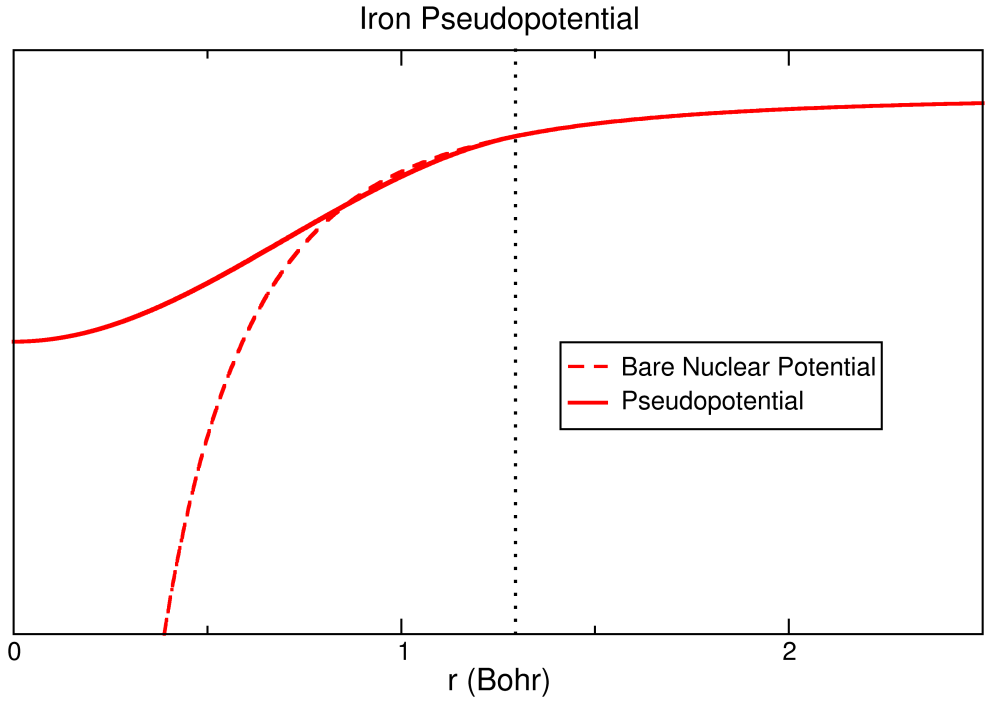

Figure 2.1: The bare nuclear potential is compared to the pseudopotential employed for iron atoms. The potentials differ in the core region where $r < 1.3$ Bohr, but are identical outside the core region.

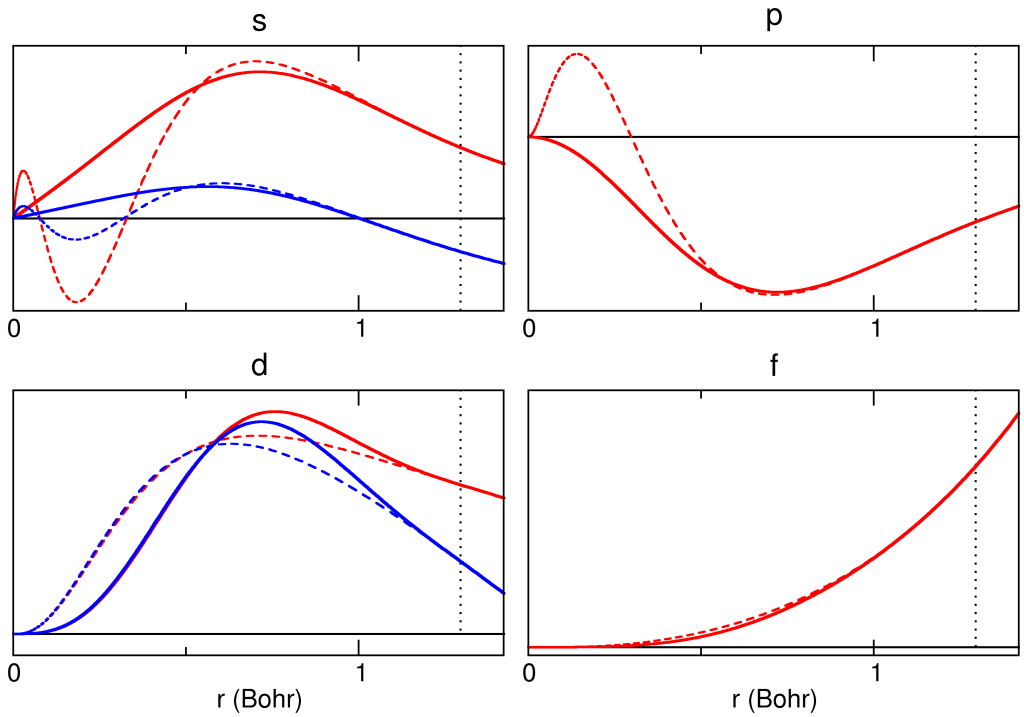

Figure 2.2: Pseudo wavefunctions for an iron pseudopotential for different angular momentum channels. The solid lines show the pseudo wavefunctions and the dashed lines show the all electron wavefunctions. Outside of the core region, $r > 1.3$ Bohr the all electron wavefunctions and the pseudo wavefunctions are in exact agreement.

plane waves. This reduces the computational expense of the calculation with, in principle, little or no compromise in accuracy.

Major efforts have recently been made to improve the accuracy of pseudopotential methods. The "Delta Project" [70] took several of the most popular methods for generating pseudopotentials and the DFT codes that use them and made a careful comparison of the physical properties calculated in these approaches. They made further comparisons of the pseudopotentials methods and equivalent all-electron calculations. In some cases, large discrepancies were found. By making several changes to the parametrisations used to generate the pseudopotentials, e.g. the core radius used, most of these discrepancies could be eliminated, vastly improving the reproducibility across DFT codes and pseudopotential methods.

2.4.4.1 Norm-conserving Pseudopotentials

There are a few different types of pseudopotentials that can be devised. In norm-conserving pseudopotentials (NCPs) [71], it is required that the normalisation of the wavefunctions within the core region should be preserved, i.e. the integral of the square amplitude of the valence pseudo wavefunctions should be equal to that of the all-electron wavefunctions, this helps to ensure the scattering properties of the ion are reproduced correctly. Kleinman and Bylander [72] showed that it was possible to construct separable pseudopotentials with a local part and non-local part which projects onto angular momentum states. The Kleinman and Bylander pseudopotentials are of the form,

$$\hat{V}^{\text{ext}} = V^{\text{local}}(\boldsymbol{r}) + \sum_{i,j} |\beta_i\rangle \, D_{i,j} \, \langle\beta_j| \,, \tag{2.35}$$

where $D_{i,j}$ is a matrix parametrized by reference to the all electron result and β_i is a projector onto an angular momentum state, i. For pseudopotentials constructed using a mGGA functional[73, 74, 75], there is an additional term in the local potential such that the pseudopotentials take the form,

$$\hat{V}^{\text{ext}} = \hat{V}^{\text{ext}}_{\text{loc}} + \hat{V}^{\text{ext}}_{\tau} + \hat{V}^{\text{ext}}_{\text{nl}} \tag{2.36}$$

$$= V^{\text{local}}(\boldsymbol{r}) - \frac{1}{2}\nabla \cdot \left(V^{\text{local}}_{\tau}(\boldsymbol{r})\,\nabla\right) + \sum_{i,j} |\beta_i\rangle \, D_{i,j} \, \langle\beta_j| \,. \tag{2.37}$$

The pseudopotentials generated and used by CASTEP are of this form.

Both the projector augmented wave method (PAW) [76] and the ultrasoft pseudopotential method (USP) [77] relax the norm-conserving constraint and compensate by introducing additional "augmentation charge" terms to the valence density. This allows the potential to be made smoother, affording additional

computational savings by reducing the number of plane-waves required to represent the valence states. CASTEP can produce and use USPs for several local and semi-local functional approximations, including mGGA functionals. Unfortunately, the additional complexity of the implementation for PAW or USP methods means that when performing perturbative methods, speed gain from reducing the number of plane-waves required is quickly lost. For this reason, this thesis shall confine itself to considering only the norm-conserving scheme described above.

2.4.4.2 Non-Linear Core corrections

Many pseudopotentials also make use of nonlinear core corrections (NLCCs) [78] when computing the XC energy integral for a better representation of the XC interaction between the core electrons and the valence electrons. The correction is done by adding the "pseudised" electron density of the core electrons to the electron density of the valence electrons for a total electron density which is then used to calculate the XC energy. This is more accurate than trying to incorporate these effects into the pseudopotential since XC functionals are nearly always non-linear, therefore the interaction is significantly different when the core charge is not included. In the case of mGGA functionals, we require not only a core charge, but also a core kinetic energy density when calculating the XC energy. The NLCC terms do, however, cause additional complexity when considering perturbations to the system.

2.5 Total Energy Functional in Plane-Wave DFT

We have now defined the major components involved in the plane-wave pseudopotential approach to DFT calculations. In this section, we shall summarise the total energy functional and explicitly describe how the additional terms that appear when using mGGA functionals are calculated in the plane-wave DFT.

In plane-wave DFT we generally employ periodic boundary conditions; therefore, we are interested in the total energy per unit cell. The ground state energy for the system is found by minimising the total energy functional for the system. The total energy functional can be written in term of a set of states, $|\psi_{kb}\rangle$, the electron density of those states, ρ, and the kinetic energy density of those states, τ,

$$E^{\text{tot}} = \sum_{b,k} w_k f_{bk} \left\langle \psi_{bk} \middle| \hat{T} + \hat{V}^{\text{ext}} \middle| \psi_{bk} \right\rangle + E^{\text{H}}\left[\rho\right] + E^{\text{XC}}\left[\rho_{\text{t}}, \left|\nabla \rho_{\text{t}}\right|, \tau_{\text{t}}\right] + E^{\text{Ion-Ion}}, \tag{2.38}$$

where the sum is weighted by w_k when a symmetry reduced set of k-points is used

(see 2.4.1.1), and f_{bk} are the wavefunction occupancies. The states at the same k-point and in the same spin channel are subject to the orthogonality constraint $\left\langle \psi_{ik} | \psi_{jk} \right\rangle = \delta_{ij}$. Here, $\hat{T}$ and $\hat{V}^{\text{ext}}$ are the kinetic energy and external potential operators, respectively, E^{H} and E^{XC} are the Hartree and XC energy functionals, respectively. The $E^{\text{Ion-Ion}}$ term is the interaction energy of the ions, which for periodic systems must be computed by Ewald summations [79].

The set of states that minimise the total energy functional are the self-consistent solutions to the Kohn-Sham equations,

$$\hat{H} \left| \psi_{bk} \right\rangle = \left[\hat{T} + \hat{V}^{\text{ext}} + \hat{V}^{\text{H}} + \hat{V}^{\text{XC}} \right] \left| \psi_{bk} \right\rangle = \epsilon_{bk} \left| \psi_{bk} \right\rangle , \tag{2.39}$$

where $\hat{H}$ is the effective Hamiltonian operator, $\hat{V}^{\text{H}}$ and $\hat{V}^{\text{XC}}$ are the Hartree and XC potential operators (although the Hartree potential is purely local potential).

2.5.1 Wavefunctions and Densities

The Kohn-Sham wavefunctions are expressed as a sum over plane waves,

$$\psi_{bk} \left(\boldsymbol{G} \right) = \sum_{\boldsymbol{G}}^{|\boldsymbol{k}+\boldsymbol{G}| \leq G_{\text{cut}}} c_{bkG} e^{i(\boldsymbol{k}+\boldsymbol{G}) \cdot \boldsymbol{r}} \tag{2.40}$$

where c_{bkG} is the coefficient for that plane-wave in the expansion of that state.

The charge density due to the valence electrons is calculated from the Kohn Sham states in the following way,

$$\rho \left(\boldsymbol{r} \right) = \Omega^{-1} \sum_{b,k}^{\text{occ}} w_k f_{bk} | \psi_{bk} \left(\boldsymbol{r} \right) |^2, \tag{2.41}$$

and the orbital kinetic energy density of the valence electrons is calculated as,

$$\tau \left(\boldsymbol{r} \right) = \Omega^{-1} \frac{1}{2} \sum_{b,k}^{\text{occ}} w_k f_{bk} \left| \nabla \psi_{bk} \left(\boldsymbol{r} \right) \right|^2 . \tag{2.42}$$

Integration by parts can be used to derive an equivalent expression for τ which requires fewer FFTs to compute [75],

$$\tau \left(\boldsymbol{r} \right) = \frac{1}{4} \nabla^2 \rho \left(\boldsymbol{r} \right) - \Omega^{-1} \frac{1}{2} \sum_{b,k}^{\text{occ}} w_k f_{bk} \left(\nabla^2 \psi_{bk}^* \left(\boldsymbol{r} \right) \right) \psi_{bk} \left(\boldsymbol{r} \right) . \tag{2.43}$$

When the choice of pseudopotential requires the use of NLCCs (see 2.4.4.2), the XC energy functional requires the "total" charge and kinetic energy density, $\rho_{\text{t}} \left(\boldsymbol{r} \right)$

and $\tau_{\mathrm{t}}(\boldsymbol{r})$, including contributions from the core electrons, $\rho_{\mathrm{c}}(\boldsymbol{r})$ and $\tau_{\mathrm{c}}(\boldsymbol{r})$.

$$\rho_{\mathrm{t}}(\boldsymbol{r}) = \rho(\boldsymbol{r}) + \rho_{\mathrm{c}}(\boldsymbol{r}), \tag{2.44}$$

$$\tau_{\mathrm{t}}(\boldsymbol{r}) = \tau(\boldsymbol{r}) + \tau_{\mathrm{c}}(\boldsymbol{r}). \tag{2.45}$$

Once computed in real space on a regular FFT grid, densities and the KEDs can be expressed as a sum over plane-waves,

$$\rho(\boldsymbol{r}) = \sum_{\boldsymbol{G}}^{|\boldsymbol{G}|\leq 2G_{\mathrm{cut}}} a_{\boldsymbol{G}} e^{i\boldsymbol{G}\cdot\boldsymbol{r}}, \tag{2.46}$$

$$\tau(\boldsymbol{r}) = \sum_{\boldsymbol{G}}^{|\boldsymbol{G}|\leq 2G_{\mathrm{cut}}} b_{\boldsymbol{G}} e^{i\boldsymbol{G}\cdot\boldsymbol{r}}. \tag{2.47}$$

2.5.2 Gradient and Laplacian Operators

Gradient operators and Laplacian operators take the derivative of a function with respect to the position vector, $\boldsymbol{r}$. This is straightforward to compute for any function that can be represented in the plane-wave expansion, for instance the gradient and Laplacian of the density can be calculated in reciprocal space as,

$$\nabla_\alpha \rho(\boldsymbol{G}) = iG_\alpha a_{\boldsymbol{G}} e^{i\boldsymbol{G}\cdot\boldsymbol{r}}, \tag{2.48}$$

$$\nabla^2 \rho(\boldsymbol{G}) = -|\boldsymbol{G}|^2 a_{\boldsymbol{G}} e^{i\boldsymbol{G}\cdot\boldsymbol{r}}, \tag{2.49}$$

where α is an index representing the Cartesian directions. The gradient and Laplacian of real space functions can therefore be found by Fourier transforming the function to reciprocal space, multiplying by the appropriate components of the reciprocal lattice vector, and Fourier transforming the function back. This can be carried out efficiently with the use of FFTs, provided that the representation of the real space function forms a regular grid in the unit cell.

2.5.3 Kinetic Energy

The kinetic energy operator is just the Laplacian operator with a prefactor,

$$\hat{T} = -\frac{1}{2}\nabla^2. \tag{2.50}$$

The kinetic energy of a state, ϵ^T_{bk}, can therefore easily be computed using the reciprocal space representation of the wavefunctions,

$$\langle \psi_{bk} | \hat{T} | \psi_{bk} \rangle = \epsilon^T_{bk} \langle \psi_{bk} | \psi_{bk} \rangle = \sum_{\boldsymbol{G}} |\boldsymbol{k}+\boldsymbol{G}|^2 c^*_{bkG} c_{bkG}. \tag{2.51}$$

2.5.4 Hartree Energy

In real space, the Hartree energy can be expressed as a convolution of the density with itself,

$$E^{\mathrm{H}}[\rho] = \frac{1}{2}\iint_{\Omega} \frac{4\pi\ \rho(\boldsymbol{r})\,\rho(\boldsymbol{r}')}{|\boldsymbol{r}-\boldsymbol{r}'|}\mathrm{d}^3\boldsymbol{r}\mathrm{d}^3\boldsymbol{r}' \tag{2.52}$$

where the integrals are over the volume of the unit cell. In Fourier space, this convolution can neatly be expressed as a product of the density with its complex conjugate,

$$E^{\mathrm{H}}[\rho] = \frac{1}{2}\sum_{\boldsymbol{G}}^{|G|\neq 0} \frac{4\pi\ \rho^*(\boldsymbol{G})\,\rho(\boldsymbol{G})}{|\boldsymbol{G}|^2}. \tag{2.53}$$

The Hartree potential at a point, $V^{\mathrm{H}}(\boldsymbol{r})$ is the functional derivative of E^{H} with respect to $\rho(\boldsymbol{r})$, expressed as,

$$V^{\mathrm{H}}(\boldsymbol{r}) = \frac{\delta E^{\mathrm{H}}}{\delta\rho(\boldsymbol{r})} = \sum_{\boldsymbol{G}}^{|\boldsymbol{G}|\neq 0} \frac{4\pi\ \rho(\boldsymbol{G})}{|\boldsymbol{G}|^2} e^{i\boldsymbol{G}\cdot\boldsymbol{r}}. \tag{2.54}$$

2.5.5 External Potential

Pseudopotentials are often used to replace the bare nuclear potential and the core electrons that contribute little to the properties of the material (§2.4.4). Common practice for generating pseudopotentials is to compute the pseudopotential from an all-electron calculation of the isolated atom using a spherically symmetric localised basis set. In this basis, the pseudopotential and its projectors onto each angular momentum state are calculated on a radial grid and then Fourier transformed to reciprocal space. A pseudopotential that is of the Kleinman-Bylander form in equation 2.35, is defined by a set of spherically symmetric, reciprocal space functions for the local part of the potential and the angular momentum projectors.

First, we shall focus on the local part of the external potential operator. The pseudopotential for an ion, I, is stored as a spherically symmetric function in reciprocal space, $v_I(|\boldsymbol{G}|)$, which can then be interpolated onto the plane-wave basis,

$$V_I(\boldsymbol{G}) = \Omega^{-1} v_I(|\boldsymbol{G}|)\, e^{i\boldsymbol{G}\cdot\boldsymbol{r}}, \tag{2.55}$$

The conventional prefactor of 4π has be absorbed into the $v_I(|\boldsymbol{G}|)$ function. The expression given above describes an ion that is positioned at the origin. To position the pseudopotential so that is centred around the ion's position, $\boldsymbol{R}_I$, we must apply a "structure factor",

$$V_I(\boldsymbol{G}) = \Omega^{-1} v_I(|\boldsymbol{G}|)\, e^{-i\boldsymbol{G}\cdot\boldsymbol{R}_I} e^{i\boldsymbol{G}\cdot\boldsymbol{r}}, \tag{2.56}$$

which can be transformed from reciprocal-space to real-space via a Fourier transform,

$$V_I(\boldsymbol{r}) = \Omega^{-1} \sum_{\boldsymbol{G}} v_I(|\boldsymbol{G}|) e^{-i\boldsymbol{G}\cdot\boldsymbol{R}_I} e^{i\boldsymbol{G}\cdot\boldsymbol{r}}. \tag{2.57}$$

The total local part of the external potential, $V^{\text{local}}(\boldsymbol{r})$, can therefore be computed as the sum of the contributions from each ion,

$$V^{\text{local}}(\boldsymbol{r}) = \sum_I V_I(\boldsymbol{r}) = \Omega^{-1} \sum_I \sum_{\boldsymbol{G}} v_I(|\boldsymbol{G}|) e^{-i\boldsymbol{G}\cdot\boldsymbol{R}_I} e^{i\boldsymbol{G}\cdot\boldsymbol{r}}. \tag{2.58}$$

Equation 2.37 is the expression for the external potential operator that is constructed using a mGGA functional. This expression contains the $V^{local}(\boldsymbol{r})$ term and two more terms, a differential part of the operator due to the dependence on τ and the non-local part of the operator. The non-local projectors are also stored in a radially symmetric reciprocal space representation and are handled in a similar manner to the local part of the pseudopotential, whilst also applying the appropriate spherical harmonic. The full expression for the non-local potential operator is superfluous to the remainder of this thesis and is therefore omitted.

The non-linear core corrections are handled in a similar way to the local part of the operator, the contribution from each ion is stored in the radial reciprocal space representation which is then interpolated onto the plane-wave basis and the appropriate structure factor applied,

$$\rho_{\text{c}}(\boldsymbol{r}) = \sum_I \rho_{\text{c},I}(\boldsymbol{r}) = \Omega^{-1} \sum_I \sum_{\boldsymbol{G}} \rho_{\text{c},I}(|\boldsymbol{G}|) e^{-i\boldsymbol{G}\cdot\boldsymbol{R}_I} e^{i\boldsymbol{G}\cdot\boldsymbol{r}}, \tag{2.59}$$

$$\tau_{\text{c}}(\boldsymbol{r}) = \sum_I \tau_{\text{c},I}(\boldsymbol{r}) = \Omega^{-1} \sum_I \sum_{\boldsymbol{G}} \tau_{\text{c},I}(|\boldsymbol{G}|) e^{-i\boldsymbol{G}\cdot\boldsymbol{R}_I} e^{i\boldsymbol{G}\cdot\boldsymbol{r}}. \tag{2.60}$$

The differential part of the operator contains a $V_\tau^{local}(\boldsymbol{r})$ that can be extracted for each pseudopotential and stored in the radial reciprocal space representation. The total $V_\tau^{local}(\boldsymbol{r})$ can then be computed in the same manner as the local part,

$$V_\tau^{\text{local}}(\boldsymbol{r}) = \sum_I V_{\tau,I}(\boldsymbol{r}) = \Omega^{-1} \sum_I \sum_{\boldsymbol{G}} v_{\tau,I}(|\boldsymbol{G}|) e^{-i\boldsymbol{G}\cdot\boldsymbol{R}_I} e^{i\boldsymbol{G}\cdot\boldsymbol{r}}, \tag{2.61}$$

and then applied to the states in combination with the gradient operator. Again, the expression above has incorporated the conventional prefactor of 4π into the function $v_{\tau,I}(|\boldsymbol{G}|)$.

The contribution to the energy arising from the local part of the external potential, $E_{\text{loc}}^{\text{ext}}$, can be computed from a simple integral over the density multiplied by

the potential and does not require a summation of the occupied states.

$$E_{\mathrm{loc}}^{\mathrm{ext}} = \sum_{i}^{\mathrm{occ}} \int \psi_i^* (\boldsymbol{r})\, V^{\mathrm{local}} (\boldsymbol{r})\, \psi_i (\boldsymbol{r})\ \mathrm{d}^3\boldsymbol{r} = \Omega \int V^{\mathrm{local}} (\boldsymbol{r})\, \rho (\boldsymbol{r})\ \mathrm{d}^3\boldsymbol{r}. \tag{2.62}$$

Using integration by parts, a similar expression can be derived for the energy contribution arising from the differential part of the operator, E_{τ}^{ext}.

$$E_{\tau}^{\mathrm{ext}} = \sum_{i}^{\mathrm{occ}} \int -\frac{1}{2} \psi_i^* (\boldsymbol{r}) \nabla \left(V_{\tau}^{\mathrm{local}} (\boldsymbol{r}) \nabla \psi_i (\boldsymbol{r}) \right)\ \mathrm{d}^3\boldsymbol{r} = \Omega \int V_{\tau}^{\mathrm{local}} (\boldsymbol{r})\, \tau (\boldsymbol{r})\ \mathrm{d}^3\boldsymbol{r}. \tag{2.63}$$

These integrals can then be handled as a sum over the product of the two functions in real space.

2.5.6 XC energy

Expressions for the XC energy and XC potential when using a mGGA functional are given in equations 2.26 and 2.27 (§2.3.3.3) but are repeated below for convenience.

$$E_{\mathrm{mGGA}}^{\mathrm{XC}} = F\left[\rho, |\nabla\rho|, \tau\right] = \int_{\Omega} f_{\mathrm{mGGA}}^{\mathrm{XC}} \left(\rho(\boldsymbol{r}), |\nabla\rho(\boldsymbol{r})|, \tau(\boldsymbol{r})\right)\ \mathrm{d}^3\boldsymbol{r}. \tag{2.64}$$

$$V^{\mathrm{XC}} (\boldsymbol{r}) = \frac{\partial f^{\mathrm{XC}}}{\partial \rho (\boldsymbol{r})} - \nabla \left(\frac{\partial f^{\mathrm{XC}}}{\partial |\nabla\rho(\boldsymbol{r})|} \frac{\nabla\rho(\boldsymbol{r})}{|\nabla\rho(\boldsymbol{r})|} \right) - \frac{1}{2} \nabla \cdot \left(\frac{\partial f^{\mathrm{XC}}}{\partial \tau (\boldsymbol{r})} \nabla \right). \tag{2.65}$$

It is often convenient to separate the expression for the XC potential above into the local terms and the differential terms. To do this we define two new local potentials which can be combined to make the full XC potential,

$$V_{\rho}^{\mathrm{XC}} (\boldsymbol{r}) = \frac{\partial f^{\mathrm{XC}}}{\partial \rho (\boldsymbol{r})} - \nabla \left(\frac{\partial f^{\mathrm{XC}}}{\partial |\nabla\rho(\boldsymbol{r})|} \frac{\nabla\rho(\boldsymbol{r})}{|\nabla\rho(\boldsymbol{r})|} \right) \tag{2.66}$$

$$V_{\tau}^{\mathrm{XC}} (\boldsymbol{r}) = \frac{\partial f^{\mathrm{XC}}}{\partial \tau (\boldsymbol{r})} \tag{2.67}$$

This notation makes a few derivatives much easier to express.

Strictly speaking, equations 2.64 and 2.65 only consider the case of a non-spin-polarised system, where the up and down spin channels are degenerate in energy and there is an even number of electrons such that the spin channels can be equally occupied.

Equation 2.64 shows E^{XC} evaluated as a continuous integral of f^{XC}. However, there is no convenient way to express this functional in the plane wave basis, therefore, in practice, the evaluation of E^{XC} is performed as a sum over a discrete

set of N_p points in real space, $\{\boldsymbol{r}_i\}$, for example in the spin degenerate case equation 2.64 becomes

$$E^\mathrm{XC} = \frac{\Omega}{N_\mathrm{p}} \sum_i^{N_\mathrm{p}} f^\mathrm{XC}\left(\rho\left(\boldsymbol{r}_i\right), \left|\nabla\rho\left(\boldsymbol{r}_i\right)\right|, \tau\left(\boldsymbol{r}_i\right)\right). \tag{2.68}$$

In this expression, the XC energy is assumed to be constant across the volume of the i^th grid point. In plane-wave DFT, the set $\{\boldsymbol{r}_i\}$ is defined by the choice of FFT grid used to represent the density. The value of the density (and other ingredients to f^XC) varies between the sampled points according to the plane-wave expansion, and so the contribution to the XC energy will also vary between the sampled points, in a highly non-linear fashion. The grid is chosen to accurately represent all the non-negligible components of the density, not the function f^XC and its derivatives.

The errors associated from numerically integrating the XC energy are generally assumed to be small enough to be negligible, however, as shown by Lehtola and Marques [35], this is highly-dependent on the numerical behaviour of the XC functional, and for many published XC functionals, the errors can be far from small. Numerical errors can be avoided by increasing the fineness of the grid used in the calculation, in CASTEP this means increasing `FINE_GRID_SCALE`. The downside to this approach is that all the other energy contributions such as the Hartree energy, the local and differential parts of the external potential operator must now be represented and computed on a unnecessarily fine grid. Chapter 5 covers some of the issues that can arise from the numerical behaviour of the XC functional. In that chapter a practical method to quantify errors related to XC energy integration is put forward, as well as an approach to the XC energy integration that avoids increasing the scale of the grid for every part of the calculation.

2.5.7 Solving the Kohn-Sham equations

The Kohn-Sham equations must be solved iteratively until a self-consistent solution is achieved. A self-consistent solution is found when the density produced from a set of Kohn-Sham states, can be used to compute the Kohn-Sham potential, which forms part of the effective Hamiltonian, the eigenstates of which are the original Kohn-Sham states that were used to compute the density.

The iterative process begins with a trial guess for the Kohn-Sham states, from these trial states an electron density can be computed and a total energy for the system calculated using the functional. The Kohn-Sham potential is also computed from the density, giving us all the ingredients for the Hamiltonian. A new

set of states of states is found by diagonalising the Hamiltonian. Explicit diagonalisation of the Hamiltonian is a very computationally expensive operation and generates far more eigenvectors than are required. Therefore, iterative diagonalisation and conjugate-gradient methods are most often used to minimise the total energy functional [80]. This is done until the total energy of the system stops decreasing to within a certain tolerance, indicating that the minimum energy and therefore ground state density has been found.

2.6 Application to this work

The purpose of this work is to extend the framework of density functional perturbation theory (DFPT) to allow more accurate and efficient calculations of material properties using mGGA functionals. The framework of DFPT focusses on computing derivatives of the total energy with respect to sets of perturbations.

In practice, this requires a careful understanding of the total energy functional and how those perturbations relate to it. It was therefore important in this chapter to set out the contributions in gory detail so that when we come to taking the derivative of, for example, the XC potential with respect to a perturbation, we already have a clear understanding of what the XC potential is and the derivation is a straightforward process. The framework of DFPT will be discussed in the following chapter.

Chapter 3

Density Functional Perturbation Theory

This chapter covers some of the key principles of density functional perturbation theory (DFPT) as it relates to the remainder of the work in this thesis. Perturbation theory allows us to access quantities beyond the ground state energy in the form of its derivatives, where first order derivatives such as atomic forces, or higher order derivatives such as elastic constants, phonon modes or other response functions. A brief description of the response functions we are interested in is given before a description of density functional perturbation theory.

3.1 Introduction

Density Functional Theory (DFT) has developed over the last 50 years to be very powerful and efficient tool for predicting ground-state properties of materials. DFT is limited to determining the ground state density and total energy, often falling short when it comes to accurately depicting electronic excited states. However, if the ground state undergoes a slight perturbation, generally keeping the system near its electronic ground state, traditional perturbation theory methods can be employed. This leads to the Density Functional Perturbation Theory (DFPT) approach. Developed in the late 1980s, this method has been notably effective in anticipating numerous quantities observable through experiments.

The focus of much of the work on DFPT has been on quantities obtained as derivatives of the total energy with respect to a small change of the external potential. For example, the force exerted on a nucleus is equal to minus the derivative of the total energy of the system with respect to the displacement of the atom. Successful approaches have also been proposed for derivatives of the total energy with respect to an infinitesimal strain; this can be used to compute

the stress tensor for a material [81, 82]. The examples given above describe only first-order derivatives of the energy, which are extremely useful as they enable geometry optimisation techniques [83, 84], which allow us to compute the relaxed structure of the atoms, and molecular dynamics simulations. However, when comparing experimental results, we are often interested in the system's *response* to an external perturbation, i.e. if an atom moves, how will the other atoms move. This can be calculated from 2^{nd}, 3^{rd} and higher-order derivatives of the total energy with respect to perturbations.

The calculation of such higher-order energy derivatives can be done using the finite-difference method. For instance, this method can be used to calculate the second derivative of the energy with respect to two atomic displacements by obtaining the ground state and calculating the forces for atomic configurations that have been slightly shifted from their equilibrium positions. Then, the derivative of the forces with respect to the small displacement is extracted numerically, which is equal to minus the second derivative of the energy with respect to two atomic displacements. Whilst the finite-difference method is very convenient (since virtually no extra coding effort is required to specifically deal with derivatives), the numeric nature of the derivatives limits their accuracy. The DFPT techniques are quickly seen to be much more powerful, as they can be used to compute the derivatives with respect to certain perturbations far more efficiently.

3.2 Response Functions

The response function of a material describes how the material responds to a perturbation. Experimentally, the response functions of a material are much more accessible than most ground-state properties; measuring the ground-state density requires careful spectroscopy experiments, measuring the elastic constants of a material requires applying a stress and measuring the resultant strain, which is far easier. The response functions of a material tell us how effective a particular material might be for any specific application.

Our aim as theorists is to be able to make accurate but crucially *useful* predictions about material properties; being able to directly calculate response functions is therefore important since it allows us to make predictions of the effectiveness of a particular material for a set of applications. Provided an accurate model is used to do this, it can be done without having to physically make and test the material, which can be time-consuming and expensive. In order to do this, we first need to formulate the response functions in a manner that they can be computed, the focus here shall be on response functions that can be written as derivatives of the

total energy.

3.2.1 Lattice Dynamics

Lattice dynamics is the movement of the nuclei in a material around their equilibrium positions in the lattice. The dynamics takes the form of quantised vibrations in the lattice, phonons. The phonon modes are of importance to material properties as they can carry thermal energy to transport heat, they can be excited by external stimuli such as photons, neutrons etc, and they can interact with the electron states in material via electron-phonon coupling.

The Born-Oppenheimer (BO) approximation explicitly decouples the nuclear (vibrational) and electronic degrees of freedom in the Hamiltonian. This treatment of the nuclei means that the energy of the system depends parametrically on the atomic positions. The atomic positions of a system, $\boldsymbol{R}_I^{\boldsymbol{c}}$, can be written as,

$$\boldsymbol{R}_I^{\boldsymbol{c}} = \boldsymbol{R}^{\boldsymbol{c}} + \boldsymbol{\tau}_I + \boldsymbol{u}_I^{\boldsymbol{c}}, \tag{3.1}$$

where $\boldsymbol{c}$ is a vector of integers which are the linear combination of the Bravais lattice vectors which gives the position origin of the unit cell containing the atom of interest, $\boldsymbol{R}^{\boldsymbol{c}}$, $\boldsymbol{\tau}_I$ is the equilibrium position of the atom I in a single cell and $\boldsymbol{u}_I^{\boldsymbol{c}}$ denotes the displacement vector from the equilibrium position of atom I in the unit cell denoted by $\boldsymbol{c}$.

Using this definition of the atomic displacements we can perform a Taylor series expansion of the energy as a function of the atomic displacements from the equilibrium configuration with energy E_0,

$$\begin{aligned} E = E_0 + \sum_{I,\boldsymbol{c}} \frac{\mathrm{d}E}{\mathrm{d}\boldsymbol{u}_I^{\boldsymbol{c}}} \boldsymbol{u}_I^{\boldsymbol{c}} + \frac{1}{2} \sum_{I,\boldsymbol{c},J,\boldsymbol{c}'} \frac{\mathrm{d}^2 E}{\mathrm{d}\boldsymbol{u}_I^{\boldsymbol{c}} \mathrm{d}\boldsymbol{u}_J^{\boldsymbol{c}'}} \boldsymbol{u}_I^{\boldsymbol{c}} \boldsymbol{u}_J^{\boldsymbol{c}'} \\ + \frac{1}{6} \sum_{I,\boldsymbol{c},J,\boldsymbol{c}',K,\boldsymbol{c}''} \frac{\mathrm{d}^3 E}{\mathrm{d}\boldsymbol{u}_I^{\boldsymbol{c}} \mathrm{d}\boldsymbol{u}_J^{\boldsymbol{c}'} \mathrm{d}\boldsymbol{u}_K^{\boldsymbol{c}''}} \boldsymbol{u}_I^{\boldsymbol{c}} \boldsymbol{u}_J^{\boldsymbol{c}'} \boldsymbol{u}_K^{\boldsymbol{c}''} + \cdots . \end{aligned} \tag{3.2}$$

The second term in the expansion contains the 1^{st} derivative of the energy with respect to the atomic displacement, which are equal to the minus the atomic forces. At equilibrium, the forces are of course zero; therefore, the second term disappears and we are left with the higher-order derivatives.

A major simplification is to assume that we can work in the harmonic approximation, i.e. that the 3^{rd} order derivatives and higher are all negligible. This allows for the separation of phonons into well-defined modes that add linearly. These second derivatives of the energy are called the interatomic force constants (IFCs), analogous to the spring constant of a simple harmonic oscillator. They

are defined as,

$$\Phi^{\alpha\beta}_{I,\boldsymbol{c},J,\boldsymbol{c'}} = \frac{\mathrm{d}^2 E}{\mathrm{d}u^{\boldsymbol{c}}_{I,\alpha}\mathrm{d}u^{\boldsymbol{c'}}_{J,\beta}}, \tag{3.3}$$

where α and β are indices referring to Cartesian directions of the vectors $\boldsymbol{u}^{\boldsymbol{c}}_I$ and $\boldsymbol{u}^{\boldsymbol{c'}}_J$.

Although the harmonic approximation vastly reduces the number of derivatives that are required for our model of the phonon modes, it still requires knowing the IFCs for every pair of atoms in the material. To make this problem tractable, we can again apply Bloch's theorem.

First, we assume that the material is large enough that the displacements in an arbitrary origin unit cell, $\boldsymbol{u}^{\boldsymbol{c}}_I$, are likely to repeat over some large number of unit cells so that another unit cell denoted by the vector $\boldsymbol{c'}$ has the exact same displacements. Applying Bloch's theorem, the displacements in cell $\boldsymbol{c'}$ are of the form

$$u^{c'}_{I,\alpha} = e^{i\boldsymbol{q}\cdot\boldsymbol{r}}\mu^{\boldsymbol{q}}_{I,\alpha}, \tag{3.4}$$

where $\boldsymbol{r} = \boldsymbol{R^c} - \boldsymbol{R^{c'}}$ is the distance between the origins of the two unit cells (between two points on the Bravais lattice), $\boldsymbol{q}$ is the wave-vector of the periodic displacement, and $\mu^{\boldsymbol{q}}_{I,\alpha}$ is the displacement of atom I, in unit cell $\boldsymbol{c}$, along direction α. In other words, $\mu^{\boldsymbol{q}}_{I,\alpha}$ is the cell-periodic part of the function for the displacement.

The periodicity of the displacements means that we can take the Fourier transform of the IFCs. This is related to the Dynamical Matrix, $D^{\alpha\beta}_{\boldsymbol{q},IJ}$, which is also expressed as the second-order energy derivative with respect to periodic displacements,

$$\sqrt{M_I M_J}D^{\alpha\beta}_{\boldsymbol{q},IJ} = \sum_{\boldsymbol{c'}} e^{-i\boldsymbol{q}\cdot\boldsymbol{r}}\Phi^{\alpha\beta}_{I,\boldsymbol{c},J,\boldsymbol{c'}} = \frac{\partial^2 E}{\partial\left(\mu^{\boldsymbol{q}}_{I,\alpha}\right)^*\partial\mu^{\boldsymbol{q}}_{J,\beta}} \tag{3.5}$$

where M_I is the mass of atom labelled I.

If the dynamical matrix is known for a particular wave-vector $\boldsymbol{q}$, the phonon modes at that wave-vector can be found by solving the following eigenvalue problem,

$$D^{\alpha\beta}_{\boldsymbol{q},IJ}\varepsilon_{\boldsymbol{q},p} = \omega^2_{\boldsymbol{q},p}\varepsilon_{\boldsymbol{q},p} \tag{3.6}$$

where $\omega_{\boldsymbol{q},p}$ is the frequency of the phonon mode labelled p and $\varepsilon_{\boldsymbol{q},p}$ are the cell-periodic functions of the phonon mode describing the displacements of the atoms.

3.2.1.1 Electron-Phonon Coupling

The decoupling of nuclear and electronic degrees of freedom in the BO approximation means that under this approximation, there is no interaction between the

electron and phonon states and there is zero electron-phonon coupling. The process of electron-phonon coupling is important since the interaction between the two causes the electrons and phonons to scatter, impeding both the phononic and electronic transport in the material. This is of particular importance to theories of superconducting and thermoelectric materials.

The electron-phonon coupling can be recovered through the treatment of the Eliashberg equations [85]. The important quantity in the Eliashberg equations is the electron-phonon scattering matrix. The elements of the electron-phonon matrix determine the probability of the scattering occurring. The matrix element, g, for scattering an electron from state $b, \boldsymbol{k}$ to state $b', \boldsymbol{k}+\boldsymbol{q}$ while emitting or absorbing a phonon labelled p, with frequency $\omega_{\boldsymbol{q},p}$ and wave-vector $\boldsymbol{q}$, is given by,

$$g^{p}_{b,\boldsymbol{k};b'\boldsymbol{k}+\boldsymbol{q}} = \sqrt{\frac{\hbar}{2\omega_{\boldsymbol{q},p}}} \left\langle \psi_{b',\boldsymbol{k}+\boldsymbol{q}} \middle| \delta V_{\boldsymbol{q},p} \middle| \psi_{b,\boldsymbol{k}} \right\rangle. \tag{3.7}$$

$\delta V_{\boldsymbol{q},p}$ is the change in the potential that the electrons experience under the perturbation of the phonon mode p. The matrix elements are valid for any arbitrary pair of states and phonon mode; however, only those close to the Fermi surface of the material affect the transport properties. In order to capture the total electron-phonon coupling of the system, the matrix elements must be determined across the whole Fermi surface, which can be an extremely large number of calculations.

3.2.2 Stress and Strain

Stress is a system's response to a deformation. There are several ways of defining the deformation; however, the practical choice for perturbation theory is a homogeneous strain $\eta_{\alpha\beta}$. The strain tensor defines a deformation as a "stretching" of space that transforms a point in the system to another point via a scaling of the strain tensor,

$$r_\alpha \to r_\alpha = \left(\delta_{\alpha\beta} + \eta_{\alpha\beta}\right) r_\beta, \tag{3.8}$$

where the strain tensor is symmetric, i.e. $\eta_{\alpha\beta} = \eta_{\beta\alpha}$.

The stress tensor is defined as the derivative of the energy with respect to strain, per unit volume,

$$\sigma^{\alpha\beta} = \Omega^{-1} \frac{\mathrm{d}E}{\mathrm{d}\eta_{\alpha\beta}}. \tag{3.9}$$

The system stress tells us how the energy will change under the system deforming, such as a change in the lattice vector length, this can be very useful when trying to calculate the ground state structure as we can search for a structure where the stress is zero.

3.2.3 Elastic Constants

The elastic constants are a measure of the "stiffness" of the material, describing how an applied strain $\eta_{\gamma\delta}$, results in a stress $\sigma^{\alpha\beta}$. Among the basic mechanical properties that can be obtained from the elastic constants are the bulk modulus, Young's modulus, the shear modulus, and Poisson's ratio, which tells us about the materials hardness and other properties such as the speed of sound in the material, the constant of thermal expansion and the Debye temperature [86]. The elastic constants can also be used as input to other simulation software, such as finite element modelling, which can allow the simulation of materials on a much larger scale than is available from DFT. This can enable approaches such as digital twinning of real-world devices. In short, knowledge of the elastic constants tensor of a material can be sufficient to determine a wide variety of other material properties and can be utilised in other predictive models. Accurate predictions of the elastic constants is therefore a powerful theoretical tool.

The elastic constants tensor, $C^{\alpha\beta\gamma\delta}$, is a rank-4 tensor that relates the deformation or strain $\eta_{\gamma\delta}$ to the resultant stress, $\sigma^{\alpha\beta}$,

$$\sigma^{\alpha\beta} = C^{\alpha\beta\gamma\delta}\eta_{\gamma\delta} \tag{3.10}$$

This can be expressed as a derivative of the total energy,

$$C^{\alpha\beta\gamma\delta} = \Omega^{-1}\frac{\mathrm{d}^2 E}{\mathrm{d}\eta_{\alpha\beta}\mathrm{d}\eta_{\gamma\delta}}. \tag{3.11}$$

provided the system is at equilibrium, i.e. the atomic forces and stress are zero. Much like the approach described for the phonon modes, this assumes a harmonic model for the elasticity. The are higher order terms which cause non-linear elastic properties in a material, however, in many approximations they are considered to have negligible effect.

3.2.3.1 Frozen- versus Relaxed-Ion Tensors

There is some subtlety to the above definition, since the energy of the system is dependent on the deformation and the displacement of atoms from their equilibrium positions, $E\left(\boldsymbol{u}^I, \eta_{\alpha\beta}\right)$. Expanding this function of the energy around the relaxed ground-state configuration, which has energy E_0 and the atomic forces and stress that are zero, one finds,

$$E\left(\boldsymbol{R}_I, \eta_{\alpha\beta}\right) = E_0 + \frac{1}{2}\Omega_0 \bar{C}^{\alpha\beta\gamma\delta}\eta_{\alpha\beta}\eta_{\gamma\delta} + \frac{1}{2}\sum_I \Lambda_I^{\alpha\beta\gamma}\eta_{\alpha\beta}u_\gamma^I + \frac{1}{2}\sum_{I,J}\Phi_{I,J}^{\alpha\beta}u_\alpha^I u_\beta^J + \cdots, \tag{3.12}$$

where Ω_0 is the volume of the unperturbed unit cell, $\boldsymbol{u}^I$ is the displacement of atom labelled I, $\Phi^{\alpha\beta}_{I,J} = \frac{\partial^2 E}{\partial R^I_\alpha \partial R^J_\beta}$ is again the interatomic force constant matrix, $\Lambda^{\alpha\beta\gamma}_I = \frac{\partial^2 E}{\partial \eta_{\alpha\beta} \partial R^I_\gamma}$ is the force-response internal-strain tensor i.e. the change in the atomic forces under a strain, $\bar{C}^{\alpha\beta\gamma\delta} = \Omega_0^{-1} \frac{\partial^2 E}{\partial \eta_{\alpha\beta} \partial \eta_{\gamma\delta}}$ is the *frozen-ion* elastic constant tensor. The frozen-ion elastic constant tensor is the second derivative of the energy *assuming the atomic positions remain fixed.*

In general, we must take into account atomic relaxations as the deformations are slow enough to allow the atoms to move according to the change in the atomic forces; therefore, we are interested in the *relaxed-ion* elastic constant tensor. The relaxed-ion elastic constants can be found from a combination of the frozen-ion tensor, the force-response internal-strain tensor and the displacement-response internal-strain tensor, $\Gamma^{\alpha\beta}_\gamma$, which are the change in atomic positions under strain, these can be calculated from $\Lambda^{\alpha\beta\gamma}_I$ and the phonon modes at $\boldsymbol{q} = 0$, which are the inverse of $D^{\alpha\beta}_{0,I,J}$,

$$\Gamma^{\alpha\beta}_{\gamma,J} = \Lambda^{\alpha\beta\mu}_I \left(D^{-1}_{0,I,J}\right)_{\gamma\mu}. \tag{3.13}$$

From this we can write an expression for the relaxed-ion elastic constants tensor using the following definition,

$$C^{\alpha\beta\gamma\delta} = \bar{C}^{\alpha\beta\gamma\delta} - \Omega^{-1} \sum_{I,J} \Lambda^{\alpha\beta\mu}_I \left(D^{-1}_{0,I,J}\right)_{\mu\nu} \Lambda^{\gamma\delta\nu}_I. \tag{3.14}$$

From this expression we can see that to determine the elastic constant tensor for a material, we require 3 ingredients; the frozen-ion elastic constants, the phonon modes and the force-response internal-strain tensor [87].

3.2.3.2 Deformation Potential

The description of the electron-phonon coupling given in 3.2.1.1 is cumbersome to make predictions of transport properties, as it requires the calculation of many matrix elements across the Fermi surface for all phonon modes. For small systems with low numbers of atoms and electrons, this calculation remains possible, but for larger simulations with more complex structures, the required computational cost becomes unfeasible. An alternative approach for larger systems is to estimate the electron-phonon coupling using the deformation potential.

The deformation potential theory dates back to the 1950s [88] and approximates the relaxation times due to the coupling of the electrons and the acoustic phonons by considering the acoustic phonons in the long wavelength limit. In the long-wavelength limit the acoustic phonons can be considered as a localised strain on the system, either as a compression or a relaxation of the lattice. From this

approximation we can calculate the effect this has on the electronic states by determining the change in the band edge of the material due to the strain. This change in the band edge due to the strain is the Acoustical Deformation Potential (ADP),

$$\lambda_{\mathrm{ADP}} = \frac{\mathrm{d}\epsilon^{\mathrm{BE}}}{\mathrm{d}\eta_{\alpha\beta}}, \tag{3.15}$$

where λ_{ADP} is the acoustic deformation potential, ϵ^{BE} is the energy of the band edge, which will be either the band energies of the Conduction or Valence Band Minimum or Maximum respectively (CBM, VBM), ϵ^{CBM} and ϵ^{VBM}. The ADP can then be used to calculate an estimate for scattering times of the electrons and holes (using the VBM and CBM respectively) due to the electron-phonon interactions with acoustic phonons using the expression derived by Bardeen and Shockley,

$$\frac{1}{\tau_{\text{e-ph}}} = \frac{\lambda_{\mathrm{ADP}}^2 \pi N\left(\epsilon_{\mathrm{F}}\right) k_{\mathrm{B}} T}{\hbar C^{\alpha\beta\alpha\beta}}, \tag{3.16}$$

where $\tau_{\text{e-ph}}$ is the average time between electron-phonon/hole-phonon scattering events, $N\left(\epsilon_{\mathrm{F}}\right)$ is the density of states at the Fermi level, $k_{\mathrm{B}}T$ is the temperature times the Boltzmann constant and $C^{\alpha\beta\alpha\beta}$ is a diagonal element of the elastic constants tensor.

It can often be the case that the band edges are degenerate, i.e. there are multiple states with the energy of the band edge, or there are multiple (symmetry equivalent) places in the 1st Brillouin zone that also form the band edge. Under the deformation of the phonon, i.e. strain, the degeneracy can be lifted, and the degenerate bands can have different derivatives. Under a positive applied strain, the largest derivatives will be the observed change in the band edge, whereas under a negative strain, the smallest derivatives will be the observed change in the band edge. If we consider the change in band edge under positive and negative strains as two different scattering processes, the scattering rates of each process can then simply be combined via Matthiessen's rule as,

$$\frac{1}{\tau_{\mathrm{tot}}} = \frac{1}{\tau_{+}} + \frac{1}{\tau_{-}}. \tag{3.17}$$

Acoustic deformation potential theory is most relevant to semiconductors and insulators, since acoustic phonons serve as the primary thermal carriers within the phonon spectrum at low temperatures. This model of charge-carrier scattering might be a sufficient approximation for modelling electron-phonon interactions. At higher temperatures, the ADP can serve as a proxy calculation to show how important the effects of electron-phonon coupling are. The deformation potential can be used to make several predictions of transport properties [23, 89]. Since

the deformation potential does not require the integration of many elements of the electron-phonon coupling matrix across the Fermi surface, it is more efficient than the full treatment of electron-phonon coupling via the Eliashberg equations. This makes it much more tractable for high-throughput studies in which many materials are screened for desirable properties [90].

3.3 Perturbation Theory

Let us start with a generic quantum system, a generic perturbation associated with the parameter λ and a generic physical quantity X. When the perturbation is applied, it causes a change to the physical quantity compared to the unperturbed system, ΔX. The physical quantity can be written in the perturbed system as a function of λ and then expressed in terms of a series expansion,

$$X + \Delta X = X(\lambda) = X + \lambda X^{(1)} + \lambda^2 X^{(2)} + \lambda^3 X^{(3)} + \ldots, \tag{3.18}$$

where each term in the expansion is related to the derivative of X with respect to λ,

$$\hat{X}^{(n)} = \frac{1}{n!}\frac{\mathrm{d}^n \hat{X}}{\mathrm{d}\lambda^n}, \tag{3.19}$$

when $n = 0$ this is the physical quantity in the unperturbed system.

All quantities can be treated as perturbative expansions, for instance, we can write the single electron Schrödinger equation where all the terms are now functions of some perturbation,

$$\hat{H}(\lambda)\,|\psi_i(\lambda)\rangle = \epsilon_i(\lambda)\,|\psi_i(\lambda)\rangle\,. \tag{3.20}$$

Now if we expand the Hamiltonian, $\hat{H}$, the wavefunction states $|\psi_i\rangle$ and their eigenvalues, ϵ_i, in the same way as was done in equation 3.18,

$$\hat{H} + \Delta\hat{H} = \hat{H}(\lambda) = \hat{H}^{(0)} + \lambda\hat{H}^{(1)} + \lambda^2\hat{H}^{(2)} + \ldots \tag{3.21}$$

$$|\psi_i\rangle + |\Delta\psi_i\rangle = |\psi_i(\lambda)\rangle = \left|\psi_i^{(0)}\right\rangle + \lambda\left|\psi_i^{(1)}\right\rangle + \lambda^2\left|\psi_i^{(2)}\right\rangle + \ldots \tag{3.22}$$

$$\epsilon_i + \Delta\epsilon_i = \epsilon_i(\lambda) = \epsilon_i^{(0)} + \lambda\epsilon_i^{(1)} + \lambda^2\epsilon_i^{(2)} + \ldots. \tag{3.23}$$

Substituting these expressions into the original Schrödinger equation and separating the resulting equations into powers of λ leads to a series of equations, one equation per order of lambda. At the zeroth order of λ, we recover the Schrödinger equation,

$$\hat{H}^{(0)}\left|\psi_i^{(0)}\right\rangle = \epsilon_i^{(0)}\left|\psi_i^{(0)}\right\rangle, \tag{3.24}$$

and at the first order we get,

$$\hat{H}^{(1)}\left|\psi_i^{(0)}\right\rangle + \hat{H}^{(0)}\left|\psi_i^{(1)}\right\rangle = \epsilon_i^{(1)}\left|\psi_i^{(0)}\right\rangle + \epsilon_i^{(0)}\left|\psi_i^{(1)}\right\rangle. \tag{3.25}$$

This can straightforwardly be rearranged to give us the Sternheimer equation,

$$\left(\hat{H}^{(0)} - \epsilon_i^{(0)}\right)\left|\psi_i^{(1)}\right\rangle = -\left(\hat{H}^{(1)} - \epsilon_i^{(1)}\right)\left|\psi_i^{(0)}\right\rangle. \tag{3.26}$$

In this manner, we can find relations between derivatives of the physical quantities with respect to perturbations to determine ways to compute energy derivatives and therefore material properties.

3.3.1 Density Functional Perturbation Theory

Above we applied the idea of perturbations to a generic quantum system, and the single electron Schrödinger equation. Here we shall apply these ideas to the DFT total energy functional and the Kohn-Sham system. Applying the same method as was used for the single electron system, Taylor expanding quantities as functions of the perturbation and separating the resultant equations by powers of λ we can determine relations between the derivatives.

By substituting the expansion of the Kohn-Sham wavefunctions into the expression for the density one can derive an expression for the first order density,

$$\rho^{(1)}(\boldsymbol{r}) = \Omega^{-1}\sum_b^{\text{occ}}\int_{\text{BZ}} \psi_b^{(1)*}(\boldsymbol{r})\,\psi_b^{(0)}(\boldsymbol{r}) + \psi_b^{(0)*}(\boldsymbol{r})\,\psi_b^{(1)}(\boldsymbol{r})\ \mathrm{d}^3\boldsymbol{k}, \tag{3.27}$$

and a similar expression can be derived for the first order KED,

$$\tau^{(1)}(\boldsymbol{r}) = \Omega^{-1}\sum_b^{\text{occ}}\int_{\text{BZ}} \nabla\psi_b^{(1)*}(\boldsymbol{r})\cdot\nabla\psi_b^{(0)}(\boldsymbol{r}) + \nabla\psi_b^{(0)*}(\boldsymbol{r})\cdot\nabla\psi_b^{(1)}(\boldsymbol{r})\ \mathrm{d}^3\boldsymbol{k}. \tag{3.28}$$

The expressions for $\rho^{(1)}$ and $\tau^{(1)}$ do not take into account possible changes in occupancies of the states around the Fermi energy. Therefore, these expressions are valid only for insulators and wide-band-gap semiconductors. For metals, further terms have been derived that take into account these changes have be derived for the density [91]. These terms only require derivatives of the occupancies and zeroth-order wavefunctions; the additional terms for the first-order KED can be obtained by substituting wavefunctions for the gradient of wavefunction in these expressions.

By substituting the expanded wavefunctions into the expression of the orthogonality constraint, $\langle\psi_i|\psi_j\rangle = \delta_{ij}$, constraints can be found for the first-order wave-

functions,

$$\left\langle \psi_i^{(1)} | \psi_i^{(0)} \right\rangle = 0 \tag{3.29}$$

A Sternheimer equation for the Kohn-Sham Hamiltonian can also be derived,

$$\left(\hat{H}_{KS}^{(0)} - \epsilon_i^{(0)}\right) \left|\psi_i^{(1)}\right\rangle = -\left(\hat{H}_{KS}^{(1)} - \epsilon_i^{(1)}\right) \left|\psi_i^{(0)}\right\rangle. \tag{3.30}$$

3.4 Energy Derivatives

Derivatives of the total energy functional with respect to perturbations can be calculated, provided that we know how the perturbation relates to the energy functional. This allows us to calculate the systems response to a perturbation, i.e. response functions.

3.4.1 First-order Energy Derivatives

First-order derivatives of the energy are very straightforward to compute since the total energy functional has been minimised with respect to any variation in the states. If the total energy has an explicit dependence on a perturbation λ, the first order energy derivative is therefore,

$$\frac{\mathrm{d}E^{\mathrm{tot}}\left[\{\psi_i\},\lambda\right]}{\mathrm{d}\lambda} = \left.\frac{\partial E^{\mathrm{tot}}}{\partial \lambda}\right|_{\psi_i} + \sum_i \frac{\delta E^{\mathrm{tot}}}{\delta \psi_i} \frac{\mathrm{d}\psi_i}{\mathrm{d}\lambda}, \tag{3.31}$$

where the second term in this equation is the change in energy due to variation in the states. For the ground state, the energy has been minimised with respect to these states, therefore, the first-order change in the energy with respect to any variation due to a change in the states *has* to be zero $\left(\frac{\delta E^{\mathrm{tot}}}{\delta \psi_i} = 0\right)$ This is the Hellmann-Feynman theorem [92] for DFT and means that provided the ground state has been found, any change to the wavefunction states or density can be assumed to have negligible contribution to the first-order energy derivatives. To compute the first derivatives of the total energy functional with respect to perturbations, we need only consider the total energy's explicit dependence on the perturbations, not the implicit dependence through changing of the wavefunctions and density.

Above I have used partial derivatives to denote derivatives which include only contributions from explicit dependence, and full derivatives to denote derivatives which include the implicit dependence and the relaxation of the states and wavefunction. I shall continue this practice for the remainder of the thesis.

3.4.1.1 Forces

The atomic forces, $\boldsymbol{F}_I$, are easy to express as a derivative of the total energy, being minus the derivative with respect to atomic positions,

$$-\boldsymbol{F}_I = \frac{\partial E^{\text{tot}}}{\partial \boldsymbol{R}_I} = \left.\frac{\partial E^{\text{tot}}}{\partial \boldsymbol{R}_I}\right|_{\psi_i}. \tag{3.32}$$

The atomic positions explicitly appear in the energy functional in only a few terms, the derivative of the total energy can therefore be computed as the derivative of these terms,

$$\frac{\mathrm{d}E^{\text{tot}}}{\mathrm{d}\boldsymbol{R}_I} = \frac{\partial}{\partial \boldsymbol{R}_I}\left(E^{\text{ext}}_{\text{loc}} + E^{\text{ext}}_{\tau} + E^{\text{ext}}_{\text{nl}} + E^{\text{XC}} + E^{\text{Ion-Ion}}\right). \tag{3.33}$$

3.4.1.2 Stress

Stress is a systems response to strain, $\eta_{\alpha\beta}$. Although the strain tensor never explicitly appears in the total energy functionals, a strain perturbation causes changes to real- and reciprocal-space vectors r_γ, G^γ, and the volume of the unit cell Ω. The derivatives of these quantities under strain are,

$$\frac{\partial r_\gamma}{\partial \eta_{\alpha\beta}} = \delta_{\alpha\gamma} r_\beta, \tag{3.34}$$

$$\frac{\partial G^\gamma}{\partial \eta_{\alpha\beta}} = -\delta_{\alpha\gamma} G^\beta, \tag{3.35}$$

$$\frac{\partial \Omega}{\partial \eta_{\alpha\beta}} = \delta_{\alpha\beta}\Omega, \tag{3.36}$$

where $\delta_{\alpha\beta}$ or $\delta_{\alpha\gamma}$ are the Kronecker delta's. The change of these quantities causes changes throughout every term in the total energy expression which may be derived by application of the chain rule. There is a conceptual difficulty with a strain perturbation in a system with periodic boundary conditions. When an infinitesimal strain is applied to a single unit cell, there is a corresponding infinitesimal change in the other physical quantities; however, when one considers the infinite periodic system, two problems arise.

- The scaling of space will always be a large perturbation. This can be seen in equation 3.8, although $\eta_{\alpha\beta}$ is infinitesimally small, in the infinite system r_β can be infinity large.
- There is a change in boundary conditions, therefore, perturbation theory is no longer applicable.

This difficulty can be avoided by redefining the total energy expression in "re-

duced coordinates", by introducing real- and reciprocal-space metric tensors into every term in this expression [93]. The advantage of the reduced coordinates formulation is that the boundary conditions never change, and perturbations of the metric remain small. There is very little practical difference from how one has to approach deriving the derivatives, but it does place the calculations on firmer conceptual ground.

3.4.1.3 Band energy derivatives

Changes in the band energies due to a perturbation are not as straightforward as changes to the total energy. The band energies derivatives

$$\begin{aligned}\epsilon_b^{(1)} &= \frac{\mathrm{d}\epsilon_b}{\mathrm{d}\lambda} = \frac{\mathrm{d}}{\mathrm{d}\lambda}\left(\langle\psi_b|\,\hat{H}\,|\psi_b\rangle\right) \\ &= \left\langle\psi_b^{(1)}\middle|\,\hat{H}^{(0)}\,\middle|\psi_b^{(0)}\right\rangle + \left\langle\psi_b^{(0)}\middle|\,\hat{H}^{(1)}\,\middle|\psi_b^{(0)}\right\rangle + \left\langle\psi_b^{(0)}\middle|\,\hat{H}^{(0)}\,\middle|\psi_b^{(1)}\right\rangle. \end{aligned} \tag{3.37}$$

The first and third terms are zero from the requirement that $\left\langle\psi_b^{(0)}\middle|\psi_b^{(1)}\right\rangle = 0$, leaving,

$$\epsilon_b^{(1)} = \left\langle\psi_b^{(0)}\middle|\,\hat{H}^{(1)}\,\middle|\psi_b^{(0)}\right\rangle = \left\langle\psi_b^{(0)}\middle|\,\frac{\mathrm{d}\hat{H}}{\mathrm{d}\lambda}\,\middle|\psi_b^{(0)}\right\rangle. \tag{3.38}$$

Note the use of the full derivative rather than a partial derivative on the Hamiltonian operator. The perturbation will cause a change in the states, and therefore the density which alters the Kohn-Sham Hamiltonian via the Hartree and XC potentials. These changes cannot be ignored as can be done with the energy, since the band energy is not at a variational minimum with respect to the wavefunctions. The full change in the Hamiltonian under the perturbation must be computed.

3.4.2 Second-order Energy Derivatives

Second-order derivatives of the energy are more complicated than the first-order derivatives. Several expressions for the second order energy derivatives can be derived depending on how the perturbation changes each term in the Hamiltonian. This is a general expression for second order derivatives with respect to the same perturbation,

$$\begin{aligned}\frac{\mathrm{d}^2E^{\mathrm{tot}}}{\mathrm{d}\lambda^2} =& \sum_b^{\mathrm{occ}}\left\langle\psi_b^{(0)}\middle|\,\frac{\partial^2}{\partial\lambda^2}\left(\hat{T}+\hat{V}^{\mathrm{ext}}\right)\middle|\psi_b^{(0)}\right\rangle + \sum_b^{\mathrm{occ}}\left\langle\psi_b^{(1)}\middle|\,\frac{\partial\hat{H}}{\partial\lambda}\middle|\psi_b^{(0)}\right\rangle + c.c. \\ &+ \left.\frac{\partial^2E^{\mathrm{H}}}{\partial\lambda^2}\right|_{\rho^{(0)}} + \left.\frac{\partial^2E^{\mathrm{XC}}}{\partial\lambda^2}\right|_{\rho^{(0)},\tau^{(0)}} + \frac{\partial^2E^{\text{Ion-Ion}}}{\partial\lambda^2}, \end{aligned} \tag{3.39}$$

where *c.c.* denotes the complex conjugate of the previous term. Note that the second term and its complex conjugate are dependent on the first-order wavefunctions, but no where else are the derivatives of the wavefunctions required. Only the first-order derivatives of the wavefunction are required to calculate the second-order energy derivative. This is a consequence of the $2N+1$ theorem for DFT [94]. The $2N+1$ theorem states that the response of the total energy can be calculated up to the order $2N+1$ with knowledge of only up to the N^{th} derivative of the electronic wavefunctions.

The expression above relies on the correct first-order wavefunctions being known. To find them, an alternate expression to equation 3.39 can be derived for the second-order energies which can be minimised relative to variations in the first-order wavefunctions,

$$\begin{aligned}\frac{\mathrm{d}^2E^{\mathrm{tot}}}{\mathrm{d}\lambda^2} =& \sum_b^{\mathrm{occ}} \left\langle \psi_b^{(1)} \right| \left(\hat{H}^{(0)} - \epsilon^{(0)}\right) \left| \psi_b^{(1)} \right\rangle + \sum_b^{\mathrm{occ}} \left\langle \psi_b^{(0)} \right| \frac{\partial^2}{\partial\lambda^2} \left(\hat{T} + \hat{V}^{\mathrm{ext}}\right) \left| \psi_b^{(0)} \right\rangle + \\ & \sum_b^{\mathrm{occ}} \left\langle \psi_b^{(1)} \right| \frac{\mathrm{d}\hat{H}}{\mathrm{d}\lambda} \left| \psi_b^{(0)} \right\rangle + \sum_b^{\mathrm{occ}} \left\langle \psi_b^{(0)} \right| \frac{\mathrm{d}\hat{H}}{\mathrm{d}\lambda} \left| \psi_b^{(1)} \right\rangle \\ & + \left.\frac{\partial^2 E^{\mathrm{H}}}{\partial\lambda^2}\right|_{\rho^{(0)}} + \left.\frac{\partial^2 E^{\mathrm{XC}}}{\partial\lambda^2}\right|_{\rho^{(0)},\tau^{(0)}} + \frac{\partial^2 E^{\text{Ion-Ion}}}{\partial\lambda^2}. \end{aligned} \tag{3.40}$$

The additional terms in this expression compared to the expression of 3.39 should vanish when the first-order wavefunctions which minimise the above expression are found. Equation 3.39 is a non-variational expression and equation 3.40 is the variational expression. Using the variational expression, conjugate gradient algorithms can be devised that minimise the second-order energy and thus find the first-order wavefunctions.[95, 96]. However, the variational approach can be quite a slow method for finding the first-order wavefunction and has only been implemented in CASTEP for systems with a wide band-gap (insulating systems). An alternative approach is to use the Sternheimer equations to find $\psi_b^{(1)}$.

3.4.2.1 Sternheimer Equation

Calculating the second-order energy derivatives requires the first-order wavefunction $\left|\psi_i^{(1)}\right\rangle$. In order to compute this, we start with the Sternheimer equation,

$$\left(\hat{H}^{(0)} - \epsilon_i^{(0)}\right) \left|\psi_i^{(1)}\right\rangle = -\left(\hat{H}^{(1)} - \epsilon_i^{(1)}\right) \left|\psi_i^{(0)}\right\rangle, \tag{3.41}$$

where in this case the Hamiltonian and states are the Kohn-Sham Hamiltonian and states.

The set of eigenstates to the unperturbed Hamiltonian, $\left|\psi_i^{(0)}\right\rangle$, form a complete

and orthogonal set for this system, making it a natural basis to expand other functions in, such as the first order wavefunctions,

$$\left|\psi_i^{(1)}\right\rangle = \sum_j c_{ij} \left|\psi_j^{(0)}\right\rangle. \tag{3.42}$$

Following some algebra, it can be shown that $\left|\psi_i^{(1)}\right\rangle$ can be expressed as a sum over the zeroth order wavefunction states,

$$\left|\psi_i^{(1)}\right\rangle = \sum_{j\neq i} \left|\psi_j^{(0)}\right\rangle \frac{\left\langle\psi_i^{(0)}\right| \hat{H}^{(1)} \left|\psi_j^{(0)}\right\rangle}{\epsilon_i - \epsilon_j}. \tag{3.43}$$

If we substitute this expression into the expression for the first-order density (equation 3.27), yielding,

$$\begin{aligned}\rho^{(1)}(\boldsymbol{r}) = \Omega^{-1} \sum_b^{\text{occ}} \left(\sum_{j\neq b} \frac{\left\langle\psi_b^{(0)}\right| \hat{H}^{(1)} \left|\psi_j^{(0)}\right\rangle}{\epsilon_b - \epsilon_j} \psi_j^{(0)}(\boldsymbol{r}) \right)^* \cdot \psi_b^{(0)}(\boldsymbol{r}) + \\ \left(\psi_b^{(0)}(\boldsymbol{r})\right)^* \cdot \sum_{j\neq b} \frac{\left\langle\psi_b^{(0)}\right| \hat{H}^{(1)} \left|\psi_j^{(0)}\right\rangle}{\epsilon_b - \epsilon_j} \psi_j^{(0)}(\boldsymbol{r}).\end{aligned} \tag{3.44}$$

Due to the orthogonality conditions on the zeroth order wavefunctions, the contributions from pairs of occupied bands cancel and the first-order densities are only affected by coupling to unoccupied bands. The value of the index j is thus restricted to the conduction bands. We can modify the Sternheimer equation by projecting the first-order wavefunctions onto the conduction subset of the conduction states using a projection operator,

$$P_c = \sum_k^{\text{unocc}} \left|\psi_k^{(0)}\right\rangle \left\langle\psi_k^{(0)}\right| = \mathbb{1} - \sum_l^{\text{occ}} \left|\psi_l^{(0)}\right\rangle \left\langle\psi_l^{(0)}\right|, \tag{3.45}$$

where $\mathbb{1}$ is the identity matrix. The second form of this equation is used in practice as the occupied subspace is much smaller than the unoccupied subspace.

The Sternheimer equation is then written as,

$$P_c \left(\hat{H}^{(0)} - \epsilon_i^{(0)}\right) P_c \left|\psi_i^{(1)}\right\rangle = -P_c \hat{H}^{(1)} \left|\psi_i^{(0)}\right\rangle, \tag{3.46}$$

which projects the first order wavefunction states onto the correct subspace, this can be solved by using a Green's function technique [97].

The difficulty in solving this equation comes from another problem of self-consistency, to find the first-order Hamiltonian one needs the first-order wavefunctions for

which one needs the first-order Hamiltonian. This can be solved by using a Green's function technique [97], where the above equation is iteratively solved. Starting by using $\frac{\partial \hat{H}}{\partial \lambda}$ for $\hat{H}^{(1)}$ on the RHS of the above equation and finding the states $\psi_b^{(1)}$ that solves this equation, then using these solutions to calculate a trial first-order density and first-order Hamiltonian, for which new solutions are found. This continues until the energy derivative of equation 3.39 is converged to an acceptable level, at which point $\psi_b^{(1)}$ are considered converged.

3.4.2.2 Mixed Derivatives

For mixed second derivatives of the energy with respect to two different perturbations, λ and μ, a further expression can be derived,

$$\begin{aligned}\frac{\mathrm{d}^2 E^{\mathrm{tot}}}{\mathrm{d}\lambda \mathrm{d}\mu} =& \sum_b^{\mathrm{occ}} \left\langle \psi_b^{(0)} \middle| \frac{\partial^2}{\partial\lambda\partial\mu}\left(\hat{T}+\hat{V}^{\mathrm{ext}}\right)\middle|\psi_b^{(0)}\right\rangle + \sum_b^{\mathrm{occ}} \left\langle \psi_b^{(\lambda_1)} \middle| \frac{\partial \hat{H}}{\partial\mu}\middle|\psi_b^{(0)}\right\rangle + \\ & \sum_b^{\mathrm{occ}} \left\langle \psi_b^{(0)} \middle| \frac{\partial \hat{H}}{\partial\mu}\middle|\psi_b^{(\lambda_1)}\right\rangle + \left.\frac{\partial^2 E^{\mathrm{H}}}{\partial\lambda\partial\mu}\right|_{\rho^{(0)}} + \left.\frac{\partial^2 E^{\mathrm{XC}}}{\partial\lambda\partial\mu}\right|_{\rho^{(0)},\tau^{(0)}} + \frac{\partial^2 E^{\text{Ion-Ion}}}{\partial\lambda\partial\mu}.\end{aligned} \tag{3.47}$$

Here $\psi_b^{(\lambda_1)}$ denotes the first-order wavefunction with respect to the perturbation λ. This is again a non-variational expression for the mixed derivative. What is convenient about this expression is that it only depends on the first-order wavefunctions for *one* of the perturbations, λ. Therefore, if the first-order wavefunctions with respect to λ can be found, either by a variational approach or by solving the Sternheimer equations, many mixed second order energy derivatives can be calculated that involve λ.

3.4.2.3 Incommensurate Perturbations

So far the perturbation theory formalism has been constrained to perturbations that follow the exact periodic boundary conditions of the unit cell, commensurate perturbations. DFPT can also allow us to consider incommensurate perturbations, provided they can be expressed as a Bloch function, with a cell periodic part, u_λ, and a wave-like part, $e^{i\boldsymbol{q}\cdot\boldsymbol{r}}$ where $\boldsymbol{q}$ is the wave-vector of the perturbation. This is particularly useful in the case of atomic perturbations and calculating the dynamical matrix for phonons with arbitrary wave-vectors $\boldsymbol{q}$.

Physical quantities can be written as a function of the perturbation strength, λ and Taylor expanded in a similar manner to commensurate perturbations, with some subtle differences. Again, taking a generic physical quantity X, it can be

expanded as

$$X(\lambda) = X^{(0)} + \left(\lambda X^{(1)}_{\boldsymbol{q}} + \lambda^* X^{(1)}_{-\boldsymbol{q}}\right) + \left(\lambda^2 X^{(2)}_{\boldsymbol{q},\boldsymbol{q}} + 2\lambda\lambda^* X^{(2)}_{\boldsymbol{q},-\boldsymbol{q}} + \lambda^{*2} X^{(2)}_{-\boldsymbol{q},-\boldsymbol{q}}\right) + \cdots . \tag{3.48}$$

Bloch Factorisation

Under the perturbation the response of wavefunction $\psi_{b\boldsymbol{k}}(\boldsymbol{r})$ must now be expressed as a Bloch function where the wave-like part has periodicity $\boldsymbol{k}+\boldsymbol{q}$,

$$\psi^{(1)}_{b\boldsymbol{k},\boldsymbol{q}}(\boldsymbol{r}) = e^{i(\boldsymbol{k}+\boldsymbol{q})\cdot\boldsymbol{r}} u^{(1)}_{b\boldsymbol{k},\boldsymbol{q}}(\boldsymbol{r}), \tag{3.49}$$

where $u^{(1)}_{b\boldsymbol{k},\boldsymbol{q}}(\boldsymbol{r})$ is a cell-periodic function.

The first-order density and the KED can also be expressed in a Bloch function fashion, with a wave-like part and a cell periodic part,

$$\rho^{(1)}_{\boldsymbol{q}}(\boldsymbol{r}) = e^{i\boldsymbol{q}\cdot\boldsymbol{r}} \bar{\rho}^{(1)}_{\boldsymbol{q}}(\boldsymbol{r}), \tag{3.50}$$

$$\tau^{(1)}_{\boldsymbol{q}}(\boldsymbol{r}) = e^{i\boldsymbol{q}\cdot\boldsymbol{r}} \bar{\tau}^{(1)}_{\boldsymbol{q}}(\boldsymbol{r}), \tag{3.51}$$

where $\bar{\rho}^{(1)}_{\boldsymbol{q}}$ and $\bar{\tau}^{(1)}_{\boldsymbol{q}}$ are the cell-periodic functions, these are the functions that are calculated and handled directly. The cell periodic functions for the density and KED are used to calculate the cell periodic functions for the change in local potentials, for example, which are similarly expressed in the Bloch function form.

Incommensurate Response Density

Expanding $\psi_{b\boldsymbol{k}}$ as a function of the perturbation, and substituting into the expressions for the density and the KED, one finds the following expressions,

$$\bar{\rho}^{(1)}_{\boldsymbol{q}}(\boldsymbol{r}) = \Omega^{-1} \sum_i^{\text{occ}} \int_{\text{BZ}} \left(u^{(0)}_{i,\boldsymbol{k}}(\boldsymbol{r})\right)^* u^{(1)}_{i,\boldsymbol{k},\boldsymbol{q}}(\boldsymbol{r}) + \left(u^{(1)}_{i,\boldsymbol{k},-\boldsymbol{q}}(\boldsymbol{r})\right)^* u^{(0)}_{i,\boldsymbol{k}}(\boldsymbol{r}) \ \mathrm{d}^3\boldsymbol{k}, \tag{3.52}$$

$$\bar{\tau}^{(1)}_{\boldsymbol{q}}(\boldsymbol{r}) = \Omega^{-1} \sum_i^{\text{occ}} \int_{\text{BZ}} \left(\nabla u^{(0)}_{i,\boldsymbol{k}}(\boldsymbol{r})\right)^* \nabla u^{(1)}_{i,\boldsymbol{k},\boldsymbol{q}}(\boldsymbol{r}) + \left(\nabla u^{(1)}_{i,\boldsymbol{k},-\boldsymbol{q}}(\boldsymbol{r})\right)^* \nabla u^{(0)}_{i,\boldsymbol{k}}(\boldsymbol{r}) \ \mathrm{d}^3\boldsymbol{k}. \tag{3.53}$$

These expressions are inconvenient, as they involve a first-order wavefunction in both $\boldsymbol{q}$ and $-\boldsymbol{q}$. However, due to time-reversal symmetry, wavefunctions and the first-order response wavefunctions at $\boldsymbol{k}$ and $-\boldsymbol{k}$ are related by a phase [95]. Therefore we can rewrite the above expressions as,

$$\bar{\rho}^{(1)}_{\boldsymbol{q}}(\boldsymbol{r}) = \Omega^{-1} \sum_i^{\text{occ}} \int_{\text{BZ}} 2\left(u^{(0)}_{i,\boldsymbol{k}}(\boldsymbol{r})\right)^* u^{(1)}_{i,\boldsymbol{k},\boldsymbol{q}}(\boldsymbol{r}) \ \mathrm{d}^3\boldsymbol{k}, \tag{3.54}$$

$$\bar{\tau}^{(1)}_{\boldsymbol{q}}(\boldsymbol{r}) = \Omega^{-1} \sum_{i}^{\text{occ}} \int_{\text{BZ}} 2 \left(\nabla u^{(0)}_{i,\boldsymbol{k}}(\boldsymbol{r}) \right)^{*} \nabla u^{(1)}_{i,\boldsymbol{k},\boldsymbol{q}}(\boldsymbol{r}) \ \mathrm{d}^3\boldsymbol{k}, \tag{3.55}$$

which can be computed much more conveniently. For incommensurate perturbations, equations 3.54 and 3.55 must be used to calculate the first-order response densities, *not* equations 3.27 and 3.28.

Modified Sternheimer Equation

The first order wavefunction can be found by solving a set of Sternheimer equations which for incommensurate perturbations take the form,

$$P_c \left(\hat{H}^{(0)}_{\boldsymbol{k}+\boldsymbol{q}} - \epsilon^{(0)}_{i,\boldsymbol{k}} \right) P_c \left| \psi^{(1)}_{i,\boldsymbol{k},\boldsymbol{q}} \right\rangle = -P_c \hat{H}^{(1)}_{\boldsymbol{k},\boldsymbol{q}} \left| \psi^{(0)}_{i\boldsymbol{k}} \right\rangle, \tag{3.56}$$

where the projection operator is now,

$$P_c = \mathbb{1} - \sum_{l}^{\text{occ}} \left| \psi^{(0)}_{l,\boldsymbol{k}+\boldsymbol{q}} \right\rangle \left\langle \psi^{(0)}_{l,\boldsymbol{k}+\boldsymbol{q}} \right|. \tag{3.57}$$

The first-order wavefunctions $\psi^{(1)}_{i,\boldsymbol{k},\boldsymbol{q}}$ are now subject to a constraint with zeroth-order wavefunctions at $\boldsymbol{k}+\boldsymbol{q}$,

$$\left\langle \psi^{(0)}_{i,\boldsymbol{k}+\boldsymbol{q}} \middle| \psi^{(1)}_{j,\boldsymbol{k},\boldsymbol{q}} \right\rangle = 0. \tag{3.58}$$

The Sternheimer equations are solved iteratively using a Green's function technique [59].

Energy Derivatives

The first-order response to the energy to such perturbations must be zero to conserve translational symmetry, unless $\boldsymbol{q}$ is a reciprocal lattice vector, in which case the perturbation can be treated as commensurate [95]. The calculation of the element $E^{(2)}_{\boldsymbol{q},-\boldsymbol{q}}$ is required for phonon modes. This value can be calculated according to the following variational expression,

$$\begin{aligned} \frac{\mathrm{d}^2 E^{\text{tot}}}{\mathrm{d}\lambda^* \mathrm{d}\lambda} = \int_{\text{BZ}} \Bigg[& \sum_{b}^{\text{occ}} \left\langle \psi^{(1)}_{b,\boldsymbol{k},\boldsymbol{q}} \right| \left(\hat{H}^{(0)}_{\boldsymbol{k}+\boldsymbol{q}} - \epsilon^{(0)}_{\boldsymbol{k}} \right) \left| \psi^{(1)}_{b,\boldsymbol{k},\boldsymbol{q}} \right\rangle + \sum_{b}^{\text{occ}} \left\langle \psi^{(1)}_{b,\boldsymbol{k},\boldsymbol{q}} \right| \frac{\mathrm{d}\hat{H}_{\boldsymbol{k},\boldsymbol{q}}}{\mathrm{d}\lambda} \left| \psi^{(0)}_{b,\boldsymbol{k}} \right\rangle + \\ & \sum_{b}^{\text{occ}} \left\langle \psi^{(0)}_{b,\boldsymbol{k}} \right| \frac{\mathrm{d}\hat{H}_{\boldsymbol{k},\boldsymbol{q}}}{\mathrm{d}\lambda} \left| \psi^{(1)}_{b,\boldsymbol{k},\boldsymbol{q}} \right\rangle + \sum_{b}^{\text{occ}} \left\langle \psi^{(0)}_{b,\boldsymbol{k}} \right| \frac{\partial^2}{\partial\lambda^* \partial\lambda} \left(\hat{T} + \hat{V}^{\text{ext}} \right) \left| \psi^{(0)}_{b,\boldsymbol{k}} \right\rangle \Bigg] \ \mathrm{d}^3\boldsymbol{k} \\ & + \frac{\partial^2 E^{\text{H}}}{\partial\lambda^* \partial\lambda}\bigg|_{\rho^{(0)}} + \frac{\partial^2 E^{\text{XC}}}{\partial\lambda^* \partial\lambda}\bigg|_{\rho^{(0)},\tau^{(0)}} + \frac{\partial^2 E^{\text{Ion-Ion}}}{\partial\lambda^* \partial\lambda}. \end{aligned} \tag{3.59}$$

A non-variational expression can also be constructed for the mixed derivative of the energy with respect to a pair of incommensurate perturbations that both have

wave-vector $\boldsymbol{q}$,

$$\frac{\mathrm{d}^2 E^{\mathrm{tot}}}{\mathrm{d}\mu^* \mathrm{d}\lambda} = \int_{\mathrm{BZ}} \left[\sum_b^{\mathrm{occ}} \left\langle \psi_{b,\boldsymbol{k},\boldsymbol{q}}^{(\mu_1)} \middle| \frac{\partial \hat{H}_{\boldsymbol{k},\boldsymbol{q}}}{\partial \lambda} \middle| \psi_{b,\boldsymbol{k}}^{(0)} \right\rangle + \sum_b^{\mathrm{occ}} \left\langle \psi_{b,\boldsymbol{k}}^{(0)} \middle| \frac{\partial \hat{H}_{\boldsymbol{k},\boldsymbol{q}}}{\partial \lambda} \middle| \psi_{b,\boldsymbol{k},\boldsymbol{q}}^{(\mu_1)} \right\rangle + \right.$$
$$\left. + \sum_b^{\mathrm{occ}} \left\langle \psi_{b,\boldsymbol{k}}^{(0)} \middle| \frac{\partial^2}{\partial \mu^* \partial \lambda} \left(\hat{T} + \hat{V}^{\mathrm{ext}} \right) \middle| \psi_{b,\boldsymbol{k}}^{(0)} \right\rangle \right] \mathrm{d}^3 \boldsymbol{k}$$
$$+ \frac{\partial^2 E^{\mathrm{H}}}{\partial \mu^* \partial \lambda}\bigg|_{\rho^{(0)}} + \frac{\partial^2 E^{\mathrm{XC}}}{\partial \mu^* \partial \lambda}\bigg|_{\rho^{(0)},\tau^{(0)}} + \frac{\partial^2 E^{\text{Ion-Ion}}}{\partial \mu^* \partial \lambda}. \tag{3.60}$$

where, $\left| \psi_{b,\boldsymbol{k},\boldsymbol{q}}^{(\mu_1)} \right\rangle$ is the 1st order response wavefunction with respect to μ. Note that in both expressions the second partial derivatives of quantities are not incommensurate, as the $\boldsymbol{q}$ and $-\boldsymbol{q}$ wave-vectors of the two perturbations cancel.

3.4.3 Derivatives of the mGGA Quantities

There are additional terms in the Kohn-Sham Hamiltonian and the total energy expression when using mGGA functionals. The additional contributions must also be considered under perturbations. Here we shall again only consider the definitions for non-spin-polarised systems, as they are directly relevant to the practical calculations in the remainder of the thesis.

3.4.3.1 First-Order mGGA Hamiltonian

When using mGGA functionals the Hamiltonian becomes,

$$\hat{H} = \hat{T} + V^H + \hat{V}_{\mathrm{loc}}^{\mathrm{ext}} + \hat{V}_{\mathrm{nl}}^{\mathrm{ext}} + \hat{V}_{\tau}^{\mathrm{ext}} + \hat{V}^{\mathrm{XC}}. \tag{3.61}$$

with the extra terms that arise in two places, the differential part of the external potential, $\hat{V}_{\tau}^{\mathrm{ext}}$ and the exchange and correlation potential operator, $\hat{V}^{\mathrm{XC}}$. The handling of the other terms is well understood; here we shall devote our attention to the new terms.

First-Order External Potential

Starting with $\hat{V}_{\tau}^{\mathrm{ext}}$, the expression for this operator is shown in Equation 2.37. Taking the derivative of the operator must be done with care, if the perturbation causes any changes to the gradient operator, e.g. a strain perturbation, those

changes must also be taken into account,

$$\begin{aligned}\frac{\mathrm{d}\hat{V}_\tau^{\mathrm{ext}}(\boldsymbol{r})}{\mathrm{d}\lambda} =& \frac{\mathrm{d}}{\mathrm{d}\lambda}\left(-\frac{1}{2}\nabla\cdot\left(V_\tau^{\mathrm{local}}(\boldsymbol{r})\,\nabla\right)\right)\\ =& -\frac{1}{2}\left(\frac{\mathrm{d}\nabla}{\mathrm{d}\lambda}\cdot\left(V_\tau^{\mathrm{local}}(\boldsymbol{r})\,\nabla\right)+\nabla\cdot\left(\frac{\mathrm{d}V_\tau^{\mathrm{local}}(\boldsymbol{r})}{\mathrm{d}\lambda}\nabla\right)+\right.\\ &\left.\nabla\cdot\left(V_\tau^{\mathrm{local}}(\boldsymbol{r})\frac{\mathrm{d}\nabla}{\mathrm{d}\lambda}\right)\right).\end{aligned} \tag{3.62}$$

First-Order mGGA XC potential

Now we shall consider the XC potential operator, $\hat{V}^{\mathrm{XC}}$. The operator is defined in equation 2.65, however, it is more convenient to work in terms of the local potentials defined in equations 2.66 and 2.67,

$$\hat{V}^{\mathrm{XC}}(\boldsymbol{r}) = V_\rho^{\mathrm{XC}}(\boldsymbol{r}) - \frac{1}{2}\nabla\cdot\left(V_\tau^{\mathrm{XC}}(\boldsymbol{r})\,\nabla\right). \tag{3.63}$$

The first-order XC potential can then be calculated as the derivative of this expression with respect to λ, again handling any changes to the gradient operator under the perturbation,

$$\begin{aligned}\frac{\mathrm{d}\hat{V}^{\mathrm{XC}}(\boldsymbol{r})}{\mathrm{d}\lambda} =& \frac{\mathrm{d}}{\mathrm{d}\lambda}\left(V_\rho^{\mathrm{XC}}(\boldsymbol{r}) - \frac{1}{2}\nabla\cdot\left(V_\tau^{\mathrm{XC}}(\boldsymbol{r})\,\nabla\right)\right)\\ =& \frac{\mathrm{d}V_\rho^{\mathrm{XC}}(\boldsymbol{r})}{\mathrm{d}\lambda} - \frac{1}{2}\left[\frac{\mathrm{d}\nabla}{\mathrm{d}\lambda}\cdot\left(V_\tau^{\mathrm{XC}}(\boldsymbol{r})\,\nabla\right)+\right.\\ &\left.\nabla\cdot\left(\frac{\mathrm{d}V_\tau^{\mathrm{XC}}(\boldsymbol{r})}{\mathrm{d}\lambda}\nabla\right)+\nabla\cdot\left(V_\tau^{\mathrm{XC}}(\boldsymbol{r})\frac{\mathrm{d}\nabla}{\mathrm{d}\lambda}\right)\right].\end{aligned} \tag{3.64}$$

Each of the local potentials have derivatives arising from the changes in the density, the gradient of the density, and the KED under the perturbation. Starting with $V_\rho^{\mathrm{XC}}(\boldsymbol{r})$,

$$\begin{aligned}\frac{\mathrm{d}V_\rho^{\mathrm{XC}}(\boldsymbol{r})}{\mathrm{d}\lambda} =& \frac{\mathrm{d}}{\mathrm{d}\lambda}\left(\frac{\partial f^{\mathrm{XC}}}{\partial\rho} - \nabla^\nu\left(\frac{\partial f^{\mathrm{XC}}}{\partial|\nabla\rho|}\frac{\nabla^\nu\rho}{|\nabla\rho|}\right)\right)\\ =& \frac{\partial^2 f^{\mathrm{XC}}}{\partial\rho^2}\frac{\mathrm{d}\rho}{\mathrm{d}\lambda} + \frac{\partial^2 f^{\mathrm{XC}}}{\partial\rho\partial|\nabla\rho|}\frac{\mathrm{d}|\nabla\rho|}{\mathrm{d}\lambda} + \frac{\partial^2 f^{\mathrm{XC}}}{\partial\rho\partial\tau}\frac{\mathrm{d}\tau}{\mathrm{d}\lambda} - \frac{\mathrm{d}\nabla^\nu}{\mathrm{d}\lambda}\left(\frac{\partial f^{\mathrm{XC}}}{\partial|\nabla\rho|}\frac{\nabla^\nu\rho}{|\nabla\rho|}\right)\\ &- \nabla^\nu\left[\left(\frac{\partial^2 f^{\mathrm{XC}}}{\partial|\nabla\rho|\,\partial\rho}\frac{\mathrm{d}\rho}{\mathrm{d}\lambda} + \frac{\partial^2 f^{\mathrm{XC}}}{\partial|\nabla\rho|^2}\frac{\mathrm{d}|\nabla\rho|}{\mathrm{d}\lambda} + \frac{\partial^2 f^{\mathrm{XC}}}{\partial|\nabla\rho|\,\partial\tau}\frac{\mathrm{d}\tau}{\mathrm{d}\lambda}\right)\frac{\nabla^\nu\rho}{|\nabla\rho|}\right.\\ &\left.+\frac{\partial f^{\mathrm{XC}}}{\partial|\nabla\rho|}\left(\frac{1}{|\nabla\rho|}\frac{\mathrm{d}(\nabla^\nu\rho)}{\mathrm{d}\lambda} - \frac{\nabla^\nu\rho}{|\nabla\rho|^2}\frac{\mathrm{d}|\nabla\rho|}{\mathrm{d}\lambda}\right)\right].\end{aligned} \tag{3.65}$$

Applying the chain rule to $\frac{\mathrm{d}(|\nabla\rho|)}{\mathrm{d}\lambda}$ we get,

$$\frac{\mathrm{d}\left(|\nabla\rho|\right)}{\mathrm{d}\lambda} = \frac{\nabla^\zeta\rho}{|\nabla\rho|}\frac{\mathrm{d}\left(\nabla^\zeta\rho\right)}{\mathrm{d}\lambda}, \tag{3.66}$$

which we can then substitute into the expression above and with some rearranging, we get,

$$\begin{aligned}\frac{\mathrm{d}V_\rho^{\mathrm{XC}}(\boldsymbol{r})}{\mathrm{d}\lambda} = {} & \frac{\partial^2 f^{\mathrm{XC}}}{\partial\rho^2}\frac{\mathrm{d}\rho}{\mathrm{d}\lambda} + \frac{\partial^2 f^{\mathrm{XC}}}{\partial\rho\partial|\nabla\rho|}\frac{\nabla^\zeta\rho}{|\nabla\rho|}\frac{\mathrm{d}\left(\nabla^\zeta\rho\right)}{\mathrm{d}\lambda} + \frac{\partial^2 f^{\mathrm{XC}}}{\partial\rho\partial\tau}\frac{\mathrm{d}\tau}{\mathrm{d}\lambda} - \frac{\mathrm{d}\nabla^\nu}{\mathrm{d}\lambda}\left(\frac{\partial f^{\mathrm{XC}}}{\partial|\nabla\rho|}\frac{\nabla^\nu\rho}{|\nabla\rho|}\right) \\ & - \nabla^\nu\Bigg[\left(\frac{\partial^2 f^{\mathrm{XC}}}{\partial|\nabla\rho|\partial\rho}\frac{\mathrm{d}\rho}{\mathrm{d}\lambda} + \frac{\partial^2 f^{\mathrm{XC}}}{\partial|\nabla\rho|\partial\tau}\frac{\mathrm{d}\tau}{\mathrm{d}\lambda}\right)\frac{\nabla^\nu\rho}{|\nabla\rho|} + \frac{\partial f^{\mathrm{XC}}}{\partial|\nabla\rho|}\frac{1}{|\nabla\rho|}\frac{\mathrm{d}\left(\nabla^\nu\rho\right)}{\mathrm{d}\lambda} \\ & + \left(\frac{\partial^2 f^{\mathrm{XC}}}{\partial|\nabla\rho|^2}\frac{\nabla^\zeta\rho\nabla^\nu\rho}{|\nabla\rho|^2} - \frac{\partial f^{\mathrm{XC}}}{\partial|\nabla\rho|}\frac{\nabla^\zeta\rho\nabla^\nu\rho}{|\nabla\rho|^3}\right)\frac{\mathrm{d}\left(\nabla^\zeta\rho\right)}{\mathrm{d}\lambda}\Bigg],\end{aligned} \tag{3.67}$$

where the expressions $\nabla^\zeta\rho\nabla^\nu\rho$ on the last line are interpreted as the outer product of the gradient of the density at point $\boldsymbol{r}$. This creates a rank-2 tensor-like object with indices ζ and ν, which is multiplied by the vector, the derivative of the gradient of the density with respect to μ, which has the index ζ, resulting in an object with an ν index, which can safely have the gradient operator outside the square brackets applied to it.

Now we consider the far simpler $V_\rho^{\mathrm{XC}}(\boldsymbol{r})$,

$$\frac{\mathrm{d}V_\tau^{\mathrm{XC}}(\boldsymbol{r})}{\mathrm{d}\lambda} = \frac{\partial^2 f^{\mathrm{XC}}}{\partial\tau\partial\rho}\frac{\mathrm{d}\rho}{\mathrm{d}\lambda} + \frac{\partial^2 f^{\mathrm{XC}}}{\partial\tau\partial|\nabla\rho|}\frac{\nabla^\zeta\rho}{|\nabla\rho|}\frac{\mathrm{d}\left(\nabla^\zeta\rho\right)}{\mathrm{d}\lambda} + \frac{\partial^2 f^{\mathrm{XC}}}{\partial\tau^2}\frac{\mathrm{d}\tau}{\mathrm{d}\lambda}. \tag{3.68}$$

These equations define the first-order response XC potential for a mGGA functional under a perturbation λ. For brevity, $\rho(\boldsymbol{r})$, $\tau(\boldsymbol{r})$, and $f^{\mathrm{XC}}(\rho(\boldsymbol{r}),|\nabla\rho(\boldsymbol{r})|,\tau(\boldsymbol{r}))$ have not been shown as functions. ρ and τ are also the total density and KED, including contributions from the non-linear core corrections. In the case of incommensurate perturbations, we calculate the cell periodic function of the potential, using the cell-periodic function for the density and KED as described in [96].

Analytical derivation of the second-order partial derivatives of f^{XC} by hand would be cumbersome and error-prone. Instead of deriving these derivatives by hand, we have two options:

1. Numerical derivatives - efficient for programmer but are obviously prone to numerical errors.

2. Algorithmic differentiation and automatic code generation - requires rewriting the XC functional in a computer algebra system which is less efficient for the programmer but should provide "error-free" code. Thankfully, LibXC,

a library of XC functionals, has already implemented many XC functionals in computer algebra and can provide functions to calculate up to the 4^{th} order derivatives.

Numerical derivatives and an interface to LibXC to calculate the 2^{nd} order partial derivatives of f^{XC} have been implemented in CASTEP and are trialled in this work.

3.4.3.2 Total Energy derivatives

Expressions for the second derivatives of the total energy are given in equations 3.40, 3.39, 3.47 and 3.59. We shall consider equation 3.47, the non-variational expression for a mixed second derivative of the energy,

$$\begin{aligned}\frac{\mathrm{d}^2E^{\text{tot}}}{\mathrm{d}\lambda\mathrm{d}\mu} =& \sum_b^{\text{occ}} \left\langle \psi_b^{(0)} \middle| \frac{\partial^2}{\partial\lambda\partial\mu}\left(\hat{T}+\hat{V}_{\text{loc}}^{\text{ext}}+\hat{V}_{\text{nl}}^{\text{ext}}\right) \middle| \psi_b^{(0)} \right\rangle + \sum_b^{\text{occ}} \left\langle \psi_b^{(\lambda_1)} \middle| \frac{\partial\hat{H}}{\partial\mu} \middle| \psi_b^{(0)} \right\rangle + \\ & \sum_b^{\text{occ}} \left\langle \psi_b^{(0)} \middle| \frac{\partial\hat{H}}{\partial\mu} \middle| \psi_b^{(\lambda_1)} \right\rangle + \left.\frac{\partial^2 E^{\text{H}}}{\partial\lambda\partial\mu}\right|_{\rho^{(0)}} + \frac{\partial^2 E^{\text{Ion-Ion}}}{\partial\lambda\partial\mu}, \\ & + \left.\frac{\partial^2 E_\tau^{\text{ext}}}{\partial\lambda\partial\mu}\right|_{\tau^{(0)}} + \left.\frac{\partial^2 E^{\text{XC}}}{\partial\lambda\partial\mu}\right|_{\rho^{(0)},\tau^{(0)}}\end{aligned} \tag{3.69}$$

This is a rewriting of equation 3.47, such that the external potential operator has been separated into its different contributions and contribution to the energy from the differential operator E_τ^{ext} has been moved from the first term to its own expression. This makes the following derivations more straightforward. Now, the last line of this expression contains the only two terms that are different in the meta-GGA formalism.

External Potential Energy

Recall from equation 2.63 that E_τ^{ext} can be more conveniently computed as an integral over the product of the local potential part of $\hat{V}_\tau^{\text{ext}}$ and the KED,

$$E_\tau^{\text{ext}} = \Omega \int_\Omega V_\tau^{\text{ext}}(\boldsymbol{r})\,\tau(\boldsymbol{r})\ \mathrm{d}^3\boldsymbol{r}. \tag{3.70}$$

The energy derivatives are also far more straightforward to derive from this expression.

Starting from the first derivative of E_τ^{ext} with respect to λ,

$$\frac{\partial E_\tau^{\text{ext}}}{\partial\lambda} = \frac{\partial\Omega}{\partial\lambda}\int_\Omega V_\tau^{\text{ext}}(\boldsymbol{r})\,\tau(\boldsymbol{r})\ \mathrm{d}^3\boldsymbol{r} + \Omega\int_\Omega\left(\frac{\partial V_\tau^{\text{ext}}(\boldsymbol{r})}{\partial\lambda}\tau(\boldsymbol{r}) + V_\tau^{\text{ext}}(\boldsymbol{r})\frac{\partial\tau(\boldsymbol{r})}{\partial\lambda}\right)\mathrm{d}^3\boldsymbol{r}. \tag{3.71}$$

We can then obtain the mixed derivative by differentiating again, this time with respect to the other perturbation μ,

$$\begin{aligned}\frac{\partial^2 E_\tau^{\text{ext}}}{\partial\lambda\partial\mu} = &\frac{\partial^2\Omega}{\partial\lambda\partial\mu}\int_\Omega V_\tau^{\text{ext}}(\boldsymbol{r})\,\tau(\boldsymbol{r})\ \mathrm{d}^3\boldsymbol{r} \\ &+\frac{\partial\Omega}{\partial\mu}\int_\Omega\left(\frac{\partial V_\tau^{\text{ext}}(\boldsymbol{r})}{\partial\lambda}\tau(\boldsymbol{r})+V_\tau^{\text{ext}}(\boldsymbol{r})\frac{\partial\tau(\boldsymbol{r})}{\partial\lambda}\right)\mathrm{d}^3\boldsymbol{r} \\ &+\frac{\partial\Omega}{\partial\lambda}\int_\Omega\left(\frac{\partial V_\tau^{\text{ext}}(\boldsymbol{r})}{\partial\mu}\tau(\boldsymbol{r})+V_\tau^{\text{ext}}(\boldsymbol{r})\frac{\partial\tau(\boldsymbol{r})}{\partial\mu}\right)\mathrm{d}^3\boldsymbol{r} \\ &+\Omega\int_\Omega\left[\frac{\partial^2 V_\tau^{\text{ext}}(\boldsymbol{r})}{\partial\mu\partial\lambda}\tau(\boldsymbol{r})+\frac{\partial V_\tau^{\text{ext}}(\boldsymbol{r})}{\partial\mu}\frac{\partial\tau(\boldsymbol{r})}{\partial\lambda}\right. \\ &\qquad\left.+\frac{\partial V_\tau^{\text{ext}}(\boldsymbol{r})}{\partial\lambda}\frac{\partial\tau(\boldsymbol{r})}{\partial\mu}+V_\tau^{\text{ext}}(\boldsymbol{r})\frac{\partial^2\tau(\boldsymbol{r})}{\partial\mu\partial\lambda}\right]\mathrm{d}^3\boldsymbol{r}. \end{aligned} \tag{3.72}$$

For many cases the full detail of this expression is unnecessary. For a pair of volume preserving perturbations that also do not change the definition of τ the expression is far simpler,

$$\frac{\partial^2 E_\tau^{\text{ext}}}{\partial\lambda\partial\mu} = \Omega\int_\Omega\frac{\partial^2 V_\tau^{\text{ext}}(\boldsymbol{r})}{\partial\mu\partial\lambda}\tau(\boldsymbol{r})\ \mathrm{d}^3\boldsymbol{r}, \tag{3.73}$$

however, the full expression given in 3.72 is required when considering pairs of strain perturbations.

XC Energy

For the XC energy, we shall take follow the approach of Hamman *et al* in [98] and start from the numerical expression for the XC energy given in equation 2.68 rather than the analytic expression given in equation 2.64,

$$E^{\text{XC}} = \frac{\Omega}{N_{\text{p}}}\sum_i^{N_{\text{p}}} f^{\text{XC}}\left(\rho_{\text{t}}(\boldsymbol{r}_i), |\nabla\rho_{\text{t}}(\boldsymbol{r}_i)|, \tau_{\text{t}}(\boldsymbol{r}_i)\right) \tag{3.74}$$

where the integral of the f^{XC} is instead expressed as it is computed as a sum over points.

Taking the derivative of this expression with respect to λ we get,

$$\begin{aligned}\frac{\partial E^{\text{XC}}}{\partial\lambda} = &\frac{\partial\Omega}{\partial\lambda}\frac{1}{N_{\text{p}}}\sum_i^{N_{\text{p}}} f^{\text{XC}}\left(\rho(\boldsymbol{r}_i), |\nabla\rho(\boldsymbol{r}_i)|, \tau(\boldsymbol{r}_i)\right) \\ &+\frac{\Omega}{N_{\text{p}}}\sum_i^{N_{\text{p}}}\left[\frac{\partial f^{\text{XC}}}{\partial\rho}\frac{\partial\rho}{\partial\lambda}+\frac{\partial f^{\text{XC}}}{\partial|\nabla\rho|}\frac{\nabla^\nu\rho}{|\nabla\rho|}\frac{\partial(\nabla^\nu\rho)}{\partial\lambda}+\frac{\partial f^{\text{XC}}}{\partial\tau}\frac{\partial\tau}{\partial\lambda}\right]\end{aligned} \tag{3.75}$$

An alternate expression can be derived which instead uses the local potentials

defined in equations 2.66 and 2.67,

$$\frac{\partial E^{\mathrm{XC}}}{\partial \lambda} = \frac{\partial \Omega}{\partial \lambda}\frac{1}{N_{\mathrm{p}}}\sum_{i}^{N_{\mathrm{p}}} f^{\mathrm{XC}}\left(\rho\left(\boldsymbol{r}_i\right), \left|\nabla\rho\left(\boldsymbol{r}_i\right)\right|, \tau\left(\boldsymbol{r}_i\right)\right) + \frac{\Omega}{N_{\mathrm{p}}}\sum_{i}^{N_{\mathrm{p}}}\left[V_{\rho}^{\mathrm{XC}}\frac{\partial \rho}{\partial \lambda} + V_{\tau}^{\mathrm{XC}}\frac{\partial \tau}{\partial \lambda} + \frac{\partial f^{\mathrm{XC}}}{\partial\left|\nabla\rho\right|}\frac{\nabla^{\nu}\rho}{\left|\nabla\rho\right|}\frac{\partial \nabla^{\nu}}{\partial \lambda}\left(\rho\right)\right], \tag{3.76}$$

which can be obtained by expanding from the application of the chain rule to $\frac{\partial|\nabla\rho|}{\partial\lambda}$ and then the product rule to $\nabla^{\nu}\rho$.

Taking the derivative of this second expression with respect to the second perturbation μ gives,

$$\begin{aligned}
\frac{\partial^2 E^{\mathrm{XC}}}{\partial\lambda\partial\mu} =& \frac{\partial^2\Omega}{\partial\lambda\partial\mu}\frac{1}{N_{\mathrm{p}}}\sum_{i}^{N_{\mathrm{p}}} f^{\mathrm{XC}}\left(\rho\left(\boldsymbol{r}_i\right), \left|\nabla\rho\left(\boldsymbol{r}_i\right)\right|, \tau\left(\boldsymbol{r}_i\right)\right) \\
&+ \frac{\partial\Omega}{\partial\mu}\frac{1}{N_{\mathrm{p}}}\sum_{i}^{N_{\mathrm{p}}}\left[V_{\rho}^{\mathrm{XC}}\frac{\partial\rho}{\partial\lambda} + V_{\tau}^{\mathrm{XC}}\frac{\partial\tau}{\partial\lambda} + \frac{\partial f^{\mathrm{XC}}}{\partial\left|\nabla\rho\right|}\frac{\nabla^{\nu}\rho}{\left|\nabla\rho\right|}\frac{\partial\nabla^{\nu}}{\partial\lambda}\left(\rho\right)\right] \\
&+ \frac{\partial\Omega}{\partial\lambda}\frac{1}{N_{\mathrm{p}}}\sum_{i}^{N_{\mathrm{p}}}\left[V_{\rho}^{\mathrm{XC}}\frac{\partial\rho}{\partial\mu} + V_{\tau}^{\mathrm{XC}}\frac{\partial\tau}{\partial\mu} + \frac{\partial f^{\mathrm{XC}}}{\partial\left|\nabla\rho\right|}\frac{\nabla^{\nu}\rho}{\left|\nabla\rho\right|}\frac{\partial\nabla^{\nu}}{\partial\mu}\left(\rho\right)\right] \\
&+ \frac{\Omega}{N_{\mathrm{p}}}\sum_{i}^{N_{\mathrm{p}}}\left[V_{\rho}^{\mathrm{XC}}\frac{\partial^2\rho}{\partial\lambda\partial\mu} + V_{\tau}^{\mathrm{XC}}\frac{\partial^2\tau}{\partial\lambda\partial\mu} + \frac{\partial V_{\rho}^{\mathrm{XC}}}{\partial\mu}\frac{\partial\rho}{\partial\lambda} + \frac{\partial V_{\tau}^{\mathrm{XC}}}{\partial\mu}\frac{\partial\tau}{\partial\lambda}\right. \\
&+ \left\{\frac{\partial^2 f^{\mathrm{XC}}}{\partial\left|\nabla\rho\right|\partial\rho}\frac{\partial\rho}{\partial\mu} + \frac{\partial^2 f^{\mathrm{XC}}}{\partial\left|\nabla\rho\right|\partial\tau}\frac{\partial\tau}{\partial\mu}\right\}\frac{\nabla^{\nu}\rho}{\left|\nabla\rho\right|}\frac{\partial\nabla^{\nu}}{\partial\lambda}\left(\rho\right) \\
&+ \left(\frac{\partial^2 f^{\mathrm{XC}}}{\partial\left|\nabla\rho\right|^2}\frac{\nabla^{\nu}\rho\nabla^{\zeta}\rho}{\left|\nabla\rho\right|^2} - \frac{\partial f^{\mathrm{XC}}}{\partial\left|\nabla\rho\right|}\frac{\nabla^{\nu}\rho\nabla^{\zeta}\rho}{\left|\nabla\rho\right|^3}\right)\frac{\partial\left(\nabla^{\zeta}\rho\right)}{\partial\mu}\frac{\partial\left(\nabla^{\nu}\right)}{\partial\lambda}\left(\rho\right) \\
&+ \frac{\partial f^{\mathrm{XC}}}{\partial\left|\nabla\rho\right|}\left\{\frac{1}{\left|\nabla\rho\right|}\frac{\partial\left(\nabla^{\nu}\rho\right)}{\partial\mu}\frac{\partial\nabla^{\nu}}{\partial\lambda}\left(\rho\right)\right. \\
&\left.\left.+ \frac{\nabla^{\nu}\rho}{\left|\nabla\rho\right|^2}\frac{\partial^2\nabla^{\nu}}{\partial\lambda\partial\mu}\left(\rho\right) + \frac{\nabla^{\nu}\rho}{\left|\nabla\rho\right|^2}\frac{\partial\nabla^{\nu}}{\partial\lambda}\left(\frac{\partial\rho}{\partial\mu}\right)\right\}\right],
\end{aligned} \tag{3.77}$$

where we again have terms that are outer products of the gradient of the density at $\boldsymbol{r}$.

The Reader can now appreciate the choice of using the local potentials V_{ρ}^{XC} and V_{τ}^{XC}, whose derivatives have already been derived above, making the current expression slightly simpler. The above expression is by choice as general as possible hence leading to a disproportionate number of terms. In most cases, the majority of these terms can be neglected as perturbations cause no changes to the volume and the gradient operators, however as shall be seen, for strain derivatives, the unholy mess above is required. I can only apologise to the Reader.

3.5 Application to this work

In this chapter, we discuss the common response functions of material systems that we shall consider in the rest of this thesis, the phonon modes and elastic properties. A description of how the response functions are related to the derivatives of the total energy of the system was given. We then discussed perturbation theory as it is applied to the DFT formalism resulting in Density Functional Perturbation Theory formalism, which enables us to compute response properties directly by calculating the derivative of the total energy. General expressions have been given for the second-order derivatives of the total energy, and the additional terms that must be considered when using a meta-generalised-gradient approximation have been derived (and I apologise for inflicting them on you, Reader). The expressions derived for these additional terms are key results for this thesis and will be used in the subsequent chapters to calculate material response functions using the meta-GGA functionals.

Chapter 4

Calculating Dynamical Matrices using meta-GGAs

This chapter covers the implementation of the necessary additional terms to calculate the Dynamical matrix from DFPT using a meta-GGA functional. The Dynamical matrix is the response function of a system that is required to calculate the phonon modes in the Harmonic approximation and was defined in Section 3.2.1 of the previous chapter. First, we cover the derivation of the additional terms required for a meta-GGA functional, then the implementation is verified by performing a comparison between dynamical matrices and phonon-mode energies calculated from DFPT, and those computed from the finite displacement method. It is found that the well-known grid sensitivity of meta-GGA functionals causes severe issues when calculating the dynamical matrix in both methods, leading to major disagreement. The two approaches can only be reconciled by turning off some of the symmetry-preserving features or by using very dense grids for the density representation calculation. A more intelligent approach to the grid sensitivity issue is discussed in the following chapter.

4.1 Introduction

The accuracy of the SCAN family of meta-GGA functionals has been widely studied, showing a significant improvement in the calculation of material and molecular properties over the commonly used LDA and GGA functionals. The accuracy of the SCAN family is often found to be comparable to methods beyond semi-local DFT methods, such as hybrid functionals. In particular, the accuracy of SCAN and r2SCAN for structural properties such as; lattice parameters, interlayer separation, and phonon spectra has been across a wide range of materials and molecules [28, 29, 36, 38, 41, 42, 44, 45, 99]. A key finding in

many of these studies was that the SCAN functional, and sometimes r2SCAN, is particularly sensitive to the real-space grid sampling used, which causes significant systematic errors when calculating relaxed structures, often leading to the phonon modes calculated having imaginary frequencies, suggesting spurious instability in the relaxed ground-state structure.

Those studies looking at the accuracy of phonon modes when using meta-GGAs make use of the finite-displacement method to calculate the dynamical matrices for materials. The finite displacement method; a) suffers particularly from the grid sensitivity since it requires moving atoms and the use of supercells which can significantly alter the grid sampling, and b) is an expensive method of calculating the phonon modes since the use of supercells necessitates including more electrons in the calculations. However, a density functional perturbation theory method would avoid the change in grid sampling and the use of supercells, which would eliminate any changes to the real-space sampling and keep the computational cost to a minimum. The work in this chapter is devoted to the novel derivation of the necessary additional terms to be computed in the meta-GGA formalism. The verification of the derivation of the additional meta-GGA terms and their implementation in CASTEP is confirmed by careful comparison with finite displacement calculations for a test system. This work has yet to be published.

4.2 Calculating the Dynamical Matrix

The phonon modes of a material can be computed as the eigenvectors of the dynamical matrix. The dynamical matrix is related to the derivative of the total energy with respect to periodic atomic perturbations, as previously discussed (§3.2.1). Equation 3.5 defines the relation between the dynamical matrix and the total energy derivative,

$$D^{\alpha\beta}_{\boldsymbol{q},IJ} = \frac{1}{\sqrt{M_I M_J}} \frac{\partial^2 E}{\partial \left(\mu^{\boldsymbol{q}}_{I,\alpha}\right)^* \partial \mu^{\boldsymbol{q}}_{J,\beta}}, \tag{4.1}$$

where $D^{\alpha\beta}_{\boldsymbol{q},IJ}$ is an element of the dynamical matrix, M_I is the mass of atom labelled I in the primitive cell and $\mu^{\boldsymbol{q}}_{I,\alpha}$ is the periodic displacement of atom labelled I along Cartesian direction α which has wave-vector of $\boldsymbol{q}$. To determine the phonon modes of a material for any $\boldsymbol{q}$, we therefore require the set of mixed second energy derivatives with respect to an incommensurate perturbation of all pairs of atoms in the unit cell.

As a reminder, the second derivative of the energy with respect to a pair of incommensurate perturbations $\lambda^{1,\boldsymbol{q}}$ and $\lambda^{2,\boldsymbol{q}}$ can be computed using the expression

given in equation 3.60, which is repeated here,

$$\frac{\mathrm{d}^2 E^{\mathrm{tot}}}{\mathrm{d}\left(\lambda^{1,\boldsymbol{q}}\right)^* \mathrm{d}\lambda^{2,\boldsymbol{q}}} = \int_{\mathrm{BZ}} \left[\sum_b^{\mathrm{occ}} \left\langle \psi^{(\lambda^1)}_{b,\boldsymbol{k},\boldsymbol{q}} \middle| \frac{\partial \hat{H}_{\boldsymbol{k},\boldsymbol{q}}}{\partial \lambda^{2,\boldsymbol{q}}} \middle| \psi^{(0)}_{b,\boldsymbol{k}} \right\rangle + \sum_b^{\mathrm{occ}} \left\langle \psi^{(0)}_{b,\boldsymbol{k}} \middle| \frac{\partial \hat{H}_{\boldsymbol{k},\boldsymbol{q}}}{\partial \lambda^{2,\boldsymbol{q}}} \middle| \psi^{(\lambda^1)}_{b,\boldsymbol{k},\boldsymbol{q}} \right\rangle + \right.$$
$$\left. + \sum_b^{\mathrm{occ}} \left\langle \psi^{(0)}_{b,\boldsymbol{k}} \middle| \frac{\partial^2}{\partial \left(\lambda^{1,\boldsymbol{q}}\right)^* \partial \lambda^{2,\boldsymbol{q}}} \left(\hat{T} + \hat{V}^{\mathrm{ext}} \right) \middle| \psi^{(0)}_{b,\boldsymbol{k}} \right\rangle \right] \mathrm{d}^3\boldsymbol{k}$$
$$+ \frac{\partial^2 E^{\mathrm{H}}}{\partial \left(\lambda^{1,\boldsymbol{q}}\right)^* \partial \lambda^{2,\boldsymbol{q}}} \bigg|_{n^{(0)}} + \frac{\partial^2 E^{\mathrm{XC}}}{\partial \left(\lambda^{1,\boldsymbol{q}}\right)^* \partial \lambda^{2,\boldsymbol{q}}} \bigg|_{n^{(0)},\tau^{(0)}} + \frac{\partial^2 E^{\text{Ion-Ion}}}{\partial \left(\lambda^{1,\boldsymbol{q}}\right)^* \partial \lambda^{2,\boldsymbol{q}}}. \tag{4.2}$$

Each element of the dynamical matrix for a particular $\boldsymbol{q}$ can be computed using this expression by setting $\lambda^{1,\boldsymbol{q}}$ and $\lambda^{2,\boldsymbol{q}}$ equal to $\mu^{\boldsymbol{q}}_{I,\alpha}$ and $\mu^{\boldsymbol{q}}_{J,\beta}$. In order to be able to compute these elements when using mGGA functionals, we will therefore need to derive:

- The change in the Hamiltonian under the other perturbation, $\frac{\partial \hat{H}_{\boldsymbol{k}}}{\partial \lambda_{\boldsymbol{q}}}$.
- The first order wavefunction with respect to one incommensurate perturbations, $\left| \psi^{(\lambda_1)}_{b,\boldsymbol{k},\boldsymbol{q}} \right\rangle$. This can be obtained by solving the Sternheimer equation (equation 3.56) or varying the first-order wavefunction to minimise the expression given in equation 3.59. Both methods requires the initial change to the Hamiltonian, $\frac{\partial \hat{H}_{\boldsymbol{k}}}{\partial \mu^{\boldsymbol{q}}}$.
- The mixed second derivative of the differential part of the external potential under both perturbations $\frac{\partial^2 E^{\mathrm{ext}}_{\tau}}{\partial \lambda^* \partial \mu}$.
- The mixed second derivative of the XC energy under both perturbations $\frac{\partial^2 E^{\mathrm{XC}}}{\partial \lambda^* \partial \mu}$.

4.2.1 Change in Hamiltonian under atomic perturbation

As a reminder the Hamiltonian of the unperturbed system is,

$$\hat{H} = \hat{T} + \hat{V}^{\mathrm{H}} + \hat{V}^{\mathrm{ext}}_{\mathrm{loc}} + \hat{V}^{\mathrm{ext}}_{\mathrm{nl}} + \hat{V}^{\mathrm{ext}}_{\tau} + \hat{V}^{\mathrm{XC}}. \tag{4.3}$$

The terms that are different for the mGGA functional from the GGA functional are the additional term in the external potential $\hat{V}^{\mathrm{ext}}_{\tau}$ and the XC potential $\hat{V}^{\mathrm{XC}}$. Expressions for the derivatives of these terms under generic perturbations are derived in the previous chapter; here we shall use these generic expressions to generate specific expressions for atomic perturbation $\mu^{\boldsymbol{q}}_{I,\alpha}$.

4.2.1.1 External potential

The expression for the derivative of $\hat{V}_\tau^{\text{ext}}$ under a generic perturbation λ is repeated below,

$$\frac{\mathrm{d}\hat{V}_\tau^{\text{ext}}(\boldsymbol{r})}{\mathrm{d}\lambda} = -\frac{1}{2}\left(\frac{\mathrm{d}\nabla}{\mathrm{d}\lambda}\cdot\left(V_\tau^{\text{local}}(\boldsymbol{r})\,\nabla\right) + \nabla\cdot\left(\frac{\mathrm{d}V_\tau^{\text{local}}(\boldsymbol{r})}{\mathrm{d}\lambda}\nabla\right) + \nabla\cdot\left(V_\tau^{\text{local}}(\boldsymbol{r})\,\frac{\mathrm{d}\nabla}{\mathrm{d}\lambda}\right)\right). \tag{4.4}$$

Immediately, we can simplify this expression by recognising that the perturbation $\mu_{I,\alpha}^{\boldsymbol{q}}$ does not change the gradient operator. The change in the operator therefore only depends on the change in the local potential part of this operator,

$$\frac{\mathrm{d}\hat{V}_\tau^{\text{ext}}(\boldsymbol{r})}{\mathrm{d}\mu_{I,\alpha}^{\boldsymbol{q}}} = -\frac{1}{2}\nabla\cdot\left(\frac{\mathrm{d}V_\tau^{\text{local}}(\boldsymbol{r})}{\mathrm{d}\mu_{I,\alpha}^{\boldsymbol{q}}}\nabla\right). \tag{4.5}$$

The expression for $V_\tau^{local}(\boldsymbol{r})$ is given in equation 2.61, repeated below,

$$V_\tau^{\text{loc}}(\boldsymbol{r}) = \Omega^{-1}\sum_J V_J^\tau(\boldsymbol{r}) = \Omega^{-1}\sum_J\sum_{\boldsymbol{G}} v_J^\tau(|\boldsymbol{G}|)\,e^{-i\boldsymbol{G}\cdot\boldsymbol{R_J}}e^{i\boldsymbol{G}\cdot\boldsymbol{r}}, \tag{4.6}$$

The perturbation is incommensurate with the unit cell, therefore we Bloch factorise the potential into a cell-periodic function and wave-like part,

$$\frac{\mathrm{d}V_\tau^{\text{local}}(\boldsymbol{r})}{\mathrm{d}\mu_{I,\alpha}^{\boldsymbol{q}}} = V_{\tau,I,\alpha,\boldsymbol{q}}^{\text{loc}^{(1)}}(\boldsymbol{r}) = \bar{V}_{\tau,I,\alpha,\boldsymbol{q}}^{\text{loc}^{(1)}}(\boldsymbol{r})\,e^{i\boldsymbol{q}\cdot\boldsymbol{r}} \tag{4.7}$$

where $\bar{V}_{\tau,I,\alpha,\boldsymbol{q}}^{\text{loc}^{(1)}}(\boldsymbol{r})$ is the cell-periodic part of the function which can then be calculated on the FFT grid of the unit cell. As was done in the previous chapter, the overbar denotes that this is the cell-periodic part of the function. A similar procedure is used to calculate the local part of the external potential operator, $\hat{V}_{\text{loc}}^{\text{ext}}$, as expressed by Gonze in equation 50 of Ref [95]. The expression for the cell-periodic part of the derivative of V_τ^{local} is analogous to the expression derived by Gonze, which is given as the derivative of each $G-$vector component of the potential,

$$\begin{aligned}\bar{V}_{\tau,I,\alpha,\boldsymbol{q}}^{\text{loc}^{(1)}}(\boldsymbol{G}) =& \Omega^{-1} v_I^\tau(|\boldsymbol{G}+\boldsymbol{q}|)\,\frac{\mathrm{d}}{\mathrm{d}R_I^\alpha}e^{i(\boldsymbol{G}+\boldsymbol{q})\cdot(\boldsymbol{r}-\boldsymbol{R}_I)} \\ =& -i\,(G_\alpha+q_\alpha)\,\Omega^{-1}v_I^\tau(|\boldsymbol{G}+\boldsymbol{q}|)\,e^{i(\boldsymbol{G}+\boldsymbol{q})\cdot(\boldsymbol{r}-\boldsymbol{R}_I)}.\end{aligned} \tag{4.8}$$

From this expression of the derivative for each $G-$vector component, we can

construct the total cell-periodic part of the potential,

$$\bar{V}^{\mathrm{loc}(1)}_{\tau,I,\alpha,\boldsymbol{q}}(\boldsymbol{r}) = \Omega^{-1}\sum_{\boldsymbol{G}} -i\left(G_\alpha + q_\alpha\right) v^\tau_I\left(|\boldsymbol{G}+\boldsymbol{q}|\right) e^{i(\boldsymbol{G}+\boldsymbol{q})\cdot(\boldsymbol{r}-\boldsymbol{R}_I)}. \tag{4.9}$$

In the case when $\boldsymbol{q} = 0$ and the perturbation is commensurate, the expression becomes,

$$V^{\mathrm{loc}(1)}_{\tau,I,\alpha}(\boldsymbol{r}) = \Omega^{-1}\sum_{\boldsymbol{G}} -i\left(G_\alpha\right) v^\tau_I\left(|\boldsymbol{G}|\right) e^{i(\boldsymbol{G})\cdot(\boldsymbol{r}-\boldsymbol{R}_I)}. \tag{4.10}$$

4.2.1.2 XC potential

Here we consider the derivative of the XC potential under the perturbation of $\mu^{\boldsymbol{q}}_{I,\alpha}$. Taking the expression for the derivative of the operator under a generic perturbation from the previous chapter (equation 3.64), we can immediately simplify the expression by again recognising that the perturbation does not change the gradient operator leading to,

$$\begin{aligned}\frac{\mathrm{d}\hat{V}^{\mathrm{XC}}(\boldsymbol{r})}{\mathrm{d}\mu^{\boldsymbol{q}}_{I,\alpha}} =& \frac{\mathrm{d}}{\mathrm{d}\mu^{\boldsymbol{q}}_{I,\alpha}}\left(V^{\mathrm{XC}}_\rho(\boldsymbol{r}) - \frac{1}{2}\nabla\cdot\left(V^{\mathrm{XC}}_\tau(\boldsymbol{r})\nabla\right)\right)\\ =& \frac{\mathrm{d}V^{\mathrm{XC}}_\rho(\boldsymbol{r})}{\mathrm{d}\mu^{\boldsymbol{q}}_{I,\alpha}} - \frac{1}{2}\nabla\cdot\left(\frac{\mathrm{d}V^{\mathrm{XC}}_\tau(\boldsymbol{r})}{\mathrm{d}\mu^{\boldsymbol{q}}_{I,\alpha}}\nabla\right).\end{aligned} \tag{4.11}$$

Now we must consider how each of the local potentials, $V^{\mathrm{XC}}_\rho(\boldsymbol{r})$ and $V^{\mathrm{XC}}_\tau(\boldsymbol{r})$, change under the perturbation. Equations 3.67 and 3.68 give the expression for a generic perturbation, each depending on changes in the density, the gradient of the density, and the KED. In this case we are also considering the *total* density and KED, i.e. with non-linear core corrections, not just the density and KED due to the valence electrons,

$$\rho_{\mathrm{t}}(\boldsymbol{r}) = \rho(\boldsymbol{r}) + \rho_{\mathrm{c}}(\boldsymbol{r}), \tag{4.12}$$

$$\tau_{\mathrm{t}}(\boldsymbol{r}) = \tau(\boldsymbol{r}) + \tau_{\mathrm{c}}(\boldsymbol{r}). \tag{4.13}$$

Under the perturbation $\mu^{\boldsymbol{q}}_{I,\alpha}$ the total density and KED change as

$$\frac{\mathrm{d}\rho_{\mathrm{t}}(\boldsymbol{r})}{\mathrm{d}\mu^{\boldsymbol{q}}_{I,\alpha}} = \rho^{(1)}_{\boldsymbol{q}}(\boldsymbol{r}) + \frac{\partial\rho_{\mathrm{c}}(\boldsymbol{r})}{\partial\mu^{\boldsymbol{q}}_{I,\alpha}}, \tag{4.14}$$

$$\frac{\mathrm{d}\tau_{\mathrm{t}}(\boldsymbol{r})}{\mathrm{d}\mu^{\boldsymbol{q}}_{I,\alpha}} = \tau^{(1)}_{\boldsymbol{q}}(\boldsymbol{r}) + \frac{\partial\tau_{\mathrm{c}}(\boldsymbol{r})}{\partial\mu^{\boldsymbol{q}}_{I,\alpha}}, \tag{4.15}$$

where the first term in both equations $\rho^{(1)}_{\boldsymbol{q}}(\boldsymbol{r})$ and $\tau^{(1)}_{\boldsymbol{q}}(\boldsymbol{r})$ are the first order response density and KED that results from the response of the wavefunction.

These are calculated according to equations 3.27 and 3.28 in the case of commensurate perturbations, and equations 3.54 and 3.55 in the case of incommensurate perturbations.

The expressions for the derivatives of the core charge and KED derivatives are very similar to each other and to the derivative of the local part of the external potential. Again, we shall follow the example of Gonze, who gives an expression for the derivative of the core charge density in equation 56 of Ref [95]. The derivatives of the core charge density for the case of a commensurate and incommensurate atomic perturbation are given by,

$$\frac{\partial \rho_{\mathrm{c}}(\boldsymbol{r})}{\partial \mu_{I,\alpha}} = \rho^{(1)}_{\mathrm{c},I,\alpha}(\boldsymbol{r}) = \Omega^{-1} \sum_{\boldsymbol{G}} -iG_\alpha \rho^{\mathrm{c}}_I(|\boldsymbol{G}|)\, e^{i\boldsymbol{G}\cdot(\boldsymbol{r}-\boldsymbol{R}_I)}, \tag{4.16}$$

$$e^{-i\boldsymbol{q}\cdot\boldsymbol{r}} \frac{\partial \rho_{\mathrm{c}}(\boldsymbol{r})}{\partial \mu^{\boldsymbol{q}}_{I,\alpha}} = \bar{\rho}^{(1)}_{\mathrm{c},I,\alpha,\boldsymbol{q}}(\boldsymbol{r}) = \Omega^{-1} \sum_{\boldsymbol{G}} -i(G_\alpha + q_\alpha) \rho^{\mathrm{c}}_I(|\boldsymbol{G}+\boldsymbol{q}|)\, e^{i(\boldsymbol{G}+\boldsymbol{q})\cdot(\boldsymbol{r}-\boldsymbol{R}_I)}, \tag{4.17}$$

In the case of incommensurate perturbations we again calculate the cell-periodic part of a Bloch factorised function, where the cell-periodic function is denoted by over-bar. The derivatives of the core KED are given by,

$$\frac{\partial \tau_{\mathrm{c}}(\boldsymbol{r})}{\partial \mu_{I,\alpha}} = \tau^{(1)}_{\mathrm{c},I,\alpha}(\boldsymbol{r}) = \Omega^{-1} \sum_{\boldsymbol{G}} -iG_\alpha \tau^{\mathrm{c}}_I(|\boldsymbol{G}|)\, e^{i\boldsymbol{G}\cdot(\boldsymbol{r}-\boldsymbol{R}_I)}, \tag{4.18}$$

$$e^{-i\boldsymbol{q}\cdot\boldsymbol{r}} \frac{\partial \tau_{\mathrm{c}}(\boldsymbol{r})}{\partial \mu^{\boldsymbol{q}}_{I,\alpha}} = \bar{\tau}^{(1)}_{\mathrm{c},I,\alpha,\boldsymbol{q}}(\boldsymbol{r}) = \Omega^{-1} \sum_{\boldsymbol{G}} -i(G_\alpha + q_\alpha) \tau^{\mathrm{c}}_I(|\boldsymbol{G}+\boldsymbol{q}|)\, e^{i(\boldsymbol{G}+\boldsymbol{q})\cdot(\boldsymbol{r}-\boldsymbol{R}_I)}. \tag{4.19}$$

Now that we have defined how the total charge density and KED change under atomic perturbation, we can now write how the potentials $V^{\mathrm{XC}}_\rho(\boldsymbol{r})$ and $V^{\mathrm{XC}}_\tau(\boldsymbol{r})$ change. First, we shall address the commensurate case, where the derivatives of the potentials are expressed as

$$\begin{aligned}
\frac{\mathrm{d}V^{\mathrm{XC}}_\rho(\boldsymbol{r})}{\mathrm{d}\mu_{I,\alpha}} =& \frac{\partial^2 f^{\mathrm{XC}}}{\partial \rho^2}\frac{\mathrm{d}\rho_{\mathrm{t}}}{\mathrm{d}\mu_{I,\alpha}} + \frac{\partial^2 f^{\mathrm{XC}}}{\partial \rho \partial |\nabla\rho|}\frac{\nabla^\nu \rho_{\mathrm{t}}}{|\nabla\rho_{\mathrm{t}}|}\frac{\mathrm{d}(\nabla^\nu\rho_{\mathrm{t}})}{\mathrm{d}\mu_{I,\alpha}} + \frac{\partial^2 f^{\mathrm{XC}}}{\partial \rho \partial \tau}\frac{\mathrm{d}\tau_{\mathrm{t}}}{\mathrm{d}\mu_{I,\alpha}} \\
&- \nabla^\nu \Bigg[\left(\frac{\partial^2 f^{\mathrm{XC}}}{\partial |\nabla\rho| \partial \rho}\frac{\mathrm{d}\rho_{\mathrm{t}}}{\mathrm{d}\mu_{I,\alpha}} + \frac{\partial^2 f^{\mathrm{XC}}}{\partial |\nabla\rho| \partial \tau}\frac{\mathrm{d}\tau_{\mathrm{t}}}{\mathrm{d}\mu_{I,\alpha}} \right) \frac{\nabla^\nu \rho_{\mathrm{t}}}{|\nabla\rho_{\mathrm{t}}|} \\
&+ \frac{\partial f^{\mathrm{XC}}}{\partial |\nabla\rho|}\frac{1}{|\nabla\rho_{\mathrm{t}}|}\frac{\mathrm{d}(\nabla^\nu\rho_{\mathrm{t}})}{\mathrm{d}\mu_{I,\alpha}} \\
&+ \left(\frac{\partial^2 f^{\mathrm{XC}}}{\partial |\nabla\rho|^2}\frac{\nabla^\zeta \rho_{\mathrm{t}} \nabla^\nu \rho_{\mathrm{t}}}{|\nabla\rho_{\mathrm{t}}|^2} - \frac{\partial f^{\mathrm{XC}}}{\partial |\nabla\rho|}\frac{\nabla^\zeta \rho_{\mathrm{t}} \nabla^\nu \rho_{\mathrm{t}}}{|\nabla\rho_{\mathrm{t}}|^3} \right) \frac{\mathrm{d}\left(\nabla^\zeta \rho_{\mathrm{t}}\right)}{\mathrm{d}\mu_{I,\alpha}} \Bigg],
\end{aligned} \tag{4.20}$$

and

$$\frac{\mathrm{d}V_{\tau}^{\mathrm{XC}}(\boldsymbol{r})}{\mathrm{d}\mu_{I,\alpha}} = \frac{\partial^2 f^{\mathrm{XC}}}{\partial\tau\partial\rho}\frac{\mathrm{d}\rho_{\mathrm{t}}}{\mathrm{d}\mu_{I,\alpha}} + \frac{\partial^2 f^{\mathrm{XC}}}{\partial\tau\partial|\nabla\rho|}\frac{\nabla^{\nu}\rho_{\mathrm{t}}}{|\nabla\rho_{\mathrm{t}}|}\frac{\mathrm{d}\left(\nabla^{\nu}\rho_{\mathrm{t}}\right)}{\mathrm{d}\mu_{I,\alpha}} + \frac{\partial^2 f^{\mathrm{XC}}}{\partial\tau^2}\frac{\mathrm{d}\tau_{\mathrm{t}}}{\mathrm{d}\mu_{I,\alpha}}. \tag{4.21}$$

Since the gradient operator is unchanged by the perturbation, $\frac{\mathrm{d}(\nabla^{\nu}\rho_{\mathrm{t}})}{\mathrm{d}\mu_{I,\alpha}}$ can be found by the applying the gradient operator to the terms in equation 4.14,

$$\frac{\mathrm{d}\left(\nabla^{\nu}\rho_{\mathrm{t}}\right)}{\mathrm{d}\mu_{I,\alpha}} = \nabla^{\nu}\left(\frac{\mathrm{d}\rho_{\mathrm{t}}}{\mathrm{d}\mu_{I,\alpha}}\right). \tag{4.22}$$

Now for the incommensurate case. The first-order XC potential can be calculated using the same expression as the commensurate, only now the change in density and KED and the resultant first-order potential are all incommensurate quantities,

$$\begin{aligned}\frac{\mathrm{d}V_{\rho}^{\mathrm{XC}}(\boldsymbol{r})}{\mathrm{d}\mu_{I,\alpha}^{\boldsymbol{q}}} =& \frac{\partial^2 f^{\mathrm{XC}}}{\partial\rho^2}\frac{\mathrm{d}\rho_{\mathrm{t}}}{\mathrm{d}\mu_{I,\alpha}^{\boldsymbol{q}}} + \frac{\partial^2 f^{\mathrm{XC}}}{\partial\rho\partial|\nabla\rho|}\frac{\nabla^{\nu}\rho_{\mathrm{t}}}{|\nabla\rho_{\mathrm{t}}|}\nabla^{\nu}\left(\frac{\mathrm{d}\rho_{\mathrm{t}}}{\mathrm{d}\mu_{I,\alpha}^{\boldsymbol{q}}}\right) + \frac{\partial^2 f^{\mathrm{XC}}}{\partial\rho\partial\tau}\frac{\mathrm{d}\tau_{\mathrm{t}}}{\mathrm{d}\mu_{I,\alpha}^{\boldsymbol{q}}} \\ &- \nabla^{\nu}\Bigg[\left(\frac{\partial^2 f^{\mathrm{XC}}}{\partial|\nabla\rho|\,\partial\rho}\frac{\mathrm{d}\rho_{\mathrm{t}}}{\mathrm{d}\mu_{I,\alpha}^{\boldsymbol{q}}} + \frac{\partial^2 f^{\mathrm{XC}}}{\partial|\nabla\rho|\,\partial\tau}\frac{\mathrm{d}\tau_{\mathrm{t}}}{\mathrm{d}\mu_{I,\alpha}^{\boldsymbol{q}}}\right)\frac{\nabla^{\nu}\rho_{\mathrm{t}}}{|\nabla\rho_{\mathrm{t}}|} \\ &+ \frac{\partial f^{\mathrm{XC}}}{\partial|\nabla\rho|}\frac{1}{|\nabla\rho_{\mathrm{t}}|}\nabla^{\nu}\left(\frac{\mathrm{d}\rho_{\mathrm{t}}}{\mathrm{d}\mu_{I,\alpha}^{\boldsymbol{q}}}\right) \\ &+ \left(\frac{\partial^2 f^{\mathrm{XC}}}{\partial|\nabla\rho|^2}\frac{\nabla^{\zeta}\rho_{\mathrm{t}}\nabla^{\nu}\rho_{\mathrm{t}}}{|\nabla\rho_{\mathrm{t}}|^2} - \frac{\partial f^{\mathrm{XC}}}{\partial|\nabla\rho|}\frac{\nabla^{\zeta}\rho_{\mathrm{t}}\nabla^{\nu}\rho_{\mathrm{t}}}{|\nabla\rho_{\mathrm{t}}|^3}\right)\nabla^{\zeta}\left(\frac{\mathrm{d}\rho_{\mathrm{t}}}{\mathrm{d}\mu_{I,\alpha}^{\boldsymbol{q}}}\right)\Bigg],\end{aligned} \tag{4.23}$$

and

$$\frac{\mathrm{d}V_{\tau}^{\mathrm{XC}}(\boldsymbol{r})}{\mathrm{d}\mu_{I,\alpha}^{\boldsymbol{q}}} = \frac{\partial^2 f^{\mathrm{XC}}}{\partial\tau\partial\rho}\frac{\mathrm{d}\rho_{\mathrm{t}}}{\mathrm{d}\mu_{I,\alpha}} + \frac{\partial^2 f^{\mathrm{XC}}}{\partial\tau\partial|\nabla\rho|}\frac{\nabla^{\nu}\rho_{\mathrm{t}}}{|\nabla\rho_{\mathrm{t}}|}\nabla^{\nu}\left(\frac{\mathrm{d}\rho_{\mathrm{t}}}{\mathrm{d}\mu_{I,\alpha}^{\boldsymbol{q}}}\right) + \frac{\partial^2 f^{\mathrm{XC}}}{\partial\tau^2}\frac{\mathrm{d}\tau_{t}}{\mathrm{d}\mu_{I,\alpha}}. \tag{4.24}$$

We again Bloch-factorise the incommensurate properties into a wave-like part and cell-periodic functions, where

$$\frac{\mathrm{d}\rho_{t}(\boldsymbol{r})}{\mathrm{d}\mu^{\boldsymbol{q}}} = \rho_{t,\boldsymbol{q}}^{(1)}(\boldsymbol{r}) = e^{i\boldsymbol{q}\cdot\boldsymbol{r}}\bar{\rho}_{t,\boldsymbol{q}}^{(1)}(\boldsymbol{r}) \tag{4.25}$$

$$\frac{\mathrm{d}\tau_{t}(\boldsymbol{r})}{\mathrm{d}\mu^{\boldsymbol{q}}} = \tau_{t,\boldsymbol{q}}^{(1)}(\boldsymbol{r}) = e^{i\boldsymbol{q}\cdot\boldsymbol{r}}\bar{\tau}_{t,\boldsymbol{q}}^{(1)}(\boldsymbol{r}) \tag{4.26}$$

$$\frac{\mathrm{d}V_{\rho}^{\mathrm{XC}}(\boldsymbol{r})}{\mathrm{d}\mu^{\boldsymbol{q}}} = V_{\rho,\boldsymbol{q}}^{\mathrm{XC}^{(1)}}(\boldsymbol{r}) = e^{i\boldsymbol{q}\cdot\boldsymbol{r}}\bar{V}_{\rho,\boldsymbol{q}}^{\mathrm{XC}^{(1)}}(\boldsymbol{r}) \tag{4.27}$$

$$\frac{\mathrm{d}V_{\tau}^{\mathrm{XC}}(\boldsymbol{r})}{\mathrm{d}\mu^{\boldsymbol{q}}} = V_{\tau,\boldsymbol{q}}^{\mathrm{XC}^{(1)}}(\boldsymbol{r}) = e^{i\boldsymbol{q}\cdot\boldsymbol{r}}\bar{V}_{\tau,\boldsymbol{q}}^{\mathrm{XC}^{(1)}}(\boldsymbol{r}) \tag{4.28}$$

where we have dropped the I and α subscripts for brevity. The gradient of the

change in the density can be written in terms of the Bloch factorised function,

$$\nabla^\nu \rho^{(1)}_{t,\boldsymbol{q}}(\boldsymbol{r}) = \nabla^\nu \left(e^{i\boldsymbol{q}\cdot\boldsymbol{r}} \bar{\rho}^{(1)}_{t,\boldsymbol{q}}(\boldsymbol{r}) \right) = e^{i\boldsymbol{q}\cdot\boldsymbol{r}} \left(iq^\nu \bar{\rho}^{(1)}_{t,\boldsymbol{q}}(\boldsymbol{r}) + \nabla^\nu \bar{\rho}^{(1)}_{t,\boldsymbol{q}}(\boldsymbol{r}) \right) \tag{4.29}$$

The cell periodic functions of the change in density and KED can then be used to calculate the first-order changes in the XC potentials,

$$\begin{aligned} e^{i\boldsymbol{q}\cdot\boldsymbol{r}} \bar{V}^{\mathrm{XC}(1)}_{\rho,\boldsymbol{q}}(\boldsymbol{r}) = & e^{i\boldsymbol{q}\cdot\boldsymbol{r}} \Bigg\{ \frac{\partial^2 f^{\mathrm{XC}}}{\partial\rho^2} \bar{\rho}^{(1)}_{\mathrm{t},\boldsymbol{q}} + \frac{\partial^2 f^{\mathrm{XC}}}{\partial\rho\partial|\nabla\rho|} \frac{\nabla^\nu \rho_\mathrm{t}}{|\nabla\rho_\mathrm{t}|} \left(iq^\nu \bar{\rho}^{(1)}_{\mathrm{t},\boldsymbol{q}} + \nabla^\nu \bar{\rho}^{(1)}_{\mathrm{t},\boldsymbol{q}} \right) + \frac{\partial^2 f^{\mathrm{XC}}}{\partial\rho\partial\tau} \bar{\tau}^{(1)}_{\mathrm{t},\boldsymbol{q}} \\ & - (iq^\nu + \nabla^\nu) \Bigg[\left(\frac{\partial^2 f^{\mathrm{XC}}}{\partial|\nabla\rho|\partial\rho} \bar{\rho}^{(1)}_{\mathrm{t},\boldsymbol{q}} + \frac{\partial^2 f^{\mathrm{XC}}}{\partial|\nabla\rho|\partial\tau} \bar{\tau}^{(1)}_{\mathrm{t},\boldsymbol{q}} \right) \frac{\nabla^\nu \rho_\mathrm{t}}{|\nabla\rho_\mathrm{t}|} \\ & + \left(\frac{\partial^2 f^{\mathrm{XC}}}{\partial|\nabla\rho|^2} \frac{\nabla^\zeta \rho_\mathrm{t} \nabla^\nu \rho_\mathrm{t}}{|\nabla\rho_\mathrm{t}|^2} - \frac{\partial f^{\mathrm{XC}}}{\partial|\nabla\rho|} \frac{\nabla^\zeta \rho_\mathrm{t} \nabla^\nu \rho_\mathrm{t}}{|\nabla\rho_\mathrm{t}|^3} \right) \left(iq^\zeta \bar{\rho}^{(1)}_{\mathrm{t},\boldsymbol{q}} + \nabla^\zeta \bar{\rho}^{(1)}_{\mathrm{t},\boldsymbol{q}} \right) \\ & + \frac{\partial f^{\mathrm{XC}}}{\partial|\nabla\rho|} \frac{1}{|\nabla\rho_\mathrm{t}|} \left(iq_\gamma \bar{\rho}^{(1)}_{\mathrm{t},\boldsymbol{q}} + \nabla^\nu \bar{\rho}^{(1)}_{\mathrm{t},\boldsymbol{q}} \right) \Bigg] \Bigg\}, \end{aligned} \tag{4.30}$$

where $e^{i\boldsymbol{q}\cdot\boldsymbol{r}}$ has been factorised out of every term on the right hand side of the equation. When factorising $e^{i\boldsymbol{q}\cdot\boldsymbol{r}}$ out of the gradient term applied to the square brackets, the gradient operator then gains a $+iq^\nu$ term. The other part of the first-order XC potential, $V^{\mathrm{XC}(1)}_{\tau,\boldsymbol{q}}$, is computed as

$$\begin{aligned} e^{i\boldsymbol{q}\cdot\boldsymbol{r}} \bar{V}^{\mathrm{XC}(1)}_{\tau,\boldsymbol{q}} = & e^{i\boldsymbol{q}\cdot\boldsymbol{r}} \Bigg[\frac{\partial^2 f^{\mathrm{XC}}}{\partial\tau\partial\rho} \bar{\rho}^{(1)}_{\mathrm{t},\boldsymbol{q}} + \frac{\partial^2 f^{\mathrm{XC}}}{\partial\tau\partial|\nabla\rho|} \frac{\nabla^\nu \rho_\mathrm{t}}{|\nabla\rho_\mathrm{t}|} \left(iq^\nu \bar{\rho}^{(1)}_{\mathrm{t},\boldsymbol{q}} + \nabla^\nu \bar{\rho}^{(1)}_{\mathrm{t},\boldsymbol{q}} \right) \\ & + \frac{\partial^2 f^{\mathrm{XC}}}{\partial\tau^2} \bar{\tau}^{(1)}_{\mathrm{t},\boldsymbol{q}} \Bigg]. \end{aligned} \tag{4.31}$$

In the expressions for both parts of the first-order XC potential, the factors of $e^{i\boldsymbol{q}\cdot\boldsymbol{r}}$ on either side of the equations can be cancelled and we are left with expressions that are only comprised of cell-periodic functions, meaning they can be computed and stored on regular FFT grids. We have followed the same procedure applied to GGA potentials as presented in Ref [96].

Now we must draw a distinction between two different quantities that must be computed. The correct first-order wavefunctions can be obtained by solving the Sternheimer equation (equations 3.41 and 3.56), which includes the total derivative of the Hamiltonian,

$$\hat{H}^{(1)}_{\boldsymbol{k}} = \frac{\mathrm{d}\hat{H}^{(0)}_{\boldsymbol{k}}}{\mathrm{d}\lambda}, \tag{4.32}$$

whereas, the expressions for the second derivatives of the total energy (equations 3.39, 3.60, 3.47 and 3.69) include the partial derivative of the Hamiltonian $\frac{\partial\hat{H}^{(0)}_{\boldsymbol{k}}}{\partial\lambda}$. The difference between the total derivative and the partial derivative is the in-

clusion of the first-order response of the wavefunctions in the Hartree and XC terms through the change in density and KED. In the case of atomic perturbations, the partial derivative of the XC potential, $\frac{\partial \hat{V}^{\mathrm{XC}}}{\partial \mu^{\boldsymbol{q}}_{I,\alpha}}$ only includes the changes from the non-linear core corrections and does not include contributions from the first-order response of the density and KED. However, the total derivative of the XC potential, $\frac{\mathrm{d}\hat{V}^{\mathrm{XC}}}{\mathrm{d}\mu^{\boldsymbol{q}}_{I,\alpha}}$, does include the contribution from the first-order response of the density and the KED.

4.2.2 Second derivative of External Potential

The energy contribution due to the differential part of the external potential can be computed according to equation 2.63,

$$E^{\mathrm{ext}}_{\tau} = \Omega \int_{\Omega} V^{\mathrm{ext}}_{\tau}(\boldsymbol{r})\,\tau(\boldsymbol{r})\ \mathrm{d}^3\boldsymbol{r}. \tag{4.33}$$

The derivative of the expression with respect to a pair of generic perturbations is derived in 3.72. Thankfully, since we are considering only atomic perturbations for now, there is no perturbation which causes a change in cell volume or a change to the definition of τ, and so we can use the far simpler expression

$$\frac{\partial^2 E^{\mathrm{ext}}_{\tau}}{\partial \left(\mu^{\boldsymbol{q}}_{I,\alpha}\right)^{*} \partial \mu^{\boldsymbol{q}}_{J,\beta}} = \Omega \int_{\Omega} \frac{\partial^2 V^{\mathrm{ext}}_{\tau}(\boldsymbol{r})}{\partial \left(\mu^{\boldsymbol{q}}_{I,\alpha}\right)^{*} \partial \mu^{\boldsymbol{q}}_{J,\beta}} \tau(\boldsymbol{r})\ \mathrm{d}^3\boldsymbol{r}, \tag{4.34}$$

therefore all that need to be derived is $\frac{\partial^2 V^{\mathrm{ext}}_{\tau}(\boldsymbol{r})}{\partial \left(\mu^{\boldsymbol{q}}_{I,\alpha}\right)^{*} \partial \mu^{\boldsymbol{q}}_{J,\beta}}$, where $\mu^{\boldsymbol{q}}_{I,\alpha}$ and $\mu^{\boldsymbol{q}}_{J,\beta}$ are the pair of incommensurate atomic perturbations with the same wave-vector $\boldsymbol{q}$.

An expression for $V^{\mathrm{ext}}_{\tau}(\boldsymbol{r})$ is given in equation 2.61, repeated again here,

$$V^{\mathrm{local}}_{\tau}(\boldsymbol{r}) = \Omega^{-1} \sum_{I} \sum_{\boldsymbol{G}} v^{\tau}_{I}(|\boldsymbol{G}|)\, e^{-i\boldsymbol{G}\cdot\boldsymbol{R}_I} e^{i\boldsymbol{G}\cdot\boldsymbol{r}}. \tag{4.35}$$

Once more we can follow the lead of Gonze, who showed how to compute the derivative of the local part of the external potential in equation 52 of Ref. [95]. Since we are taking the derivative with respect to a perturbation with wave-vector $\boldsymbol{q}$ and the complex conjugate of a perturbation with wave-vector $\boldsymbol{q}$, the wave-vector cancel and the derivative is always commensurate. Additionally, it is clear that the mixed derivative is only non-zero if the two perturbations, $\mu^{\boldsymbol{q}}_{I,\alpha}$ and $\mu^{\boldsymbol{q}}_{J,\beta}$, are applied to the same atom, i.e. $I = J$. In which case the derivative

of the potential can be expressed as,

$$\frac{\partial^2 V_\tau^{\mathrm{ext}}(\boldsymbol{r})}{\partial\left(\mu_{I,\alpha}^{\boldsymbol{q}}\right)^* \partial\mu_{J,\beta}^{\boldsymbol{q}}} = \frac{\mathrm{d}^2}{\mathrm{d}R_{I,\alpha}\mathrm{d}R_{J,\beta}}\Omega^{-1}\sum_I\sum_{\boldsymbol{G}} v_I^\tau\left(|\boldsymbol{G}|\right)e^{-i\boldsymbol{G}\cdot\boldsymbol{R}_I}e^{i\boldsymbol{G}\cdot\boldsymbol{r}}$$
$$= \Omega^{-1}\delta_{IJ}\sum_{\boldsymbol{G}} -G^\alpha G^\beta v_I^\tau\left(|\boldsymbol{G}|\right)e^{-i\boldsymbol{G}\cdot\boldsymbol{R}_I}e^{i\boldsymbol{G}\cdot\boldsymbol{r}}. \tag{4.36}$$

4.2.3 Second derivative of XC energy

The numerical expression for the XC energy given in equation 2.68 repeated here,

$$E^{\mathrm{XC}} = \frac{\Omega}{N_{\mathrm{p}}}\sum_i^{N_{\mathrm{p}}} f^{\mathrm{XC}}\left(\rho_{\mathrm{t}}(\boldsymbol{r}_i), |\nabla\rho_{\mathrm{t}}(\boldsymbol{r}_i)|, \tau_{\mathrm{t}}(\boldsymbol{r}_i)\right), \tag{4.37}$$

where again $\rho_{\mathrm{t}}(\boldsymbol{r})$ and $\tau_{\mathrm{t}}(\boldsymbol{r})$ are the total charge density and total KED respectively, which both include contributions from the non-linear core corrections.

The second derivative of the XC energy is derived for a pair of generic perturbations in equation 3.77. For a pair of incommensurate atomic perturbations, we can simplify the expression of equation 3.77 greatly since there is no change to the volume or the gradient operator, as was done for the first-order XC potential. In this case the energy derivative becomes,

$$\frac{\partial^2 E^{\mathrm{XC}}}{\partial\left(\mu_{I,\alpha}^{\boldsymbol{q}}\right)^*\partial\mu_{J,\beta}^{\boldsymbol{q}}} = \frac{\Omega}{N_{\mathrm{p}}}\sum_i^{N_{\mathrm{p}}}\Bigg[V_\rho^{\mathrm{XC}}(\boldsymbol{r}_i)\frac{\partial^2\rho_{\mathrm{t}}(\boldsymbol{r}_i)}{\partial\left(\mu_{I,\alpha}^{\boldsymbol{q}}\right)^*\partial\mu_{J,\beta}^{\boldsymbol{q}}} + V_\tau^{\mathrm{XC}}(\boldsymbol{r}_i)\frac{\partial^2\tau_{\mathrm{t}}(\boldsymbol{r}_i)}{\partial\left(\mu_{I,\alpha}^{\boldsymbol{q}}\right)^*\partial\mu_{J,\beta}^{\boldsymbol{q}}} +$$
$$\left.\frac{\partial V_\rho^{\mathrm{XC}}(\boldsymbol{r}_i)}{\partial\left(\mu_{I,\alpha}^{\boldsymbol{q}}\right)^*}\right|_{\rho_0,\tau_0}\frac{\partial\rho_{\mathrm{t}}(\boldsymbol{r}_i)}{\partial\mu_{J,\beta}^{\boldsymbol{q}}} + \left.\frac{\partial V_\tau^{\mathrm{XC}}(\boldsymbol{r}_i)}{\partial\left(\mu_{I,\alpha}^{\boldsymbol{q}}\right)^*}\right|_{\rho_0,\tau_0}\frac{\partial\tau_{\mathrm{t}}(\boldsymbol{r}_i)}{\partial\mu_{J,\beta}^{\boldsymbol{q}}}\Bigg]. \tag{4.38}$$

The first line includes mixed second derivatives of the total density and the total KED with respect to the two atomic perturbations. These perturbations only cause changes in the core correction terms and are only when the two perturbations, $\mu_\alpha^{I,\boldsymbol{q}}$ and $\mu_\beta^{J,\boldsymbol{q}}$, are applied to the same atom, i.e. $I = J$. The derivatives can be derived in very similar ways to the second derivative of external potential terms,

$$\frac{\partial^2\rho_{\mathrm{c}}(\boldsymbol{r})}{\partial\left(\mu_{I,\alpha}^{\boldsymbol{q}}\right)^*\partial\mu_{J,\beta}^{\boldsymbol{q}}} = \Omega^{-1}\delta_{IJ}\sum_{\boldsymbol{G}} -G^\alpha G^\beta\rho_{\mathrm{c}}^I\left(|\boldsymbol{G}|\right)e^{-i\boldsymbol{G}\cdot\boldsymbol{R}_I}e^{i\boldsymbol{G}\cdot\boldsymbol{r}}, \tag{4.39}$$

$$\frac{\partial^2\tau_{\mathrm{c}}(\boldsymbol{r})}{\partial\left(\mu_{I,\alpha}^{\boldsymbol{q}}\right)^*\partial\mu_{J,\beta}^{\boldsymbol{q}}} = \Omega^{-1}\delta_{IJ}\sum_{\boldsymbol{G}} -G^\alpha G^\beta\tau_{\mathrm{c}}^I\left(|\boldsymbol{G}|\right)e^{-i\boldsymbol{G}\cdot\boldsymbol{R}_I}e^{i\boldsymbol{G}\cdot\boldsymbol{r}}. \tag{4.40}$$

The second line of the expression for the energy derivative includes quantities

that are incommensurate with the unit cell. Substituting in the Bloch factorised definitions of these quantities reveals how these quantities be straightforwardly calculated from the cell-periodic functions,

$$\left.\frac{\partial V_\tau^{\mathrm{XC}}(\boldsymbol{r})}{\partial\left(\mu_{I,\alpha}^{\boldsymbol{q}}\right)^*}\right|_{\rho_0,\tau_0}\frac{\partial\tau_{\mathrm{t}}(\boldsymbol{r})}{\partial\mu_{J,\beta}^{\boldsymbol{q}}}=\left(\left.\frac{\partial V_\tau^{\mathrm{XC}}(\boldsymbol{r})}{\partial\mu_{I,\alpha}^{\boldsymbol{q}}}\right|_{\rho_0,\tau_0}\right)^*\frac{\partial\tau_{\mathrm{t}}(\boldsymbol{r})}{\partial\mu_{J,\beta}^{\boldsymbol{q}}} \tag{4.41}$$

$$=\left(e^{i\boldsymbol{q}\cdot\boldsymbol{r}}\bar{V}_{\tau,\boldsymbol{q},I,\alpha}^{\mathrm{XC}(1)}(\boldsymbol{r})\right)^* e^{i\boldsymbol{q}\cdot\boldsymbol{r}}\bar{\tau}_{\mathrm{t},\boldsymbol{q},J,\beta}^{(1)}(\boldsymbol{r}) \tag{4.42}$$

$$=\left(\bar{V}_{\tau,\boldsymbol{q},I,\alpha}^{\mathrm{XC}(1)}(\boldsymbol{r})\right)^*\bar{\tau}_{\mathrm{t},\boldsymbol{q},J,\beta}^{(1)}(\boldsymbol{r})\,. \tag{4.43}$$

Interestingly, equation 4.38 differs from the equivalent expression derived by Gonze and Lee (equation 20 of Ref [100]). Their expression of course does not include the mGGA terms, but does include a delta function which precludes terms from two different atoms arising. There does not seem to be any motivation for the delta function to appear in this expression, therefore we consider the expression derived in equation 4.38 to be the correct one.

4.2.4 Implementation

The expressions derived above were implemented in a development branch of CASTEP. The derivations and their implementations were then verified by comparing the phonon modes calculated from this implementation, to the phonon modes calculated using finite displacement with a non-diagonal supercell method. This is presented in the following section.

4.3 Verification: Diamond Silicon

To verify the implementation of the additional terms required for mGGA functionals, we shall pick a simple test case to compute the dynamical matrix and phonon modes for. If the above derivations and the implementation of the resultant terms are correct, the dynamical matrix and phonon modes computed using two different methods, DFPT using the additional terms above and finite displacement, should agree with each other. The level of agreement will depend on the convergence parameters used, but decreasing the convergence tolerances should result in better agreement.

Silicon is ideal for these benchmarking purposes because;

- silicon is a semiconductor, therefore we can fix the occupancies of the electrons and the sampling of $\boldsymbol{k}$-space does not need to be as fine.

- the silicon pseudopotential is relatively soft therefore the benchmarking calculations can be performed with minimal numbers of plane-waves
- the diamond crystal structure has symmetry (space group Fd-3m) means that only one perturbation has to be performed to get the full dynamical matrix.
- the crystal structure symmetry also means that the forces on the atoms are guaranteed to be zero before being perturbed.

4.3.1 DFPT vs. Finite Difference

When computing the phonon modes, DFPT can be used to compute the energy derivatives with respect to incommensurate perturbations of the atomic positions. These energy derivatives are related to the elements of dynamical matrix,

$$D^{\alpha\beta}_{\boldsymbol{q},IJ} = \frac{1}{\sqrt{M_I M_J}} \frac{\partial^2 E}{\partial \left(\mu^{\boldsymbol{q}}_{I,\alpha}\right)^* \partial \mu^{\boldsymbol{q}}_{J,\beta}}. \tag{4.44}$$

With all the elements of the dynamical matrix, the matrix can then be diagonalised to give us the phonon energies and modes.

The finite-displacement method works slightly differently. In the case of $\boldsymbol{q} = 0$, the finite displacement method works by moving one atom in the unit cell by a small amount in one direction from its equilibrium position, calculating the ground-state energy and forces in the displaced configuration, then the atom is displaced from its equilibrium position by an equal amount in the opposite direction, and the ground-state energy and forces for this configuration are recalculated. The derivative of the forces with respect to the atom being moved can then be calculated numerically as,

$$\frac{\mathrm{d}F^c_{J,\beta}}{\mathrm{d}\mu^c_{I,\alpha}} = \frac{1}{2\mu^c_{I,\alpha}} \left(F^{c,+}_{J,\beta} - F^{c,-}_{J,\beta}\right), \tag{4.45}$$

where $F^{J,c,+}_{\beta}$ and $F^{J,c,-}_{\beta}$ are the forces on atom J in cell c along direction β in the two displaced configurations and $\mu^{I,c}_{\alpha}$ is the displacement of atom I in cell c along direction α. The force, $F^{J,c}_{\beta}$, is minus the derivative of the energy with respect to a displacement of atom J in cell c along direction β therefore the force derivative is related to minus the dynamical matrix at $\boldsymbol{q} = 0$,

$$D^{\alpha\beta}_{\boldsymbol{q}=0,IJ} = \frac{1}{\sqrt{M_I M_J}} \frac{\mathrm{d}^2 E}{\mathrm{d}\mu^c_{I,\alpha} \mathrm{d}\mu^c_{J,\beta}} = -\frac{1}{2\mu^c_{I,\alpha}} \left(F^{c,+}_{J,\beta} - F^{c,-}_{J,\beta}\right) \tag{4.46}$$

where the atoms are both confined to the unit cell c. This is equivalent to the

dynamical matrix because of the use of periodic boundary conditions. If an atom is moved in the unit cell then it is also moved in the same way in all the periodic images of the unit cell, which is equivalent to perturbing the atom with a wave vector $\boldsymbol{q} = 0$.

In order to compute the phonon modes at general values of $\boldsymbol{q}$ from finite displacement, there are two methods, the supercell method [101] and the non-diagonal supercell method [4]. In the supercell method, we attempt to compute the interatomic force constant matrix directly, rather than the dynamical matrix.

$$\Phi^{\alpha\beta}_{I,c,J,c'} = \frac{\mathrm{d}^2 E}{\mathrm{d}\mu^{I,c}_{\alpha}\mathrm{d}\mu^{J,c'}_{\beta}}. \tag{4.47}$$

where $\Phi^{\alpha\beta}_{I,c,J,c'}$ is the IFC matrix. In order for the IFCs to be correct, the supercell has to be large enough that the displaced atom and its periodic images have minor or no effects. This relies on the decay of the IFCs with distance between the atoms; however, the size of supercells required can often be prohibitive, e.g. a $4 \times 4 \times 4$ supercell of primitive silicon already contains 128 atoms, making the supercell calculations very expensive. Once the IFCs have been calculated using the supercell method, the dynamical matrix can be calculated at a general $\boldsymbol{q}$ by taking the Fourier transform of the IFCs.

The non-diagonal supercell method works slightly differently and allows for direct calculation of the dynamical matrix by generating a supercell that is commensurate with the perturbation wave vector, such that the lattice vectors are scaled by a matrix with non-zero elements on the off-diagonal elements. The dynamical matrix of the supercell at $\boldsymbol{q} = 0$ can then be calculated using finite difference. This can be used to calculate dynamical matrices of primitive cell at non-commensurate wave-vectors; for more details, see Ref. [4]. The downside to this approach is that the construction of such supercells means that it can be impossible to generate grid samplings in the supercell that are equivalent to sampling of the primitive cell. This has a particularly disastrous effect for XC functionals that are particularly sensitive to grid sampling, such as meta-GGAs [33, 102]. We address the cause of these problems in the following chapter (§5).

The comparison of the DFPT method and the supercell method is therefore slightly subtle for the case where $\boldsymbol{q} \neq 0$. We cannot compare values that are directly computed by both methods, since in DFPT we calculate the dynamical matrix and in finite displacement we calculate either the interatomic force constants, which may not be sufficiently converged, or a dynamical matrix at $\boldsymbol{q} = 0$ for a non-diagonal supercell. At $\boldsymbol{q} = 0$ we can compare the values calculated for the dynamical matrix directly, but at non-zero $\boldsymbol{q}$, we must compare other

quantities. The easiest comparison to make is of phonon dispersions, plots of the phonon energies at different values of $\boldsymbol{q}$ calculated by each method.

4.3.2 Dynamical Matrix at q=0

We shall begin by comparing the dynamical matrix at $\boldsymbol{q} = 0$ of the silicon primitive cell calculated from finite displacement (FD) and density functional perturbation theory (DFPT). The ground-state was found for the silicon primitive cell, see figure 4.1, using a cut-off energy of 350eV which corresponds to the setting `basis_precision` being set to `extreme`. The Brillouin zone was sampled using a Monkhorst-Pack grid with a mesh of $8 \times 8 \times 8$ k-points (equivalent to a k-point spacing of 0.04 $2\pi\text{Å}^{-1}$. The crystal structure symmetry was used to reduce the number of k-points required to only those in the irreducible wedge of the Brillouin zone, and was used to symmetrise the forces and stresses. The grids used for the density and KED were the minimum needed to represent the density of the wave functions, i.e. using `grid_scale` of 2 and using the same grid for the so-called "fine grid". The system was tested using the rSCAN and r2SCAN functionals [29, 36], which are both mGGA functionals, and PBE, a GGA functional. The PBE calculations were performed so that the agreement between the DFPT and the FD calculations could be compared between the different families of functionals.

The SCF procedure to find the ground state was continued until the ground state energy converged to 10^{-10} eV per atom and the unsymmetrised ground state forces converged to 10^{-7} eV/Å. This is excessively well-converged for most calculations; however, it was done here to minimise the error in the ground-state, such that we can exclude under-convergence of the ground-state as the cause of any disagreement between the DFPT calculations and the FD calculations. FD

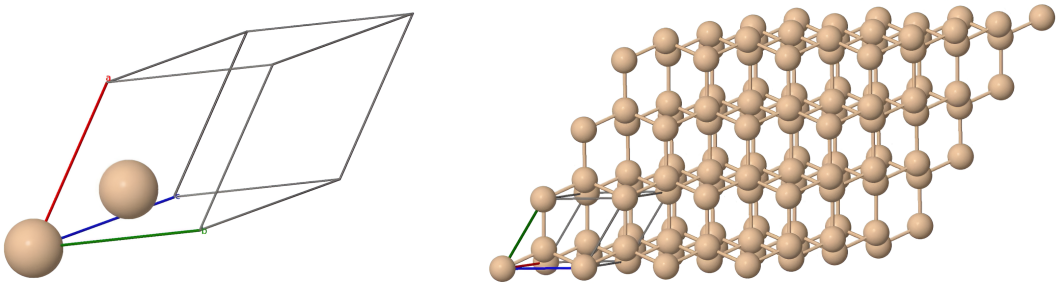

Figure 4.1: Crystal structure of diamond silicon show in both the primitive unit cell (left) and in a $4 \times 4 \times 4$ supercell of the primitive cell (right). The fractional co-ordinates of the two atoms in the primitive unit cell are at the origin, $(0, 0, 0)$, and at $\left(\frac{1}{4}, \frac{1}{4}, \frac{1}{4}\right)$.

	PBE		rSCAN		r2SCAN	
	$D^{\alpha\alpha}_{\boldsymbol{q}=0,I,I}$	$D^{\alpha\alpha}_{\boldsymbol{q}=0,I,J}$	$D^{\alpha\alpha}_{\boldsymbol{q}=0,I,I}$	$D^{\alpha\alpha}_{\boldsymbol{q}=0,I,J}$	$D^{\alpha\alpha}_{\boldsymbol{q}=0,I,I}$	$D^{\alpha\alpha}_{\boldsymbol{q}=0,I,J}$
DFPT 10^{-5} eV/Å^2	14.073258	-13.536081	12.241833	-14.046137	22.777230	-13.666064
DFPT 10^{-7} eV/Å^2	14.073220	-13.534816	12.241785	-14.046119	22.777200	-13.666032
FD $\Delta\mu = 0.01$ Å	13.802298	-13.802298	13.139783	-13.139783	18.187188	-18.187188
FD $\Delta\mu = 0.001$ Å	13.803997	-13.803997	13.143897	-13.143897	18.220542	-18.220542

Table 4.1: Comparison of the elements of the Dynamical matrix at $\boldsymbol{q} = 0$ of silicon calculated using of finite displacement and DFPT using the PBE, rSCAN and r2SCAN functionals at different convergence tolerances. The dynamical matrix elements are given in units of eV/Å^2.

calculations were performed using the same convergence criteria as the ground-state calculation, and were performed using two values for the displacement of the atoms, 0.01 Å and 0.001 Å.

DFPT calculations were performed using CASTEPs variational minimiser which uses a conjugate gradient algorithm [96] to vary the first-order wavefunctions to minimise the energy derivative calculated according to equation 3.40. The convergence criterion for the variational solver is that the second-order energy derivative varies less than a convergence tolerance between successive steps of the conjugate gradient algorithm. Two calculations were performed in which the convergence tolerance was set to 10^{-5} and 10^{-7} eV/Å^2. To calculate the off-diagonal elements of the dynamical matrix, $D^{\alpha,\beta}_{I,J}$, where $\alpha \neq \beta$ or $I \neq J$, the expression of equation 3.47 was used.

In the case of the diamond silicon primitive cell, there are only two unique elements of the dynamical matrix at $\boldsymbol{q} = 0$. The diagonal elements ($D^{\alpha,\alpha}_{I,I}$) must all be the same, and in each row of the dynamical matrix there is only one non-zero off-diagonal element, which corresponds to the other atom in the primitive cell moving in the same direction as the first perturbed atom, i.e. $D^{\alpha,\alpha}_{I,J}$. $D^{\alpha,\alpha}_{I,J}$ is the same for all the off-diagonal elements. Therefore, the first-order wavefunctions of only one of the perturbations are required to compute all the elements of the dynamical matrix at $\boldsymbol{q} = 0$. For the FD calculations, this means that only one of the atoms has to be perturbed, which yields a full row of the dynamical matrix, and the values in this row can then be used to complete the rest of dynamical matrix by symmetry.

The results for the elements of the dynamical matrix from these calculations are shown in Table 4.1. The results in Table 4.1 show that for there is severe

disagreement between the FD and DFPT calculations for the mGGA functionals, a difference of ~ 0.9 eV/Å^2 for rSCAN and ~ 4.5 eV/Å^2 for r2SCAN. Clearly something has gone very wrong; however, even the PBE results also disagree with a difference between the DFPT and FD calculations of ~ 0.25 eV/Å^2, when the PBE implementation has long since been verified for correctness [96]. The discrepancy can be explained by a hitherto unmentioned correction that is being applied to the forces to preserve translational symmetry. The direct derivatives of the energy with respect to the atomic positions calculated using the Hellman-Feynman approach may not respect translational symmetry in that there can be a net force acting on the centre of mass. This occurs because of the discrete sampling of the XC energy, which is discussed in detail in the next chapter. The centre-of-mass force effectively corresponds to the entire periodic crystal spontaneously drifting in the direction of the force, which is completely non-physical.

In order to stop the forces breaking of translational symmetry, a correction is applied to all the forces which removes the average force from the system,

$$F_\alpha^{J,corr} = F_\alpha^J - \frac{1}{N_{at}} \sum_I^{N_{at}} F_\alpha^I \tag{4.48}$$

where $\boldsymbol{F}^{J,corr}$ is the corrected force. When the numerical derivatives of the forces are taken, it is the corrected forces that are being used, whereas the DFPT derivatives evaluate the direct derivatives of the uncorrected Hellman-Feynman forces. To make a fair comparison between the DFPT and FD calculations, we must use the bare, uncorrected, Hellman-Feynman forces to calculate the numerical derivative.

The finite displacement calculations were repeated, but modified to use the derivatives of the uncorrected Hellman-Feynman forces when computing the elements of the dynamical matrix. The results of these calculations are presented with the DFPT results in Table 4.2. These results are now in much better agreement. For rSCAN and r2SCAN the discrepancies in diagonal elements between the best converged DFPT result and the FD result using a displacement of 0.001 Å is reduced to $\sim 1 \times 10^{-3}$ eV/Å^2 and $\sim 2 \times 10^{-3}$ eV/Å^2 respectively. For off-diagonal elements the disagreement has reduced to $\sim 8 \times 10^{-4}$ eV/Å^2 for rSCAN and $\sim 9 \times 10^{-5}$ eV/Å^2 for r2SCAN. For the PBE calculations, the discrepancy is slightly smaller, for both the diagonal and the off-diagonal elements, the disagreement is around 1×10^{-5} eV/Å^2. Comparing the FD calculations for the same functional using different displacement lengths, in the case of all functionals, there is disagreement between the values calculated for the dynamical matrix. For PBE the disagreements are in the diagonal and off-diagonal elements are

	PBE		rSCAN		r2SCAN	
	$D^{\alpha\alpha}_{\boldsymbol{q}=0,I,I}$	$D^{\alpha\alpha}_{\boldsymbol{q}=0,I\neq J}$	$D^{\alpha\alpha}_{\boldsymbol{q}=0,I,I}$	$D^{\alpha\alpha}_{\boldsymbol{q}=0,I\neq J}$	$D^{\alpha\alpha}_{\boldsymbol{q}=0,I,I}$	$D^{\alpha\alpha}_{\boldsymbol{q}=0,I\neq J}$
DFPT 10^{-5} eV/Å^2	14.073258	-13.536081	12.241833	-14.046137	22.777230	-13.666064
DFPT 10^{-7} eV/Å^2	14.073220	-13.534816	12.241785	-14.046119	22.777200	-13.666032
FD $\Delta\mu = 0.01$ Å (Uncorrected forces)	14.069967	-13.534626	12.233224	-14.046343	22.708047	-13.666325
FD $\Delta\mu = 0.001$ Å (Uncorrected forces)	14.073094	-13.534930	12.240823	-14.046933	22.774887	-13.666123

Table 4.2: Comparison of the elements of the Dynamical matrix at $\boldsymbol{q} = 0$ of silicon calculated using of finite displacement and DFPT using PBE, rSCAN and r2SCAN functionals at different convergence tolerances. The finite difference calculation in this case has been performed using the bare Hellman-Feynman forces of the system, rather than the forces corrected to give net zero average force. The dynamical matrix elements are given in units of eV/Å^2.

$\sim 3 \times 10^{-3}$ eV/Å^2 and $\sim 3 \times 10^{-4}$ eV/Å^2, respectively, while for r2SCAN the differences are $\sim 7 \times 10^{-2}$ eV/Å^2 and $\sim 2 \times 10^{-4}$ eV/Å^2. For all functionals, the discrepancy between the DFPT and FD calculations is smaller than the discrepancy between the FD calculations done with different step sizes. Considering the level of noise that is therefore present in the FD calculations, we can consider this excellent agreement between the DFPT and the FD calculations in the case where $\boldsymbol{q} = 0$.

The system having translational symmetry means that moving the entire system by a displacement should lead to zero energy change, equivalently, the net force acting on the system should be zero. Moving one atom will lead to a force on that atom, and by Newtons 3$^{\text{rd}}$ law there should be an equal and opposite force acting on all the other atoms in the system, the consequence of this on the dynamical matrix is that a sum over each row should be equal to zero,

$$\sum_J D^{\alpha\alpha}_{\boldsymbol{q}=0,I\neq J} = \frac{\mathrm{d}F^{CoM}_\alpha}{\mathrm{d}\mu} = 0 \tag{4.49}$$

where $\boldsymbol{F}^{av}$ is the force acting on the systems centre of mass, which if translational symmetry is preserved should be zero, therefore its derivative should be zero too.

Apart from drastically improving the agreement between the DFPT and FD calculations, working with the uncorrected Hellman-Feynman forces in the FD calculations breaks this translational symmetry law. In Table 4.1, the diagonal

	PBE		rSCAN		r2SCAN	
	$D^{\alpha\alpha}_{\boldsymbol{q}=0,I,I}$	$D^{\alpha\alpha}_{\boldsymbol{q}=0,I\neq J}$	$D^{\alpha\alpha}_{\boldsymbol{q}=0,I,I}$	$D^{\alpha\alpha}_{\boldsymbol{q}=0,I\neq J}$	$D^{\alpha\alpha}_{\boldsymbol{q}=0,I,I}$	$D^{\alpha\alpha}_{\boldsymbol{q}=0,I\neq J}$
DFPT 10^{-7} eV/Å^2	13.569470	-13.569402	13.898610	-13.905472	13.911367	-13.942388
FD $\Delta\mu = 0.001$ Å (Uncorrected forces)	13.569494	-13.569500	13.898680	-13.905478	13.911545	-13.942480

Table 4.3: Comparison of the elements of the Dynamical matrix at $\boldsymbol{q} = 0$ of silicon calculated using of finite displacement and DFPT using PBE, rSCAN and r2SCAN functionals. All calculations have been performed using an FFT grid for the XC contributions that is 4 times as dense as the density grid. The finite difference calculation in this case has been performed using the bare Hellman-Feynman forces of the system. The dynamical matrix elements are given in units of eV/Å^2.

and off-diagonal elements of the dynamical matrix calculated in the same FD calculations are always equal and opposite, whereas in table 4.2 they are very different. This is because to calculate the results in Table 4.1 the forces in the FD calculations have been 'corrected' such that there is net-zero force in the calculation, enforcing translational symmetry in the forces. By removing this correction, translational symmetry is no longer enforced, and the dynamical matrix no longer respects it.

The Hellman-Feynman forces do not respect the translational symmetry because the integral for the XC energy is calculated using a discrete set of points in real-space, the reasons for this are discussed in greater detail in the following chapter. In DFPT phonon calculations we are computing the derivatives of the Hellman-Feynman forces, therefore, it is common practice to apply a correction to the dynamical matrix to enforce translational symmetry and fix other numerical discrepancies. These corrections are often referred to as acoustic sum-rule corrections since the acoustic modes of a material at $\boldsymbol{q} = 0$ should have zero energy, which is enforced by the corrections. The corrections are designed to fix minor numerical discrepancies due to the translational symmetry breaking in XC energy and numerical errors in under-converged forces. However, they do not work well when there are large numerical errors or the XC functional is particularly sensitive to the grid used. No acoustic sum rule correction has been applied to the dynamical matrices reported in Tables 4.1 and 4.2. Considering the discrepancies between the diagonal and off-diagonal elements, and the difference between the FD calculations with different step sizes, the rSCAN and r2SCAN calculations clearly have a much higher level of noise compared to PBE, which can be attributed to the aforementioned grid sensitivity of the mGGA functionals [35].

In order to address the grid sensitivity of the mGGA functionals, the dynamical matrix at $\boldsymbol{q} = 0$ was recomputed for all functionals using both the DFPT and FD methods. For these calculations a different real-space grid was used to compute the XC contributions, the FFT grid used to compute the density and KED was a $24 \times 24 \times 24$ grid, for the XC contributions a $96 \times 96 \times 96$ FFT grid was used. For the DFPT calculations a convergence tolerance of 10^{-7} eV/Å^2 was used and for the FD calculations a step size of $\Delta\mu = 0.001$ Å was used. The results of these calculations are presented in Table 4.3. The agreement between the FD and the DFPT calculations has improved for the diagonal terms by at least an order of magnitude for all functionals, for the off-diagonal elements, the two methods agree for all functionals up to $\sim 10^{-4}$ eV/Å^2. There is also a large improvement in the sum of the dynamical matrix row which should be zero, for PBE the sum has decreased from 0.54 eV/Å^2 to 6.8×10^{-5} eV/Å^2, for rSCAN the sum has decreased from 1.8 eV/Å^2 to 6.8×10^{-3} eV/Å^2, and for r2SCAN the sum has decreased from 9.1 eV/Å^2 to 3.1×10^{-2} eV/Å^2. The results shown in Table 4.3 show that the DFPT and FD methods are in agreement with each other, which shows that the DFPT method has been derived and implemented correctly.

4.3.3 Dynamical Matrices at q≠0

Now we can try test the implementation for incommensurate perturbations. The general method for phonon calculations is to calculate the dynamical matrix at a set of q-points that samples the 1$^{\text{st}}$ Brillouin zone in a manner similar to the sampling of k-points using a Monkhorst-Pack grid [66]. As is done for the k-point sampling, an irreducible set of q-points can be found that samples the symmetry-reduced BZ. Once the dynamical matrix is found at all q-points on the grid, Fourier interpolation can then be used to calculate the dynamical matrix at any value of $\boldsymbol{q}$. The precision of the dynamical matrix at a general value of $\boldsymbol{q}$ will depend on the sampling grid of q-points used.

Since we must calculate the dynamical matrix at several values of $\boldsymbol{q}$, where each q-point requires several perturbations to be computed, it would therefore be unmanageable to perform a direct comparison of all the values calculated for the dynamical matrix at every q-point. We shall compare the values of the dynamical matrix calculated for one particular q-point and to verify the other dynamical matrices are also correct, we shall instead compare the phonon band-structure computed using the two methods. The phonon band-structure is the phonon mode energies, which are the eigenvalues of the dynamical matrices, plotted against the value of $\boldsymbol{q}$ along the high symmetry lines of the BZ. If the dynamical matrices from the DFPT and FD methods are in agreement, so too will the phonon

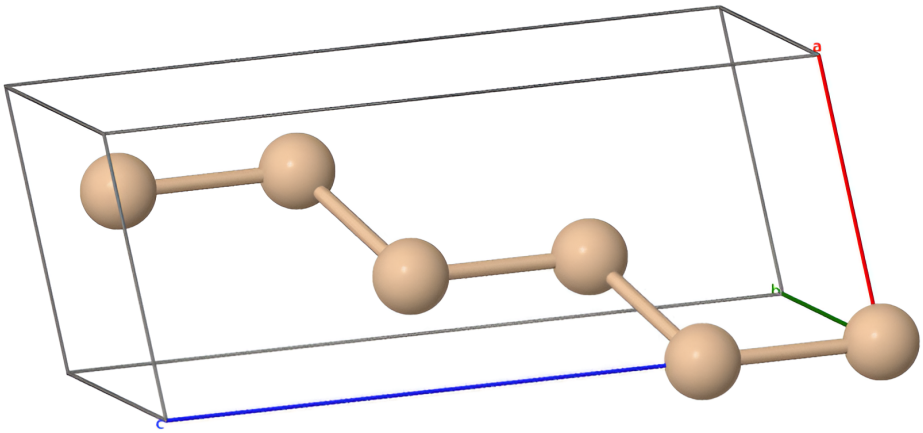

Figure 4.2: One of the supercells used to compute the dynamical matrix of silicon for perturbations which are incommensurate with the primitive cell. In this case this supercell is used to compute the dynamical matrix at $\boldsymbol{q} = \left(0, \frac{1}{3}, 0\right)$

band-structures. The dynamical matrices at the value of $\boldsymbol{q}$ along these lines are calculated using DFPT and the non-diagonal supercell methods using comparable q-point grids.

The dynamical matrix at $q = \left(0, \frac{1}{3}, 0\right)$ (in fractional co-ordinates) was computed for the silicon system used previously with the same basis set parameters as before, using the larger grid for the XC contributions. Again, three XC functionals were used, PBE, rSCAN and r2SCAN and for all functionals a DFPT calculation and an FD calculation was performed. The supercell used to calculate the dynamical matrix at $q = \left(0, \frac{1}{3}, 0\right)$ via the non-diagonal supercell method is shown in figure 4.2 and a finite displacement step of 0.001 Å was used to compute the force derivatives. For the DFPT calculations the variational solver was used to calculate again to minimised the second order energy derivative, and convergence tolerance was set to 10^{-7} eV/Å^2.

A comparison of the computed values for the dynamical matrix is shown in table 4.4, which shows that the mGGA functionals are in at least as good agreement as the PBE calculations. There is some slight disagreement between the DFPT and the FD calculations, more than was found in the $\boldsymbol{q} = 0$ calculations, however the level of disagreement is consistent across all the functionals used. The cause of this change can be attributed to the change in sampling that comes from switching from the primitive cell to the non-diagonal supercell for the finite difference calculation. The lattice vectors of the supercell are rotated compared to the primitive cell; this changes the real-space grid point sampling and the k-point sampling so that no exactly equivalent sampling between the unit cells can be devised. We have already seen how a change in the real-space grid sampling can

	PBE		rSCAN		r2SCAN	
	$D^{\alpha\alpha}_{\boldsymbol{q},I,I}$	$D^{\alpha\alpha}_{\boldsymbol{q},I\neq J}$	$D^{\alpha\alpha}_{\boldsymbol{q},I,I}$	$D^{\alpha\alpha}_{\boldsymbol{q},I\neq J}$	$D^{\alpha\alpha}_{\boldsymbol{q},I,I}$	$D^{\alpha\alpha}_{\boldsymbol{q},I\neq J}$
DFPT 10^{-7} eV/Å^2	13.758029	-8.654210 $\pm i2.443053$	14.163394	-8.870874 $\pm i2.501634$	14.176732	-8.899422 $\pm i2.506065$
FD $\Delta\mu = 0.001$ Å (Uncorrected forces)	13.734871	-8.642118 $\pm i2.440427$	14.150085	-8.860668 $\pm i2.501686$	14.196317	-8.888152 $\pm i2.502124$

Table 4.4: Comparison of the elements of the Dynamical matrix at $\boldsymbol{q} = \left(0, \frac{1}{3}, 0\right)$ of silicon calculated using of finite displacement and DFPT using PBE, rSCAN and r2SCAN functionals. All calculations have been performed using an FFT grid for the XC contributions that is 4 times as dense as the density grid. The finite difference calculation in this case has been performed using the bare Hellman-Feynman forces of the system. The dynamical matrix elements are given in units of eV/Å^2. The $\pm$ before the imaginary part of the dynamical matrix elements denotes the Hermitian nature of the dynamical matrix, i.e. $D^{\alpha\beta}_{\boldsymbol{q},I,J} = \left(D^{\beta\alpha}_{\boldsymbol{q},J,I}\right)^*$.

significantly affect XC contribution, necessitating a finer grid sampling, changing the k-point sampling will also affect the ground-state. The supercell is obviously larger, therefore in reciprocal space the first BZ is smaller, but the rotated lattice vectors means that even if a Monkhorst-Pack sampling grid of the same sampling density is used, it will not sample equivalent points in k-space. This change in sampling means that there will be a difference between the ground state in the primitive cell and the supercell, the better converged the calculation is with respect to the k-point sampling, the smaller the difference is likely to be.

Since the disagreement is fairly consistent across all XC functionals, and we are already using a much finer grid for the XC contributions, we can attribute this to the discrepancy to the change in the k-point sampling in the supercell which will be the same for all functionals. There may, however, be a cancellation of errors that is hiding some error in the implementation. A more conclusive test therefore is to compute the dynamical matrices for a grid of q-points and computing the phonon band-structure as described above. Phonon calculations were therefore performed for all 3 functionals with a q-point sampling grid of $3 \times 3 \times 3$ using both DFPT and the non-diagonal supercell FD method, using the same convergence parameters as before. The dynamical matrices computed at the points of the $3 \times 3 \times 3$ q-point grid were then used to find dynamical matrices at q-points along the high symmetry lines in the BZ via interpolation. No acoustic sum-rule was applied to the dynamical matrices.

The phonon band structures calculated shown in figure 4.3. For all functionals the DFPT and FD calculations can be seen to be in excellent agreement across the BZ. The only exception to this is for r2SCAN at Γ ($\boldsymbol{q} = 0$), where there is

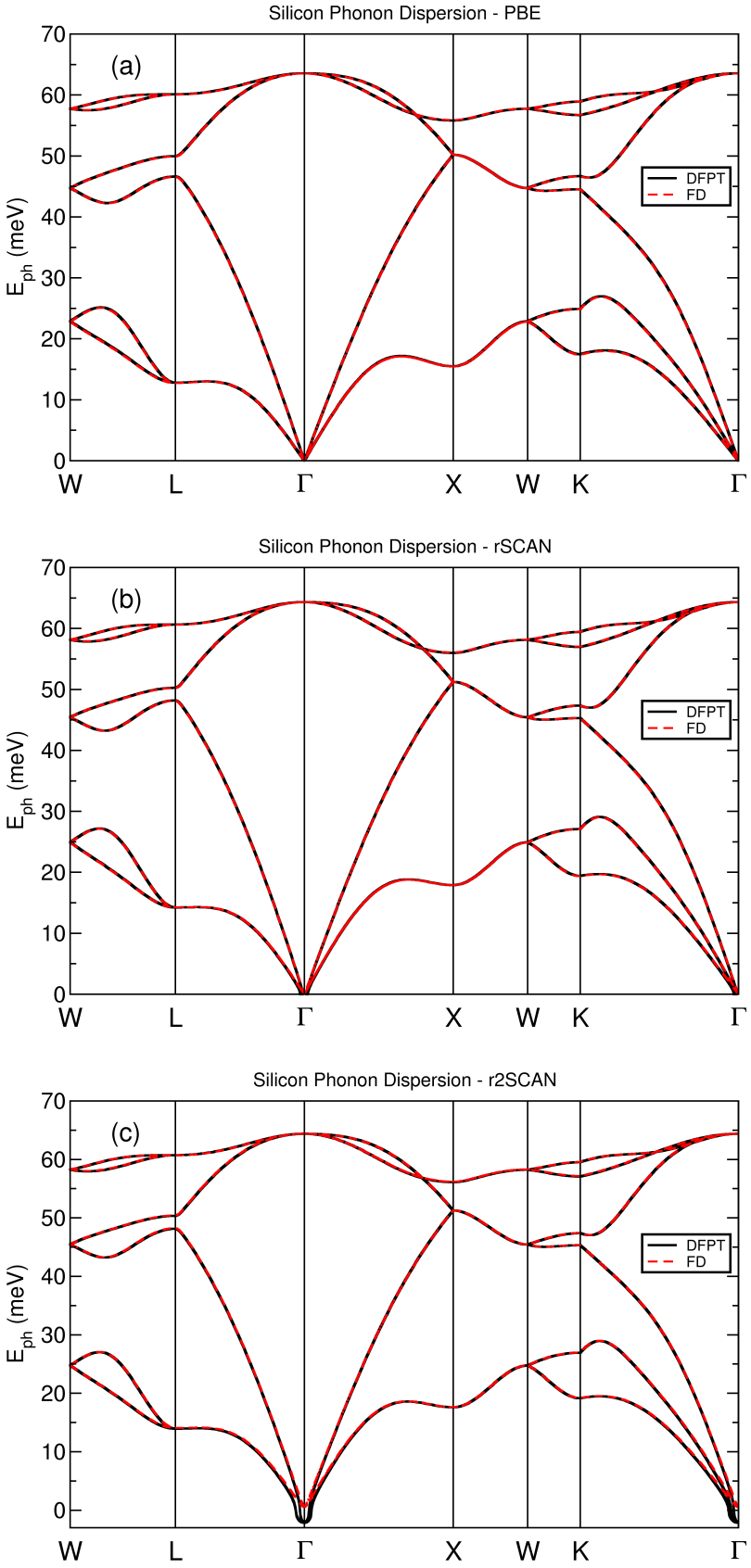

Figure 4.3: Comparison of phonon band structures calculated using DFPT and FD for silicon using a $3 \times 3 \times 3$ q-point grid for 3 XC functionals. Each sub-figure shows the comparison for each functional (a) PBE, (b) rSCAN, (c) r2SCAN.

a slight difference between the DFPT and FD phonon energies. In addition to being different from the FD modes, the DFPT modes are noticeable negative, denoting imaginary phonon modes. Imaginary modes mean that there is a mode of the system that lowers the system energy, the fact that these modes are at Γ means that these modes describe the system moving in a particular direction and the energy being lowered, i.e. the breaking of translational symmetry. Looking again at the dynamical matrix computed at $\boldsymbol{q} = 0$ in table 4.3, it can be seen that the values computed using r2SCAN have the the largest sum across a row of the dynamical matrix, i.e. the largest violation of the rule expressed in equation 4.49. It is this violation of translation symmetry that causes the imaginary modes in the r2SCAN phonon band-structure. The reason for the difference between the FD results and the DFPT is that, in the case of the FD calculation, the dynamical matrix at $\boldsymbol{q} = 0$ is *not* computed using the primitive cell, it is instead constructed from the finite displacement calculations in the non-diagonal supercells. The aforementioned change in sampling in the supercell, will change the nature of the breaking of translational symmetry causing changes in the dynamical matrix at Γ. There are also subtle differences at Γ in the PBE and rSCAN phonon band structures but they are small enough that they are difficult to see on these plots. An acoustic sum rule correction would be sufficient to address the imaginary modes here.

The comparison of phonon band structures shown in figure 4.3 satisfactorily shows that the derivations described in previous sections and the implementation of the derived terms is correct.

4.3.3.1 Alternative Methods

As has been described previously, there are some alternative choices that can be made for the calculations and the implementation of some of the derivatives. Specifically, in CASTEP there are two methods of determining the first-order wavefunctions that are implemented, a variational minimiser of the second derivative of the energy and a Greens functions solver for the Sternheimer equations. As discussed in the previous chapter (§3.4.3.1), there is also the calculation of the partial derivatives of the XC energy density function, for which two methods of calculating these derivatives were implemented, numerical differentiation via finite difference and algorithmic differentiation as implemented in LibXC. Finally, there is a discrepancy in the expression for the second order derivative derived in equation 4.38 when compared to the equivalent expression for LDA and GGA functionals, as derived by Gonze and Lee (equation 20 of Ref. [100]). Additional calculations of the dynamical matrix for the silicon system were performed, using the Greens function solver to obtain the first-order wave functions, using numer-

ical differentiation to compute the partial derivatives of the XC energy density function, and one where the additional off-diagonal terms derived in equation 4.38 were not included.

We shall first compare the results of the two different solvers, and of the two methods of evaluating the XC partial derivatives since in principle these methods should give the same answer. The change in phonon energies when switching from the variational solver to the Greens function solver is of the order 10^{-9} eV across the phonon spectrum, which is around the order of convergence tolerances used. The difference in phonon energies when computing the partial derivatives of the XC energy density using the LibXC implementation and using a finite difference method is of the order of 10^{-7} eV, which shows the derivatives must be in reasonable agreement, and some noise is expected in the derivatives calculated via the finite difference method. At this point, the Reader may expect a comparison of the phonon band structures produced from each of the different methods; however, they would make for some particularly boring plots since the phonon band-structures produced are indistinguishable from those plotted in Figure 4.3.

In equation 4.38, the expression for the second derivative of the XC energy with respect to two atomic perturbations is given. There are additional terms in the expression compared to the equivalent expression derived by Gonze and Lee for LDA and GGA functionals. Computing the additional terms makes very little qualitative difference in the results of the calculation, the difference between the calculated phonon energies in the silicon system is of the order of 10^{-8} eV which is well below the threshold of noise in the calculation. The quantitative difference is very small, of the order of 10^{-4} eV/Å^2, for all the dynamical matrices computed, which is not unexpected. The additional terms are the overlap of the change in the XC potential under the movement of the core density of one atom with the derivative of the core density of a different atom with respect to that atom being moved. In the silicon system tested, the atoms are reasonably far apart, much further apart than the core radius of the pseudopotential, meaning that there will be very little overlap in the core charges and thus these additional terms are expected to be very small. A system could be devised for which these terms may be far more significant, one where the overlap between the non-linear core correction densities from two atoms is larger e.g. a high-pressure phase of a material. Therefore, this will require further study, beyond the scope of this thesis.

4.4 Perspectives

In this chapter, the necessary terms to compute the components of dynamical matrices within the meta-generalised gradient approximation using Density Functional Perturbation Theory (DFPT) are derived. The derived terms were implemented into CASTEP and the implementation was verified by comparing the calculations to equivalent Finite Displacement (FD) calculations using the non-diagonal supercell method to calculate the dynamical matrices. The two methods produce phonon band-structures that are in mostly excellent agreement, the minor differences between the DFPT and FD results are attributed to the change in sampling in both the real-space sampling grid and the k-point sampling grid.

The method of computing phonon band-structures via DFPT has significant advantages over the FD method since only the primitive cell is required when computing the dynamical matrix for phonon modes that are incommensurate with the primitive unit cell. Whereas the FD method must use a supercell when either computing the interatomic forces constants, in which case one very large supercell is required, or when computing the dynamical matrices directly, in which case several modest sized supercells are required. The supercell and non-diagonal supercell approaches always take much longer than the DFPT approach since the supercells include far more electrons, which means many operations such as applying the Hamiltonian and orthonormalization of the states are much more expensive operations.

The results reported in this chapter show how the sensitivity of the functional to the real-space grid sampling is of particular importance when performing phonon calculations. Large violations of translational symmetry can cause dramatically wrong results, for instance comparing the results for r2SCAN in table 4.2 and table 4.3. The same system is being tested in both cases, but a much larger grid was used to compute the XC contributions in the case of table 4.3, which causes the value calculated for the diagonal elements of the dynamical matrix to differ between the two calculations by over 60%!. This leads us to the next aim of this thesis, to develop a method to understand the grid sensitivity of different XC functionals and to provide users of electronic structure codes a cheap and simple method of determining whether there is a significant grid sensitivity issue for any particular system and basis set. The choice of increasing the grid for the XC contributions is informed by the findings of the next chapter.

Chapter 5

Cracking The Egg-Box Effect

Note that the main work in this chapter has been published as a paper [103].

In this chapter, an approach to quantifying the error in E^{XC} due to the effect of the violation of translational symmetry in XC integration is presented. The method is demonstrated to accurately estimate the change in E^{XC} as the discrete grid is translated relative to the system. Importantly, this method of error estimation is efficient to compute, relies on no other data than the ground state density, and is general to all XC functionals.

Further, it is shown that the integration of the XC energy contributions can be performed more accurately by computing only the XC contribution on a finer grid to correctly sample the energy and potential. By then truncating the XC potential (V^{XC}) in Fourier space, the method reduces the aliasing of high-frequency components into the potential. This can greatly reduce the computational expense compared to computing every contribution to the total energy on this finer grid, and hence allows properties to be calculated more accurately and more efficiently than would otherwise be possible.

This chapter is set out as follows; in Section 5.1 a brief description is provided of how the numerical integration error arises in the XC energy, particularly in the plane-wave basis set, and the consequences this can have for computed properties. The uncertainty quantification method is described in Section 5.3 and finally in Section 5.4 its utility as an indication that the calculations are under-converged and likely to produce inaccurate results is demonstrated.

5.1 Introduction

Significant progress has been made over recent years in improving the accuracy of Density Functional Approximations (DFAs) for electronic structure simulations.

The Strongly Constrained and Appropriately Normed (SCAN) functional was the first meta-Generalised-Gradient Approximation (meta-GGA) to adhere to all the known constraints for a meta-GGA functional [28]. This was a major achievement for chemical accuracy; however, it was quickly observed that SCAN, as with many other meta-GGA functionals, suffered from severe numerical instability [29, 30, 31, 32, 33, 34, 35]. This led to the creation of several related functionals [29, 36, 37, 38], which attempted to regularise the numerical behaviour of SCAN, while maintaining SCAN's physical accuracy. Considerable improvements have been achieved with respect to SCAN, but, as recent work has shown, many modern DFAs including the SCAN family are numerically ill behaved [35].

The root of this poor numerical behaviour is in the integration of the contributions to the exchange and correlation (XC) energy, E^{XC}. The choice of basis set, the number of sampling points, and the position of those sampling points can greatly affect the calculated value of E^{XC}. This can lead to simulations which violate translational symmetry, with the energy of the system oscillating if the system is translated relative to the discrete sampling points. This is sometimes referred to as the egg-box effect, due to the characteristic shape of the energy landscape (see Figure 5.1). The numerical integration of the contributions to E^{XC} in real space will almost always cause some violation of the translational symmetry. However, the choice of basis set functions or representation of potentials can lead to additional causes of the violation of translational symmetry [69, 104, 105].

The numerical integration of the contributions to E^{XC} is highly dependent on the choice of numerical sampling and can have significant effects on the physical properties predicted by simulation packages. Sitkiewicz *et al.* [106, 107] have made several studies of how this numerical ill-behaviour can lead to spurious oscillations in the energy as the atoms are displaced with respect to the grid, due to numerical integration errors. These spurious oscillations have been shown to cause particular difficulty in calculating vibrational spectra [42], particularly for molecules that have low energy vibrational modes, where these oscillations cause significant noise in the spectrum.

For users of electronic structure software, it can be difficult to find a balance between the desire for high physical accuracy and the need for good numerical behaviour. Users have very little indication that there may be numerical problems arising from the combination of their choice of system, XC functional and basis set parameters. The work of Sitkiewicz *et al* [106, 107] provides useful insight into the relative size of these errors in physical properties for different DFAs on the specific molecular data set tested. The lack of any efficient and transferable method for quantifying errors related to E^{XC} means that, in general, users must perform careful and expensive testing for their system and functional choice.

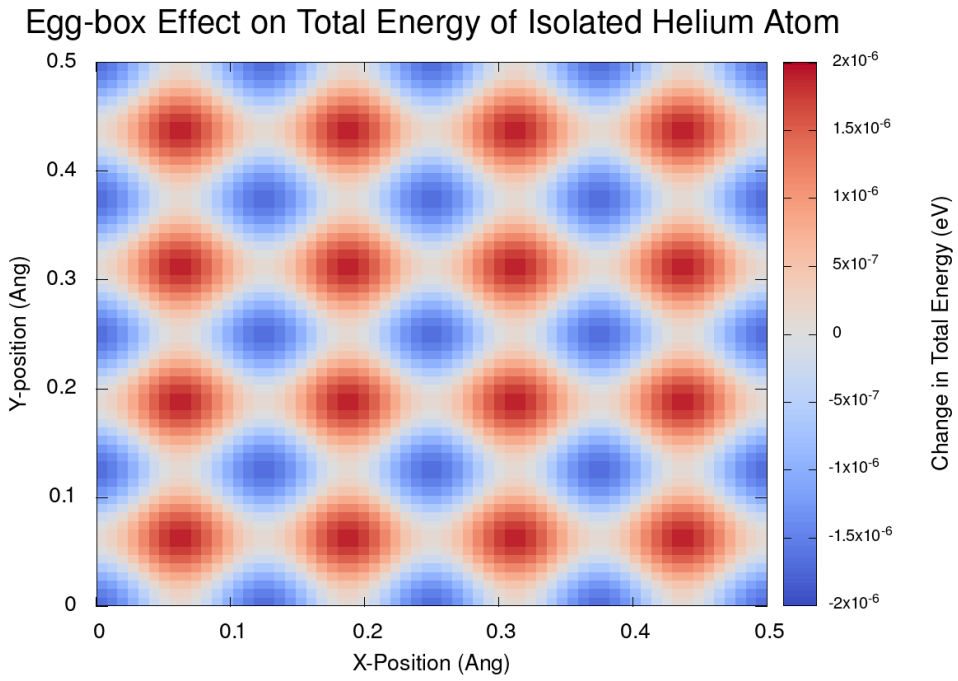

Figure 5.1: Change in the total energy of an isolated Helium atom as the atom is moved around a $(10\ \text{Å})^3$ cubic unit cell. An $(80)^3$ FFT grid was used to represent the density and a single k-point at the Gamma point was used for Brillouin zone integration. The calculation was performed with the PBE functional [2].

5.2 XC energy integration

The expression for the XC energy of the system calculated from a local/semi-local functional is,

$$\begin{aligned} E^{\mathrm{XC}} &= F\left[\rho(\boldsymbol{r}), |\nabla\rho(\boldsymbol{r})|, \nabla^2\rho(\boldsymbol{r}), \tau(\boldsymbol{r})\right] \\ &= \int_\Omega f^{\mathrm{XC}}\left(\rho(\boldsymbol{r}), |\nabla\rho(\boldsymbol{r})|, \nabla^2\rho(\boldsymbol{r}), \tau(\boldsymbol{r})\right)\, d\boldsymbol{r}, \end{aligned} \tag{5.1}$$

where ϵ^{XC} is the XC energy density function and Ω is the volume of the system. Equation 5.1 shows E^{XC} evaluated as a continuous integral of the density and other ingredients. However, in practice, the evaluation of E^{XC} is performed as a sum over a discrete set of N_{p} points. The value of the density (and other ingredients to the XC energy density) varies between the sampled points according to the basis functions, and therefore the contribution to the XC energy will also vary between the sampled points. The errors are generally assumed to be small enough to be negligible; however, as shown by Lehtola and Marques [35], this depends on the numerical behaviour of the XC functional. For many published XC functionals, the errors can be far from small.

5.2.1 "Direct" vs. "indirect" integration errors

A change in sampling affects the calculated energy in two ways. The first is as described above, a change in the real-space sampling, changes the values of the ingredients for f^{XC} which will change the final integrated value for E^{XC}, hence it has a direct effect on the systems total energy. The second effect comes via the XC potential, V^{XC}, through the minimisation of the total energy. The change in sampling leads to different values for V^{XC}, so that as the density and wavefunction states are varied to minimise the energy, a different ground-state density will be found, leading to different total energies. Here, the change in sampling indirectly affects the total energy through the other energy contributions in the Hamiltonian.

The calculated $V^{\mathrm{XC}}(\boldsymbol{r})$ is the derivative of E^{XC} with respect to a change in the density at that specific point $\boldsymbol{r}$. In order to calculate the sampling-error-free ground state, what is really required is the derivative of the contributions to E^{XC} across the *volume* of a grid point with respect to the change of the density across the volume of the grid point. With a sufficiently fine grid point sampling, the difference between the continuous integral and the discrete would be negligible, but with the default grids in most codes, this is not usually the case. An alternative but equivalent interpretation is that discretised V^{XC} includes high-frequency elements that cannot be represented on the grid, resulting in aliasing. The change in V^{XC} due to the sampling will lead to a change in the final converged density, and so will result in the other energy components of the Hamiltonian changing as well.

Sitkiewicz *et al* show that the choice of sampling in atomic basis set calculations can cause spurious oscillations in the total energy and its derivative as atoms are moved relative to each other [106]. The size of the oscillations is entirely dependent on the choice of XC functional, and for some functionals, the oscillations can only be mitigated by using grid sizes that are very expensive and far exceed those used in most routine calculations [107]. They show how this can lead to difficulties in calculating accurate molecular properties such as vibrational spectra. Similar issues occur in a plane-wave basis set.

5.2.2 XC integration errors in the plane-wave basis

The plane-wave basis set has a more straightforward expression for the evaluation of the XC energy than some of the schemes in atom-centred basis sets. Each of

the N_p grid points are given equal weight and the sum is calculated as,

$$E^{\mathrm{XC}} = \frac{\Omega}{N_{\mathrm{p}}} \sum_{i}^{N_{\mathrm{p}}} f^{\mathrm{XC}}\left(\rho(\boldsymbol{r}_i), \cdots\right) \tag{5.2}$$

The value of f^{XC} is evaluated at point $(\boldsymbol{r}_i)$ and is assumed to be constant across the volume of the grid point. This is inaccurate since the calculation involves non-linear functions of the density that must introduce Fourier components with wave-vectors that have a magnitude greater than the maximum frequency representable on the default FFT grid, i.e. $|G| > 2G_{\mathrm{cut}}$. The higher frequencies are therefore aliased to lower frequencies. A different choice of sampling points, that is, a constant offset applied to the position of all points in the grid, would lead to a different E^{XC} and V^{XC} due to a change in the sampling of the aliased frequencies [58]. As a result, the calculation of the energy can depend on the position of the real-space grid, and therefore translational invariance is lost.

This is illustrated in Figure 5.1 which shows the change in the energy of an isolated helium atom in a periodic box as it is moved around the unit cell. The results were obtained with the CASTEP code using the "on the fly" norm-conserving pseudo-potentials generated using the descriptors in the CASTEP database. The density and wavefunctions were converged until the change in the forces between successive iterations was less 1×10^{-8} eV/Å. This is excessive for most routine calculations, but was done to ensure the accuracy of the change in forces under displacement.

A change in sampling points by adding a constant offset to the grid positions is equivalent to each atom in the cell having the opposite shift applied while the grid remains stationary. It can be seen from Figure 5.1 that the energy is not constant as might be expected. Figures 5.2 and 5.3 show how the energy and force on the helium atom change as the atom is moved relative to the grid for different XC functionals. When no XC functional is used (or the XC contribution is zeroed), then there is no change in energy, i.e. the simulations are translationally invariant. However, when an XC functional is used, the energy changes and translational invariance is lost. This spurious change in energy gives rise to the rather odd predicted result of an isolated helium atom in its ground state experiencing a small, spontaneous, position-dependent force.

The results shown in Figure 5.2 are in line with the investigation of Lehtola and Marques[35] into the numerical behaviour of different functionals. The change in energy of the Perdew-Wang paramaterisation of LDA [3] is practically negligible, but for PBE [2] and r2SCAN[36], GGA and meta-GGA functionals respectively, the energy change is much greater. Lehtola and Marques also found the Perdew-

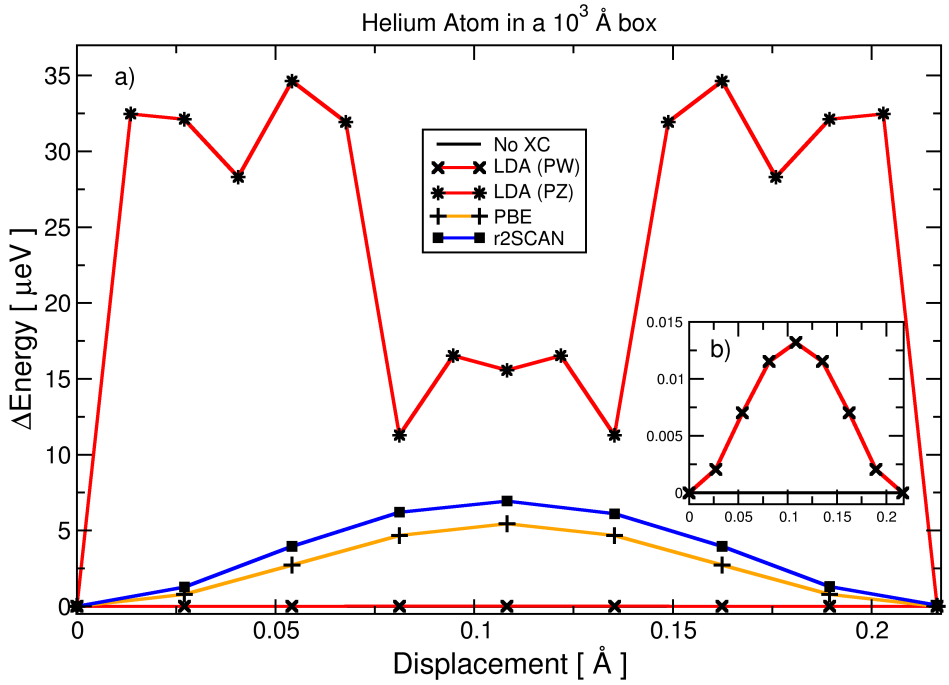

Figure 5.2: Change in the total energy of an isolated Helium atom as the atom is displaced along the (111) direction of an $(10\ \text{Å})^3$ cubic unit cell. A 80^3 FFT grid to represent the density and a single k-point at the Gamma point was used for Brillouin zone integration. Sub-figure *b)* is the same plot with the y-axis scaled to allow the LDA (PW) [3] result to be seen.

Zunger (PZ) parameterisation of the LDA functional [16] to have large numerical instability [35], failing to converge the energy with respect to grid resolution below $\approx 10\ \mu$eV. The results shown in Figure 5.2 supports their findings as the LDA-PZ parameterisation has the largest variation in energy of all the functionals tested and is seen to be the most non-linear in behaviour. This ill-behaviour is attributed to the functional form of LDA-PZ, which is a piecewise function of the density with a cusp.

There have been various methods of dealing with the consequences of the integration errors that have developed over the years, perhaps without it always being clear why these corrective schemes are necessary. The most obvious consequence is the violation of translational symmetry leading, as seen above, to net forces on the system. The spurious net force is clearly of concern in both isolated systems and crystal structures. This is often assumed to be the result of numerical noise and under-converged calculations. However, as shown in Figure 5.3, even very well converged systems can still have forces on the Centre of Mass (CoM). This force on the CoM is consistent with the energy change resulting from a change in sampling as the system moves relative to the discrete grid.

Permitting forces on the CoM mean that in a geometry optimisation or a Molecular Dynamics (MD) calculation, the entire system can spontaneously begin to

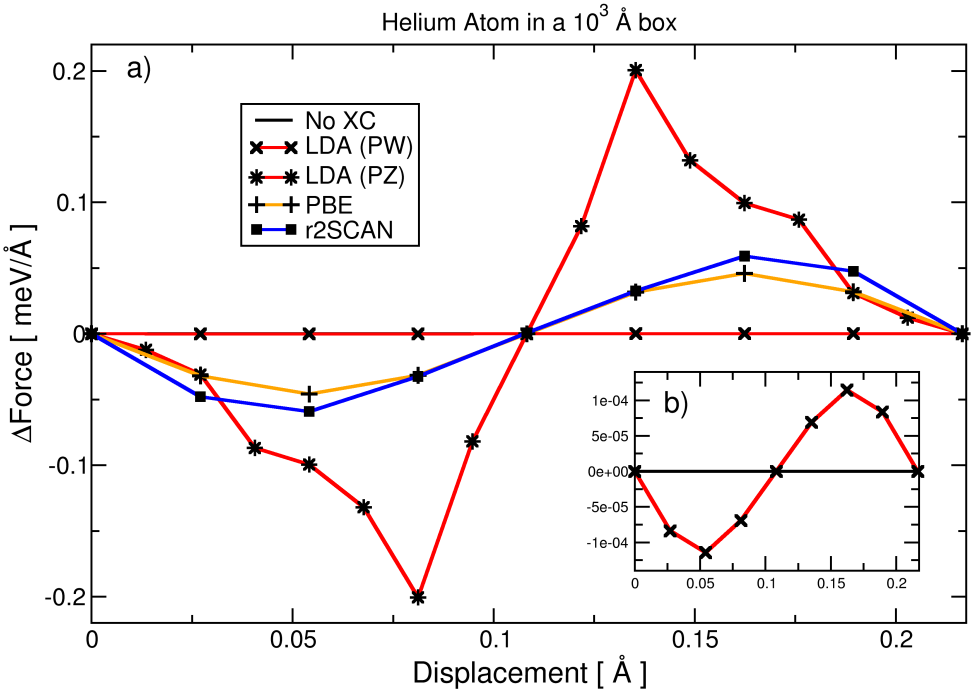

Figure 5.3: Change in the spurious force on an isolated Helium atom as the atom is displaced along the (111) direction of an $(10\ \text{Å})^3$ cubic unit cell. A 80^3 FFT grid to represent the density and a single k-point at the Gamma point was used for Brillouin zone integration. Sub-figure *b* is the same plot with the y-axis scaled to allow the LDA (PW) result to be seen.

drift which is non-physical. In most cases, this is corrected by determining the average force acting on all atoms and removing it from each individual atomic force, which therefore zeros the net force on the CoM. Although this fixes the CoM position, it fails to address the *cause* of the force on the CoM.

This spurious position-dependent effect is caused by the existence of preferred low-energy locations relative to the grid for each atom. This introduces systematic errors in the energy landscape, in turn creating systematic errors in forces and stresses, which in turn leads to complications in molecular dynamics and/or geometry optimisation calculations. For example, the preferred low-energy locations might not respect crystal symmetry, leading to difficulties in finding the correct geometries. Enforcing the crystal symmetry for known structures can aid in geometry optimisation, but if there is little symmetry or the symmetry is unknown, then the systematic errors must be overcome in some other way.

When performing lattice dynamics (phonon) calculations, further issues are caused by numerical errors in E^{XC}. Phonon calculations are calculating the derivative of the atomic forces due to an atomic displacement in the system, from which the dynamical matrix can be constructed and diagonalized, yielding the phonon modes. The necessity for an Acoustic Sum Rule (ASR) correction in almost all DFT phonon calculations to force the acoustic modes to have zero energy at

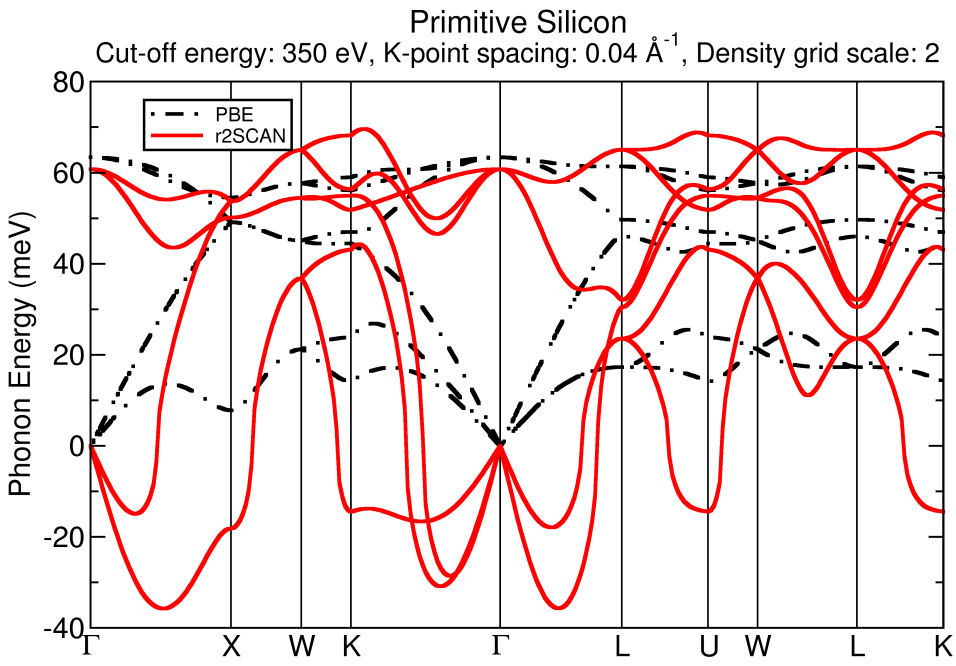

Figure 5.4: Phonon spectra calculated for a silicon primitive cell using the PBE and r2SCAN functionals. Calculated via finite displacement using the non-diagonal supercell method, equivalent to a $3 \times 3 \times 3$ q-point sampling grid.

Γ, is due to the discretisation of the contributions to E^{XC} on a real-space grid. This was noted by Gonze *et al* [100] when they first suggested their original ASR correction.

ASR corrections are similar to zeroing the CoM force, and some ASR corrections can be interpreted as accounting for the CoM force contribution to the force derivatives. An ASR correction is useful when there is slight numerical noise in the forces but does not adequately address the cause of the discrepancies [102]. When the error due to the XC integration is large, the energy landscape becomes very complicated, leading to severe problems when trying to take numerical derivatives of the forces. An ASR correction can still be applied to force the acoustic modes to zero at Γ, but the correction cannot account for the modes away from the point Γ, as seen in Figure 5.4. Figure 5.4 shows the phonon band structure calculated for silicon using the PBE functional and the r2SCAN functional using the nondiagonal supercell method [4] equivalent to a $3 \times 3 \times 3$ q-point sampling grid. Note that unlike in the previous chapter when changes were made to the grids to compensate for numerical instability, these phonon calculations used the default grid. Clearly the default grid is sufficient for the PBE calculations, but for r2SCAN, the numerical instability rears its head causing severe instabilities.

It is often found that phonon calculations require higher cut-off energies or finer grid sampling for the density, but the reason for this is not always properly appre-

ciated. Finite difference schemes that make use of supercells suffer particularly from the density sampling problem as the different discretisation in different supercells can lead to large changes in the XC integration error in each supercell, such that the overall error no longer cancels. For example, consider a system where the ground-state of the primitive cell is found using a particular cut-off wave-vector G_{cut} of the wavefunction, for which the corresponding FFT grid spacing would require a $9.2 \times 9.2 \times 9.2$ grid. Since every grid must have an integer number of points, the dimensions of the FFT grid for the wavefunction are rounded up to give a $10 \times 10 \times 10$ grid. The density grid is twice the size, so will require a $20 \times 20 \times 20$ FFT grid. For a $3 \times 3 \times 3$ supercell constructed from the primitive cell using the same wavefunction cut-off G_{cut}, the grid spacing now corresponds to a $27.6 \times 27.6 \times 27.6$ FFT grid. This is again rounded up, this time to a $28 \times 28 \times 28$ grid for the wavefunction and a $56 \times 56 \times 56$ FFT grid for the density. The rounding of the grids means the supercell's grid is *not* simply three times the original cell's grid dimensions (which would have been $30 \times 30 \times 30$), and the spacing between points will be different between the two cases. This change in grid spacing causes all real-space energy contributions to be altered slightly. However, because the XC energy is particularly sensitive to the real space grid used, there can be a very large change in E^{XC}. These changes can mean that the ground-state structure found for the primitive cell may not be equivalent to the ground-state structure in the supercell. This is particularly a problem for the non-diagonal supercell method as this method can generate supercells that involve rotations of the lattice vectors, which can therefore produce supercells where constructing an identical grid sampling to the primitive cell is impossible. In the case of diagonal supercells, the change in sampling can be avoided by ensuring that the same scaling is applied to the density grid as is applied to the lattice vectors. However, this does not avoid the systematic errors in the energy landscape that are induced by computing E^{XC} on a discrete grid. Displacing the atoms to perform a finite difference in the forces will mean that the finite derivative includes the error due to the sampling of E^{XC}. Simply increasing the cut-off energy and density grid may mask this issue, but at the cost of making phonon calculations even more computationally expensive.

The nature of phonon calculations involves perturbing the ground state structure, which will break some of the crystal symmetries. If symmetry has been enforced during geometry optimisation, the structure will have been optimised until the symmetry-constrained forces are zero, regardless of whether these symmetries are obeyed by the underlying density grid. Turning off the symmetry-constraints may therefore lead to non-zero forces even in the unperturbed system, meaning that the "relaxed" geometry is not in fact the ground state structure. This issue

is exacerbated if the CoM force is also zeroed, which is equivalent to enforcing continuous translational symmetry for the overall system.

Ordinarily, if the energy of the system decreases under an atomic perturbation, this indicates an imaginary phonon frequency and that the system is mechanically unstable under this perturbation. However, if the perturbation breaks symmetries, thus removing constraints on the energy landscape, this can allow the perturbed energy to be lowered due to numerical artefacts from the XC energy integration, regardless of the physical stability. This can lead to spurious imaginary phonon modes appearing in the calculated spectrum. This effect can clearly be seen in Figure 5.4.

These are relatively naïve calculations in terms of the basis set used, yet the PBE calculation still managed to produce physically reasonable results. However, the r2SCAN calculation returns a phonon spectrum with several imaginary modes (plotted as negative modes for convenience), suggesting that the FCC primitive cell for silicon is unstable, which is known to be physically incorrect. In this case the apparently unstable modes are not caused by structural instability, they are caused by a change in discretisation between primitive cell and super-cell and breaking of the crystal symmetry from the perturbation. Note that the only reason the modes are zeroed at the gamma point is because the force are "corrected" to remove a CoM force. In this case, applying an ASR correction has no effect on the modes.

In most cases, the errors due to the numerical integration error in E^{XC} are small enough to be negligible, particularly with a more simple XC functional such as the PW parametrisation of the LDA. When the XC integration error is large enough to cause issues, it can be mitigated by using higher cut-off energies or finer grids to represent the electron density. As noted in the literature [32, 33, 35], several modern density functionals have particular numerical pathologies. This means that it can be very difficult to eliminate numerical errors by increasing the basis set until results converge.

It is rarely obvious that a particular combination of system, functional, and basis set will cause numerical issues due to XC energy integration until after long dynamical or structural calculations have been run. This is especially true when the CoM force has been zeroed and crystal symmetry enforced, which can easily hide such problems until dynamical calculations of the system are performed or the crystal symmetry is broken by some perturbation, as in a phonon calculation. Clearly, it would be advantageous to know the uncertainty that might be introduced from the numerical integration error before running computationally expensive simulations.

5.3 Uncertainty Quantification

In this section the approach for quantifying the error related to the integration of the contributions to the XC energy is presented. As already demonstrated, these errors have important implications for the calculation of material properties. Therefore, it would be useful for a user of an *ab inito* material simulation software to have an indication of the level of error in the calculation of the total energy due to XC energy integration before performing long structural, dynamical, or phonon calculations. The aim is to provide an "on the fly" Uncertainty Quantification (UQ) method that is; (i) highly accurate, (ii) general to all XC functional approximations and all systems, i.e. requires little to no fine tuning, (iii) computationally cheap enough to allow the method to be used in live MD calculations and phonon calculations, warning a user when results may be affected.

The approach taken for the UQ method is to focus on the breaking of translation invariance, i.e. change in E^{XC} with the position of the FFT grid. Using perturbation theory, a method can be devised to compute the energy due to the change in the real-space grid position. To illustrate how this is done we shall start with a generic quantum system that obeys the following equation,

$$E_0 = \langle\psi_0|\,\hat{H}\,|\psi_0\rangle\,, \tag{5.3}$$

where $\hat{H}$ is the Hamiltonian of the system, $|\psi_0\rangle$ is the ground-state wavefunction of the system and E_0 is the ground state energy. Under a perturbation of strength λ, the energy will change. The change in states $\Delta\psi$ can be expressed as a Taylor expansion and truncated, in the usual fashion of perturbation theory (§3.3). The energy of the perturbed system, E_λ can therefore be expressed as,

$$\begin{aligned} E_\lambda = \langle\psi_\lambda|\,\hat{H}_\lambda\,|\psi_\lambda\rangle &= \langle\psi_0+\Delta\psi|\,\hat{H}+\Delta\hat{H}\,|\psi_0+\Delta\psi\rangle \\ &\approx \left\langle \psi_0+\lambda\frac{\mathrm{d}\psi}{\mathrm{d}\lambda}\right|\hat{H}+\Delta\hat{H}\left|\psi_0+\lambda\frac{\mathrm{d}\psi}{\mathrm{d}\lambda}\right\rangle. \end{aligned} \tag{5.4}$$

At the ground state of the unperturbed system, the energy is minimised with respect to all possible variations of the wavefunctions. Therefore, provided there is no explicit dependence of ψ on λ and the perturbation is small, using the same arguments as in Hellmann-Feynman [92], the $\frac{\mathrm{d}\psi}{\mathrm{d}\lambda}$ terms can be eliminated from both the state vectors, and any contributions to the Hamiltonian of the perturbed system. The Hamiltonian of the perturbed system can therefore be known exactly to all orders, and a Taylor expansion of the Hamiltonian is unnecessary. This

leaves us with,

$$E_\lambda \approx \langle\psi|\,\hat{H} + \Delta\hat{H}\,|\psi\rangle = \langle\psi|\,\hat{H}_\lambda\,|\psi\rangle\,. \tag{5.5}$$

In order to determine the energy of the perturbed system, we only have to apply the perturbed Hamiltonian to the unperturbed ground state. This argument can be applied in a very similar way to DFT, the change in energy due to a perturbation that changes the energy functional in a way that is known to all orders can be computed without having to find the minimised set of Kohn-Sham states and density under the perturbation, provided the perturbation is small. By "known to all orders", we mean that the change in the energy functional due to explicit dependence on the perturbation can be computed to all orders, *not including* any contributions from changes to the wavefunctions and density.

The perturbation we are interested in this case is a change in the position of real-space FFT sampling points. In plane-wave DFT, almost all the energy contributions are handled in reciprocal space. The XC energy contribution is the only contribution that must be evaluated explicitly at the real space grid points, and therefore is sensitive to the relative position of the grid. The energy change due to the real space position of the FFT grid being shifted by an offset $\Delta\mathbf{r}$ can therefore be calculated by Fourier interpolating the ground-state charge density onto an FFT grid offset by $\Delta\mathbf{r}$ and recalculating the XC energy. The change in XC energy between the shifted grid positions will be the same as the change in total energy were all the atoms in the system moved relative to the real space grid.

The charge density is transformed from the original FFT grid to the offset FFT grid by applying a phase factor to the terms of the Fourier expansion of the charge density and then performing an inverse transform. The value of the charge density at a particular point, $\boldsymbol{r} + \Delta\boldsymbol{r}$ can be written in terms of the original FFT grid expansion as follows:

$$\rho\left(\boldsymbol{r} + \Delta\boldsymbol{r}\right) = \sum_{\boldsymbol{G}}^{N_G} \left(a_{\boldsymbol{G}} e^{i\boldsymbol{G}\cdot\boldsymbol{r}}\right) e^{i\mathbf{G}\cdot\Delta\mathbf{r}}. \tag{5.6}$$

This displaced density is then used to compute E_Δ^{XC}, the XC energy of the system with a displaced grid,

$$E_\Delta^{\mathrm{XC}} = \frac{\Omega}{N_p} \sum_{\boldsymbol{r}_i} f^{\mathrm{XC}}\left(\rho\left(\boldsymbol{r}_i + \Delta\boldsymbol{r}\right), |\nabla\rho\left(\boldsymbol{r}_i + \Delta\boldsymbol{r}\right)|, \nabla^2\rho\left(\boldsymbol{r}_i + \Delta\boldsymbol{r}\right), \tau\left(\boldsymbol{r}_i + \Delta\boldsymbol{r}\right)\right). \tag{5.7}$$

If the theory described above is valid, the change in XC energy under this translation of the density will be the change in the total energy of the system under an equivalent rigid shift of the atoms.

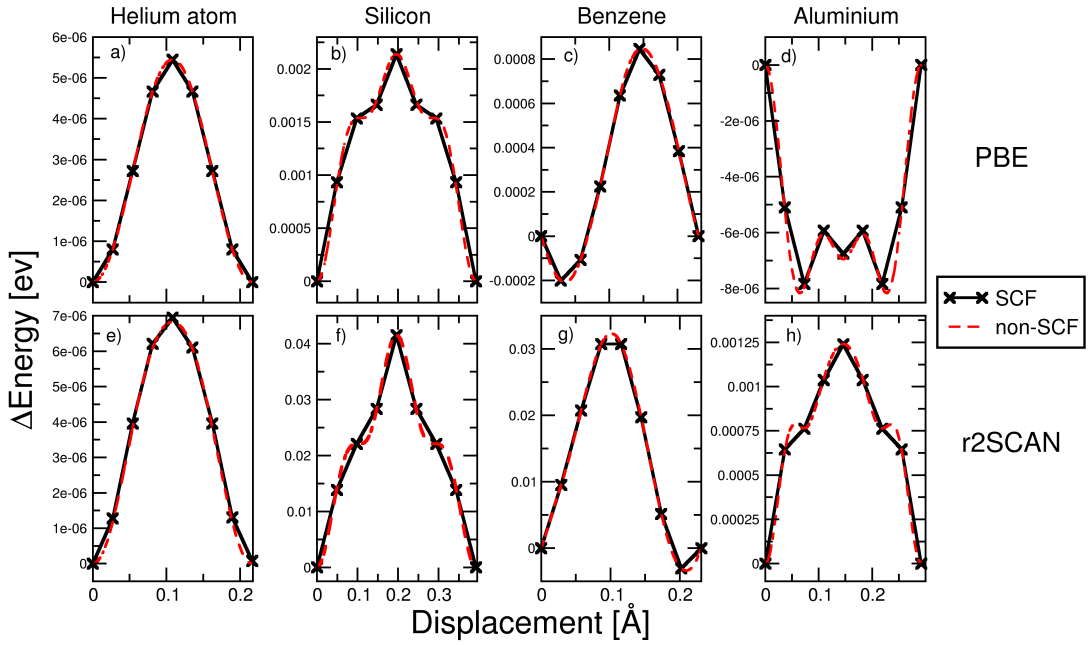

Figure 5.5: The change in energy, ΔE, calculated for various systems as the atoms are uniformly displaced by $\Delta\mathbf{r}$ along the (111) direction the width of a grid point. Each column shows results for the different systems tested; an isolated Helium atom (graphs a and e), a primitive silicon unit cell(graphs b and f), a Benzene molecule (graphs c and g) and aluminium (graphs d and h). For each system two XC functionals were tested, the top row shows the PBE results and the bottom row shows the r2SCAN results. Calculations for the same systems used consistent basis-sets and the norm-conserving pseudopotentials obtained using the same XC functional. The solid black line denotes values the change in the total energy post minimisation. The red dashed lines denotes change in XC energy from applying the offset to the density via interpolation as shown in equation 5.6 and non-self consistently recalculating the XC energy.

In Figure 5.5 there is a comparison of the change in energy found from rigidly shifting the atoms of various systems by $\Delta\mathbf{r}$ and reminimising the total energy, and the change in E^{XC} found from interpolating the density to an FFT grid that has had a $-\Delta\boldsymbol{r}$ rigid shift applied (which is an equivalent transformation). It can be clearly seen that the calculated changes in energy from both approaches are in excellent agreement across a range of different systems. This result means that we are able to probe the precision of the XC integration grid and provide an estimate of the uncertainty.

The interpolation method is general to all XC functionals, as all that is required is the translation of the density (and KED if necessary) to an offset FFT grid, from which any gradient terms can be calculated and E^{XC} re-evaluated. The interpolation method comes at the cost of a few additional Fourier transforms and the evaluation of the XC energy over the grid, but this is significantly cheaper than reminimising calculation with the atoms at different positions. As shown in

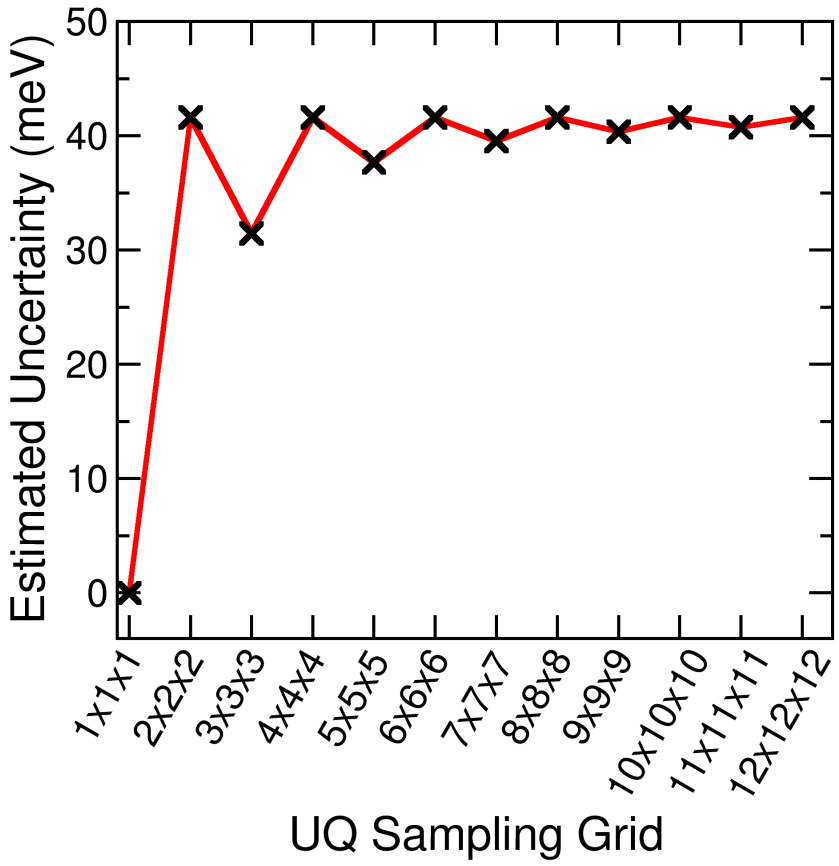

Figure 5.6: The convergence of the estimated uncertainty due to the XC energy integration as the sampling of each grid point volume is increase. The test system was a primitive unit cell of silicon using the r2SCAN functional with a cut-off energy of 350 eV, a k-point spacing of 0.04 and density grid scale of 2.

Figure 5.5, the method has been tested on a variety of systems, and in all cases the agreement between the methods is excellent.

So far, the methods described are not a complete UQ method. The issues from numerical errors in E^{XC} arise when an offset is applied to either the atoms or the real-space grid, violating translational symmetry. A useful heuristic test would therefore be the size of this violation, i.e. an estimation of the maximum change in energy under translation. With periodic boundary conditions, applying a grid offset that translates the grid points exactly so that they sit on another grid point will give the same discretisation of the density and therefore the same energy. It can be seen in Figure 5.1 that the oscillations in energy as the grids/atoms are moved have periodicity of the distance between grid points. Therefore, to sample the possible changes in energy under any arbitrary translation, only translations that span the volume of a single grid point must be considered. By sampling across the volume of the grid point using a regular grid mesh, we can sample the oscillations in energy, i.e. the violation of translational symmetry.

In Figure 5.6, this approach is used to estimate the maximum violation of trans-

lational symmetry found when using UQ sampling grids of different sizes. The same test system is used as in Figure 5.5(f), where the difference between the peak and the trough in that graph is approximately 41 meV, which is also the value at which the UQ test converges. It can also be seen from Figure 5.6 that the UQ sampling grid does not have to be very fine to give a reasonable estimate for the violation of translational symmetry and therefore the error in E^{XC}. Knowing the order of magnitude of the error is useful in deciding whether the error is at an acceptable level. Although the cost of determining the energy change from a particular translation is relatively inexpensive, using a very fine sampling for the UQ sampling grid can quickly become prohibitively expensive, involving hundreds of FFTs and evaluations of the XC energy. In practice, a $4 \times 4 \times 4$ UQ sampling grid was found to be sufficient to obtain a useful idea for the magnitude of the violation of translational symmetry, while keeping the computational cost low. Each sampling offset is independent of the others, meaning that the calculation of the full grid of offsets can be naturally parallelised. This allows the UQ test to remain inexpensive whilst still giving useful heuristic information.

5.4 Correcting the XC energy error

The Uncertainty Quantification (UQ) test described in the previous section can be used to provide the user of a plane-wave DFT software with information on how large the violation of translation symmetry is for the given calculation. The advantage of the UQ test is that the user now has a single metric from a relatively cheap test, which can then be used to tune their choice of basis set and XC functional without needing to run expensive calculations, which may eventually fail and need to be repeated. Different material properties of interest may require different levels of accuracy, and it is not always obvious whether that level of accuracy can be achieved. For example, the magnetic anisotropy energy is often $\mathcal{O}(10^{-6})$ eV for weakly anisotropic magnetic materials, and we have already seen (e.g. Figure 5.6) that the errors due to the egg-box effect can be four orders of magnitude greater than this. This UQ can inform the user if such a level of accuracy has been achieved, and if not, then the user can then take action to address the cause of the error in the XC energy integral and thus reduce the violation of translational invariance.

Since in this thesis the focus has been on the plane-wave approach, and therefore periodic boundary conditions, the XC energy integral is performed by Fourier-expanding the XC energy density, and the integral over the simulation cell is simply the zeroth order term of this Fourier expansion. Increasing the order of the expansion simply requires increasing the number of points in the Fourier-space

sampling grid, which is equivalent to using a finer real-space sampling. As finer and finer sampling is used, the numerical evaluation of the integral, and hence the value of E^{XC}, approaches the exact result. Moreover, $V^{\mathrm{XC}}(\boldsymbol{r})$ at each point will be more accurate and better represent the *change* in energy with respect to the density, as more high-frequency components of $V^{\mathrm{XC}}(\boldsymbol{r})$ will be correctly sampled, with correspondingly reduced aliasing in lower frequencies. The combination of these effects should lead to improved representation of the ground state and the physics of the system. It will reduce the magnitude of symmetry violations, including both crystal symmetry and translational symmetry, generating more accurate results.

In plane wave codes, there are a couple of common approaches that can be used to increase the sampling resolution of E^{XC}, neither of which is ideal, as will be explained. The first common approach is to increase the plane-wave cut-off energy, i.e. increase the number of basis functions in the Fourier expansion of the wavefunction. This has the side effect of significantly increasing the computational cost of every operation in the Hamiltonian, increasing the memory requirements for the calculation, and adding additional Fourier components to the density, and therefore to the XC integral. These extra components will add higher frequency terms, which should reduce in magnitude, but may also make the reduction of numerical artefacts more difficult.

The other common approach is to increase the fineness of the grid used for the density, leaving the basis functions for the wavefunctions untouched. This only increases the cost of operations involving the density and the construction of local potentials, which is computationally cheaper in both number of operations and the memory required. The caveat is that, although this will improve the XC terms, it costs a considerable amount of wasted effort/memory for many of the other terms in the Hamiltonian. There are also issues with this approach arising from using pseudo-potentials.

Both the Projector Augmented Wave method (PAW) [76] and Ultrasoft pseudo-potential method (USP) [77] add additional "augmentation charge" terms to the valence density which can require the density grid to be more than twice as fine as the wavefunction basis in order to be accurately represented (traditional norm-conserving pseudo-potentials [71] do not have these augmentation terms). Many pseudo-potentials also make use of nonlinear core corrections (NLCC) [78] when computing the XC energy integral for a better representation of the XC interaction between the core charges and the electrons treated as valence. The core charges are interpolated from a spherically symmetric radial function onto the density grid. Both of these pseudo-potential features can mean that increasing the scale of the density grid will have a similar effect to increasing the cut-off

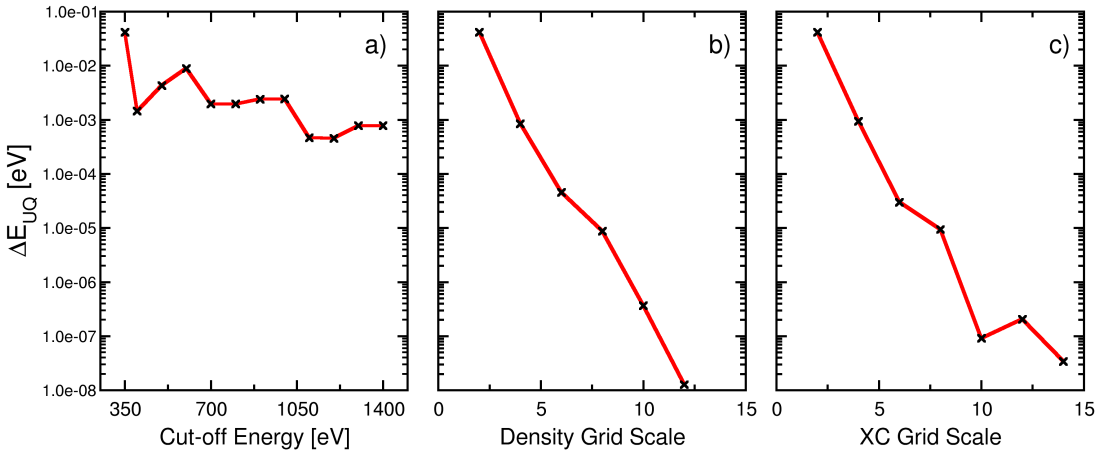

Figure 5.7: The change in the estimated uncertainty of the XC energy integration as the grid is altered in different ways. The base system is the primitive unit cell of silicon using; a cut-off energy of 350 eV, a density grid scale of 2 and a XC grid scale of 2. Each of the subplots shows the change in estimated uncertainty as; a) the cut-off energy is increased; b) the density grid scale is increased; c) the XC grid scale is increased. In each case the other parameters have been fixed at those used for the first data point.

energy, i.e. increasing the number of terms in the density expansion and therefore the XC energy, making the reduction of numerical artefacts harder.

The alternative approach proposed here, is to increase only the fineness of the grid for the XC part of the calculation. Every other term in the Hamiltonian can be handled on a grid which will accurately represent the density (including any augmentation from the PAW/USP methods). When computing the XC terms, the NLCC terms should be interpolated onto the density grid, and then we can use Fourier extrapolation to move the real-space density to a much finer grid, i.e. Fourier transform the density to reciprocal space, pad the Fourier expansion with extra zeros up to the highest frequency we want to use in the E^{XC} computation, and then back transform the density to real space on a much finer grid. The contributions to E^{XC} and V^{XC} are then computed on this finer grid in real-space, transformed to Fourier space where the potential is truncated beyond the highest frequency components representable on the original density grid, and then back transformed to real space on the original density grid. This truncation has no effect on the XC energy integral computed by multiplying the density and the potential compared to when they are computed on the finer XC grid, but it removes any aliasing of high-frequency components represented on the XC grid into the potential on the original density grid.

A comparison of these approaches is shown in Figure 5.7 where it is shown how the error estimated by the UQ test, ΔE_{UQ}, changes with the fineness of the

grid when increased by each of the methods described above. For the UQ tests a $4 \times 4 \times 4$ UQ sampling grid was used to estimate the error. All approaches were found to be effective in reducing the estimated uncertainty. The approaches of increasing the density grid scale and the XC grid scale are equally and highly effective in reducing the estimated uncertainty. Increasing the cut-off energy does cause a reduction in the estimated error; however, Figure 5.7(a) shows that the cut-off energy must be quadrupled to reduce the error by one order of magnitude. The cut-off wave vector for the plane-waves, G_{cut}, scales as the root of the cut-off energy, E_{cut}, therefore quadrupling the cut-off energy doubles the size of the density grid. The calculation with a cut-off energy of 1400 eV with a density grid scale of 2 will use the same actual density grid for the XC calculation as that used with a cut-off energy of 350 eV but with a density grid scale or XC grid scale of 4. The estimated uncertainty in these calculations is very similar, but increasing the cut-off energy by a factor of 4 causes the calculation to take ~ 8 times as long to complete. Increasing the density grid or the XC grid scale by an extra factor of 2 only increased the cost by a factor of $\sim 40\%$ and $\sim 20\%$ respectively, and so clearly these are much more efficient approaches at reducing the uncertainty compared to the cut-off energy. Figure 5.7(a) only shows the estimated uncertainty for cut-off energies in the range of $350 - 1400$ eV. Further increases in the cut-off energy would further reduce the uncertainty; however, the additional computational cost is dramatic and unjustified.

Increasing the density grid scale compared to increasing the XC grid scale has a comparable effect in terms of accuracy but also comes with additional computational cost. It has already been shown in Section 5.3 Figure 5.6 that the effect of the violation of translation symmetry was ≈ 41 meV in the original calculation without a change in the grid scaling. In Figure 5.7, it can be seen that a grid scale of 8 reduces the error to $\mathcal{O}(10^{-5})$ eV for both the density grid scale calculation and the XC grid scale. Increasing the scale of the density grid to 8 increased the time required for the energy minimisation calculation by a factor of $\sim 5.5\times$, whilst increasing the scale of the XC grid to 8 increased the time required by only a factor of $\sim 2.4\times$.

Increasing either the cut-off energy, the density grid scale or the XC grid scale leads to the total energy, forces and stresses converging to *different* values. Initially, this might seem worrying, but it is to be expected. As explained above, increasing the XC grid scale *only* improves the representation of the XC energy contributions and the XC potential. Increasing the density grid scale improves the representation of all the density and potential terms in the calculation, including the NLCC and augmentation charge terms, which will include additional contributions to the energy. Increasing the cut-off energy introduces additional

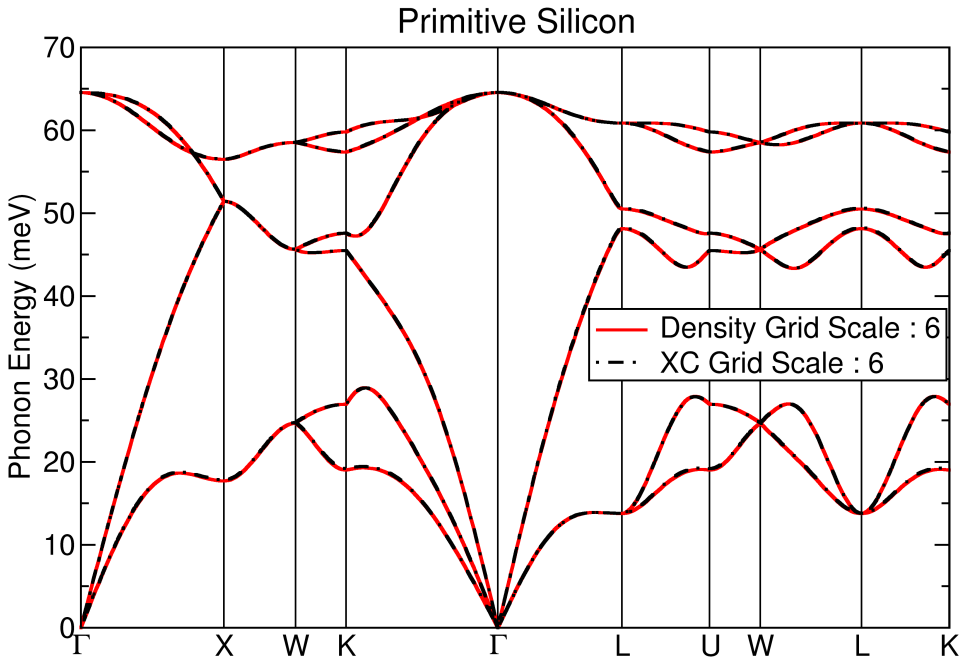

Figure 5.8: Phonon band structure calculated for a silicon primitive cell with the r2SCAN functional. Calculated via finite displacement using the non-diagonal supercell method [4] equivalent to a $3 \times 3 \times 3$ q-point sampling grid. All other parameters are the same as those used in Figure 5.4.

plane-waves into the wavefunction and the density, waves which were previously assumed to have zero weighting. This will add extra contributions to every term in the Hamiltonian and will therefore change the total energy calculated.

To illustrate the benefit of using a separate XC grid, the calculation of the phonon band structure presented in Figure 5.4 was repeated using a density grid scale of 6 and also with an XC grid scale of 6. Without increasing the fineness of the grid, the r2SCAN calculation gives imaginary phonon modes with maximum energy of ~ -40 meV, which is the same magnitude as the energy error the UQ test estimates. Increasing the grid scales to 6 can be seen in Figure 5.7 to reduce the estimated error of the energy to be below 10^{-4} eV, i.e., an order of magnitude smaller than the tolerance in the energies of the phonon modes. In both calculations, these imaginary modes are now real, and the difference between the phonon band structure calculated with either approach is negligible; see Figure 5.8. The UQ test allows an informed decision to be made on how fine a grid is needed, in order to reduce the numerical XC integration artefacts enough for accurate phonon calculations.

It is worth noting again that the UQ test relies only on the ground-state density for a particular atomic configuration. Thus, it can be used to tune the fineness of the XC grid for the desired accuracy *before* before performing any dynamical or structural calculations. This step requires multiple energy minimisation cal-

culations, with the atoms in a specific configuration, to get the ground state at different XC grid scales, but this is no worse than the convergence calculations required for the choice of cut-off energy and k-point sampling.

It is clear from the uncertainty estimates presented in Figure 5.6 that the use of the finer grid, only to calculate E^{XC} and V^{XC} is an effective method to improve the numerical accuracy of the calculations while minimising the additional computational cost. It has also been shown that when comparing the phonon band structure presented in Figure 5.8, there is no noticeable difference in the physical predictions compared to the existing approach of increasing the grid scale of the density grid for every energy contribution, while the XC grid method is cheaper to compute. The method of increasing the scale of the XC grid was used in the previous chapter with great effect when comparing phonon modes calculated via density functional perturbation theory and finite displacement.

5.5 Conclusions

A new Uncertainty Quantification (UQ) approach has been developed and presented for plane-wave DFT calculations that allows an estimation of the violation of translation symmetry due to the numerical integration of the exchange-correlation (XC) energy, sometimes referred to as "the egg-box effect". The novel UQ method fulfils all of the desired requirements of being an accurate, efficient and general purpose for all systems and exchange-correlation functionals. This is done by Fourier interpolating the ground state density to a set of shifted grid positions and re-evaluating the change in XC energy at these grid offsets. This is found to be in near-exact agreement with the change in total energy from an equivalent displacement of the entire system.

The results of using our UQ approach are in keeping with those seen elsewhere in the literature, i.e. the size of the integration error is highly dependent on; the system of interest, the choice and size of the basis set, the choice of XC functional. Performing this analysis at an early stage of a workflow can inform on the expected accuracy of subsequent calculations.

Further, a slightly different approach to improving the XC energy integration is suggested. By selectively computing the XC energy and its corresponding potential on a finer grid, via Fourier extrapolation, the energy integration error can be reduced to a level deemed appropriate by the user, without all of the additional overhead of increasing the cut-off energy and the fineness of the density grid. Coupled with the uncertainty quantification method, inaccuracies related to the XC integration error (or the egg-box effect) can confidently be avoided

with minor additional computational cost. This work offers a promising pathway towards improving accuracy in a diverse range of materials modelling applications.

Chapter 6

Elastic Constants from DFPT using meta-GGAs

This chapter covers the implementation of the necessary additional terms to calculate the Elastic constants tensor from DFPT using a meta-GGA functional. The elastic constants tensor being a response function of a system to strain, relating the internal stress in a material to an applied deformation, or strain. The chapter follows a very similar structure to Chapter 4, first, the derivation of the additional terms required for a meta-GGA functional is covered, and then the implementation is verified by calculating the elastic constants via DFPT and finite displacement calculations for a test system. The method is used to examine the accuracy of the predictions for elastic constants made using mGGA functionals and is compared to other functionals and other theoretical methods. The mGGA functional r2SCAN is found to provide predictions in excellent agreement with experimental results in the literature, far exceeding the accuracy of the tested LDA and GGA functionals.

6.1 Introduction

Elastic constant tensors are fundamental properties that describe a material's response to mechanical stress, providing insights into its stiffness and stability. Accurately predicting these tensors is crucial for designing materials with desired mechanical properties. DFT particularly within the LDA and GGA frameworks, has been extensively used for such predictions [108, 109]. However, these approximations often yield elastic constants that deviate from experimental values, for instance, LDA tends to overbind atoms, which can lead to overestimated elastic constants, while GGA, though a theoretical improvement, tends to underbind, leading to underestimated elastic constants. Both formalisms lack the precision

required for materials design, more advanced theoretical methods can yield more accurate results but at far greater computational cost [110, 111, 112].

The theoretical foundation for calculating elastic constants within a quantum mechanical framework was significantly advanced by Nielsen and Martin in the 1970s [81, 82]. They developed a comprehensive theory of stress within DFT, enabling the computation of stress tensors and, subsequently, elastic constants from first principles. In 2005, Hamann *et al.* introduced a novel approach to calculating elastic constants using Density Functional Perturbation Theory (DFPT) [93, 98]. This method reformulated the problem by introducing a reduced coordinate metric tensor, allowing for the efficient and accurate determination of elastic constants without relying solely on finite strain techniques. This work provides a more robust framework which is less sensitive to numerical noise.

Furthermore, the development of meta-Generalised Gradient Approximation (meta-GGA) functionals has shown promise in enhancing the accuracy of elastic constant predictions. Studies have demonstrated that meta-GGA functionals can provide more reliable elastic constants compared to traditional LDA and GGA approaches, [110, 111]. However, one of the limitations of these studies is that they have been forced to use finite strain techniques to calculate the elastic constants, which, as has been mentioned, are particularly sensitive to numerical noise.

As has become a theme of this thesis, there can be significantly more numerical noise in mGGA calculations than those based in lower levels of theory. The aim of this chapter is therefore to derive the additional terms required to perdict the elastic constants of a material within the mGGA formalism using DFPT. A comparison will then be made for a limited set of materials against predicted values from other levels of theory in the literature and to experimental results.

6.2 Calculating the Elastic Constants

A description of the formalism for the elastic constant tensor was given in section 3.2.3. There, the elastic constants tensor, $C^{\alpha\beta\gamma\delta}$, is defined as the tensor that gives the linear relation between a deformation or strain, $\eta_{\gamma\delta}$ applied to a material and the resultant stress, $\sigma^{\alpha\beta}$,

$$\sigma^{\alpha\beta} = C^{\alpha\beta\gamma\delta}\eta_{\gamma\delta}. \tag{6.1}$$

Expressed as derivative of the total energy the elastic constants tensor can be written as,

$$C^{\alpha\beta\gamma\delta} = \Omega^{-1}\frac{\mathrm{d}^2 E}{\mathrm{d}\eta_{\alpha\beta}\mathrm{d}\eta_{\gamma\delta}}. \tag{6.2}$$

As was explained in section 3.2.3, the total derivative of the energy with respect to strain includes contributions from atomic relaxations under strain, expressed as partial derivatives of the total energy, which are computable by DFPT, the elastic constants tensor is,

$$C^{\alpha\beta\gamma\delta} = \bar{C}^{\alpha\beta\gamma\delta} - \Omega^{-1}\sum_{I,J}\Lambda_I^{\alpha\beta\mu}\left(D^{-1}_{\boldsymbol{q}=0,,I,J}\right)_{\mu\nu}\Lambda_I^{\gamma\delta\nu} \tag{6.3}$$

where, $D_{\boldsymbol{q}=0,I,J} = \frac{\partial^2 E}{\partial R_{I,\mu}\partial R_{J,\nu}}$ is dynamical matrix at $\boldsymbol{q}=0$, $\Lambda_I^{\alpha\beta\gamma} = \frac{\partial^2 E}{\partial\eta_{\alpha\beta}\partial R_{I,\gamma}}$ is the force-response internal-strain tensor i.e. the change in the atomic forces under a strain, $\bar{C}^{\alpha\beta\gamma\delta} = \Omega_0^{-1}\frac{\partial^2 E}{\partial\eta_{\alpha\beta}\partial\eta_{\gamma\delta}}$ is the frozen ion elastic constants tensor. To compute the elastic constant tensor, these 3 sets of partial derivatives of the energy are required to computed the elastic constants from DFPT.

The dynamical matrix we have already shown how to compute in Chapter 4. The remaining two partial derivatives are the subject of this section. Expressions for these partial derivatives can be derived from the non-variational expression for second-order derivatives given in equation 3.69. The frozen-ion elastic constants are obtained by substituting a pair of strain perturbations for μ and λ into equation 3.69, giving

$$\begin{aligned}\frac{\partial^2 E^{tot}}{\partial\eta_{\alpha\beta}\partial\eta_{\gamma\delta}} =& \sum_b^{\mathrm{occ}}\left\langle\psi_b^{(0)}\middle|\frac{\partial^2}{\partial\eta_{\alpha\beta}\partial\eta_{\gamma\delta}}\left(\hat{T}+\hat{V}_{\mathrm{loc}}^{\mathrm{ext}}+\hat{V}_{\mathrm{nl}}^{\mathrm{ext}}\right)\middle|\psi_b^{(0)}\right\rangle + \\ & \sum_b^{\mathrm{occ}}\left\langle\psi_b^{(\eta_{\alpha\beta})}\middle|\frac{\partial\hat{H}}{\partial\eta_{\gamma\delta}}\middle|\psi_b^{(0)}\right\rangle + \sum_b^{\mathrm{occ}}\left\langle\psi_b^{(0)}\middle|\frac{\partial\hat{H}}{\partial\eta_{\gamma\delta}}\middle|\psi_b^{(\eta_{\alpha\beta})}\right\rangle + \left.\frac{\partial^2 E^{\mathrm{H}}}{\partial\eta_{\alpha\beta}\partial\eta_{\gamma\delta}}\right|_{\rho^{(0)}} \\ & + \frac{\partial^2 E^{\text{Ion-Ion}}}{\partial\eta_{\alpha\beta}\partial\eta_{\gamma\delta}} + \left.\frac{\partial^2 E_\tau^{\mathrm{ext}}}{\partial\eta_{\alpha\beta}\partial\eta_{\gamma\delta}}\right|_{\tau^{(0)}} + \left.\frac{\partial^2 E^{\mathrm{XC}}}{\partial\eta_{\alpha\beta}\partial\eta_{\gamma\delta}}\right|_{\rho^{(0)},\tau^{(0)}},\end{aligned} \tag{6.4}$$

where $\psi_b^{\eta_{\alpha\beta}}$ is the first order response of the wavefunction to the strain $\eta_{\alpha\beta}$.

An expression for the force-response internal strain tensor can be derived by substituting a strain perturbation and an atomic displacement for μ and λ, giving

$$\begin{aligned}\frac{\partial^2 E^{tot}}{\partial\eta_{\alpha\beta}\partial R_{I,\gamma}} =& \sum_b^{\text{occ}} \left\langle \psi_b^{(0)} \middle| \frac{\partial^2}{\partial\eta_{\alpha\beta}\partial R_{I,\gamma}} \left(\hat{T} + \hat{V}_{\text{loc}}^{\text{ext}} + \hat{V}_{\text{nl}}^{\text{ext}}\right) \middle| \psi_b^{(0)} \right\rangle + \\ & \sum_b^{\text{occ}} \left\langle \psi_b^{(\eta_{\alpha\beta})} \middle| \frac{\partial \hat{H}}{\partial R_{I,\gamma}} \middle| \psi_b^{(0)} \right\rangle + \sum_b^{\text{occ}} \left\langle \psi_b^{(0)} \middle| \frac{\partial \hat{H}}{\partial R_{I,\gamma}} \middle| \psi_b^{(\eta_{\alpha\beta})} \right\rangle + \left.\frac{\partial^2 E^{\text{H}}}{\partial\eta_{\alpha\beta}\partial R_{I,\gamma}}\right|_{\rho^{(0)}} \\ & + \frac{\partial^2 E^{\text{Ion-Ion}}}{\partial\eta_{\alpha\beta}\partial R_{I,\gamma}} + \left.\frac{\partial^2 E_\tau^{\text{ext}}}{\partial\eta_{\alpha\beta}\partial R_{I,\gamma}}\right|_{\tau^{(0)}} + \left.\frac{\partial^2 E^{\text{XC}}}{\partial\eta_{\alpha\beta}\partial R_{I,\gamma}}\right|_{\rho^{(0)},\tau^{(0)}}. \end{aligned} \tag{6.5}$$

Thankfully, the terms needed to compute these partial derivatives in the LDA and GGA schemes have already been derived and published by Hamman *et al* [93, 98]. Due to the complexity of the necessary derivatives, the only implementation of this method was that of the original publication until the work carried out in this thesis, where the method was implemented in CASTEP for LDA and GGA functionals.

The aim of this chapter is to enable the computation of elastic constants via DFPT using mGGA functionals, for which the only unknown contributions are the derivatives of the additional terms in the mGGA formalism. Specifically, the derivatives of the energy arising from the differential part of the external potential operator, E_τ^{ext}, and the XC energy E^{XC}. Also required is the partial derivative of the Hamiltonian under strain, $\frac{\partial \hat{H}}{\partial\eta_{\alpha\beta}}$, the partial derivative of the Hamiltonian under a commensurate atomic displacement has already been derived in the previous chapter. The first-order response of the wavefunction to the strain, $\psi_b^{(\eta_{\alpha\beta})}$, can be determined using the variational solver of the Green's function solver for the Sternheimer equations.

We shall proceed with this chapter's aim by defining the derivative of general system parameters, such as the cell volume, or the reciprocal lattice vectors, which we can then refer back to when deriving derivatives of the more complicated objects, like the KED or the XC potentials.

6.2.1 System Parameters Under Strain

The strain tensor, $\eta_{\alpha\beta}$, defines a deformation as a "stretching" of space that transforms a point in the system to another point,

$$r_\alpha \to r_\alpha = \left(\delta^{\alpha\beta} + \eta_{\alpha\beta}\right) r_\beta, \tag{6.6}$$

where $\delta^{\alpha\beta}$ is the Kronecker delta. For the purposes of perturbation theory, we enforce that the strain tensor is symmetric, i.e. $\eta_{\alpha\beta} = \eta_{\beta\alpha} = \frac{1}{2}\left(\eta_{\alpha\beta} + \eta_{\beta\alpha}\right)$. The

strain tensor is a dimensionless quantity; therefore, one useful property of the derivatives with respect to strain is that the derivatives of an object with respect to strain must have the same dimensionality as the original object, making it easier to spot when an error has occurred.

Under this stretching of space, we can derive the derivatives of various system parameters. Here, the first and second derivatives under strain are given for:

- Real-space vectors, R_μ:

$$\frac{\mathrm{d}R_\mu}{\mathrm{d}\eta_{\alpha\beta}} = \frac{1}{2}\left(\delta^{\mu\alpha}R_\beta + \delta^{\mu\beta}R_\alpha\right), \tag{6.7}$$

$$\frac{\mathrm{d}^2R_\mu}{\mathrm{d}\eta_{\alpha\beta}\mathrm{d}\eta_{\gamma\delta}} = \frac{1}{4}\left(\delta^{\mu\alpha}\left(\delta^{\beta\gamma}R_\delta + \delta^{\beta\delta}R_\gamma\right) + \delta^{\mu\beta}\left(\delta^{\alpha\gamma}R_\delta + \delta^{\alpha\delta}R_\gamma\right)\right). \tag{6.8}$$

- Reciprocal-space vector, G^μ:

$$\frac{\mathrm{d}G^\mu}{\mathrm{d}\eta_{\alpha\beta}} = -\frac{1}{2}\left(\delta^{\mu\alpha}G^\beta + \delta^{\mu\beta}G^\alpha\right), \tag{6.9}$$

$$\frac{\mathrm{d}^2G^\mu}{\mathrm{d}\eta_{\alpha\beta}\mathrm{d}\eta_{\gamma\delta}} = \frac{1}{4}\left(\delta^{\mu\alpha}\left(\delta^{\beta\gamma}G^\delta + \delta^{\beta\delta}G^\gamma\right) + \delta^{\mu\beta}\left(\delta^{\alpha\gamma}G^\delta + \delta^{\alpha\delta}G^\gamma\right)\right). \tag{6.10}$$

- Modulus of Reciprocal-space vector, $|\boldsymbol{G}|$:

$$\frac{\mathrm{d}\,|\boldsymbol{G}|}{\mathrm{d}\eta_{\alpha\beta}} = \frac{\mathrm{d}\sqrt{G^\mu G^\mu}}{\mathrm{d}\eta_{\alpha\beta}} = -\frac{1}{2}\frac{G^\mu}{|\boldsymbol{G}|}\left(\delta^{\mu\alpha}G^\beta + \delta^{\mu\beta}G^\alpha\right) \tag{6.11}$$

$$= -\frac{G^\alpha G^\beta}{|\boldsymbol{G}|}, \tag{6.12}$$

  where the final expression is found by summing over the μ index. For future quantities this will be done when possible, without explanation to give the simplified expressions for the derivatives. The second derivative can then be found as,

$$\frac{\mathrm{d}^2\,|\boldsymbol{G}|}{\mathrm{d}\eta_{\alpha\beta}\mathrm{d}\eta_{\gamma\delta}} = \frac{1}{2\,|\boldsymbol{G}|}\left(\left(\delta^{\alpha\gamma}G^\delta + \delta^{\alpha\delta}G^\gamma\right)G^\beta + G^\alpha\left(\delta^{\beta\gamma}G^\delta + \delta^{\beta\delta}G^\gamma\right)\right) - \frac{G^\alpha G^\beta G^\gamma G^\delta}{|\boldsymbol{G}^3|}. \tag{6.13}$$

- Unit cell volume, Ω,

$$\frac{\mathrm{d}\Omega}{\mathrm{d}\eta_{\alpha\beta}} = \delta^{\alpha\beta}\Omega, \tag{6.14}$$

$$\frac{\mathrm{d}^2\Omega}{\mathrm{d}\eta_{\alpha\beta}\mathrm{d}\eta_{\gamma\delta}} = \delta^{\alpha\beta}\delta^{\gamma\delta}\Omega. \tag{6.15}$$

- Basis functions and structure factors are invariant under strain:

$$\frac{\mathrm{d}e^{i\boldsymbol{G}\cdot\boldsymbol{R}}}{\mathrm{d}\eta_{\alpha\beta}} = iG^{\gamma}\left(\delta^{\alpha\gamma}R_{\beta}+\delta^{\beta\gamma}R_{\alpha}\right)e^{i\boldsymbol{G}\cdot\boldsymbol{R}} - i\left(\delta^{\alpha\gamma}G^{\beta}+\delta^{\beta\gamma}G^{\alpha}\right)R_{\gamma}e^{i\boldsymbol{G}\cdot\boldsymbol{R}} \tag{6.16}$$

$$= i\left(G^{\alpha}R_{\beta}+G^{\beta}R_{\alpha}\right)e^{i\boldsymbol{G}\cdot\boldsymbol{R}} - i\left(G^{\alpha}R_{\beta}+G^{\beta}R_{\alpha}\right)e^{i\boldsymbol{G}\cdot\boldsymbol{R}} = 0. \tag{6.17}$$

6.2.2 Change of Operators and Physical Quantities under strain

Above we have shown how strain perturbations change the system parameters, these then have a knock-on affect on the operators such as the gradient operator, and the construction of various physical quantities such as the density and the KED. Using the definition of these first and second derivatives of:

- Gradient operator, ∇^{μ}: The real-space gradient of a function can be calculated by transforming the function to reciprocal-space, multiplying each the functions in the plane-wave expansion by i times the reciprocal-space lattice vector of that basis function, as shown in Equation 2.48, and then back transforming to real-space. The derivatives of the gradient operator under strain are therefore very similar to the derivatives of the reciprocal-space lattice vectors,

$$\frac{\mathrm{d}\nabla^{\mu}}{\mathrm{d}\eta_{\alpha\beta}} = -\frac{1}{2}\left(\delta^{\mu\alpha}\nabla^{\beta}+\delta^{\mu\beta}\nabla^{\alpha}\right), \tag{6.18}$$

$$\frac{\mathrm{d}^2\nabla^{\mu}}{\mathrm{d}\eta_{\alpha\beta}\mathrm{d}\eta_{\gamma\delta}} = \frac{1}{4}\left(\delta^{\mu\alpha}\left(\delta^{\beta\gamma}\nabla^{\delta}+\delta^{\beta\delta}\nabla^{\gamma}\right)+\delta^{\mu\beta}\left(\delta^{\alpha\gamma}\nabla^{\delta}+\delta^{\alpha\delta}\nabla^{\gamma}\right)\right). \tag{6.19}$$

- Total charge density, ρ_{t}: The total charge density is defined in equation 2.44, which includes the charge density of the valence electrons and the core correction charge density. Both terms involve a prefactor of inverse volume, which has a derivative under strain, but the core charges also have extra contributions since they are interpolated from a radial function in reciprocal space. It is more straightforward to treat the derivatives of the inverse volume factors together and to separately handle the derivative of the core charge density multiplied by the volume, $\Omega\rho_{\mathrm{c}}$.

$$\frac{\mathrm{d}\rho_{\mathrm{t}}(\boldsymbol{r})}{\mathrm{d}\eta_{\alpha\beta}} = -\delta^{\alpha\beta}\rho_{\mathrm{t}}(\boldsymbol{r}) + \Omega^{-1}\frac{\mathrm{d}\left(\Omega\rho_{\mathrm{c}}(\boldsymbol{r})\right)}{\mathrm{d}\eta_{\alpha\beta}}, \tag{6.20}$$

$$\frac{\mathrm{d}^2\rho_\mathrm{t}(\boldsymbol{r})}{\mathrm{d}\eta_{\alpha\beta}\mathrm{d}\eta_{\gamma\delta}} = \delta^{\alpha\beta}\delta^{\gamma\delta}\rho_\mathrm{t}(\boldsymbol{r}) - \delta^{\alpha\beta}\Omega^{-1}\frac{\mathrm{d}(\Omega\rho_\mathrm{c}(\boldsymbol{r}))}{\mathrm{d}\eta_{\gamma\delta}} - \delta^{\gamma\delta}\Omega^{-1}\frac{\mathrm{d}(\Omega\rho_\mathrm{c}(\boldsymbol{r}))}{\mathrm{d}\eta_{\alpha\beta}} + \Omega^{-1}\frac{\mathrm{d}^2(\Omega\rho_\mathrm{c}(\boldsymbol{r}))}{\mathrm{d}\eta_{\alpha\beta}\mathrm{d}\eta_{\gamma\delta}}. \tag{6.21}$$

The core charge density is defined in equation 2.59, which we have then multiplied by the unit cell volume, the derivatives of this quantity are then found to be,

$$\Omega\rho_\mathrm{c}(\boldsymbol{r}) = \sum_I\sum_{\boldsymbol{G}}\rho_\mathrm{c}^I(|\boldsymbol{G}|)\,e^{-i\boldsymbol{G}\cdot\boldsymbol{R}^I}e^{i\boldsymbol{G}\cdot\boldsymbol{r}}, \tag{6.22}$$

$$\frac{\mathrm{d}(\Omega\rho_\mathrm{c}(\boldsymbol{r}))}{\mathrm{d}\eta_{\alpha\beta}} = \sum_I\sum_{\boldsymbol{G}}\frac{\mathrm{d}\rho_\mathrm{c}^I(|\boldsymbol{G}|)}{\mathrm{d}|\boldsymbol{G}|}\frac{\mathrm{d}|\boldsymbol{G}|}{\mathrm{d}\eta_{\alpha\beta}}e^{i\boldsymbol{G}\cdot(\boldsymbol{r}-\boldsymbol{R}^I)}, \tag{6.23}$$

$$\frac{\mathrm{d}^2(\Omega\rho_\mathrm{c}(\boldsymbol{r}))}{\mathrm{d}\eta_{\alpha\beta}\mathrm{d}\eta_{\gamma\delta}} = \sum_I\sum_{\boldsymbol{G}}\left(\frac{\mathrm{d}^2\rho_\mathrm{c}^I(|\boldsymbol{G}|)}{\mathrm{d}|\boldsymbol{G}|^2}\frac{\mathrm{d}|\boldsymbol{G}|}{\mathrm{d}\eta_{\alpha\beta}}\frac{\mathrm{d}|\boldsymbol{G}|}{\mathrm{d}\eta_{\gamma\delta}} + \frac{\mathrm{d}\rho_\mathrm{c}^I(|\boldsymbol{G}|)}{\mathrm{d}|\boldsymbol{G}|}\frac{\mathrm{d}^2|\boldsymbol{G}|}{\mathrm{d}\eta_{\alpha\beta}\mathrm{d}\eta_{\gamma\delta}}\right)e^{i\boldsymbol{G}\cdot(\boldsymbol{r}-\boldsymbol{R}^I)}. \tag{6.24}$$

The derivatives of the $|\boldsymbol{G}|$ can then be substituted in to this equation. We will also require the second derivative of the total charge density under a strain perturbation, and an atomic displacement perturbation, this becomes,

$$\frac{\mathrm{d}^2\rho_\mathrm{t}(\boldsymbol{r})}{\mathrm{d}\eta_{\alpha\beta}\mathrm{d}R_{I,\gamma}} = -\delta^{\alpha\beta}\frac{\mathrm{d}\rho_\mathrm{c}(\boldsymbol{r})}{\mathrm{d}R_{I,\gamma}} + \Omega^{-1}\frac{\mathrm{d}^2(\Omega\rho_\mathrm{c}(\boldsymbol{r}))}{\mathrm{d}\eta_{\alpha\beta}\mathrm{d}R_{I,\gamma}} \tag{6.25}$$

where the first derivative in the first term is defined in 4.16 and the second derivative can be calculated as,

$$\frac{\mathrm{d}^2(\Omega\rho_\mathrm{c}(\boldsymbol{r}))}{\mathrm{d}\eta_{\alpha\beta}\mathrm{d}R_{I,\gamma}} = \sum_I\sum_{\boldsymbol{G}} -iG_\gamma\frac{\mathrm{d}\rho_\mathrm{c}^I(|\boldsymbol{G}|)}{\mathrm{d}|\boldsymbol{G}|}\frac{\mathrm{d}|\boldsymbol{G}|}{\mathrm{d}\eta_{\alpha\beta}}e^{i\boldsymbol{G}\cdot(\boldsymbol{r}-\boldsymbol{R}_I)} \tag{6.26}$$

- Gradient of the density, $\nabla^\mu\rho_\mathrm{t}(\boldsymbol{r})$:

$$\frac{\mathrm{d}(\nabla^\mu\rho_\mathrm{t}(\boldsymbol{r}))}{\mathrm{d}\eta_{\alpha\beta}} = \nabla^\mu\left(\frac{\mathrm{d}\rho_\mathrm{t}(\boldsymbol{r})}{\mathrm{d}\eta_{\alpha\beta}}\right) - \frac{1}{2}\left(\delta^{\mu\alpha}\nabla^\beta\rho(\boldsymbol{r}) + \delta^{\mu\beta}\nabla^\alpha\rho(\boldsymbol{r})\right) \tag{6.27}$$

$$\frac{\mathrm{d}^2(\nabla^\mu\rho_\mathrm{t}(\boldsymbol{r}))}{\mathrm{d}\eta_{\alpha\beta}\mathrm{d}\eta_{\gamma\delta}} = \nabla^\mu\left(\frac{\mathrm{d}^2\rho_\mathrm{t}(\boldsymbol{r})}{\mathrm{d}\eta_{\alpha\beta}\eta_{\gamma\delta}}\right) + \frac{\mathrm{d}\nabla^\mu}{\mathrm{d}\eta_{\delta\gamma}}\frac{\mathrm{d}\rho_\mathrm{t}(\boldsymbol{r})}{\mathrm{d}\eta_{\alpha\beta}} + \frac{\mathrm{d}\nabla^\mu}{\mathrm{d}\eta_{\alpha\beta}}\frac{\mathrm{d}\rho_\mathrm{t}(\boldsymbol{r})}{\mathrm{d}\eta_{\delta\gamma}} + \frac{\mathrm{d}^2\nabla^\mu}{\mathrm{d}\eta_{\alpha\beta}\mathrm{d}\eta_{\delta\gamma}}\rho_\mathrm{t}(\boldsymbol{r}). \tag{6.28}$$

- Total KED, $\tau_\mathrm{t}(\boldsymbol{r})$: In same the way as the charge density, the total KED includes core corrections from the pseudopotential which have very similar derivatives to the core corrections to the charge density. The derivative of the KED with respect to strain also has contributions from the change

in the gradient operators applied to the valence electrons. Starting with the definition of equation 2.42 we will follow the same process used for the charge density, collecting all the volume derivatives together and separating the remaining terms as derivatives of the unit cell volume multiplied by the valence electron contribution to the KED, $\Omega\tau_{\mathrm{v}}$ and the core electron contribution, $\Omega\tau_{\mathrm{v}}$

$$\tau_{\mathrm{t}}(\boldsymbol{r}) = \tau_{\mathrm{v}}(\boldsymbol{r}) + \tau_{\mathrm{c}}(\boldsymbol{r}) = \Omega^{-1}\sum_{b}^{\mathrm{occ}} \frac{1}{2}\left|\nabla\psi_b(\boldsymbol{r})\right|^2 + \tau_{\mathrm{c}}(\boldsymbol{r}), \tag{6.29}$$

$$\frac{\mathrm{d}\tau_{\mathrm{t}}(\boldsymbol{r})}{\mathrm{d}\eta_{\alpha\beta}} = -\delta^{\alpha\beta}\tau_{\mathrm{t}}(\boldsymbol{r}) + \Omega^{-1}\frac{\mathrm{d}\left(\Omega\tau_{\mathrm{v}}(\boldsymbol{r})\right)}{\mathrm{d}\eta_{\alpha\beta}} + \Omega^{-1}\frac{\mathrm{d}\left(\Omega\tau_{\mathrm{c}}(\boldsymbol{r})\right)}{\mathrm{d}\eta_{\alpha\beta}}, \tag{6.30}$$

$$\begin{aligned}\frac{\mathrm{d}^2\tau_{\mathrm{t}}(\boldsymbol{r})}{\mathrm{d}\eta_{\alpha\beta}\mathrm{d}\eta_{\gamma\delta}} =& \delta^{\alpha\beta}\delta^{\gamma\delta}\tau_{\mathrm{t}}(\boldsymbol{r}) - \delta^{\alpha\beta}\Omega^{-1}\left(\frac{\mathrm{d}\left(\Omega\tau_{\mathrm{v}}(\boldsymbol{r})\right)}{\mathrm{d}\eta_{\gamma\delta}} + \frac{\mathrm{d}\left(\Omega\tau_{\mathrm{c}}(\boldsymbol{r})\right)}{\mathrm{d}\eta_{\gamma\delta}}\right) \\ & - \delta^{\gamma\delta}\Omega^{-1}\left(\frac{\mathrm{d}\left(\Omega\tau_{\mathrm{v}}(\boldsymbol{r})\right)}{\mathrm{d}\eta_{\alpha\beta}} + \frac{\mathrm{d}\left(\Omega\tau_{\mathrm{c}}(\boldsymbol{r})\right)}{\mathrm{d}\eta_{\alpha\beta}}\right) \\ & + \Omega^{-1}\left(\frac{\mathrm{d}^2\left(\Omega\tau_{\mathrm{v}}(\boldsymbol{r})\right)}{\mathrm{d}\eta_{\alpha\beta}\mathrm{d}\eta_{\gamma\delta}} + \frac{\mathrm{d}^2\left(\Omega\tau_{\mathrm{c}}(\boldsymbol{r})\right)}{\mathrm{d}\eta_{\alpha\beta}\mathrm{d}\eta_{\gamma\delta}}\right).\end{aligned} \tag{6.31}$$

We can then write expressions for the derivatives of the $\Omega\tau_{\mathrm{v}}$,

$$\Omega\tau_{\mathrm{v}}(\boldsymbol{r}) = \sum_{b}^{\mathrm{occ}} \frac{1}{2}\left|\nabla\psi_b(\boldsymbol{r})\right|^2, \tag{6.32}$$

$$\frac{\mathrm{d}\left(\Omega\tau_{\mathrm{v}}(\boldsymbol{r})\right)}{\mathrm{d}\eta_{\alpha\beta}} = -\sum_{b}^{\mathrm{occ}} \nabla^{\alpha}\psi_b(\boldsymbol{r})\,\nabla^{\beta}\psi_b(\boldsymbol{r}), \tag{6.33}$$

$$\begin{aligned}\frac{\mathrm{d}^2\left(\Omega\tau_{\mathrm{v}}(\boldsymbol{r})\right)}{\mathrm{d}\eta_{\alpha\beta}\mathrm{d}\eta_{\gamma\delta}} =& \sum_{b}^{\mathrm{occ}}\left(\frac{1}{2}\left(\delta^{\alpha\gamma}\nabla^{\delta}\psi_b(\boldsymbol{r}) + \delta^{\alpha\delta}\nabla^{\gamma}\psi_b(\boldsymbol{r})\right)\nabla^{\beta}\psi_b(\boldsymbol{r})\right. \\ & \left. + \frac{1}{2}\nabla^{\alpha}\psi_b(\boldsymbol{r})\left(\delta^{\beta\gamma}\nabla^{\delta}\psi_b(\boldsymbol{r}) + \delta^{\beta\delta}\nabla^{\gamma}\psi_b(\boldsymbol{r})\right)\right).\end{aligned} \tag{6.34}$$

Taking this expression for the second derivative, by multiplying out the brackets we find the second derivative can be written as a combination the first order derivatives with respect to different strains, leading to this expression,

$$\begin{aligned}\frac{\mathrm{d}^2\left(\Omega\tau_{\mathrm{v}}(\boldsymbol{r})\right)}{\mathrm{d}\eta_{\alpha\beta}\mathrm{d}\eta_{\gamma\delta}} =& -\frac{1}{2}\left(\delta^{\alpha\gamma}\frac{\mathrm{d}\left(\Omega\tau_{\mathrm{v}}(\boldsymbol{r})\right)}{\mathrm{d}\eta_{\delta\beta}} + \delta^{\alpha\delta}\frac{\mathrm{d}\left(\Omega\tau_{\mathrm{v}}(\boldsymbol{r})\right)}{\mathrm{d}\eta_{\gamma\beta}} + \right. \\ & \left. \delta^{\beta\gamma}\frac{\mathrm{d}\left(\Omega\tau_{\mathrm{v}}(\boldsymbol{r})\right)}{\mathrm{d}\eta_{\alpha\delta}} + \delta^{\beta\delta}\frac{\mathrm{d}\left(\Omega\tau_{\mathrm{v}}(\boldsymbol{r})\right)}{\mathrm{d}\eta_{\alpha\gamma}}\right).\end{aligned} \tag{6.35}$$

This second expression means that by computing and storing the first derivatives of $\Omega\tau_{\mathrm{v}}$ with respect to all possible strain directions, we can also very easily compute the second derivatives without having to do a sum over the occupied electron states in the wavefunction. When calculating the

first derivatives of $\Omega\tau_{\mathrm{v}}$ using the symmetry reduced set of k-points for the Brillouin zone sampling, the derivatives calculated must be symmetrised to obtain the correct value for $\Omega\tau_{\mathrm{v}}$. When performing this symmetrisation, each of the Fourier components of $\frac{\mathrm{d}\Omega\tau_{\mathrm{v}}(\boldsymbol{r})}{\mathrm{d}\eta_{\alpha\beta}}$ must be treated as a rank-2 tensor which also transforms under the symmetry operation, unlike the charge density and KED which are scalars and do not change under the symmetry transformation.

The contributions from the core electrons to the derivatives of the total KED are very similar in form to those from the core charge density,

$$\Omega\tau_{\mathrm{c}}(\boldsymbol{r}) = \sum_I \sum_{\boldsymbol{G}} \tau_{\mathrm{c}}^I(|\boldsymbol{G}|)\, e^{-i\boldsymbol{G}\cdot\boldsymbol{R}^I} e^{i\boldsymbol{G}\cdot\boldsymbol{r}}, \tag{6.36}$$

$$\frac{\mathrm{d}(\Omega\tau_{\mathrm{c}}(\boldsymbol{r}))}{\mathrm{d}\eta_{\alpha\beta}} = \sum_I \sum_{\boldsymbol{G}} \frac{\mathrm{d}\tau_{\mathrm{c}}^I(|\boldsymbol{G}|)}{\mathrm{d}|\boldsymbol{G}|} \frac{\mathrm{d}|\boldsymbol{G}|}{\mathrm{d}\eta_{\alpha\beta}} e^{i\boldsymbol{G}\cdot(\boldsymbol{r}-\boldsymbol{R}^I)}, \tag{6.37}$$

$$\begin{aligned}\frac{\mathrm{d}^2(\Omega\tau_{\mathrm{c}}(\boldsymbol{r}))}{\mathrm{d}\eta_{\alpha\beta}\mathrm{d}\eta_{\gamma\delta}} = \sum_I \sum_{\boldsymbol{G}} \Bigg(& \frac{\mathrm{d}^2\tau_{\mathrm{c}}^I(|\boldsymbol{G}|)}{\mathrm{d}|\boldsymbol{G}|^2} \frac{\mathrm{d}|\boldsymbol{G}|}{\mathrm{d}\eta_{\alpha\beta}} \frac{\mathrm{d}|\boldsymbol{G}|}{\mathrm{d}\eta_{\gamma\delta}} \\ & + \frac{\mathrm{d}\tau_{\mathrm{c}}^I(|\boldsymbol{G}|)}{\mathrm{d}|\boldsymbol{G}|} \frac{\mathrm{d}^2|\boldsymbol{G}|}{\mathrm{d}\eta_{\alpha\beta}\mathrm{d}\eta_{\gamma\delta}} \Bigg) e^{i\boldsymbol{G}\cdot(\boldsymbol{r}-\boldsymbol{R}^I)}.\end{aligned} \tag{6.38}$$

The derivatives of the $|\boldsymbol{G}|$ can then be substituted in to the above equations. We will also require the second derivative of the total kinetic energy density under a strain perturbation, and an atomic displacement perturbation, this becomes,

$$\frac{\mathrm{d}^2\tau_{\mathrm{t}}(\boldsymbol{r})}{\mathrm{d}\eta_{\alpha\beta}\mathrm{d}R_\gamma^I} = -\delta^{\alpha\beta}\frac{\mathrm{d}\tau_{\mathrm{c}}(\boldsymbol{r})}{\mathrm{d}R_\gamma^I} + \Omega^{-1}\frac{\mathrm{d}^2(\Omega\tau_{\mathrm{c}}(\boldsymbol{r}))}{\mathrm{d}\eta_{\alpha\beta}\mathrm{d}R_\gamma^I} \tag{6.39}$$

where the first derivative in the first term is defined in 4.18 and the second derivative can be calculated as,

$$\frac{\mathrm{d}^2(\Omega\tau_{\mathrm{c}}(\boldsymbol{r}))}{\mathrm{d}\eta_{\alpha\beta}\mathrm{d}R_\gamma^I} = \sum_I \sum_{\boldsymbol{G}} -iG_\gamma \frac{\mathrm{d}\tau_{\mathrm{c}}^I(|\boldsymbol{G}|)}{\mathrm{d}|\boldsymbol{G}|} \frac{\mathrm{d}|\boldsymbol{G}|}{d\eta_{\alpha\beta}} e^{i\boldsymbol{G}\cdot(\boldsymbol{r}-\boldsymbol{R}^I)}. \tag{6.40}$$

- Local part of the differential part of the external potential, $V_\tau^{\mathrm{loc}}(\boldsymbol{r})$: The differential part of the external potential operator includes a local potential term that has derivatives under strain. The local potential part is obtained in a similar fashion to the core corrections to the charge density and KED, via interpolating a radial function in reciprocal space onto the FFT grid. The expression for $V_\tau^{local}(\boldsymbol{r})$ is given in equation 2.61, repeated below,

$$V_\tau^{\mathrm{loc}}(\boldsymbol{r}) = \Omega^{-1}\sum_J \sum_{\boldsymbol{G}} v_J^\tau(|\boldsymbol{G}|)\, e^{i\boldsymbol{G}\cdot(\boldsymbol{r}-\boldsymbol{R_J})}. \tag{6.41}$$

The derivatives of the local potential part are therefore found to be,

$$\frac{\mathrm{d}V_\tau^{\mathrm{loc}}(\boldsymbol{r})}{\mathrm{d}\eta_{\alpha\beta}} = -\delta^{\alpha\beta}V_\tau^{\mathrm{loc}}(\boldsymbol{r}) + \Omega^{-1}\sum_J\sum_{\boldsymbol{G}}\frac{\mathrm{d}v_J^\tau(|\boldsymbol{G}|)}{\mathrm{d}|\boldsymbol{G}|}\frac{\mathrm{d}|\boldsymbol{G}|}{\mathrm{d}\eta_{\alpha\beta}}e^{i\boldsymbol{G}\cdot(\boldsymbol{r}-\boldsymbol{R_J})}, \quad (6.42)$$

$$\begin{aligned}\frac{\mathrm{d}^2V_\tau^{\mathrm{loc}}(\boldsymbol{r})}{\mathrm{d}\eta_{\alpha\beta}\mathrm{d}\eta_{\gamma\delta}} =& \delta^{\alpha\beta}\delta^{\gamma\delta}V_\tau^{\mathrm{loc}}(\boldsymbol{r}) - \delta^{\alpha\beta}\Omega^{-1}\sum_J\sum_{\boldsymbol{G}}\frac{\mathrm{d}v_J^\tau(|\boldsymbol{G}|)}{\mathrm{d}|\boldsymbol{G}|}\frac{\mathrm{d}|\boldsymbol{G}|}{\mathrm{d}\eta_{\gamma\delta}}e^{i\boldsymbol{G}\cdot(\boldsymbol{r}-\boldsymbol{R_J})} \\ &- \delta^{\gamma\delta}\Omega^{-1}\sum_J\sum_{\boldsymbol{G}}\frac{\mathrm{d}v_J^\tau(|\boldsymbol{G}|)}{\mathrm{d}|\boldsymbol{G}|}\frac{\mathrm{d}|\boldsymbol{G}|}{\mathrm{d}\eta_{\alpha\beta}}e^{i\boldsymbol{G}\cdot(\boldsymbol{r}-\boldsymbol{R_J})} \\ &+ \Omega^{-1}\sum_J\sum_{\boldsymbol{G}}\left(\frac{\mathrm{d}^2v_J^\tau(|\boldsymbol{G}|)}{(\mathrm{d}|\boldsymbol{G}|)^2}\frac{\mathrm{d}|\boldsymbol{G}|}{\mathrm{d}\eta_{\alpha\beta}}\frac{\mathrm{d}|\boldsymbol{G}|}{\mathrm{d}\eta_{\gamma\delta}}\right. \\ &\left.+ \frac{\mathrm{d}v_J^\tau(|\boldsymbol{G}|)}{\mathrm{d}|\boldsymbol{G}|}\frac{\mathrm{d}^2|\boldsymbol{G}|}{\mathrm{d}\eta_{\alpha\beta}\mathrm{d}\eta_{\gamma\delta}}\right)e^{i\boldsymbol{G}\cdot(\boldsymbol{r}-\boldsymbol{R_J})}. \end{aligned} \quad (6.43)$$

The expression derived above can now be used to derive the derivatives of the contributions to the Hamiltonian operator and the total energy.

6.2.3 Change of the mGGA Hamiltonian Under Strain

The Hamiltonian of a system using an mGGA functional differs from the Hamiltonian of system using an LDA or GGA functional in two ways, the differential part of the external pseudopotential, and the XC potential operator.

6.2.3.1 External Potential Operator

The derivatives of the local part and the non-local parts of the external potential operator with respect to strain perturbations have already been derived by Hamman *et al* [93], the derivative of the additional differential part of external potential is all that needs to be derived here. The differential part of the external pseudopotential, $\hat{V}_\tau^{\mathrm{ext}}$ is defined in equation 2.37, and an expression for the derivative of this operator under a general perturbation is given in equation 3.62. Using these expressions, we can find the derivative of this operator under strain,

$$\hat{V}_\tau^{\mathrm{ext}} = -\frac{1}{2}\nabla\cdot\left(V_\tau^{\mathrm{loc}}(\boldsymbol{r})\nabla\right), \quad (6.44)$$

$$\frac{d\hat{V}_\tau^{\mathrm{ext}}}{d\eta_{\alpha\beta}} = \frac{1}{2}\left(\nabla^\alpha V_\tau^{\mathrm{loc}}(\boldsymbol{r})\nabla^\beta + \nabla\cdot\left(\frac{dV_\tau^{\mathrm{loc}}(\boldsymbol{r})}{d\eta_{\alpha\beta}}(\boldsymbol{r})\nabla\right) + \nabla^\beta V_\tau^{\mathrm{loc}}(\boldsymbol{r})\nabla^\alpha\right) \quad (6.45)$$

where an expression for $\frac{dV_\tau^{\mathrm{loc}}(\boldsymbol{r})}{d\eta_{\alpha\beta}}$ has been derived above in equation 6.42.

6.2.3.2 XC Potential Operator

Now we shall consider the XC potential operator, $\hat{V}^{\mathrm{XC}}$. The operator is defined in equation 2.65, however, it is more convenient work in terms of the local potentials defined in equations 2.66 and 2.67,

$$\hat{V}^{\mathrm{XC}}(\boldsymbol{r}) = V_{\rho}^{\mathrm{XC}}(\boldsymbol{r}) - \frac{1}{2}\nabla\cdot\left(V_{\tau}^{\mathrm{XC}}(\boldsymbol{r})\,\nabla\right). \tag{6.46}$$

A general expression for first-order mGGA XC potential is given in 3.64. By substituting $\eta_{\alpha\beta}$ for λ in that expression we can get the change first-order mGGA XC potential under strain,

$$\begin{aligned}\frac{\partial\hat{V}^{\mathrm{XC}}(\boldsymbol{r})}{\partial\eta_{\alpha\beta}} =& \frac{\partial V_{\rho}^{\mathrm{XC}}(\boldsymbol{r})}{\partial\eta_{\alpha\beta}} - \frac{1}{2}\Bigg[\nabla^{\alpha}\left(V_{\tau}^{\mathrm{XC}}(\boldsymbol{r})\,\nabla^{\beta}\right) + \\ & \nabla\cdot\left(\frac{\partial V_{\tau}^{\mathrm{XC}}(\boldsymbol{r})}{\partial\eta_{\alpha\beta}}\nabla\right) + \nabla^{\beta}\left(V_{\tau}^{\mathrm{XC}}(\boldsymbol{r})\,\nabla^{\alpha}\right)\Bigg].\end{aligned} \tag{6.47}$$

Partial derivatives have been used here to signify that this is the non-self consistent response of the XC potential operator, and does not include first-order density and KED contributions. The self-consistent response can be calculated separately and linearly added in as part of the self-consistent work-flow.

Each of the local potentials has derivatives arising from the changes in the density, the gradient of the density, and the KED under the strain perturbation. Starting with $V_{\rho}^{\mathrm{XC}}(\boldsymbol{r})$,

$$\begin{aligned}\frac{\partial V_{\rho}^{\mathrm{XC}}(\boldsymbol{r})}{\partial\eta_{\alpha\beta}} =& \frac{\partial^2 f^{\mathrm{XC}}}{\partial\rho^2}\frac{\mathrm{d}\rho_{\mathrm{t}}}{\mathrm{d}\eta_{\alpha\beta}} + \frac{\partial^2 f^{\mathrm{XC}}}{\partial\rho\partial|\nabla\rho|}\frac{\nabla^{\mu}\rho_{\mathrm{t}}}{|\nabla\rho_{\mathrm{t}}|}\frac{\mathrm{d}\left(\nabla^{\mu}\rho_{\mathrm{t}}\right)}{\mathrm{d}\eta_{\alpha\beta}} + \frac{\partial^2 f^{\mathrm{XC}}}{\partial\rho\partial\tau}\frac{d\tau_{\mathrm{t}}}{d\eta_{\alpha\beta}} - \frac{\mathrm{d}\nabla^{\gamma}}{\mathrm{d}\eta_{\alpha\beta}}\left(\frac{\partial f^{\mathrm{XC}}}{\partial|\nabla\rho|}\frac{\nabla^{\gamma}\rho_{\mathrm{t}}}{|\nabla\rho_{\mathrm{t}}|}\right) \\ & - \nabla^{\gamma}\Bigg[\left(\frac{\partial^2 f^{\mathrm{XC}}}{\partial|\nabla\rho|\,\partial\rho}\frac{\mathrm{d}\rho_{\mathrm{t}}}{\mathrm{d}\eta_{\alpha\beta}} + \frac{\partial^2 f^{\mathrm{XC}}}{\partial|\nabla\rho|\,\partial\tau}\frac{\mathrm{d}\tau_{\mathrm{t}}}{\mathrm{d}\eta_{\alpha\beta}}\right)\frac{\nabla^{\gamma}\rho_{\mathrm{t}}}{|\nabla\rho_{\mathrm{t}}|} + \frac{\partial f^{\mathrm{XC}}}{\partial|\nabla\rho_{\mathrm{t}}|}\frac{1}{|\nabla\rho_{\mathrm{t}}|}\frac{\mathrm{d}\left(\nabla^{\gamma}\rho_{\mathrm{t}}\right)}{\mathrm{d}\eta_{\alpha\beta}} \\ & + \left(\frac{\partial^2 f^{\mathrm{XC}}}{\partial|\nabla\rho_{\mathrm{t}}|^2}\frac{\nabla^{\mu}\rho_{\mathrm{t}}\nabla^{\gamma}\rho_{\mathrm{t}}}{|\nabla\rho_{\mathrm{t}}|^2} - \frac{\partial f^{\mathrm{XC}}}{\partial|\nabla\rho_{\mathrm{t}}|}\frac{\nabla^{\mu}\rho_{\mathrm{t}}\nabla^{\gamma}\rho_{\mathrm{t}}}{|\nabla\rho_{\mathrm{t}}|^3}\right)\frac{\mathrm{d}\left(\nabla^{\mu}\rho_{\mathrm{t}}\right)}{\mathrm{d}\eta_{\alpha\beta}}\Bigg],\end{aligned} \tag{6.48}$$

where the expressions $\nabla^{\mu}\rho_{\mathrm{t}}\nabla^{\gamma}\rho_{\mathrm{t}}$ on the last line are interpreted as the outer product of the vector, the gradient of the density at point $\boldsymbol{r}$. This creates a rank-2 tensor like object with indices μ and γ, which is multiplied by the vector, the derivative of the gradient of the density, which has the index μ, resulting in an object with an γ index, which can safely have the gradient operator outside the square brackets applied to it.

Now we consider the far simpler derivative of $V_\tau^{\mathrm{XC}}(\boldsymbol{r})$,

$$\frac{\mathrm{d}V_\tau^{\mathrm{XC}}(\boldsymbol{r})}{\mathrm{d}\eta_{\alpha\beta}} = \frac{\partial^2 f^{\mathrm{XC}}}{\partial\tau\partial\rho}\frac{\mathrm{d}\rho_{\mathrm{t}}}{\mathrm{d}\eta_{\alpha\beta}} + \frac{\partial^2 f^{\mathrm{XC}}}{\partial\tau\partial|\nabla\rho|}\frac{\nabla^\mu\rho_{\mathrm{t}}}{|\nabla\rho|}\frac{\mathrm{d}(\nabla^\mu\rho_{\mathrm{t}})}{\mathrm{d}\eta_{\alpha\beta}} + \frac{\partial^2 f^{\mathrm{XC}}}{\partial\tau^2}\frac{\mathrm{d}\tau_{\mathrm{t}}}{\mathrm{d}\eta_{\alpha\beta}}. \tag{6.49}$$

These equations define the first-order response XC potential for a mGGA functional under a strain perturbation $\eta_{\alpha\beta}$. For brevity, $\rho_{\mathrm{t}}(\boldsymbol{r})$, $\tau_{\mathrm{t}}(\boldsymbol{r})$, have not been shown as functions of position, they should all be taken to be at position $\boldsymbol{r}$, f^{XC} and its derivatives have not been shown as functions of the charge density, its gradient, and the KED.

Together with the existing derivation of Hamann *et al* [93, 98], the response of the Hamiltonian under strain, $\frac{\partial\hat{H}}{\partial\eta_{\alpha\beta}}$, has been derived for mGGA systems. Derivation of the energy terms is all that remains now.

6.2.4 Second order energy derivatives

Now we shall turn our attention to the contributions to the second-order energy derivatives arising from the differential part of the external potential operator, E_τ^{ext}, and the XC energy E^{XC}. To compute the elastic constants of a material, there are three sets of energy derivatives required, the dynamical matrix at $\boldsymbol{q}=0$ which has already been derived in Chapter 4, the frozen-ion elastic constants, and the force-response internal-strain tensor. We shall start with the contributions from E_τ^{ext}.

6.2.4.1 External Potential

Again, the derivatives of the local part and the non-local parts of the external potential energy contributions with respect to strain perturbations are already defined in the literature [93]. Only the energy contribution from the differential part of the external potential must therefore be derived here. The relevant expression for this energy contribution E_τ^{ext}, is given in equation 2.63, repeated here,

$$E_\tau^{\mathrm{ext}} = \Omega\int_\Omega V_\tau^{\mathrm{ext}}(\boldsymbol{r})\,\tau(\boldsymbol{r})\ \mathrm{d}^3\boldsymbol{r}, \tag{6.50}$$

where in this case τ is the KED arising from the valence electrons, with no core electron contribution, i.e. τ_{v}. The derivative of this expression for a general pair of perturbations is given in equation 3.72.

Frozen-Ion Elastic Constants

We can obtain the expression for the E_τ^{ext} contribution to the frozen-ion elastic constants by substituting a pair of strain perturbations $\eta_{\alpha\beta}$ and $\eta_{\gamma\delta}$ for the general

perturbations λ and μ in equation 3.72. The derivative can be simplified to the following expression,

$$\begin{aligned}\frac{\partial^2 E_\tau^{\text{ext}}}{\partial\eta_{\alpha\beta}\partial\eta_{\gamma\delta}} = \delta^{\alpha\beta}\delta^{\gamma\delta}E_\tau^{\text{ext}} \\ -\delta^{\gamma\delta}\Omega\int_\Omega\left(\frac{\partial V_\tau^{\text{ext}}(\boldsymbol{r})}{\partial\eta_{\alpha\beta}}\tau_{\text{v}}(\boldsymbol{r}) + V_\tau^{\text{ext}}(\boldsymbol{r})\frac{\partial\tau_{\text{v}}(\boldsymbol{r})}{\partial\eta_{\alpha\beta}}\right)\,\mathrm{d}^3\boldsymbol{r} \\ -\delta^{\alpha\beta}\Omega\int_\Omega\left(\frac{\partial V_\tau^{\text{ext}}(\boldsymbol{r})}{\partial\eta_{\gamma\delta}}\tau_{\text{v}}(\boldsymbol{r}) + V_\tau^{\text{ext}}(\boldsymbol{r})\frac{\partial\tau_{\text{v}}(\boldsymbol{r})}{\partial\eta_{\gamma\delta}}\right)\,\mathrm{d}^3\boldsymbol{r} \\ +\Omega\int_\Omega\left[\frac{\partial^2 V_\tau^{\text{ext}}(\boldsymbol{r})}{\partial\eta_{\gamma\delta}\partial\eta_{\alpha\beta}}\tau_{\text{v}}(\boldsymbol{r}) + \frac{\partial V_\tau^{\text{ext}}(\boldsymbol{r})}{\partial\eta_{\gamma\delta}}\frac{\partial\tau_{\text{v}}(\boldsymbol{r})}{\partial\eta_{\alpha\beta}}\right. \\ \left. + \frac{\partial V_\tau^{\text{ext}}(\boldsymbol{r})}{\partial\eta_{\alpha\beta}}\frac{\partial\tau_{\text{v}}(\boldsymbol{r})}{\partial\eta_{\gamma\delta}} + V_\tau^{\text{ext}}(\boldsymbol{r})\frac{\partial^2\tau_{\text{v}}(\boldsymbol{r})}{\partial\eta_{\gamma\delta}\partial\eta_{\alpha\beta}}\right]\,\mathrm{d}^3\boldsymbol{r}. \quad (6.51)\end{aligned}$$

Internal Strain

We can obtain the expression for the E_τ^{ext} contribution to the force response internal strain tensor by substituting a strain perturbation $\eta_{\alpha\beta}$ and an atomic displacement perturbation $R_{I,\gamma}$ for the general perturbations λ and μ in equation 3.72. The derivative can be simplified to the following expression,

$$\begin{aligned}\frac{\partial^2 E_\tau^{\text{ext}}}{\partial\eta_{\alpha\beta}\partial R_{I,\gamma}} = -\delta^{\alpha\beta}\Omega\int_\Omega\frac{\partial V_\tau^{\text{ext}}(\boldsymbol{r})}{\partial R_{I,\gamma}}\tau_{\text{v}}(\boldsymbol{r})\,\mathrm{d}^3\boldsymbol{r} \\ +\Omega\int_\Omega\left[\frac{\partial^2 V_\tau^{\text{ext}}(\boldsymbol{r})}{\partial R_{I,\gamma}\partial\eta_{\alpha\beta}}\tau_{\text{v}}(\boldsymbol{r}) + \frac{\partial V_\tau^{\text{ext}}(\boldsymbol{r})}{\partial R_{I,\gamma}}\frac{\partial\tau_{\text{v}}(\boldsymbol{r})}{\partial\eta_{\alpha\beta}}\right]\,\mathrm{d}^3\boldsymbol{r}. \quad (6.52)\end{aligned}$$

6.2.4.2 XC energy terms

The expression for the XC energy in the mGGA formalism is given in equation 2.68. Expression for the derivatives of the energy contribution in the LDA formalism and GGA formalism are given in [93] and [98] respectively. Here, we shall follow the approach taken in the second reference, which starts with the energy expression as a sum of discrete points,

$$E^{\text{XC}} = \frac{\Omega}{N_{\text{p}}}\sum_i^{N_{\text{p}}} f^{\text{XC}}\left(\rho(\boldsymbol{r}_i), |\nabla\rho(\boldsymbol{r}_i)|, \tau(\boldsymbol{r}_i)\right). \quad (6.53)$$

An expression is given in equation 3.77 for the second derivative of this energy contribution with respect to a pair of general perturbations λ and μ. Using that expression, we can find the contribution from the XC energy to the frozen-ion elastic constants and the force-response internal-strain tensor.

Frozen-Ion Elastic Constants

We can obtain the expression for the XC energy contribution to the frozen-ion elastic constants by substituting a pair of strain perturbations $\eta_{\alpha\beta}$ and $\eta_{\gamma\delta}$ for the general perturbations λ and μ in equation 3.77. This gives,

$$\begin{aligned}
\frac{\partial^2 E^{\mathrm{XC}}}{\partial\eta_{\alpha\beta}\partial\eta_{\gamma\delta}} =& \delta^{\alpha\beta}\delta^{\gamma\delta}E^{\mathrm{XC}} \\
&+ \delta^{\gamma\delta}\frac{\Omega}{N_{\mathrm{p}}}\sum_i^{N_{\mathrm{p}}}\left[V_\rho^{\mathrm{XC}}\frac{\partial\rho_{\mathrm{t}}}{\partial\eta_{\alpha\beta}} + V_\tau^{\mathrm{XC}}\frac{\partial\tau_{\mathrm{t}}}{\partial\eta_{\alpha\beta}} + \frac{\partial f^{\mathrm{XC}}}{\partial|\nabla\rho|}\frac{\nabla^\nu\rho}{|\nabla\rho|}\frac{\partial\nabla^\nu}{\partial\eta_{\alpha\beta}}(\rho)\right] \\
&+ \delta^{\alpha\beta}\frac{\Omega}{N_{\mathrm{p}}}\sum_i^{N_{\mathrm{p}}}\left[V_\rho^{\mathrm{XC}}\frac{\partial\rho}{\partial\eta_{\gamma\delta}} + V_\tau^{\mathrm{XC}}\frac{\partial\tau}{\partial\eta_{\gamma\delta}} + \frac{\partial f^{\mathrm{XC}}}{\partial|\nabla\rho|}\frac{\nabla^\nu\rho}{|\nabla\rho|}\frac{\partial\nabla^\nu}{\partial\eta_{\gamma\delta}}(\rho)\right] \\
&+ \frac{\Omega}{N_{\mathrm{p}}}\sum_i^{N_{\mathrm{p}}}\left[V_\rho^{\mathrm{XC}}\frac{\partial^2\rho}{\partial\eta_{\alpha\beta}\partial\eta_{\gamma\delta}} + V_\tau^{\mathrm{XC}}\frac{\partial^2\tau}{\partial\eta_{\alpha\beta}\partial\eta_{\gamma\delta}}\right. \\
&+ \frac{\partial V_\rho^{\mathrm{XC}}}{\partial\eta_{\gamma\delta}}\frac{\partial\rho}{\partial\eta_{\alpha\beta}} + \frac{\partial V_\tau^{\mathrm{XC}}}{\partial\eta_{\gamma\delta}}\frac{\partial\tau}{\partial\eta_{\alpha\beta}} \\
&+ \left\{\frac{\partial^2 f^{\mathrm{XC}}}{\partial|\nabla\rho|\partial\rho}\frac{\partial\rho}{\partial\eta_{\gamma\delta}} + \frac{\partial^2 f^{\mathrm{XC}}}{\partial|\nabla\rho|\partial\tau}\frac{\partial\tau}{\partial\eta_{\gamma\delta}}\right\}\frac{\nabla^\nu\rho}{|\nabla\rho|}\frac{\partial\nabla^\nu}{\partial\eta_{\alpha\beta}}(\rho) \\
&+ \left(\frac{\partial^2 f^{\mathrm{XC}}}{\partial|\nabla\rho|^2}\frac{\nabla^\nu\rho\nabla^\zeta\rho}{|\nabla\rho|^2} - \frac{\partial f^{\mathrm{XC}}}{\partial|\nabla\rho|}\frac{\nabla^\nu\rho\nabla^\zeta\rho}{|\nabla\rho|^3}\right)\frac{\partial\left(\nabla^\zeta\rho\right)}{\partial\eta_{\gamma\delta}}\frac{\partial(\nabla^\nu)}{\partial\eta_{\alpha\beta}}(\rho) \\
&+ \frac{\partial f^{\mathrm{XC}}}{\partial|\nabla\rho|}\left\{\frac{1}{|\nabla\rho|}\frac{\partial(\nabla^\nu\rho)}{\partial\eta_{\gamma\delta}}\frac{\partial\nabla^\nu}{\partial\eta_{\alpha\beta}}(\rho)\right. \\
&\left.\left.+ \frac{\nabla^\nu\rho}{|\nabla\rho|^2}\frac{\partial^2\nabla^\nu}{\partial\eta_{\alpha\beta}\partial\eta_{\gamma\delta}}(\rho) + \frac{\nabla^\nu\rho}{|\nabla\rho|^2}\frac{\partial\nabla^\nu}{\partial\eta_{\alpha\beta}}\left(\frac{\partial\rho}{\partial\eta_{\gamma\delta}}\right)\right\}\right]. \qquad (6.54)
\end{aligned}$$

This expression is less than ideal! It does not appear symmetric under the interchange of $\alpha\beta$ and $\gamma\delta$ indices, and includes a large number of terms which have to be computed separately from straightforward XC potentials. However, as was found for the GGA expression in Ref [98], this expression can be simplified. The exact process of this simplification involves many steps, too many to be shown in full, however it is achieved by substituting in the derivatives of each quantity under strain derived above, at which point, it can be found that there are some terms that cancel and some terms that appear multiple times, which we can use to simplify our expression.

The approach here follows the same process as Ref [98]. Instead of using the expressions for the strain derivatives of the local potentials that were derived above, i.e. $\frac{\partial V_\rho^{\mathrm{XC}}}{\partial\eta_{\alpha\beta}}$ and $\frac{\partial V_\tau^{\mathrm{XC}}}{\partial\eta_{\alpha\beta}}$, we use modified versions of these expressions, where some of the terms are doubled. Specifically, we double every derivative of the gradient operator with respect to strain, such that we have a modified derivative

of the gradient of the charge density,

$$\frac{d\left(\nabla^{\mu}\rho_{\mathrm{t}}\left(\boldsymbol{r}\right)\right)^{*}}{d\eta_{\alpha\beta}}=\nabla^{\mu}\left(\frac{d\rho_{\mathrm{t}}\left(\boldsymbol{r}\right)}{d\eta_{\alpha\beta}}\right)-\left(\delta^{\mu\alpha}\nabla^{\beta}\rho\left(\boldsymbol{r}\right)+\delta^{\mu\beta}\nabla^{\alpha}\rho\left(\boldsymbol{r}\right)\right) \tag{6.55}$$

where the factor of a half in front of the second set of brackets cancelled when compared to the unmodified expression in equation 6.27.

The expressions for the modified potentials become,

$$\begin{aligned}\frac{\partial V_{\rho}^{\mathrm{XC}}\left(\boldsymbol{r}\right)^{*}}{\partial\eta_{\alpha\beta}}=&\frac{\partial^{2}f^{\mathrm{XC}}}{\partial\rho^{2}}\frac{d\rho_{\mathrm{t}}}{d\eta_{\alpha\beta}}+\frac{\partial^{2}f^{\mathrm{XC}}}{\partial\rho\partial\left|\nabla\rho\right|}\frac{\nabla^{\mu}\rho_{\mathrm{t}}}{\left|\nabla\rho_{\mathrm{t}}\right|}\frac{d\left(\nabla^{\mu}\rho_{\mathrm{t}}\right)^{*}}{d\eta_{\alpha\beta}}\\&+\frac{\partial^{2}f^{\mathrm{XC}}}{\partial\rho\partial\tau}\frac{d\tau_{\mathrm{t}}}{d\eta_{\alpha\beta}}-2\frac{d\nabla^{\gamma}}{d\eta_{\alpha\beta}}\left(\frac{\partial f^{\mathrm{XC}}}{\partial\left|\nabla\rho\right|}\frac{\nabla^{\gamma}\rho_{\mathrm{t}}}{\left|\nabla\rho_{\mathrm{t}}\right|}\right)\\&-\nabla^{\gamma}\left[\left(\frac{\partial^{2}f^{\mathrm{XC}}}{\partial\left|\nabla\rho\right|\partial\rho}\frac{d\rho_{\mathrm{t}}}{d\eta_{\alpha\beta}}+\frac{\partial^{2}f^{\mathrm{XC}}}{\partial\left|\nabla\rho\right|\partial\tau}\frac{d\tau_{\mathrm{t}}}{d\eta_{\alpha\beta}}\right)\frac{\nabla^{\gamma}\rho_{\mathrm{t}}}{\left|\nabla\rho_{\mathrm{t}}\right|}+\frac{\partial f^{\mathrm{XC}}}{\partial\left|\nabla\rho_{\mathrm{t}}\right|}\frac{1}{\left|\nabla\rho_{\mathrm{t}}\right|}\frac{d\left(\nabla^{\gamma}\rho_{\mathrm{t}}\right)^{*}}{d\eta_{\alpha\beta}}\right.\\&\left.+\left(\frac{\partial^{2}f^{\mathrm{XC}}}{\partial\left|\nabla\rho_{\mathrm{t}}\right|^{2}}\frac{\nabla^{\mu}\rho_{\mathrm{t}}\nabla^{\gamma}\rho_{\mathrm{t}}}{\left|\nabla\rho_{\mathrm{t}}\right|^{2}}-\frac{\partial f^{\mathrm{XC}}}{\partial\left|\nabla\rho_{\mathrm{t}}\right|}\frac{\nabla^{\mu}\rho_{\mathrm{t}}\nabla^{\gamma}\rho_{\mathrm{t}}}{\left|\nabla\rho_{\mathrm{t}}\right|^{3}}\right)\frac{d\left(\nabla^{\mu}\rho_{\mathrm{t}}\right)^{*}}{d\eta_{\alpha\beta}}\right],\end{aligned} \tag{6.56}$$

and,

$$\frac{\partial V_{\tau}^{\mathrm{XC}}\left(\boldsymbol{r}\right)^{*}}{\partial\eta_{\alpha\beta}}=\frac{\partial^{2}f^{\mathrm{XC}}}{\partial\tau\partial\rho}\frac{d\rho_{\mathrm{t}}}{d\eta_{\alpha\beta}}+\frac{\partial^{2}f^{\mathrm{XC}}}{\partial\tau\partial\left|\nabla\rho\right|}\frac{\nabla^{\mu}\rho_{\mathrm{t}}}{\left|\nabla\rho_{\mathrm{t}}\right|}\frac{d\left(\nabla^{\mu}\rho_{\mathrm{t}}\right)^{*}}{d\eta_{\alpha\beta}}+\frac{\partial^{2}f^{\mathrm{XC}}}{\partial\tau^{2}}\frac{d\tau_{\mathrm{t}}}{d\eta_{\alpha\beta}}. \tag{6.57}$$

By using these modified potentials, many of the terms become incorporated into the potentials and the complexity of the expression can be reduced, such that resultant expression is,

$$\begin{aligned}\frac{\partial^{2}E^{\mathrm{XC}}}{\partial\eta_{\alpha\beta}\partial\eta_{\gamma\delta}}=&\delta^{\alpha\beta}\delta^{\gamma\delta}E^{\mathrm{XC}}\\&+\frac{\Omega}{N_{\mathrm{p}}}\sum_{i}^{N_{\mathrm{p}}}\left[\delta^{\gamma\delta}V_{\rho}^{\mathrm{XC}}\frac{\partial\rho_{\mathrm{t}}}{\partial\eta_{\alpha\beta}}+\delta^{\gamma\delta}V_{\tau}^{\mathrm{XC}}\frac{\partial\tau_{\mathrm{t}}}{\partial\eta_{\alpha\beta}}\right.\\&+\delta^{\alpha\beta}V_{\rho}^{\mathrm{XC}}\frac{\partial\rho_{\mathrm{t}}}{\partial\eta_{\gamma\delta}}+\delta^{\alpha\beta}V_{\tau}^{\mathrm{XC}}\frac{\partial\tau_{\mathrm{t}}}{\partial\eta_{\gamma\delta}}+V_{\rho}^{\mathrm{XC}}\frac{\partial^{2}\rho_{\mathrm{t}}}{\partial\eta_{\alpha\beta}\partial\eta_{\gamma\delta}}+V_{\tau}^{\mathrm{XC}}\frac{\partial^{2}\tau_{\mathrm{t}}}{\partial\eta_{\alpha\beta}\partial\eta_{\gamma\delta}}\\&+\frac{1}{2}\left(\frac{\partial V_{\rho}^{\mathrm{XC}}{}^{*}}{\partial\eta_{\gamma\delta}}\frac{\partial\rho_{\mathrm{t}}}{\partial\eta_{\alpha\beta}}+\frac{\partial V_{\tau}^{\mathrm{XC}}{}^{*}}{\partial\eta_{\gamma\delta}}\frac{\partial\tau_{\mathrm{t}}}{\partial\eta_{\alpha\beta}}+\frac{\partial V_{\rho}^{\mathrm{XC}}{}^{*}}{\partial\eta_{\alpha\beta}}\frac{\partial\rho_{\mathrm{t}}}{\partial\eta_{\gamma\delta}}+\frac{\partial V_{\tau}^{\mathrm{XC}}{}^{*}}{\partial\eta_{\alpha\beta}}\frac{\partial\tau_{\mathrm{t}}}{\partial\eta_{\gamma\delta}}\right)\\&+\frac{1}{2}\frac{\partial f^{\mathrm{XC}}}{\partial\left|\nabla\rho\right|}\left(-2\delta^{\alpha\beta}\frac{\nabla^{\gamma}\rho_{\mathrm{t}}\nabla^{\delta}\rho_{\mathrm{t}}}{\left|\nabla\rho_{\mathrm{t}}\right|}-2\delta^{\gamma\delta}\frac{\nabla^{\alpha}\rho_{\mathrm{t}}\nabla^{\beta}\rho_{\mathrm{t}}}{\left|\nabla\rho_{\mathrm{t}}\right|}\right.\\&\left.+\delta^{\alpha\gamma}\frac{\nabla^{\beta}\rho_{\mathrm{t}}\nabla^{\delta}\rho_{\mathrm{t}}}{\left|\nabla\rho_{\mathrm{t}}\right|}+\delta^{\beta\gamma}\frac{\nabla^{\alpha}\rho_{\mathrm{t}}\nabla^{\delta}\rho_{\mathrm{t}}}{\left|\nabla\rho_{\mathrm{t}}\right|}+\delta^{\alpha\delta}\frac{\nabla^{\beta}\rho_{\mathrm{t}}\nabla^{\gamma}\rho_{\mathrm{t}}}{\left|\nabla\rho_{\mathrm{t}}\right|}+\delta^{\beta\delta}\frac{\nabla^{\alpha}\rho_{\mathrm{t}}\nabla^{\gamma}\rho_{\mathrm{t}}}{\left|\nabla\rho_{\mathrm{t}}\right|}\right)\\&\left.+\left(\frac{\partial^{2}f^{\mathrm{XC}}}{\partial\left|\nabla\rho\right|^{2}}-\frac{\partial f^{\mathrm{XC}}}{\partial\left|\nabla\rho\right|}\frac{1}{\left|\nabla\rho_{\mathrm{t}}\right|}\right)\frac{\nabla^{\alpha}\rho_{\mathrm{t}}\nabla^{\beta}\rho_{\mathrm{t}}\nabla^{\gamma}\rho_{\mathrm{t}}\nabla^{\delta}\rho_{\mathrm{t}}}{\left|\nabla\rho_{\mathrm{t}}\right|^{2}}\right].\end{aligned} \tag{6.58}$$

While this expression may not seem particularly simple, it has the advantage of being mostly comprised of already derived quantities, with some small modifications. Indeed, in this expression some terms themselves contain terms, subterms, which will cancel with subterms from other terms, however attempting to do this results in an expression which is more ugly. This expression can more straightforwardly be extended to spin-polarised systems, with the first 4 lines only gaining an extra sum over spin channels. The final three lines of this expression which are not comprised of potentials and density derivatives can be understood as the terms that arise solely from the change of the gradient operator under strain. These additional terms also have the advantage of being unchanged from the expression for GGA functionals, as shown in equation 12 of Ref [98] although in subtly different notation. If all the τ dependent terms are dropped from this expression, we do recover the GGA expression of equation 12 of Ref [98], however that expression is missing the very first term, $\delta^{\alpha\beta}\delta^{\gamma\delta}E^{\mathrm{XC}}$. Given what they undoubtedly went through to get that expression, they can perhaps be forgiven this minor slip.

Internal Strain terms

For the XC energy contribution to the force-response internal-strain tensor, we can obtain the expression by substituting a pair of strain perturbations $\eta_{\alpha\beta}$ and $R_{I,\gamma}$ for the general perturbations λ and μ in equation 3.77. This gives,

$$\begin{aligned}\frac{\partial^2 E^{\mathrm{XC}}}{\partial\eta_{\alpha\beta}\partial R_{I,\gamma}} = \delta^{\alpha\beta}\frac{\Omega}{N_{\mathrm{p}}}\sum_i^{N_{\mathrm{p}}}\left[V_\rho^{\mathrm{XC}}\frac{\partial\rho_{\mathrm{t}}}{\partial R_{I,\gamma}} + V_\tau^{\mathrm{XC}}\frac{\partial\tau_{\mathrm{t}}}{\partial R_{I,\gamma}}\right] \\ + \frac{\Omega}{N_{\mathrm{p}}}\sum_i^{N_{\mathrm{p}}}\left[V_\rho^{\mathrm{XC}}\frac{\partial^2\rho_{\mathrm{t}}}{\partial\eta_{\alpha\beta}\partial R_{I,\gamma}} + V_\tau^{\mathrm{XC}}\frac{\partial^2\tau_{\mathrm{t}}}{\partial\eta_{\alpha\beta}\partial R_{I,\gamma}}\right. \\ \left. + \frac{\partial V_\rho^{\mathrm{XC}}}{\partial\eta_{\alpha\beta}}\frac{\partial\rho_{\mathrm{t}}}{\partial R_{I,\gamma}} + \frac{\partial V_\tau^{\mathrm{XC}}}{\partial\eta_{\alpha\beta}}\frac{\partial\tau_{\mathrm{t}}}{\partial R_{I,\gamma}}\right],\end{aligned} \tag{6.59}$$

where it can be seen that many of the terms of the general expression cancel due to the fact that there is zero change to the cell volume and gradient operator under an atomic displacement perturbation.

6.2.5 Implementation

The expressions derived above were implemented in a development branch of CASTEP. The derivations and their implementations were then verified by comparing the elastic constant tensor calculated from this implementation to the elastic constants tensor calculated using a finite-displacement (FD) method. The FD method is performed by applying a small strain to the unit cell lattice, re-

calculating the ground-state density, and calculating the stress and forces in the strained configuration. By performing forward and backward steps of strain, the second-order energy derivatives can be calculated from the displaced stress and forces using the centred difference formula. Provided both the DFPT and FD calculations are well-converged, the derivatives obtained should be in excellent agreement. The results of this comparison are presented in the following section.

6.3 Verification: Silicon

For a verification test, silicon was again chosen as our test system. First, we shall compare the explicit energy derivatives, the frozen-ion elastic constants, and the force-response internal-strain, tensor computed using the DFPT and FD methods for silicon. Then, we shall move on to comparing the values calculated for the relaxed-ion elastic constant tensor against experiment and against different theoretical methods for silicon and other materials.

6.3.1 Energy Derivatives

Due to the symmetry of silicon's crystal structure, the frozen-ion elastic constants has only 3 unique, non-zero values and the force-response internal-strain tensors have only 1 unique, non-zero values. The relaxed-ion elastic constant tensor also has only 3 unique, non-zero values. Using Voigt notation to denote the different strain directions, where $1 = xx$, $2 = yy$, $3 = zz$, $4 = yz$, $5 = zx$, $6 = yx$, the elastic constant tensor can be reduced from a rank-4 tensor to a 6×6 matrix with no loss of information, i.e. $C^{\alpha\beta\gamma\delta} = C^{ij}$, the 6×6 matrix is sometimes referred to as the compliance matrix. In Voigt notation, the 3 unique values of the elastic constant tensor for silicon are C^{11}, C^{21} and C^{44}, other non-zero elements of the tensor will be equal to the value of one of these 3 elements.

The force-response internal-strain tensors, $\Lambda_I^{\alpha\beta\gamma}$, can also be reduced from a rank-3 tensor to a 6×3 matrix using Voigt notation for the strain directions, $\Lambda_I^{i\gamma}$. For the silicon primitive cell, the only non-zero values of $\Lambda_I^{\alpha\beta\gamma}$ are when each of the 3 indices in the rank-3 tensor notation are different, i.e. $\alpha \neq \beta \neq \gamma$, and the two different ions should have equal and opposite values $\Lambda_I^{\alpha\beta\gamma} = -\Lambda_J^{\alpha\beta\gamma}$ to preserve translational symmetry.

The ground-state was found for the silicon primitive cell, see figure 4.1, however this time using a cut-off energy which was slightly higher. The cut-off was increased until the value computed for stress converged to 0.01 GPa, this was found to be 600 eV. The Brillouin zone was sampled using a Monkhorst-Pack grid with

a mesh of $8 \times 8 \times 8$ k-points (equivalent to a k-point spacing of 0.04 2πÅ). The crystal structure symmetry was used to reduce the number k-points required to only those in the irreducible wedge of the Brillouin zone and to symmetrise the forces and stresses. This level of k-point sampling was found to be well converged. The grids used for the density and KED were the minimum needed to represent the density of the wave functions, i.e. using `grid_scale` of 2 and using the same grid for the so-called "fine grid". The system was tested using the PBE and r2SCAN functionals, a GGA and a mGGA functional respectively. The PBE calculations were performed so that the agreement between the DFPT and the FD calculations could be compared between the different families of functionals. An XC grid was used to bring the XC integration error below 1 μeV per cell, for the PBE calculations, this corresponds to an XC grid scale of 4, and for the r2SCAN calculations this corresponds to an XC grid scale of 10.

The SCF procedure to find the ground state was continued until the ground state energy converged to 10^{-10} eV per atom and the unsymmetrised ground state forces converged to 10^{-8} eV/Å. The ground-state structure of the silicon primitive cell was also computed for both functionals. In the case of both functionals, the geometry optimisation procedure was continued until the stress was found to be less than 10^{-3} GPa. For the PBE calculation the lattice vectors of the primitive cell were found to be $a = 3.865$ Å whereas the r2SCAN structure was found to have lattice vectors of $a = 3.817$ Å. This is excessively well converged for most calculations; however, it was done here to minimise the error in the ground-state, such that we can exclude under convergence of the ground-state as the cause of any disagreement between the DFPT calculations and the FD calculations.

DFPT calculations were performed using CASTEP's variational minimiser which uses a conjugate gradient algorithm [96] to vary the first-order wavefunctions to minimise the energy derivative calculated according to equation 3.40. The convergence criterion for the variational solver is that the second-order energy derivative varies less than a convergence tolerance between successive steps of the conjugate gradient algorithm, this tolerance was set to 10^{-7} eV. To calculate the off-diagonal elements of the elastic constant tensor, and the force-response internal-strain tensor, the expressions given in equations 6.4 and 6.5 were used. FD calculations were performed using the same convergence criteria as the ground-state calculation and were performed using a finite strain of 0.001, corresponding to a 0.1% stretching of the lattice vectors.

Table 6.1 shows the results of these calculations, which show the DFPT and FD methods to be in excellent agreement, with the largest discrepancy in the r2SCAN results for C^{ij} being 8×10^{-4} GPa which is the same order of magnitude as the largest error in the PBE results of 5×10^{-4} GPa. The discrepancy in the mGGA

	PBE			r2SCAN		
	DFPT	FD	Difference	DFPT	FD	Difference
C^{11}	153.175247	153.175286	0.000039	168.849882	168.850593	0.000711
C^{12}	56.080631	56.081199	0.000568	61.101629	61.102407	0.000778
C^{44}	99.762010	99.762156	0.000146	108.816242	108.816474	0.000232
$\Lambda^{\alpha\beta\gamma}$	9.065613	9.065604	0.000009	9.516626	9.516705	0.000079

Table 6.1: Comparison of the elements of the elastic constants tensor, C^{ij}, and the force-response internal-strain tensors, $\Lambda^{\alpha\beta\gamma}$, of silicon calculated using finite displacement and DFPT using the PBE and r2SCAN functionals. The C^{ij} elements are given in units of GPa and the $\Lambda^{\alpha\beta\gamma}$ elements are given in units of eV/Å.

results for $\Lambda^{\alpha\beta\gamma}$ is 8×10^{-4} $eV/$ Å which although an order of magnitude larger than the discrepancy in the PBE results, is still very small. These results are comparable to the agreement between DFPT and FD achieved by Hamann *et al* in their original publication of the method of calculating the elastic constants. This is sufficient evidence for the derivations described in the previous section and their implementation into CASTEP to be considered correct.

6.4 Comparison With Experiment

Now that the method has been verified as correct, we can start drawing a comparison between the values computed for the elastic constants tensor using r2SCAN, the values computed using other theoretical methods and those found experimentally. There are various different theoretical methods that can be used to model the exchange and correlation interaction; local and semi-local DFT methods are more simple and computationally efficient methods with reasonable yet limited accuracy, wavefunction methods or "hybrid functionals" which include some fraction of Hartree-Fock exchange can be more accurate, however the computational cost is significantly higher, and further there are many-body perturbation theory methods, which are yet more accurate, but suffer from enormous computational cost when compared to semi-local DFT. One recent publication, [5], makes a comparison of the elastic constants of silicon and diamond carbon calculated using a range of theoretical methods against experiment, including HSE, a hybrid functional, and the Random Phase Approximation (RPA), a many-body perturbation theory method.

In tables 6.2 and 6.3 the results of Ref [5] are shown. The Mean Average Error (MAE) is calculated from the difference between the predicted result and the average of the experimental values. The results of Ref [5] show that among the

	LDA	PBE	HSE	RPA	r2SCAN (this work)	Expt [113]	Expt [114]	Expt [115]
C^{11}	160.4	152.64	169.7	166.08	168.850	165.64	165.77	165.7
C^{12}	64.8	56.66	63.01	65.82	61.102	63.94	63.92	63.9
C^{44}	75.45	74.79	82	89.58	82.936	79.51	79.62	79.5
MAE	3.43	8.35	2.45	4.10	3.12	-	-	-

Table 6.2: Comparison of experimental and theoretical elastic constants of silicon. The values given for the elements of the elastic constants tensor are in units of GPa. The values quoted for the LDA, PBE, HSE and RPA results were found by [5], the different experimental values are quoted with their reference, the r2SCAN result is derived from this work.

	LDA	PBE	HSE	RPA	r2SCAN (this work)	Expt [116]	Expt [117]	Expt [118]
C^{11}	1105.6	1053	1141.6	1074.4	1099.850	1079	1076.4	1080.4
C^{12}	129.4	125	140.2	128.6	118.730	124	125.2	127
C^{44}	592.6	560.2	620	576.9	579.833	578	577.4	578.16
MAE	15.24	14.55	39.98	2.78	9.97	-	-	-

Table 6.3: Comparison of experimental and theoretical elastic constants of diamond carbon. The values given for the elements of the elastic constants tensor are in units of GPa. The values quoted for the LDA, PBE, HSE and RPA results were found by [5], the different experimental values are quoted with their reference, the r2SCAN result is derived from this work.

	LDA (this work)	PBE (this work)	PBE [109]	HSE [119]	r2SCAN (this work)	Expt [6, 7]
C^{11}	397.16	372.69	379	413.0	409.08	411 ±10
C^{12}	143.10	126.61	128	142.1	137.31	149 ±10
C^{33}	375.65	356.79	355	380.8	390.29	389 ±10
C^{31}	111.07	96.09	96	110.2	103.36	99 ±4
C^{44}	115.26	111.01	112	123.5	123.04	125 ±5
C^{66}	127.03	123.04	125	135.45	135.88	131±10
MAE	9.81	19.62	18.16	5.76	4.23	-

Table 6.4: Comparison of experimental and theoretical elastic constants of AlN. The values given for the elements of the elastic constants tensor are in units of GPa. The experimental values are those recommended by Ref [6] which reviewed several experimental techniques and suggests the results of Ref [7] to be most accurate.

theoretical methods tested, the RPA consistently performs well in both systems; however, HSE is the most accurate for silicon, but for diamond it is by far the least accurate of the methods tested. Of the local and semi-local functionals tested, LDA performs better than PBE for silicon, and their performance is fairly comparable for diamond, despite the significantly stronger theoretical grounding of PBE. This is not an unexpected result given the LDA tendency to "overbind" and the GGA tendency to "underbind". However, their chosen methods do not include any mGGA functionals in their comparisons.

DFPT calculations were performed for the elastic constants of silicon and diamond carbon using the r2SCAN functional to draw a comparison with each of the theoretical methods used in Ref [5]. For the silicon calculations a cut-off energy of 600 eV was used with an $8 \times 8 \times 8$ k-point grid for sampling of the first Brillouin zone, with a grid scale and a fine grid scale of 2. An XC grid scale of 10 was used, which was found to reduce the translational energy variance to less than 1 μeV. For the diamond calculations a cut-off energy of 1500 eV was used with an $14 \times 14 \times 14$ k-point grid for sampling of the first Brillouin zone, with a grid scale and a fine grid scale of 2. An XC grid scale of 8 was used, which was found to reduce the translational energy variance to less than 1 μeV per cell. For each system, the convergence tolerance for energy in the SCF procedure was 10^{-10} eV and for geometry relaxation, the convergence tolerance was a stress less than 5×10^{-4} GPa. The lattice parameter of the silicon and diamond carbon primitive cell was found to be $a = 3.817$ Å and $a = 2.5238$ Å, respectively. The DFPT calculations used the variational solver and the second derivatives of the energy converged to a change of less than 10^{-7} eV between each step of the solver.

The results for the elastic constants of silicon and diamond carbon are also presented in 6.2 and 6.3 together with the results of Ref [5]. Compared to the results of the LDA and PBE, r2SCAN is clearly much closer to the experimental results, with a much smaller MAE compared LDA and PBE in both silicon and diamond.

Aluminium Nitride, AlN, is a very wide band-gap semiconductor with a strong piezoelectric response and can be used to make LEDs in the ultra-violet wavelength [120]. An advantage of AlN for the purposes of this study is that the stable phase of AlN at ambient conditions is a wurtzite structure which has hexagonal symmetry, which is significantly different from the crystal structure of the materials discussed so far. Materials with a wurtzite crystal structure have 6 unique values in their elastic constants tensor, however only 5 of those values are independent, C^{11}, C^{21}, C^{33}, C^{31} & C^{44}, the final value, C^{66} is a linear combination of the independent values, such that $C^{66} = \frac{C^{11} - C^{21}}{2}$. A further advantage is that there are also a number of experimental and theoretical predictions of elastic constants in the literature against which we can compare the values calculated using

the methods developed in this thesis [6, 7, 109, 119].

The calculations of the AlN elastic properties were performed using a selection of XC functionals, the LDA (PW parametrisation [3]), PBE [2], and r2SCAN [36]. A cut-off energy of 1500 eV was used for all functionals, with a $13 \times 13 \times 7$ Monkhorst-pack grid of k-points, which corresponds to a reciprocal space sampling of 0.03 $2\pi\text{Å}^{-1}$. The default grids were used for density and potentials, except for when computing the XC components of the energy, where the grid size was chosen to reduce the translational symmetry breaking to below 1 μeV, which was found to be an XC grid scale of 4 for LDA, 6 for PBE, and 10 for r2SCAN. The SCF procedure in the ground-state calculations converged the total energy per atom to 10^{-10} eV, the geometry relaxations the atomic forces and cell stress were minimised to be smaller than 10^{-3} eV/Å and 10^{-3} GPa respectively. In the self-consistent calculation of the first order wavefunctions, the diagonal elements of the dynamical matrix and elastic constants were converged using the Green's function solver to 10^{-6} eV/Å^2 and 10^{-6} eV respectively.

The results of each calculation of the AlN elastic constants are shown in table 6.4, also shown in table 6.4 are previous theoretical predictions and experimental results. Comparing the results of this work to previous theoretical predictions, the results of PBE calculation performed in this work is in reasonable agreement with the PBE calculation of Ref [109], with the slight discrepancies being attributable to different code bases and different pseudopotentials, coming before the work of the Delta project, which significantly improved reproducibility across DFT simulation packages [70]. Comparing each of the methods shown against the experimental result, it can be seen that r2SCAN has the smallest MAE, marginally smaller than the MAE of HSE, a significantly more expensive theoretical method, and the r2SCAN MAE is almost a quarter the MAE of the PBE calculations and is half that of the LDA calculation. r2SCAN and HSE are both with in the error bars of all the experimental results bar one, the C^{31} element for HSE and the C^{12} element for r2SCAN.

6.5 Conclusion

In this chapter the derivation of the necessary additional terms to calculate the Elastic constants tensor from DFPT using a meta-GGA functional has been presented. Results from the presented DFPT method are found to be in excellent agreement with finite difference calculations, verifying the derivations and their implementation within CASTEP. Comparison was then made between the predictions of a selection of XC functionals, including the mGGA functional r2SCAN,

and wavefunction methods where available in the literature. These predictions are compared against the experimentally measured values and it was found that the LDA and GGA functional tested were far less accurate than r2SCAN in all cases. When compared against the wavefunction methods r2SCAN is either found to be fairly comparable in accuracy, but as a semi-local XC approximation, is far less computationally demanding.

These results again demonstrate that DFT calculations using r2SCAN are a powerful theoretical technique, with an accuracy comparable to that of high-level theoretical methods, at a fraction of the computational cost. A larger study including a wider variety of materials is needed to determine the extent of r2SCAN's accuracy for elastic constants across the material landscape with the enhanced accuracy that DFPT provides; however, these initial results are very promising.

Chapter 7

Conclusions

The aim of this thesis was to extend the theoretical framework of DFPT to include meta-GGA functionals. Having covered the necessary details of the theoretical framework in previous chapters, this chapter attempts to bring the need for this work into focus by using the methods developed throughout the thesis to make a coarse prediction of the thermoelectric properties of TaFeSb using the meta-GGA functional r2SCAN. Recall from chapter 1 that the change from a GGA functional, PBE, to r2SCAN had a very small effect on the relaxed lattice parameters and most of the features of the electronic structure, other than the band gap which increased by 20%. Therefore, it could be expected that there would be similarly small changes in qualitative behaviour in the predicted values of the thermoelectric figure of merit, ZT. However, as illustrated in this chapter, this is not necessarily the case.

To conclude, the work presented in the thesis is summarised, and the outlook on future work is discussed.

7.1 ZT of TaFeSb : a meta-GGA Prediction

As a promising thermoelectric material, there have been several publications investigating the various properties of TaFeSb, both experimental and theoretical [23, 24, 27]. These results tend to focus on the electronic structure and change of the thermoelectric figure of merit, ZT, under the effect of doping. Here, we shall use the methods developed in the thesis to explore the change in the prediction of ZT under a change of the XC functional, going from the GGA functional PBE, to the meta-GGA functional r2SCAN. The presented results are intended to show that a change in XC functional can make a significant difference to predicted material properties. In the case of TaFeSb, this is despite the fact that beyond the band gap there is very little change in the electronic structure. The results

in this section should not be interpreted as an earnest prediction of the ZT of TaFeSb since the choice of transport models is not necessarily applicable. With that in mind, we shall continue.

As discussed in the introductory chapter, the expression for ZT is,

$$ZT = \frac{S^2\sigma}{\kappa_{\text{elec}} + \kappa_{\text{lat}}}T, \tag{7.1}$$

where σ is the electrical conductivity of the material; κ_{elec} and κ_{lat} are the thermal conductivity of the material due to the electrons and the lattice vibrations (phonons) respectively, and S is the Seebeck coefficient of the material. BoltzTraP2 [47] can take the electronic density of states from a DFT simulation and determine values for $\frac{S^2\sigma}{\tau}$ and $\frac{\kappa_{\text{elec}}}{\tau}$ where τ is the scattering time of the charge carriers. In order to make a prediction of the thermoelectric efficiency for TaFeSb, two additional quantities are required, the scattering time of the charge carriers, τ, and the thermal conductivity due to the lattice, κ_{lat}.

7.1.1 Charge Carrier Scattering Time, τ

At low temperatures and low doping levels, τ is dominated by electron-phonon interactions and therefore can be approximated as purely the electron-phonon contribution, $\tau = \tau_{\text{e-ph}}$. We shall discuss two approaches of calculating $\tau_{\text{e-ph}}$ here, direct calculation of the electron-phonon coupling matrix elements, and the deformation potential approximation.

Direct calculation of the electron-phonon coupling matrix elements requires the first-order change in Hamiltonian under the perturbation of a phonon mode, see Section 3.2.1.1 equation 3.7. This can be obtained from the sum over the first-order changes in the Hamiltonian under the movement of each atom in the phonon mode, weighted by their contribution to the phonon eigenvector. The first-order change of the Hamiltonian under the movement of each atom can be obtained via the methods set out in Chapter 4 of this thesis, thus the work set out there enables direct calculation of the electron-phonon coupling matrix elements within the meta-GGA formalism. The electron-phonon coupling matrix elements have wider applicability, beyond just thermoelectric materials, to any material property involving transport, including superconductivity [121, 122]. The number of calculations necessary to predict a value for $\tau_{\text{e-ph}}$ using the electron-phonon coupling matrix elements is still vast, so for the illustrative purposes of this section, we instead turn to a far less computationally intense method.

The acoustic deformation potential approximation is often applied to semiconductors, and assumes that the long wavelength acoustic phonon modes are the

dominant modes involved in the electron-phonon scattering process (§3.2.3.2). The predictions of ZT for TaFeSb in the literature [23, 24] have all made use of the deformation potential theory to calculate $\tau_{\text{e-ph}}$. The expression for $\tau_{\text{e-ph}}$ is given in 3.16 but is repeated here,

$$\frac{1}{\tau_{\text{e-ph}}} = \frac{\lambda_{\text{ADP}}^2 \pi N(\epsilon_{\text{F}}) k_{\text{B}} T}{\hbar C^{\alpha\beta\alpha\beta}}, \tag{7.2}$$

which involves several material properties, the diagonal element of the elastic constants tensor, $C^{\alpha\beta\alpha\beta}$, the density of states at the Fermi level, $N(\epsilon_{\text{F}})$, which is a function of both material doping and temperature. The elastic constants tensor can be straightforwardly be obtained using the methods described in Chapter 6, and $N(\epsilon_{\text{F}})$ is determined by BoltzTraP2.

Finally, recall that λ_{ADP} is the acoustic deformation potential, which can be expressed as the derivative of the band edge energies, ϵ_{BE}, with respect to a strain,

$$\lambda_{\text{ADP}} = \frac{d\epsilon_{\text{BE}}}{d\eta_{\alpha\beta}}, \tag{7.3}$$

where the derivative of the valence band maximum is used to determine the scattering rate of the p-doped material and the derivative of the conduction band minimum is used to determine the scattering rate of the n-doped material. The derivatives of the band energies with respect to a perturbation can be obtained directly from DFPT calculations as described in 3.4.1.3.

7.1.2 Lattice Thermal Conductivity, κ_{lat}

Prediction of the lattice thermal conductivity, κ_{lat}, can be done in several ways. The work set out in this thesis should be impactful when using any of the existing methods in combination with meta-GGA functionals. For molecular dynamics based methods such as the Green-Kubo approach [123], the work presented in chapter 5 will remove the numerical noise from the energy landscape and improve their accuracy. The work presented in chapter 4 allows the calculation of the phonon density of states and group velocities to be used with the Callaway-Holland model [124, 125]. This work enables far more efficient calculation of the harmonic interatomic force constants via DFPT, which can then be used to solve the Boltzmann transport equation for phonons [126, 127, 128]. However, the necessary additional terms to calculate the anharmonic interatomic force constants, which are required to go beyond the constant relaxation-time approximation, have not yet been handled. The anharmonic interatomic force constants must still be calculated by finite difference calculation, where the work of Chapter 5 again becomes useful in removing the numerical noise from the energy landscape.

Again, for the illustrative purposes of this section, we shall choose to use a less computationally intense method. The Slack model [129] is an empirically fitted model that has limited applicability beyond the materials for which it was originally fitted. However, it has the advantage that it depends only on a handful of material constants. It should be made clear that there is little to no expectation that the values for κ_{lat} obtained from Slack's model are in any way accurate predictions; it merely serves a purpose here to show how the predictions from a GGA and a meta-GGA functional can vary.

It is a somewhat convoluted journey from the elastic constants to the lattice thermal conductivity, which here we shall follow in reverse, starting with the expression for the lattice thermal conductivity. In Slack's model, κ_{lat} can be computed as follows,

$$\kappa_{\text{lat}} = \frac{2.61 \times 10^{-6}}{1 - \frac{0.514}{\gamma} + \frac{0.288}{\gamma^2}} \frac{\Theta_{\text{D}}^3 V_{at}^{\frac{1}{3}} m_{\text{av}}}{\gamma^2 n_{\text{at}}^{\frac{2}{3}} T}, \tag{7.4}$$

where, Θ_{D} is the Debye temperature and γ is the Gruneisen parameter. The other quantities in the equation are V_{at}, the volume per atom in units of angstroms, m_{av}, the average atomic mass in atomic mass units, n_{at}, the number of atoms per unit cell, and T the temperature [129]. Both Θ_{D} and γ can be determined from the elastic constant tensor through v_{av}, the average velocity of sound in the material [86]. This can be done using the following relations; the longitudinal sound velocity v_{L} and the transverse sound velocity v_{T} can be determined from the density of the material, ρ, and the Bulk (B) and Shear (G) moduli,

$$v_{\text{L}} = \sqrt{\frac{B + \frac{4}{3}G}{\rho}}, \tag{7.5}$$

$$v_{\text{T}} = \sqrt{\frac{G}{\rho}}, \tag{7.6}$$

note that the Bulk and Shear moduli can be determined directly from the elastic constants tensor. The longitudinal and transverse sound velocity can then be combined to produce the average sound velocity, v_{av},

$$v_{\text{av}} = \left[\frac{1}{3} \left(\frac{1}{v_{\text{L}}^3} + \frac{2}{v_{\text{T}}^3} \right) \right]^{-\frac{1}{3}}. \tag{7.7}$$

The Debye temperature is calculated from the average velocity of sound using

the following expression,

$$\Theta_{\mathrm{D}} = \frac{\hbar}{k_{\mathrm{B}}} v_{\mathrm{av}} \left(\frac{6\pi^2 n_{\mathrm{at}}}{\Omega} \right)^{\frac{1}{3}}, \tag{7.8}$$

where n_{at} is again the number of atoms per unit cell and Ω is the volume of the unit cell. The acoustic Gruneisen parameter can be determined from the Poisson ratio, ν, which can be calculated from the transverse and longitudinal velocities of sound,

$$\nu = \frac{1 - 2\left(v_{\mathrm{T}}^2 / v_{\mathrm{L}}^2\right)}{2 - 2\left(v_{\mathrm{T}}^2 / v_{\mathrm{L}}^2\right)}, \qquad \gamma = \frac{3}{2}\left(\frac{1+\nu}{2-3\nu}\right). \tag{7.9}$$

7.1.3 TaFeSb calculations

The calculations of the TaFeSb properties were performed using two XC functionals, PBE [2], and r2SCAN [36]. A cut-off energy of 2000 eV was used for all functionals, with a $9 \times 9 \times 9$ Monkhorst-pack grid of k-points, which corresponds to a reciprocal space sampling of 0.021 $2\pi\text{Å}^{-1}$.

The default grids were used for the density and potentials, except for when computing the XC components of the energy, where the grid size was chosen to reduce the translational symmetry breaking to below 1 μeV, which was found to be an XC grid scale of 4 for LDA (Perdew-Wang parametrisation), 6 for PBE and 10 for r2SCAN. The SCF procedure in the ground-state calculations converged the total energy per atom to 10^{-10} eV, the geometry relaxations the atomic forces and cell stress were minimised to be smaller than 10^{-3} eV/Å and 10^{-3} GPa respectively. In the self-consistent calculation of the first-order wavefunctions, the diagonal elements of the dynamical matrix and elastic constants were converged using the Green's function solver to 10^{-6} eV/Å^2 and 10^{-6} eV respectively.

The values determined for the elastic constants and the deformation potentials in the case of each functional are presented in Table 7.1 and Table 7.2, respectively. Also presented are the results reported in Ref [23]. The results of Ref [23] are in reasonable agreement with the prediction made in this work using the PBE functional. The difference could be ascribed to a change in the method used to calculate the elastic constants or a change in the pseudopotential library used. The calculations of Ref [23] used a finite difference method to calculate the elastic constants and the "C9" library, while the calculations in this work used the "NCP19" set. In the intervening time between the development of the 'C9" and "NCP19" pseudopotential libraries, significant work was undertaken to ensure the accuracy and transferability of pseudopotentials as part of the Delta project [70].

	PBE [23]	PBE (this work)	r2SCAN (this work)
C^{11}	326.8	329.38	363.68
C^{12}	100.3	97.77	103.81
C^{44}	77.6	76.56	80.14

Table 7.1: Comparison of theoretical predictions of the elastic constants of TaFeSb. The values given for the elements of the elastic constants tensor are in units of GPa.

	PBE [23]	PBE (this work)	r2SCAN (this work)
λ_{VBM} [eV]	11.06	12.69	12.92
λ_{CBM} [eV]	11.81	13.85	14.164

Table 7.2: Comparison of the values obtained for the deformation potentials of the valence band maximum and conduction band minimum of TaFeSb.

This is most likely to account for the differences in the predicted values for the elastic constants, and suggests that the values predicted in this work are likely to be marginally more accurate.

The change in value predicted by the elastic constants when switching from PBE to r2SCAN is more significant, for the C^{12} and C^{44} elements the difference in values is only a few GPa, a percentage change of $\sim 4\%$. However, for the C^{11} element, the difference is over 30 GPa, or a percentage change of $\sim 10\%$. When comparing the deformation potentials obtained from the two functionals, they only differ by $\sim 2\%$. Once again, the values obtained from the meta-GGA functional do not appear to differ dramatically from the values obtained from the GGA functional.

The elastic constants tensors found using each functional can then be used to determine values for the Debye temperature and Gruneisen parameter to then be used in Slack's model for κ_{lat}. The values of the deformation potential can then be combined with the elastic constant tensor to determine the values for $\tau_{\text{e-ph}}$. The values determined for κ_{lat} and $\tau_{\text{e-ph}}$ can then be combined with the values for $\frac{S^2\sigma}{\tau}$ and $\frac{\kappa_{\text{elec}}}{\tau}$ produced by BoltzTrap2.

We can now finally arrive at our predictions of ZT for TaFeSb, with the results of the PBE and r2SCAN calculations presented in Figures 7.1 and 7.2 respectively. Although there have only been quite modest changes when switching XC func-

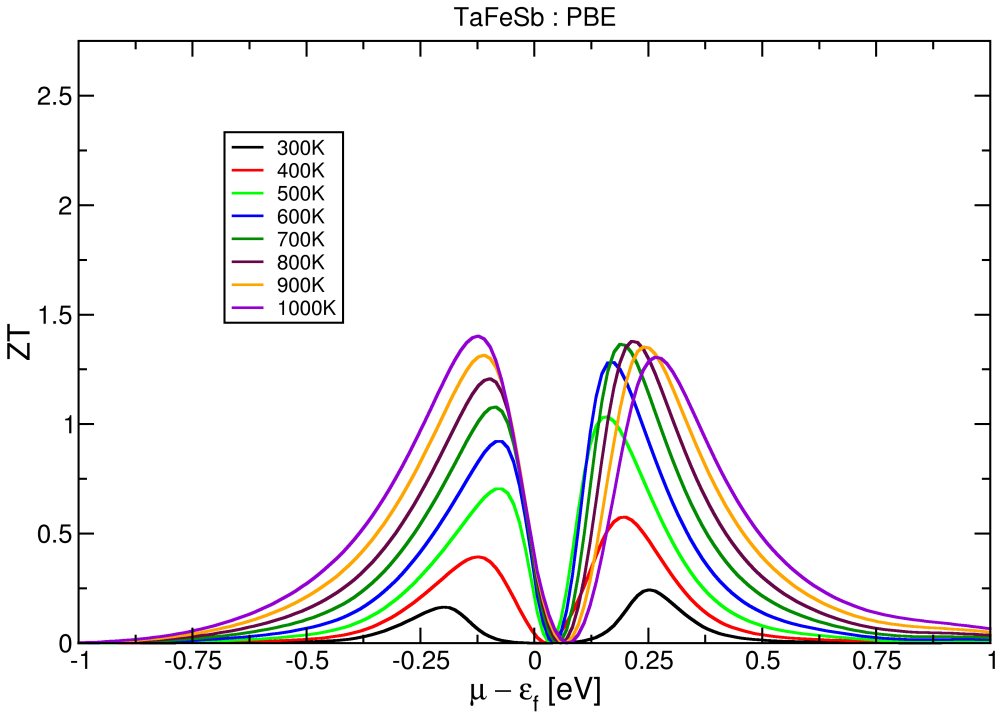

Figure 7.1: *ZT* of TaFeSb calculated using PBE, plotted as a function of the shifted Fermi energy under doping. Each line represents the calculation at a different temperature.

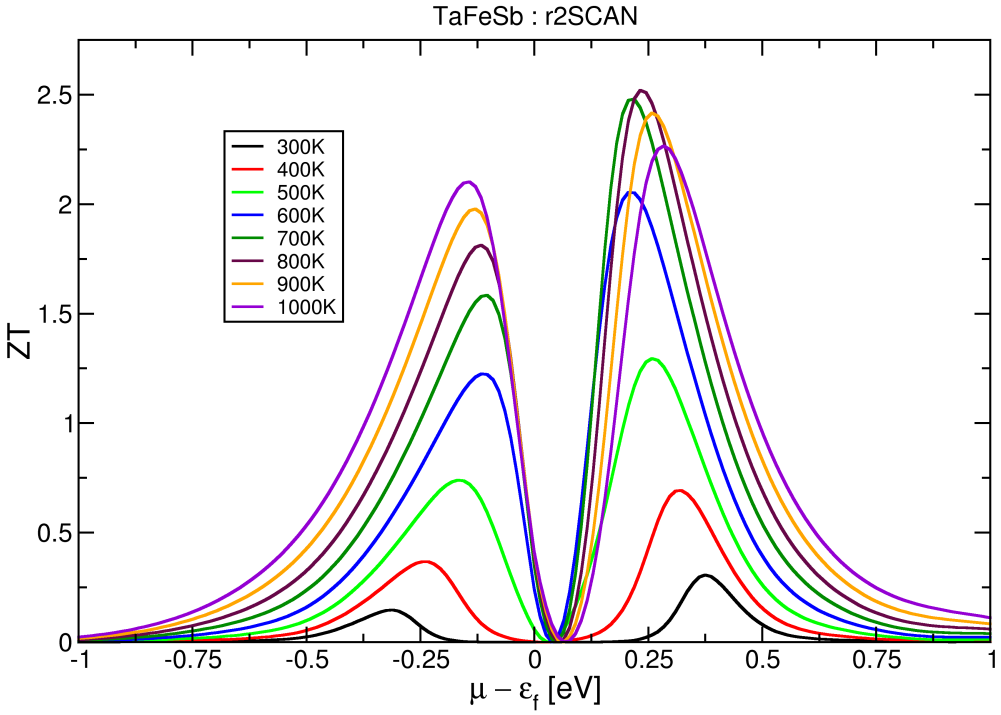

Figure 7.2: *ZT* of TaFeSb calculated using r2SCAN, plotted as a function of the shifted Fermi energy under doping. Each line represents the calculation at a different temperature.

tional in the majority of the properties directly discussed so far, it can be seen that the predicted values of ZT from the r2SCAN calculations are significantly higher than those predicted by PBE, particularly at higher temperatures. For p-doping, the behaviour of ZT is very similar between the two functionals, except the maximum ZT obtained is ~ 1.5 for PBE, and ~ 2.15 for r2SCAN, both at 1000 K and with the Fermi energy shifted down by 0.125 eV. Interestingly, r2SCAN calculations predict a much higher ZT for n-doped TaFeSb showing a qualitative difference in the behaviour of ZT under doping compared to PBE, with a maximum ZT above 2.5 predicted by r2SCAN compared to the maximum ZT just below 1.5 predicted by PBE, both at 800 K and the Fermi energy increased by ~ 0.25 eV. It should not be forgotten that these results are obtained using a very crude model for κ_{lat}, and it is likely that these results are far from accurate. However, the qualitative difference in the doping behaviour between functionals is likely to persist were more accurate method used to calculate values for κ_{lat}, as the effects on κ_{lat} from such minor doping of the material are likely to be minimal.

7.2 Summary and Future Work

The topic of this thesis has been to build the theoretical framework necessary to simultaneously utilise the chemical accuracy of the recently introduced meta-GGA functionals and the computational efficiency of DFPT. However, of the material response functions that can be obtained via DFPT, only the dynamical matrix, the internal-strain force-response matrix, and the frozen-ion elastic constants tensor have been directly touched upon in this thesis. As has been seen, this is sufficient to calculate many interesting and useful material properties, but it is by no means the limit of what is possible using DFPT.

One obvious example of something that has not been touched upon in this thesis is a materials response to applied electric and magnetic fields. The former can be used to calculate the dielectric permittivity of a material [95, 100], the latter can be used to predict the chemical shifts of molecules/materials in Nuclear Magnetic Resonance (NMR) spectroscopy experiments [130]. Both of these applications yield yet more interesting and important materials properties, at potentially increased accuracy with the meta-GGAs. Chapter 3 presents the general derivations of the meta-GGA + DFPT theoretical framework, this should mean that future work to incorporate more response functions should be relatively more straightforward.

The work described in Chapter 5 also has significant and interesting implications.

In that chapter a method was presented for estimating the uncertainty in the calculated energy introduced by a numerical sampling of the XC energy integral, as well as a more efficient method of avoiding the numerical issues. The cut-off energy and k-point mesh are other examples where it would be useful to determine an energy uncertainty related to numerical sampling parameters.

This is becoming more relevant as it becomes increasingly common to automate DFT calculations for a wide range of materials using a predetermined best guess at the appropriate cut-off energy and k-point mesh for the materials under study. This usually leads to one of three possibilities, either, the researcher chooses a set of parameters which are overkill for the majority of materials under study and wastes a considerable amount of compute power, the researcher chooses a set of parameters which are significantly under-converged for most materials under study and generates inaccurate results of little use, or, some mixture of these possibilities with few ways to tell which results fall into which category. Clearly, a methodology which could provide some estimate of the accuracy of the chosen numerical parameters would be of immense use in these applications and others. There is a possibility that the work described in Chapter 5 could be the foundation of such a methodology.

Bibliography

[1] J. He and T. M. Tritt. Advances in thermoelectric materials research: Looking back and moving forward. *Science*, 357(6358), 2017.

[2] John P. Perdew, Kieron Burke, and Matthias Ernzerhof. Generalized Gradient Approximation Made Simple. *Phys. Rev. Lett.*, 77:3865–3868, Oct 1996.

[3] John P. Perdew and Yue Wang. Accurate and simple analytic representation of the electron-gas correlation energy. *Phys. Rev. B*, 45:13244–13249, Jun 1992.

[4] Jonathan H. Lloyd-Williams and Bartomeu Monserrat. Lattice dynamics and electron-phonon coupling using nondiagonal supercells,. *Phys. Rev. B*, 92:184301, 2015.

[5] M. Barhoumi, D. Rocca, M. Said, and S. Lebègue. Elastic and mechanical properties of cubic diamond and silicon using density functional theory and the random phase approximation. *Solid State Communications*, 324:114136, 2021.

[6] I. Vurgaftman and J. R. Meyer. Band parameters for nitrogen-containing semiconductors. *Journal of Applied Physics*, 94(6):3675–3696, 09 2003.

[7] Laurie E. McNeil, Marcos Grimsditch, and Roger H. French. Vibrational spectroscopy of aluminum nitride. *Journal of the American Ceramic Society*, 76(5):1132–1136, 1993.

[8] IEA. Global Energy Review 2025. Technical report, IEA, Paris, 2025.

[9] IEA. Government Energy Spending Tracker. Technical report, IEA, Paris, 2023.

[10] Mohamed Elsheikh, Dhafar Shnawah, Mohd Faizul Mohd Sabri, Suhana Mohd Said, H.H. Masjuki, Mohamed Bashir, and Mahazani Mohamad. A review on thermoelectric renewable energy: Principle parameters that affect

their performance. *Renewable and Sustainable Energy Reviews*, 30:337–355, 02 2014.

[11] Geoffroy Hautier, Anubhav Jain, bullet Shyue, and Shyue Ong. From the computer to the laboratory: Materials discovery and design using first-principles calculations. *Journal of Materials Science*, 47, 05 2012.

[12] R. O. Jones. Density Functional Theory: Its origins, rise to prominence, and future. *Rev. Mod. Phys.*, 87:897–923, Aug 2015.

[13] P. Hohenberg and W. Kohn. Inhomogeneous electron gas. *Phys. Rev.*, 136:B864–B871, 1964.

[14] W. M. C. Foulkes, L. Mitas, R. J. Needs, and G. Rajagopal. Quantum Monte Carlo simulations of solids. *Rev. Mod. Phys.*, 73:33–83, Jan 2001.

[15] Rodney J. Bartlett and Monika Musiał. Coupled-cluster theory in quantum chemistry. *Rev. Mod. Phys.*, 79:291–352, Feb 2007.

[16] J. P. Perdew and Alex Zunger. Self-interaction correction to density-functional approximations for many-electron systems. *Phys. Rev. B*, 23:5048–5079, May 1981.

[17] Rabeya Bosry Smriti, Wenjie Li, Amin Nozariasbmarz, Subrata Ghosh, Na Liu, Christopher D. Rahn, Mohan Sanghadasa, Shashank Priya, and Bed Poudel. Thermoelectric Energy Harvesting for Exhaust Waste Heat Recovery: A System Design. *ACS Applied Materials & Interfaces*, 17(3):4904–4912, Jan 2025.

[18] J. R. Sootsman, D. Y. Chung, and M. G. Kanatzidis. New and old concepts in thermoelectric materials. *Angewandte Chemie International Edition*, 48(46):8616–8639, 2009.

[19] D. A. Wright. Thermoelectric properties of bismuth telluride and its alloys. *Nature*, 181(4612):834–834, Mar 1958.

[20] Hayati Mamur, M.R.A. Bhuiyan, Fatih Korkmaz, and Mustafa Nil. A review on bismuth telluride (Bi_2Te_3) nanostructure for thermoelectric applications. *Renewable and Sustainable Energy Reviews*, 82:4159–4169, 2018.

[21] A. J. Hong, L. Li, R. He, J. J. Gong, Z. B. Yan, K. F. Wang, J.-M. Liu, and Z. F. Ren. Full-scale computation for all the thermoelectric property parameters of half-heusler compounds. *Scientific Reports*, 6(1):22778, Mar 2016.

[22] Djallal Eddine Mellah, Kamel Demmouche, and Djamel Bezzerga. Strain effects on electronic and dynamical properties of half-Heusler semiconductors: insights from meta-GGA. *Physica Scripta*, 99(6):065955, may 2024.

[23] G A Naydenov, P J Hasnip, V K Lazarov, and M I J Probert. Huge power factor in p-type half-Heusler alloys NbFeSb and TaFeSb. *Journal of Physics: Materials*, 2(3):035002, Jun 2019.

[24] Hangtian Zhu, Jun Mao, Yuwei Li, Jifeng Sun, Yumei Wang, Qing Zhu, Guannan Li, Qichen Song, Jiawei Zhou, Yuhao Fu, Ran He, Tian Tong, Zihang Liu, Wuyang Ren, Li You, Zhiming Wang, Jun Luo, Andrei Sotnikov, Jiming Bao, Kornelius Nielsch, Gang Chen, David J. Singh, and Zhifeng Ren. Discovery of TaFeSb-based half-Heuslers with high thermoelectric performance. *Nature Communications*, 10(1):270, Jan 2019.

[25] G A Naydenov, P J Hasnip, V K Lazarov, and M I J Probert. Effective modelling of the Seebeck coefficient of Fe_2VAl. *Journal of Physics: Condensed Matter*, 32(12):125401, dec 2019.

[26] Siyuanyang Yin, Qizhu Li, Shaoqin Wang, Jiajun Chen, Zirui Dong, Yubo Zhang, Binghui Ge, Jiye Zhang, and Jun Luo. Structure and thermoelectric properties of half-Heusler-like $TiFeCu_xSb$ alloys. *Journal of Materiomics*, 10(3):523–530, 2024.

[27] A. Grytsiv, V.V. Romaka, N. Watson, G. Rogl, H. Michor, B. Hinterleitner, S. Puchegger, E. Bauer, and P. Rogl. Thermoelectric half-heusler compounds TaFeSb and $Ta_{1-x}Ti_xFeSb$ ($0 \leq x \leq 0.11$): Formation and physical properties. *Intermetallics*, 111:106468, 2019.

[28] Jianwei Sun, Adrienn Ruzsinszky, and John P. Perdew. Strongly constrained and appropriately normed semilocal density functional. *Phys. Rev. Lett.*, 115:036402, Jul 2015.

[29] Albert P. Bartók and Jonathan R. Yates. Regularized SCAN functional. *The Journal of Chemical Physics*, 150(16):161101, 04 2019.

[30] Yoh Yamamoto, Carlos M. Diaz, Luis Basurto, Koblar A. Jackson, Tunna Baruah, and Rajendra R. Zope. Fermi-Löwdin orbital self-interaction correction using the strongly constrained and appropriately normed meta-GGA functional. *The Journal of Chemical Physics*, 151(15):154105, 10 2019.

[31] Zeng-hui Yang, Haowei Peng, Jianwei Sun, and John P. Perdew. More realistic band gaps from meta-generalized gradient approximations: Only in a generalized Kohn-Sham scheme. *Phys. Rev. B*, 93:205205, May 2016.

[32] Steven E. Wheeler and K. N. Houk. Integration grid errors for Meta-GGA-predicted reaction energies: Origin of grid errors for the M06 suite of functionals. *Journal of Chemical Theory and Computation*, 6(2):395–404, 2010. PMID: 20305831.

[33] Erin R. Johnson, Axel D. Becke, C. David Sherrill, and Gino A. DiLabio. Oscillations in meta-generalized-gradient approximation potential energy surfaces for dispersion-bound complexes. *The Journal of Chemical Physics*, 131(3):034111, 07 2009.

[34] James W. Furness and Jianwei Sun. Enhancing the efficiency of density functionals with an improved iso-orbital indicator. *Phys. Rev. B*, 99:041119, Jan 2019.

[35] Susi Lehtola and Miguel A. L. Marques. Many recent density functionals are numerically ill-behaved. *The Journal of Chemical Physics*, 157(17):174114, 11 2022.

[36] J. W. Furness, A. D. Kaplan, J. Ning, J. P. Perdew, , and J. Sun. Accurate and numerically efficient r2SCAN meta-generalized gradient approximation. *J. Phys. Chem. Lett.*, 11:8208, 2020.

[37] James W. Furness, Aaron D. Kaplan, Jinliang Ning, John P. Perdew, and Jianwei Sun. Construction of meta-GGA functionals through restoration of exact constraint adherence to regularized SCAN functionals. *The Journal of Chemical Physics*, 156(3):034109, 01 2022.

[38] Pál D. Mezei, Gábor I. Csonka, and Mihály Kállay. Simple modifications of the SCAN Meta-Generalized Gradient Approximation functional. *Journal of Chemical Theory and Computation*, 14(5):2469–2479, 2018. PMID: 29565589.

[39] Manish Kothakonda, Aaron D. Kaplan, Eric B. Isaacs, Christopher J. Bartel, James W. Furness, Jinliang Ning, Chris Wolverton, John P. Perdew, and Jianwei Sun. Testing the r2SCAN density functional for the thermodynamic stability of solids with and without a van der Waals correction. *ACS Materials Au*, 3(2):102–111, Mar 2023.

[40] Stefan Grimme, Andreas Hansen, Sebastian Ehlert, and Jan-Michael Mewes. r2SCAN-3c: A "swiss army knife" composite electronic-structure method. *The Journal of Chemical Physics*, 154(6):064103, 02 2021.

[41] Ryan Kingsbury, Ayush S. Gupta, Christopher J. Bartel, Jason M. Munro, Shyam Dwaraknath, Matthew Horton, and Kristin A. Persson. Performance comparison of r^2SCAN and SCAN metaGGA density functionals for

solid materials via an automated, high-throughput computational workflow. *Phys. Rev. Mater.*, 6:013801, Jan 2022.

[42] Jinliang Ning, James W. Furness, and Jianwei Sun. Reliable lattice dynamics from an efficient density functional approximation. *Chemistry of Materials*, 34(6):2562–2568, 2022.

[43] Pedro Borlido, Thorsten Aull, Ahmad W. Huran, Fabien Tran, Miguel A. L. Marques, and Silvana Botti. Large-scale benchmark of exchange–correlation functionals for the determination of electronic band gaps of solids. *Journal of Chemical Theory and Computation*, 15(9):5069–5079, Sep 2019.

[44] Sebastian Ehlert, Uwe Huniar, Jinliang Ning, James W. Furness, Jianwei Sun, Aaron D. Kaplan, John P. Perdew, and Jan Gerit Brandenburg. r2SCAN-D4: Dispersion corrected meta-generalized gradient approximation for general chemical applications. *The Journal of Chemical Physics*, 154(6):061101, 02 2021.

[45] S. Swathilakshmi, Reshma Devi, and Gopalakrishnan Sai Gautam. Performance of the r2SCAN functional in transition metal oxides. *Journal of Chemical Theory and Computation*, 19(13):4202–4215, Jul 2023.

[46] Jonathan R. Yates and Albert P. Bartók. Accurate predictions of chemical shifts with the rSCAN and r2SCAN mGGA exchange–correlation functionals. *Faraday Discuss.*, 255:192–202, 2025.

[47] Georg K.H. Madsen, Jesús Carrete, and Matthieu J. Verstraete. BoltzTraP2, a program for interpolating band structures and calculating semi-classical transport coefficients. *Computer Physics Communications*, 231:140–145, 2018.

[48] R. Peierls. Zur kinetischen theorie der wärmeleitung in kristallen. *Annalen der Physik*, 395(8):1055–1101, 1929.

[49] S. J. Clark, M. D. Segall, C. J. Pickard, P. J. Hasnip, M. J. Probert, K. Refson, and M.C. Payne. First principles methods using CASTEP. *Z. Kristall.*, 220:567–570, 2005.

[50] Susi Lehtola, Conrad Steigemann, Micael J.T. Oliveira, and Miguel A.L. Marques. Recent developments in libxc — a comprehensive library of functionals for density functional theory. *SoftwareX*, 7:1–5, 2018.

[51] Warren E. Pickett. Pseudopotential methods in condensed matter applications. *Computer Physics Reports*, 9(3):115–197, 1989.

[52] M. Born and R. Oppenheimer. Zur quantentheorie der molekeln. *Annalen der Physik*, 389(20):457–484, 1927.

[53] L. H. Thomas. The calculation of atomic fields. *Mathematical Proceedings of the Cambridge Philosophical Society*, 23(5):542–548, 1927.

[54] E. Fermi. Un metodo statistico per la determinazione di alcune priorieta dell'atome. *Rend. Accad. Naz. Lincei*, 6(32):602–607, 1927.

[55] W. Kohn and L. J. Sham. Self-consistent equations including exchange and correlation effects. *Phys. Rev.*, 140:A1133–A1138, 1965.

[56] John P. Perdew and Karla Schmidt. Jacob's ladder of density functional approximations for the exchange-correlation energy. *AIP Conference Proceedings*, 577(1):1–20, 07 2001.

[57] Xinguo Ren, Patrick Rinke, Christian Joas, and Matthias Scheffler. Random-phase approximation and its applications in computational chemistry and materials science. *Journal of Materials Science*, 47(21):7447–7471, Nov 2012.

[58] J. A. White and D. M. Bird. Implementation of gradient-corrected exchange-correlation potentials in Car-Parrinello total-energy calculations. *Phys. Rev. B*, 50:4954–4957, Aug 1994.

[59] A. D. Becke. Hartree–Fock exchange energy of an inhomogeneous electron gas. *International Journal of Quantum Chemistry*, 23(6):1915–1922, 1983.

[60] Axel D. Becke. A new inhomogeneity parameter in density-functional theory. *The Journal of Chemical Physics*, 109(6):2092–2098, 08 1998.

[61] Alexei V Arbuznikov and Martin Kaupp. The self-consistent implementation of exchange-correlation functionals depending on the local kinetic energy density. *Chemical Physics Letters*, 381(3):495–504, 2003.

[62] James D. Talman and William F. Shadwick. Optimized effective atomic central potential. *Phys. Rev. A*, 14:36–40, Jul 1976.

[63] R. T. Sharp and G. K. Horton. A variational approach to the unipotential many-electron problem. *Phys. Rev.*, 90:317–317, Apr 1953.

[64] Ross H. Nobes Ralf Neumann and Nicholas C. Handy. Exchange functionals and potentials. *Molecular Physics*, 87(1):1–36, 1996.

[65] A. Seidl, A. Görling, P. Vogl, J. A. Majewski, and M. Levy. Generalized Kohn-Sham schemes and the band-gap problem. *Phys. Rev. B*, 53:3764–3774, Feb 1996.

[66] H. J. Monkhorst and J. D. Pack. Special points for Brillouin-zone integrations. *Phys. Rev. B*, 13:5188–5192, 1976.

[67] S. F. Boys and Alfred Charles Egerton. Electronic wave functions - i. a general method of calculation for the stationary states of any molecular system. *Proceedings of the Royal Society of London. Series A. Mathematical and Physical Sciences*, 200(1063):542–554, 1950.

[68] Joost VandeVondele, Matthias Krack, Fawzi Mohamed, Michele Parrinello, Thomas Chassaing, and Jürg Hutter. Quickstep: Fast and accurate density functional calculations using a mixed Gaussian and plane waves approach. *Computer Physics Communications*, 167(2):103–128, 2005.

[69] Álvaro Ruiz-Serrano, Nicholas D. M. Hine, and Chris-Kriton Skylaris. Pulay forces from localized orbitals optimized *in situ* using a psinc basis set. *The Journal of Chemical Physics*, 136(23):234101, 06 2012.

[70] Kurt Lejaeghere, Gustav Bihlmayer, Torbjörn Björkman, Peter Blaha, Stefan Blügel, Volker Blum, Damien Caliste, Ivano E. Castelli, Stewart J. Clark, Andrea Dal Corso, Stefano de Gironcoli, Thierry Deutsch, John Kay Dewhurst, Igor Di Marco, Claudia Draxl, Marcin Dułak, Olle Eriksson, José A. Flores-Livas, Kevin F. Garrity, Luigi Genovese, Paolo Giannozzi, Matteo Giantomassi, Stefan Goedecker, Xavier Gonze, Oscar Grånäs, E. K. U. Gross, Andris Gulans, François Gygi, D. R. Hamann, Phil J. Hasnip, N. A. W. Holzwarth, Diana Iuşan, Dominik B. Jochym, François Jollet, Daniel Jones, Georg Kresse, Klaus Koepernik, Emine Küçükbenli, Yaroslav O. Kvashnin, Inka L. M. Locht, Sven Lubeck, Martijn Marsman, Nicola Marzari, Ulrike Nitzsche, Lars Nordström, Taisuke Ozaki, Lorenzo Paulatto, Chris J. Pickard, Ward Poelmans, Matt I. J. Probert, Keith Refson, Manuel Richter, Gian-Marco Rignanese, Santanu Saha, Matthias Scheffler, Martin Schlipf, Karlheinz Schwarz, Sangeeta Sharma, Francesca Tavazza, Patrik Thunström, Alexandre Tkatchenko, Marc Torrent, David Vanderbilt, Michiel J. van Setten, Veronique Van Speybroeck, John M. Wills, Jonathan R. Yates, Guo-Xu Zhang, and Stefaan Cottenier. Reproducibility in density functional theory calculations of solids. *Science*, 351(6280):aad3000, 2016.

[71] D. R. Hamann, M. Schlüter, and C. Chiang. Norm-conserving pseudopotentials. *Phys. Rev. Lett.*, 43:1494–1497, Nov 1979.

[72] Leonard Kleinman and D. M. Bylander. Efficacious form for model pseudopotentials. *Phys. Rev. Lett.*, 48:1425–1428, May 1982.

[73] Yi Yao and Yosuke Kanai. Plane-wave pseudopotential implementation and performance of SCAN meta-GGA exchange-correlation functional for extended systems. *The Journal of Chemical Physics*, 146(22):224105, 06 2017.

[74] Jianwei Sun, Martijn Marsman, Gábor I. Csonka, Adrienn Ruzsinszky, Pan Hao, Yoon-Suk Kim, Georg Kresse, and John P. Perdew. Self-consistent meta-generalized gradient approximation within the projector-augmented-wave method. *Phys. Rev. B*, 84:035117, Jul 2011.

[75] Albert P. Bartók and Jonathan R. Yates. Ultrasoft pseudopotentials with kinetic energy density support: Implementing the Tran-Blaha potential. *Phys. Rev. B*, 99:235103, Jun 2019.

[76] P. E. Blöchl. Projector augmented-wave method. *Phys. Rev. B*, 50:17953–17979, Dec 1994.

[77] David Vanderbilt. Soft self-consistent pseudopotentials in a generalized eigenvalue formalism. *Phys. Rev. B*, 41:7892–7895, Apr 1990.

[78] Steven G. Louie, Sverre Froyen, and Marvin L. Cohen. Nonlinear ionic pseudopotentials in spin-density-functional calculations. *Phys. Rev. B*, 26:1738–1742, Aug 1982.

[79] P. P. Ewald. Die Berechnung optischer und elektrostatischer Gitterpotentiale [On the calculation of optical and electrostatic grid potentials]. *Annalen der Physik*, 369(3):253–287, 1921.

[80] M. C. Payne, M. P. Teter, D. C. Allan, T.A. Arias, and J. D. Joannopoulos. Iterative minimization techniques for *ab initio* total-energy calculations - molecular-dynamics and conjugate gradients. *Rev. Mod. Phys.*, 64:1045–1097, 1992.

[81] O. H. Nielsen and Richard M. Martin. Quantum-mechanical theory of stress and force. *Phys. Rev. B*, 32:3780–3791, Sep 1985.

[82] O. H. Nielsen and Richard M. Martin. Stresses in semiconductors: Ab initio calculations on Si, Ge, and GaAs. *Phys. Rev. B*, 32:3792–3805, Sep 1985.

[83] B. G. Pfrommer, M. Cote, S. G. Louie, and M. L. Cohen. Relaxation of crystals with the quasi-Newton method. *J. Comput. Phys.*, 131:233–240, 1997.

[84] R. H. Byrd, J. Nocedal, and R. B. Schnabel. Representations of quasi-Newton matrices and their use in limited memory methods. *Math. Prog.*, 63:129–156, 1994.

[85] Philip B. Allen. Fermi-surface harmonics: A general method for nonspherical problems. application to Boltzmann and Eliashberg equations. *Phys. Rev. B*, 13:1416–1427, Feb 1976.

[86] Orson L. Anderson. A simplified method for calculating the debye temperature from elastic constants. *Journal of Physics and Chemistry of Solids*, 24(7):909–917, 1963.

[87] Xifan Wu, David Vanderbilt, and D. R. Hamann. Systematic treatment of displacements, strains, and electric fields in density-functional perturbation theory. *Phys. Rev. B*, 72:035105, Jul 2005.

[88] J. Bardeen and W. Shockley. Deformation potentials and mobilities in non-polar crystals. *Phys. Rev.*, 80:72–80, Oct 1950.

[89] Jianming Chen, Dong Wang, and Zhigang Shuai. First-principles predictions of thermoelectric figure of merit for organic materials: Deformation potential approximation. *Journal of Chemical Theory and Computation*, 8(9):3338–3347, Sep 2012.

[90] Yeqing Jin, Xiangdong Wang, Mingjia Yao, Di Qiu, David J. Singh, Jinyang Xi, Jiong Yang, and Lili Xi. High-throughput deformation potential and electrical transport calculations. *npj Computational Materials*, 9(1):190, Oct 2023.

[91] Stefano de Gironcoli. Lattice dynamics of metals from density-functional perturbation theory. *Phys. Rev. B*, 51:6773–6776, 1995.

[92] R. P. Feynman. Forces in molecules. *Phys. Rev.*, 56:340–343, Aug 1939.

[93] D. R. Hamann, Xifan Wu, Karin M. Rabe, and David Vanderbilt. Metric tensor formulation of strain in density-functional perturbation theory. *Phys. Rev. B*, 71:035117, Jan 2005.

[94] X. Gonze and J.-P. Vigneron. Density-functional approach to nonlinear-response coefficients of solids. *Phys. Rev. B*, 39:13120–13128, Jun 1989.

[95] Xavier Gonze. First-principles responses of solids to atomic displacements and homogeneous electric fields: Implementation of a conjugate-gradient algorithm. *Phys. Rev. B*, 55:10337–10354, Apr 1997.

[96] K. Refson, P. R. Tulip, and Stewart J. Clark. Variational density-functional perturbation theory for dielectrics and lattice dynamics. *Phys. Rev. B*, 73:155114, 2006.

[97] Stefano Baroni, Paolo Giannozzi, and Andrea Testa. Green's-function approach to linear response in solids. *Phys. Rev. Lett.*, 58:1861–1864, May 1987.

[98] D. R. Hamann, Karin M. Rabe, and David Vanderbilt. Generalized-gradient-functional treatment of strain in density-functional perturbation theory. *Phys. Rev. B*, 72:033102, Jul 2005.

[99] Jinliang Ning, Manish Kothakonda, James W. Furness, Aaron D. Kaplan, Sebastian Ehlert, Jan Gerit Brandenburg, John P. Perdew, and Jianwei Sun. Workhorse minimally empirical dispersion-corrected density functional with tests for weakly bound systems: r^2SCAN + rVV10. *Phys. Rev. B*, 106:075422, Aug 2022.

[100] Xavier Gonze and Changyol Lee. Dynamical matrices, Born effective charges, dielectric permittivity tensors, and interatomic force constants from density-functional perturbation theory. *Phys. Rev. B*, 55:10355–10368, Apr 1997.

[101] K. Kunc and Richard M. Martin. Ab initio force constants of GaAs: A new approach to calculation of phonons and dielectric properties. *Phys. Rev. Lett.*, 48:406–409, Feb 1982.

[102] Ioanna Pallikara, Prakriti Kayastha, Jonathan M Skelton, and Lucy D Whalley. The physical significance of imaginary phonon modes in crystals. *Electronic Structure*, 4(3):033002, jul 2022.

[103] Ben Durham, Matt I J Probert, and Phil J Hasnip. Beating the egg-box effect in plane-wave DFT simulations. *Electronic Structure*, 7(2):025004, may 2025.

[104] Maxim Tafipolsky and Rochus Schmid. A general and efficient pseudopotential Fourier filtering scheme for real space methods using mask functions. *The Journal of Chemical Physics*, 124(17):174102, 05 2006.

[105] Emilio Artacho, E Anglada, O Diéguez, J D Gale, A García, J Junquera, R M Martin, P Ordejón, J M Pruneda, D Sánchez-Portal, and J M Soler. The SIESTA method; developments and applicability. *Journal of Physics: Condensed Matter*, 20(6):064208, jan 2008.

[106] Sebastian P. Sitkiewicz, Rubén R. Ferradás, Eloy Ramos-Cordoba, Robert Zaleśny, Eduard Matito, and Josep M. Luis. Spurious oscillations caused by density functional approximations: Who is to blame? exchange or correlation? *Journal of Chemical Theory and Computation*, 20(8):3144–3153, 2024. PMID: 38570186.

[107] Sebastian P. Sitkiewicz, Robert Zaleśny, Eloy Ramos-Cordoba, Josep M. Luis, and Eduard Matito. How reliable are modern density functional approximations to simulate vibrational spectroscopies? *The Journal of Physical Chemistry Letters*, 13(25):5963–5968, 2022. PMID: 35735354.

[108] Stefano Curtarolo, Gus L. W. Hart, Marco Buongiorno Nardelli, Natalio Mingo, Stefano Sanvito, and Ohad Levy. The high-throughput highway to computational materials design. *Nature Materials*, 12(3):191–201, Mar 2013.

[109] Maarten de Jong, Wei Chen, Thomas Angsten, Anubhav Jain, Randy Notestine, Anthony Gamst, Marcel Sluiter, Chaitanya Krishna Ande, Sybrand van der Zwaag, Jose J. Plata, Cormac Toher, Stefano Curtarolo, Gerbrand Ceder, Kristin A. Persson, and Mark Asta. Charting the complete elastic properties of inorganic crystalline compounds. *Scientific Data*, 2(1):150009, Mar 2015.

[110] M. Råsander and M. A. Moram. On the accuracy of commonly used density functional approximations in determining the elastic constants of insulators and semiconductors. *The Journal of Chemical Physics*, 143(14):144104, 10 2015.

[111] Fabien Tran, Julia Stelzl, and Peter Blaha. Rungs 1 to 4 of DFT Jacob's ladder: Extensive test on the lattice constant, bulk modulus, and cohesive energy of solids. *The Journal of Chemical Physics*, 144(20):204120, 05 2016.

[112] Judith Harl, Laurids Schimka, and Georg Kresse. Assessing the quality of the random phase approximation for lattice constants and atomization energies of solids. *Phys. Rev. B*, 81:115126, Mar 2010.

[113] John J. Hall. Electronic effects in the elastic constants of n-type silicon. *Phys. Rev.*, 161:756–761, Sep 1967.

[114] F. Decremps, L. Belliard, M. Gauthier, and B. Perrin. Equation of state, stability, anisotropy and nonlinear elasticity of diamond-cubic (ZB) silicon by phonon imaging at high pressure. *Phys. Rev. B*, 82:104119, Sep 2010.

[115] H. J. McSkimin and Jr. Andreatch, P. Elastic moduli of silicon vs hydrostatic pressure at 25.0°C and - 195.8°C. *Journal of Applied Physics*, 35(7):2161–2165, 07 1964.

[116] H. J. McSkimin and Jr. Andreatch, P. Elastic moduli of diamond as a function of pressure and temperature. *Journal of Applied Physics*, 43(7):2944–2948, 07 1972.

[117] M. H. Grimsditch and A. K. Ramdas. Brillouin scattering in diamond. *Phys. Rev. B*, 11:3139–3148, Apr 1975.

[118] E. S. Zouboulis, M. Grimsditch, A. K. Ramdas, and S. Rodriguez. Temperature dependence of the elastic moduli of diamond: A Brillouin-scattering study. *Phys. Rev. B*, 57:2889–2896, Feb 1998.

[119] S P Łepkowski and Abdur-Rehman Anwar. Third-order elastic constants and biaxial relaxation coefficient in wurtzite group-iii nitrides by hybrid-density functional theory calculations. *Journal of Physics: Condensed Matter*, 33(35):355402, jul 2021.

[120] Yoshitaka Taniyasu, Makoto Kasu, and Toshiki Makimoto. An aluminium nitride light-emitting diode with a wavelength of 210 nanometres. *Nature*, 441(7091):325–328, May 2006.

[121] E Karaca, P J P Byrne, P J Hasnip, H M Tütüncü, and M I J Probert. Electron–phonon interaction and superconductivity in hexagonal ternary carbides Nb_2AC (A: Al, S, Ge, As and Sn). *Electronic Structure*, 3(4):045001, 2021.

[122] E. Karaca, P. J. P. Byrne, P. J. Hasnip, and M. I. J. Probert. Prediction of phonon-mediated superconductivity in new Ti-based M_2AX phases. *Scientific Reports*, 12(1):13198, Aug 2022.

[123] R. Kubo, M. Yokota, and S. Nakajima. Statistical-mechanical theory of irreversible processes. ii. response to thermal disturbance. *Journal of the Physical Society of Japan*, 12(11):1203–1211, 1957.

[124] J. Callaway. Model for lattice thermal conductivity at low temperatures. *Phys. Rev.*, 113:1046–1051, Feb 1959.

[125] M. G. Holland. Analysis of lattice thermal conductivity. *Phys. Rev.*, 132:2461–2471, Dec 1963.

[126] M Omini and A Sparavigna. An iterative approach to the phonon Boltzmann equation in the theory of thermal conductivity. *Physica B: Condensed Matter*, 212(2):101 – 112, 1995.

[127] D. A. Broido, M. Malorny, G. Birner, Natalio Mingo, and D. A. Stewart. Intrinsic lattice thermal conductivity of semiconductors from first principles. *Applied Physics Letters*, 91(23):231922, 2007.

[128] W. Li, J. Carrete, N. A. Katcho, and N. Mingo. ShengBTE: a solver of the Boltzmann transport equation for phonons. *Comp. Phys. Commun.*, 185:1747–1758, 2014.

[129] G.A. Slack. Nonmetallic crystals with high thermal conductivity. *Journal of Physics and Chemistry of Solids*, 34(2):321–335, 1973.

[130] Chris J. Pickard and Francesco Mauri. All-electron magnetic response with pseudopotentials: NMR chemical shifts. *Phys. Rev. B*, 63:245101, May 2001.